THE UNIVERSITY OF WARWICK

CHARACTERISATION OF ADVANCED HIGH STRENGTH STRIP STEELS USING ELECTROMAGNETIC SENSOR SYSTEM

By

Mohsen Aghadavoudi Jolfaei

A thesis submitted to
The University of Warwick
For the degree of
DOCTOR OF PHILOSOPHY
January 2019

Steel Processing Group
WMG, University of Warwick

Abstract

The mechanical properties of steel are strongly influenced by its microstructural features such as phase balance, grain size, dislocations and precipitates. In order to obtain accurate quality control of steel products, it is desirable to be able to monitor the mechanical properties non-destructively. It is known that the low frequency inductance (where the effect of eddy currents are negligible) measured using an EM sensor depends on the relative permeability of the sample and that the permeability is affected by microstructural parameters (i.e. phase fraction / distribution and, to a lesser extent, grain size are the important features in dual phase, DP, steel).

A variety of electromagnetic sensors have been reported for non-destructively assessing the state of steel microstructures including; monitoring the recovery and recrystallisation processes in-situ during heat treatment, phase transformation and detecting decarburisation in steel rod both on-line and off-line, etc. Recently it has been shown that electromagnetic sensors can measure the phase fraction in DP steel but the effect of strip thickness was not assessed.

This research work discusses the development of an EM sensor system that can be used to assess the microstructure (and hence mechanical properties) of commercially produced DP steels (in particular phase balance and grain size) with a range of

thicknesses in a steel works test house environment, specifically, it focuses on employing an EM sensor system in the prediction of ultimate tensile strength for DP steels of any sheet thickness.

In this project, a set of heat treated DP600 grade of 1.4mm thickness and commercial DP steel samples, including DP600, DP800 and DP1000 with a range of strength levels and thicknesses, and produced in different strip mills, have been assessed. The sensor outputs have been correlated to microstructural phase fraction and mechanical properties.

Firstly, the magnetic properties of commercial DP steel samples were investigated through the major hysteresis loop and minor hysteresis loops. Measured coercivity from the major loop showed that the coercivity was affected by phase fraction (ferrite/martensite percentage) and ferrite grain size where the coercivity decreased with increased ferrite fraction.

Three types of minor loop configurations were used to derive incremental permeability values; the minor loop deviations from the initial magnetisation curve (μ_{Ic}); the minor loop deviations from the main B-H loop (μ_{BH}) and the minor loop deviations from amplitude sweep (μ_i). It was found that although the incremental permeability values are not precisely the same for the three sets of measurements, similar trends for the DP samples can be observed where the incremental permeability values are affected by the phase fraction and ferrite grain size.

The effect of magnetic field on permeability for the DP steels was studied. It was shown that the incremental permeability increases with the applied field amplitude until

reaching a maximum value at a certain applied field amplitude (i.e. very close to the coercivity values) and then drop at higher applied field amplitude and converge to a similar permeability value. The initial gradient and the peak position for the samples are different and would allow them to be distinguished from each other. It was observed in the commercial DP steels with a range of ferrite fraction (72 to 79%) and a range of average ferrite grain size (from 6 to 10μm), that the effect of ferrite grain boundaries on permeability is more significant than the effect of ferrite fraction within the range studied.

Finally, the measured magnetic properties were used to develop a link between microstructure and mechanical properties for DP steels, using a readily deployable EM sensor that can be used with large strip steel samples. The deployable sensor geometry and operation rely on a relatively low magnetic field being generated in the sample and therefore low field incremental permeability being the relevant material parameter being assessed. Initially, the effect of ferrite fraction for the laboratory heat-treated DP600 samples, with the same thickness (1.4mm), on EM sensor output signal (i.e. mutual real inductance) was investigated. It was found that the real inductance value at a low frequency (below approx.100 Hz) is dominated by differences in the relative permeability of the samples, showing an approximately linear trend of increasing low frequency inductance value with increasing ferrite content. The increasing amount of ferrite, which possesses a much higher relative permeability than martensite, showed higher real inductance value (in the range of 35 -70% ferrite fraction in these DP steels). The measured real inductance at a frequency of 10Hz was compared with the mechanical property (hardness). An approximately linear decrease in real inductance at 10 Hz with the hardness value was found for these samples.

EM sensor measurements were then carried out for the commercial DP600, DP800 and DP1000 samples with different thicknesses (1 to 4 mm). The EM sensor system showed a significant effect of thickness on the signal with thicker strip showing a much higher mutual inductance value for the same microstructure. This is due to the skin depth (for this sensor, operation frequency and material characteristics) being larger than the sample thickness, therefore a thicker sample gives a large sensor response. To deal with this problem, a calibration curve (a plot of real inductance versus permeability for different thickness of material) was constructed using a FE model for the sensor and sample geometry. Therefore, an electromagnetic sensor – sample FE model, developed in COMSOL multi-physics software, has been developed to determine the relationship between the low magnetic field relative permeability and microstructure (phase balance and grain size). The model has been validated using commercial DP steel sheets of 1 to 4 mm.

It was found that the ferrite grain size affects the magnetic properties in DP steels as the grain boundaries act as effective pinning points to magnetic domain movement. Therefore, the magnetic permeability in DP steels is affected by ferrite grain size and ferrite fraction, both of which affect the tensile strength, therefore a single relationship between permeability and tensile strength results. The low field relative permeability, which is the permeability value derived from the EM sensor (e.g. U-shaped sensor), can therefore be used to predict the tensile strength in commercial DP steels.

The relationship between permeability and field was employed to develop the technique. Therefore, U-shaped sensor modification was carried out to increase the accuracy of tensile strength determination, this was done as part of a case study for Tata Steel Jamshedpur to evaluate DP steels.

List of Publications

1. M. Jolfaei, J. Shen, A. Smith, L. Zhou, C. Davis, Non-Destructive Measurement of Microstructure and Tensile Strength in varying thickness commercial DP Steel Strip using an EM Sensor, Journal of Magnetism and Magnetic Materials, 473 (2019) pp 477-483

2. M. Jolfaei, J. Shen, A. Smith, L. Zhou, C. Davis, EM Sensor System for Characterisation of Advanced High Strength Strip Steels, in: Dominique Lesselier, C. Reboud (Eds.) Electromagnetic Non-Destructive Evaluation (XXI), IOS Press, Paris, 2017, pp. 49-56.

In addition there are papers under preparation:

- Magnetic characterisation of microstructural feature distribution in DP steels by major and minor BH loop measurements, Journal of Magnetism and Magnetic Materials
- Non-Destructive Measurement of Microstructure and Tensile Strength in varying thickness commercial DP Steel Strip using Magnetic Barkhausen Noise technique, NDT & E International

Acknowledgements

I would like to extend my heartfelt thanks to a variety of people, groups, universities and organizations for their enormous contribution to this PhD research.

First and foremost, I am eternally grateful for the precious assistance given by my academic supervisor, Professor Claire Davis, who has provided me extensive professional guidance and constructive suggestions during the planning and development of this research work. As my truly dedicated teacher and mentor, she has perfectly shown me, by her example, what a good scientist and person should be. Her enthusiastic encouragement and invaluable advice in keeping my progress on schedule have been very much appreciated, even during tough times in the PhD pursuit. Without her patience, unending inspiration, persistent support, excellent technical guidance and immense knowledge this work would not have materialized.

My deepest appreciation goes to Dr Lei (Frank) Zhou for sharing his expertise so willingly and for being so dedicated to his role as my co supervisor.

My special and sincere thanks are extended to my colleague Dr Jialong Shen for his support in modelling part of this research.

I am also especially indebted to my industrial supervisors, Dr Andrew Smith and Dr Kees Bos from Tata Steel. My special and sincere thanks Dr Jun Liu, for his generous contribution of time and professional expertise.

Professor Anthony Peyton and Dr John Wilson from the University of Manchester who have been supportive of my research and worked actively to provide me a part of equipment during my PhD.

I am also hugely appreciative to all of my colleagues at the University of Warwick: Dr Carl Slater, Dr Russ Hall, Dr Mo Ji, Dr Daniela Proprentner, Dr Geoff West, Dr Stephen Spooner, Dr Panos Efthymiadis, Raul Chinchilla and Will Jacobs for always creating a great environment and for their experienced guidance and continued support.

My profound gratitude also goes to Dr Martin Strangwood from the University of Birmingham, Professor Reza Ebrahimi- kahrizsangi from IAU-Iran, Dr Rajat K. Roy from Tata Steel Jamshedpur, John Hinton from Primetals Technologies Limited, Dr Sally Parker from British Steel and Dr Evans Mogire from Buehler.

And also to the United Kingdom Engineering and Physical Sciences Research Council (EPSRC) and Tata Steel UK for financially funding this research.

Nobody has been more significant to me in the pursuit of this project than my family members and friends. I would like to profoundly thank my lovely wife Baharak Askarikeya for her unwavering and faithful support, mass sacrifices, and utmost patience throughout my entire PhD journey, especially my daughter for understanding my difficult situation and I deeply apologize for not being able to spend time with her during these years.

I gratefully thank my mother Zohre Zamani and my father Dr Nasrolah Jolfaei, who gave me the best education and catered for all our needs. No matter where life takes me, I will forever remember him with love.

Table of contents

Word Count = 46,726

List of figures

List of tables

1 Introduction

1.1 Background

The increasing requirements of fuel efficiency as well as the need to comply with the international environmental regulations regarding greenhouses gas (GHG) emissions, recyclability and resource reduction, have motivated and/or even forced the automakers to produce more fuel-efficient models by decreasing their weight. In order to provide passenger safety and vehicle performance that fulfils the automakers' requirements and takes advantage of the new high strength steels, a new vehicle architecture based on novel design concepts has been developed. The use of advanced high strength strip steels with both high strength and excellent formability offers the unique option of combining weight reduction (by using thinner gauge of material) with improved passenger safety.

Dual phase (DP) steels, a first generation of Advanced High Strength Strip (AHSS) alloys, are being increasingly used by the automotive industries, as they are a suitable alternative for plain carbon steel components such as bumper, body side inner/outer and other automotive applications [1, 2] . The DP steels are characterised by a combination of continuous yielding behaviour and relatively large tensile strength that results in excellent formability [3].

DP steels have a microstructure consisting of a continuous soft ferrite matrix and hard dispersed second phase (martensite) particles throughout the matrix. This

microstructure can be compared with a composite where the hard-soft mixture contributes to a high ultimate tensile strength, high strain hardening rate and long period of yielding [4]. Therefore it is possible to get a combination of high strength and suitable ductility which is almost impossible in conventional steels [5].

The simplest way to achieve this microstructure is intercritical annealing of an initial ferritic-pearlitic structure in the austenite-ferrite region then followed by adequately rapid cooling to allow the transformation of austenite to martensite [6]. An alternate approach is via controlled cooling on the run out table and subsequently on coiling after hot rolling of strip. This has the advantage of increased efficiency (no subsequent heat treatment stages) but is also more challenging to control to achieve the desired microstructures, Figure 1.1.

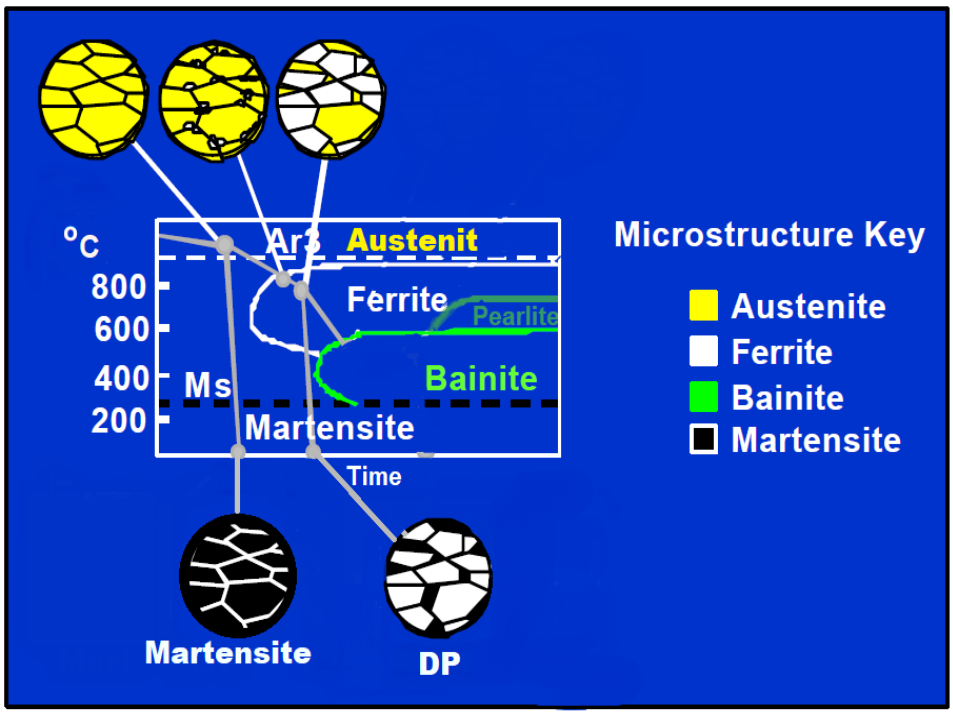

Figure 1.1: Cooling patterns and microstructural evolution in the production of martensite and DP steel. Martensitic steels are produced from the austenite phase by rapid quenching, dual phase steels are produced by controlled cooling from the austenite phase (in hot rolled products) or from the two-phase ferrite + austenite phase

(for continuously annealed and hot dip coated products) to transform some austenite to ferrite before rapid cooling to transform the remaining austenite to martensite [6].

Much research has been done on the role of phase percentage of martensite, as one of the most important features affecting the mechanical properties of DP steels. It has been found that a higher volume fraction of martensite gives an increase in the yield, ultimate tensile and hardness of DP steel, while a decrease in the elongation of DP steel is seen [7-10]. For example, Marder et al. [11] discovered a linear relationship between martensite volume fraction between 10 - 65% and ultimate tensile strength. Determination of phase percentage (i.e. martensite fraction) is therefore very important to allow prediction of mechanical properties from microstructure in DP steels.

A variety of techniques can be used to characterise the microstructure of DP steels, the most frequently used is optical microscopy and/or scanning electron microscopy (SEM) on polished and etched samples. These conventional methods to obtain phase information are destructive, and time consuming, as they require a small piece of material to be removed from the strip / component.

In recent years, the use of magnetic techniques based on EM sensors, for non-destructive testing have increased [12-21]. These range from systems where high magnetic fields can be generated so that coercivity can be determined, to those where low magnetic fields are used. It has been shown [22] that there is potential for using a low magnetic field U-shaped EM sensor to distinguish the microstructure in DP steels within a certain range of ferrite fraction (i.e. 35-72%).

Previous work [22] has established finite element (FE) based models to relate the microstructure (phase balance) to the magnetic property of low field permeability, allowing the microstructure (ferrite fraction) to be determined from the EM sensor

signal. In that work only single sheet thickness DP steel samples were considered and a full sensor model, which could take into account sample geometry, was not available. Only simple correlative relationships between the EM sensor signal and mechanical properties were therefore available for the single sheet thicknesses, and only a limited number of samples had been tested.

To develop a deployable system for accurate quantification of all DP steel strip samples, and hence properties, a much larger range of samples needs to be considered, and a calibrated sensor that can measure different thicknesses is required.

In addition the role of applied magnetic field on the signal to allow sensor optimisation is important.

1.2 Aim

The aim of this research is to investigate and develop the link between EM sensor measurements, microstructure and mechanical properties in a range of advanced high strength strip steels in varying thickness, in particular dual phase steels. Whilst it is known that EM sensors are sensitive to the phase fraction in DP steels, and hence there is potential for a deployable sensor to be used in a steel works test house environment to determine microstructure, the effect of strip thickness and applied magnetic field, within the range generated by the deployable EM sensors, has not been assessed. The aim of this research is to develop and calibrate an EM sensor system that can measure the permeability of commercial strip steel, with a range of thicknesses, and to relate this to the microstructure, specifically phase fraction. The effect of ferrite fraction and ferrite grain size on the permeability, and hence EM sensor signal and consequently predictability of mechanical properties was also be assessed in the latter stages of the work. In addition a modified sensor system is proposed to increase the reproducibility and sensitivity to measuring tensile strength in DP steels, based on the understanding developed for the effect of applied field on permeability and making changes to the sensor design through use of an FE model.

1.3 Achievements and Contributions of this Thesis

This thesis presents an approach for characterisation of dual phase steel microstructure and the technique has been implemented to predict the tensile strength (and phase fraction) by designing an EM sensor system for the EM properties of commercial DP steels.

The designed laboratory sensor system can quantitatively predict mechanical properties (i.e. tensile strength) of commercially produced DP steels for any sheet thickness. As the sensor is relatively small (sensor dimensions of 100mm x 25mm) it could be used to assess any variations in properties across large sheets for product uniformity assessment and/or to allow more targeted microstructural or mechanical property characterisation. Moreover, information about the ferrite fraction in the steel can be obtained from the EM sensor if the grain size remains similar (i.e. similar prior-processing history), which can be used to assess the quality of the heat treatment (for example temperature-time achieved during annealing to produce the DP microstructure).

In addition, the relative influences of grain size and phase balance on the tensile strength and magnetic properties in dual phase steels are presented to provide fundamental understanding for the relationship between EM sensor values and strength in these materials.

2 Theory of magnetism and magnetic properties

This chapter presents an overview of the fundamental theories related to magnetism and magnetic properties of materials. First, the theory of magnetism and magnetic fields will be explained. Then, the fundamental magnetic division of material, magnetic domain, hysteresis loops and Barkhausen noise effect will be covered. Following that, the different classes of permeability and the effective factors on magnetic properties of steel will be discussed.

2.1 History of magnetism

The history of magnetism dates back to 600 B.C and magnetism has initially been explained to the ancient world as the “tractive force that exists between two bodies” [23]. The Englishman William Gilbert was the first one who investigated the phenomena of magnetism scientifically. W. Gilbert’s findings suggested that magnetism was the soul of the Earth. Oersted found a link between magnetism and electricity. The effect of magnetic and electric fields on one another was reported by Ampere and Faraday but the theoretical foundation to the physics of electromagnetism was established by Maxwell [24]. The fundamental electromagnetism relationships rely on Maxwell’s equations, which describe how electric charges and electric currents

create electric and magnetic fields. Moreover, they describe how a magnetic field can generate an electric field and vice versa [25].

2.2 Magnetic field

Magnetic field strength and the intensity of magnetisation are two fundamental magnetism quantities. When a magnet is placed close to a piece of iron, a magnet attracts the piece of iron even though the two are not in contact; this action at a distance is said to be caused by the magnetic force or magnetic field [23]. This field might be explored when iron filings are sprinkled around a magnet; they appear in lines, converging towards the poles. These lines indicate the direction of the magnetic field and show the lines of force emanating from the S pole and converging on the N pole [26]. The conceived endless lines pass from a magnetised material into the air at a north pole, enter again at a south pole, and pass through the material from the south pole back to the north pole to form a closed loop. [23].

2.3 Magnetic field vectors

It is important to define the magnetic properties of materials in terms of a number of quantitative field vectors. The magnetic field can be generated either by an electrical current or by a permanent magnet. One of the simplest ways to generate the magnetic

field is by passing an electric current through a multi turn coil or solenoid and hence producing a magnetic field, which is calculated by Equation 2-1 [23];

$$H = \frac{NI}{L} \qquad \textit{Equation 2-1}$$

Where *N* is the number of turns in the coil, *I* is the electric current in the coil in ampere, *L* is the length of the coil. A schematic diagram of such arrangement is shown in Figure 2.1. As it is clear from Figure 2.1 and Equation 2.1, the magnetic field strength *H* within a coil depends on the number of the turns *N*, carrying a current magnitude *I*, and the length of the coil *L*. The units of magnetic field strength *H* are ampere-turns per meter, or just amperes per meter. The magnitude of the internal field strength in a substance that is related to an *H* field is called the magnetic induction or magnetic flux density, donated by symbol *B*. The units for *B* are webers per square meter (Wb/m^2) or teslas (*T*). Both *H* and *B* are field vectors, being characterised by direction and magnitude. As can be seen in Figure 2.1, the relationship between the magnetic flux density *B* and the magnetic field strength *H* can be expressed by Equation 2.2 [23];

$$B = \mu . H \qquad \textit{Equation 2-2}$$

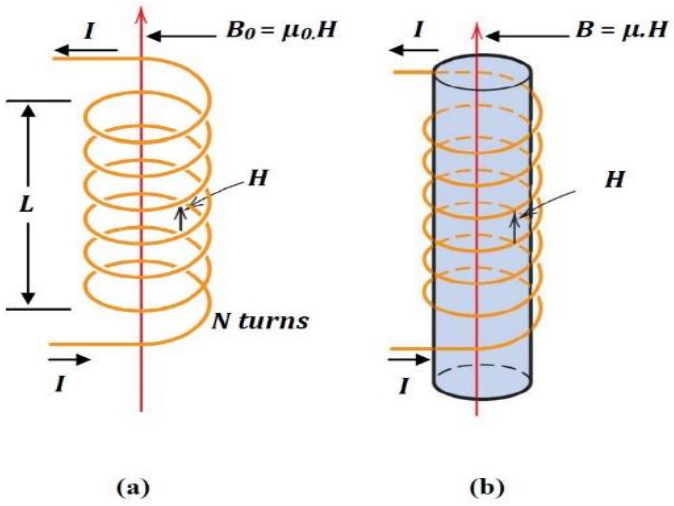

Figure 2.1: (a) The magnetic field strength (H) as generated by a cylindrical coil depends on the number of turns (N), the applied current (I) and the coil length (L). The magnetic flux density in the presence of a vacuum (B_0) is equal to permeability of a vacuum (μ_0 =1.257 x 10^{-6} Henries /metre) or 4π x 10^{-7} (H/m) multiplied by the magnetic field (H). (b)The magnetic flux density within a solid material (B) is equal to the permeability of the solid material (μ) multiplied by the magnetic field (i.e. B = μ. H) [27].

The parameter μ is called the permeability, which is a property of the material through which the magnetic field passes and in which *B* is measured. This indicates that the value of magnetic flux density *B* depends on the material and the applied magnetic field strength [23].

The units of permeability are henries per meter *(H/m)* or webers per ampere-meter *(Wb/A.m).* This is also the case for in vacuum illustrated in Figure 2.1, where the magnetic flux density in vacuum can be expressed by Equation 2-3 [23];

$$B_0 = \mu_0 . H \qquad \textit{Equation 2-3}$$

In addition to the above parameters, several parameters may be used to describe the magnetic properties of a material. One of these parameters is the relative permeability which is the ratio of the permeability in a material to the permeability of free space, denoted by symbol μ_r, as presented in Equation 2.4. The permeability or relative permeability of a material is described as the measure of the degree to which the material can be magnetised or the degree of magnetisation in a material when a *B* field can be induced in the presence of an external *H* field [23].

$$\mu_r = \frac{\mu}{\mu_0} \qquad \textit{Equation 2-4}$$

Magnetisation, M, is another field quantity of the solid, defined by Equation 2.5. It is clear that the magnetic flux density *(B)* is a function of magnetic field strength (*H)* and magnetisation of the material (*M*) in the presence of a magnetic field strength (*H*), the magnetic moments are likely to line up with the field and to reinforce it by virtue of their magnetic fields; in Equation 2.5, the term $\mu_0 M$ is a measure of this contribution [28].

$$B = \mu_0 H + \mu_0 M \qquad \text{Equation 2-5}$$

2.4 Origins of Magnetic Moments

The variation in macroscopic magnetic properties of materials is a consequence of magnetic moments associated with individual electrons. Since some of these concepts are relatively complicated and involve some quantum-mechanical principles, only an overview will be provided.

Each electron in an atom possesses magnetic moments which originate from two sources, one is from the orbiting electron's motion as illustrated in Figure 2.2 (a) and the second one is from the spinning electron which is directed along the spin axis as shown in Figure 2.2(b). A moving charge (electron) may be considered as a small current loop and causes a very small magnetic field to be generated, which in turn makes a small magnetic moment along its axis of rotation [29].

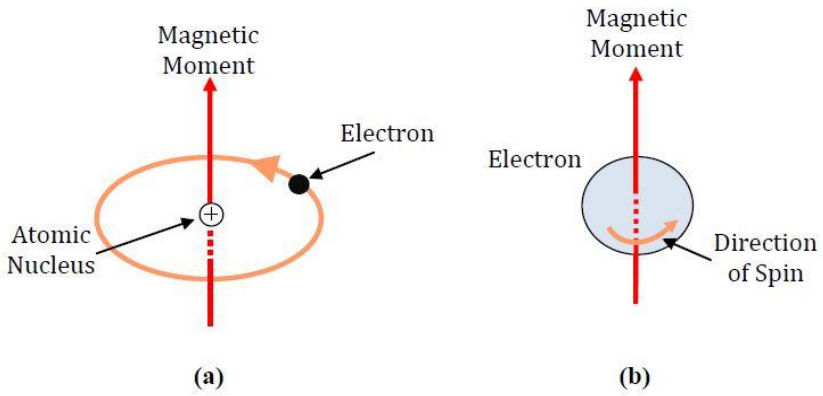

Figure 2.2: Schematic illustration of the magnetic moment originates from orbital motion (a) and electron spin (b)[27].

Electron spin generates another magnetic moment that can be only in an "up" direction or in an antiparallel "down" direction. Therefore, every electron in an atom may be

considered as a small magnet with permanent orbital and spinning magnetic moments [29].

2.5 Fundamental Magnetic Division of Materials

Solids and materials can be classified into three major groups based on their magnetic properties behaviour. The types of magnetism include ferromagnetism, paramagnetism and diamagnetism. All materials show at least one of these types, and the behaviour depends on the response of electron and atomic magnetic dipoles to the application of an externally applied magnetic field. The following section will initially include an explanation on the characteristic of the three main classes of magnetisation; from which the base material for this thesis will also be stated.

2.5.1 Ferromagnetism

Ferromagnetic material can be magnetised by an external magnetic field and these materials have the ability to maintain their magnetic property in the absence of the external field [30]. In ferromagnetic materials, in the absence of an external field there are local magnetic moments with random alignments (domains) and hence, zero overall magnetisation. The presence of an external magnetic field aligns such local magnetic moments into a larger domain, generating a greater magnetisation for the material. In addition, an increase in the magnetic field will increase the material's magnetisation. Moreover, these materials have the ability to maintain their magnetic properties in conditions where there is no external magnetic field. It means on removing the external

magnetic field, magnetisation does not return to zero and a record of the applied field remains in these materials, as depicted in Figure 2.3 (a) [23].

As mentioned earlier for each electron in an atom the spin magnetic moment is $\pm \mu_B$ (spin up and down) and for the magnetic moment originated from the orbital motion is $m_l \mu_B$, where m_l is the magnetic quantum number of the electron. The net magnetic moment includes both spin and orbital contributions. In an atom with completely filled electron shells there is total cancellation when all electrons are considered. In this case, materials composed of atoms with completely filled electron shells cannot be capable of being permanently magnetized [31, 32].

Common ferromagnetic materials are iron, cobalt, nickel and their alloys [30, 33, 34]. In the transition metals that possess unpaired electrons, the energy levels in 3s and 3d shells are similar and the electron clouds in these shells show an overlapping state. The quantum mechanical forces of exchange acting between electrons in neighbouring atoms cause the electrons to align such that their spins are parallel to each other [34]. The local alignments result in local magnetisation but in the absence of any external field, overall magnetisation is zero [30, 34] . In the presence of a magnetic field, the magnetic dipole experiences a torque which tends to be aligned into the magnetic field direction. When all the local magnetic moments are aligned with the external magnetic field at a given level of magnetic field, a stable magnetic structure is formed and at this stage the material remains permanently magnetic [30]. The important attributes of ferromagnetic materials are dependence of permeability on the magnetic field strength and on the prior magnetic history (hysteresis). These materials approach a finite limit of the magnetisation as the field strength is indefinitely increased [23].

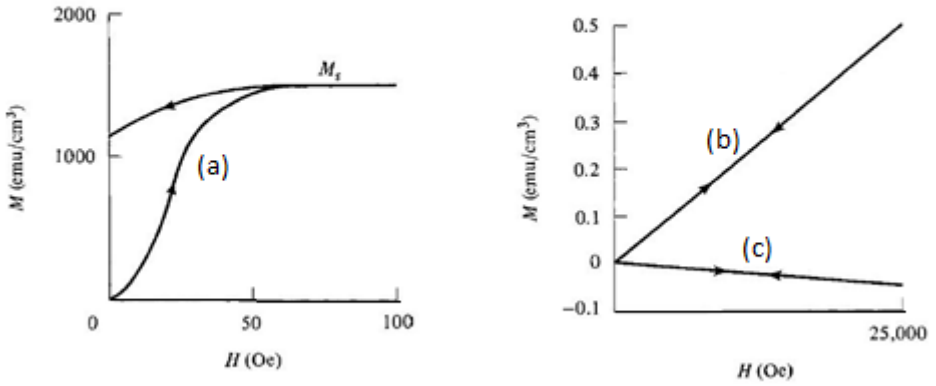

Figure 2.3: Typical magnetisation curves of (a) a ferromagnetic; (b) a paramagnetic; and (c) a diamagnetic material [23].

2.5.2 Paramagnetism

The total magnetic moment in paramagnetic materials with a complete electron shell becomes zero due a balance in the spin up / down directions. The permeability of paramagnetic materials is only slightly greater than one usually between 1 and 1.001. These materials do not show any hysteresis and their permeability is independent of temperature and field strength and they cannot be magnetised using a field [30, 35]. Among the paramagnetic substances are many of the salts of iron, the elements potassium, sodium and oxygen and ferromagnetic materials above their Curie temperature point [23].

2.5.3 Diamagnetism

Diamagnetic materials are a class of materials with a very weak form of magnetism, where the magnetisation is directed oppositely to the field. It means that their permeability is somewhat less than one. Figure 2.3(c) illustrates the response of magnetisation for a diamagnetic material with applied magnetic field. The magnitude of the induced magnetic moment is extremely small, and in a direction opposite to that of the applied field. Diamagnetic substances, therefore, are repelled from the poles of an electromagnet, moving towards weaker fields [23] .

2.6 Magnetic domains

In magnetic materials, a magnetic domain is a region within the material in which the magnetisation is in a uniform direction and the magnetic fields (dipole moments) of atoms are aligned and grouped together [23, 35]. Figure 2.4 illustrates a clear example of the domain structure in ferrite grains of a specimen of fully killed normalized steel (FKN). Several domains with different shapes and sizes can be observed in each grain. In Figure 2.4 (a) and Figure 2.4 (b), the domain walls can be clearly revealed with their contrast reversing from bright to dark or vice versa between the over and under focused images. Figure 2.4 (c) indicates the grain boundaries in the microstructure. For more clarity, Figure 2.4 (d) schematically illustrates the grain boundaries and domain walls. The grain boundaries have a major effect on the domain size and configuration. Closure domain structures (e.g. A and B) are visible next to grain boundaries and the grain boundary orientation changes sharply (e.g. at C, D and E) throughout the microstructure. Complex interactions take place between domain walls within the

ferrite grains (e.g. at F, G, H and I) [36]. Magnetic domains are separated by boundaries called Bloch walls [35], the ease of movement of these walls is a very important factor in the use of magnetic non-destructive measurement techniques such as electromagnetic sensors and MBN [20].

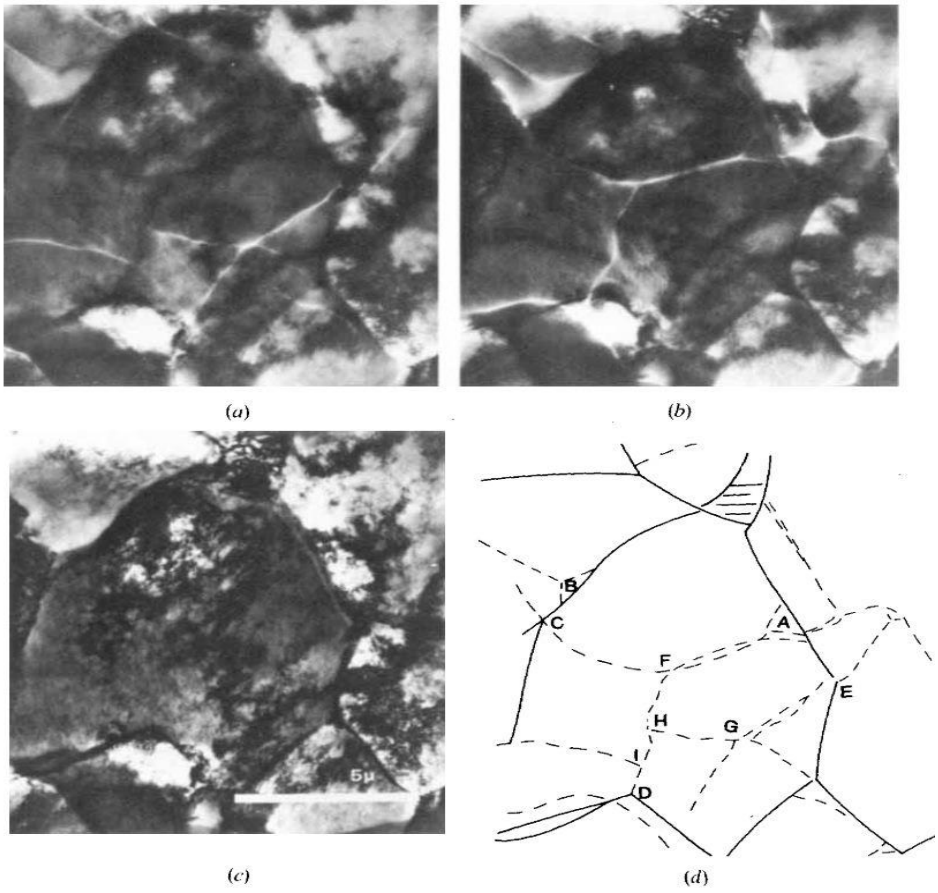

Figure 2.4: Electron micrographs of the domain structure, the domain boundaries and the grain boundaries in ferrite grains of an FKN steel. (a) under focused and (b) over focused images revealing the domain structure, (c) grain boundaries, (d) illustrating domain boundaries (dashed lines and the grain boundaries (continuous lines), A, B closure domain structures; C, D, E sharp changes in grain boundary orientation; F, G, H, I interactions between domain walls within a ferrite grain [36].

The domain wall is shown schematically in Figure 2.5. In ferromagnetic materials, the domain walls are where the magnetisation rotates from one easy direction to another direction, the domains rotate towards the direction of applied field and consequently makes a greater flux density in the material [33, 35]. Therefore, domain walls must move to allow the domain to grow in size. Figure 2.6 illustrates the magnetisation process and the effect of the applied field on the domain structure of a typical ferromagnetic material and Figure 2.7 shows the domain wall movement and pinning in the magnetisation process. For the initial applied field only the domains aligned in the direction of the applied field will grow while domains that are perpendicular to the applied field may change shape but there is no change in their polar direction [32]. The domains that are perpendicular to the applied field will start to rotate when stronger fields are applied and are destroyed once the material reaches saturation [37]. If the domain walls return to their original position this means that the magnetisation is weak [23]. If the applied fields are strong enough and have adequate energy to move domain walls past crystalline imperfections such as precipitates, dislocations and grain boundaries then returning back for the domain wall to its original position may not possible, i.e. when the field is removed from the material, these defects may act as obstacles to domain wall movements and prevent the domain walls from returning to their original position. Therefore, an opposite applied field is required to return the material to its original state [37].

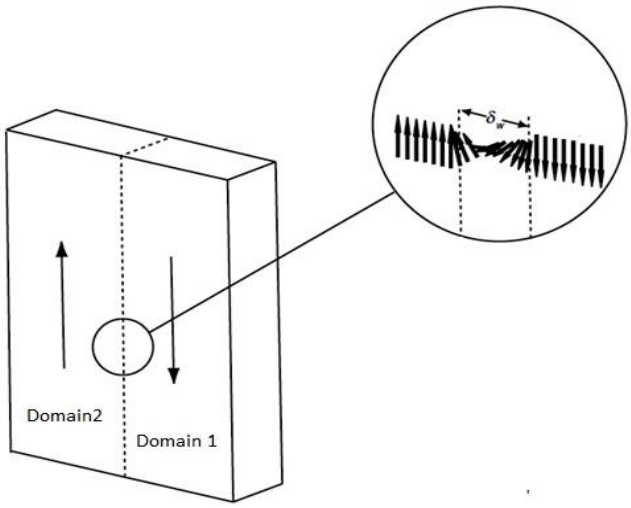

Figure 2.5: Schematic diagram of 180° domain wall structure [34]

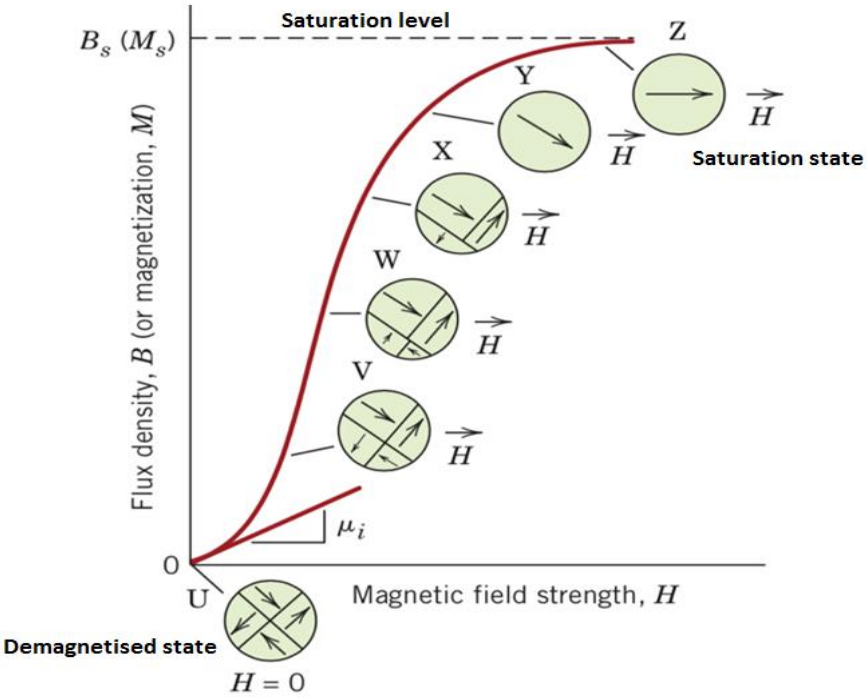

Figure 2.6: Magnetisation process and effect of applied field on the domain structure of a typical ferromagnetic material [32].

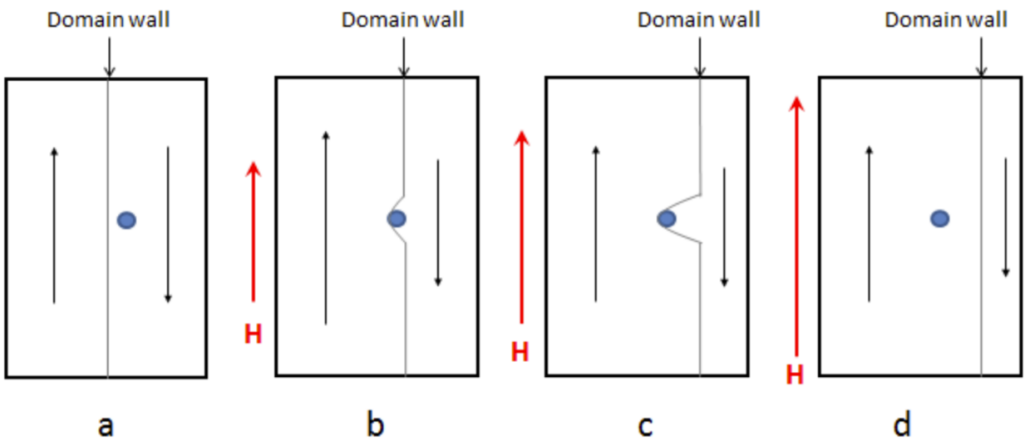

Figure 2.7: Schematic illustration of domain wall movement and pinning in the magnetisation process. (a) Sample in initial state without any external field (unmagnetised state), domains are evenly sized; (b) low magnetic field H applied to the sample, domain parallel with the applied magnetic field grows at the expense of the domain which is antiparallel to the applied field, domain wall becomes pinned; (c) stronger magnetic field H is applied, further movement of the domain wall takes place but the defect (pinning point) cannot be overcome; (d) high magnetic field H is applied and domain wall passed through defect, the domain wall is now free to move and the favourable domain grows [32, 38].

In ferromagnetic materials, the formation of magnetic domains reduces the overall magnetic energy. Although due to the demagnetising field, the number of magnetic domains increases, and as the dipoles within domain walls are not aligned in the easy magnetisation direction this makes the overall energy of the system increase. Therefore a steady state (i.e. minimum energy state) can be reached, by a specific number of

domains in a special arrangement, which is influenced by parameters such as the grain size and shape, any crystallographic texture and the intrinsic magnetic properties of the material [39].

2.7 Magnetic Hysteresis

The relation between magnetic field strength *H* and magnetic flux density *B* was mentioned in Equation 2.2 and that equation can be expanded as Equation 2.6;

$$B = \mu H = \mu_0 \mu_r H = \mu_0 (H + M) = \mu_0 (1 + \chi) H \qquad \textit{Equation 2-6}$$

where *M* represents the magnetisation of the material which represents how strongly a region is magnetised and χ is the magnetic susceptibility which indicates the degree of magnetisation of the material in response to an applied magnetic field. Equation 2.6 indicates the flux density is influenced by the magnetic field strength, via permeability and by the magnetic susceptibility of the material [23].

The relation between magnetic field strength *H* and magnetic flux density *B* in a ferromagnetic material can be illustrated in a complete hysteresis loop (Figure 2.8). In a ferromagnetic material without previous magnetising history (demagnetised material) when the magnetic field strength (*H*) increases, magnetic flux density increases proportionally along "*Oa"* in Figure 2.8, until the saturation point *"a". The point "a" is* called the magnetic saturation point at which most of the magnetic

domains are aligned. If the magnetic field strength (*H*) reduces to zero, *B* does not reach zero due to the residual magnetism remaining within the material. This value of induction (*B*) for when field strength is zero (i.e. $H = 0$) is referred to as the residual induction (B_r) and called remanence. Ferromagnetic materials have this ability to maintain a magnetic field more easily after an applied magnetic field has been removed [23, 35].

A reverse magnetic force *H* (called coercive force H_c) is needed to reduce the magnetic flux to zero, at point "*c*" in Figure 2.8, this point is called the "coercive point" and this process is called demagnetisation. The coercivity (*Hc*) describes the intensity of the magnetic field required to reduce magnetisation to zero after a ferromagnetic material has been magnetised to its saturation point [30, 35]. Thus in ferromagnetic materials, coercivity may determine the materials resistance to demagnetisation. The coercivity is measured in Oersted or ampere/meter [23].

Ferromagnetic materials with low coercivity are known as magnetically soft and can be used to make components which require rapid magnetisation or demagnetisation such as magnetic tapes or transformer cores and materials with high coercivity are known as magnetically hard and are used to make permanent magnets [23].

Further increasing the reverse field causes the material to reach the opposite saturation point *"d"* (the path *cd* in Figure 2.8). If the magnetic force gradually decreases to zero, the residual magnetism present in the material would be equal to the value of "*b"* , but in reverse at point *"e" in* Figure 2.8 [35, 40].

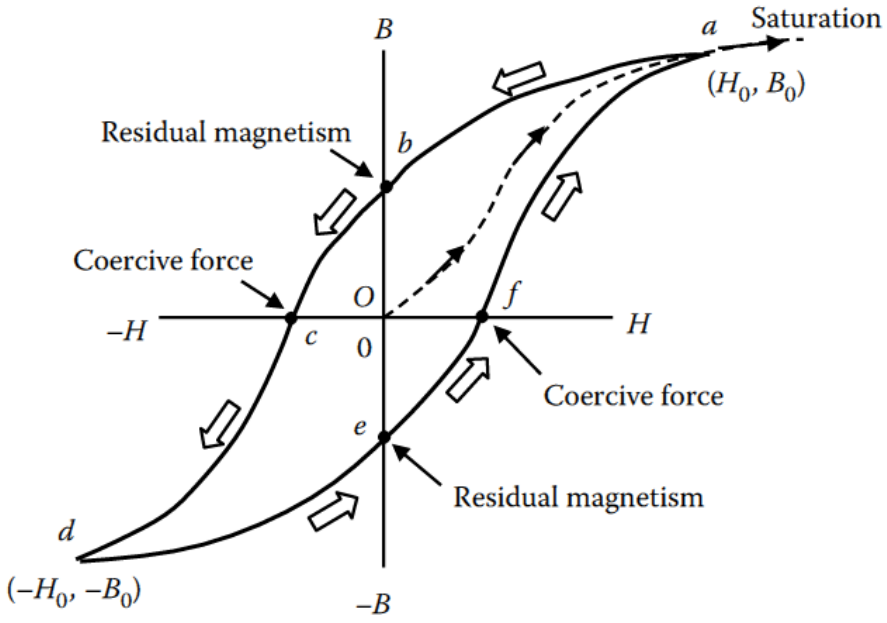

Figure 2.8: A magnetic hysteresis loop for a ferromagnetic material, magnetisation curve (dotted) and hysteresis loop (solid), some important magnetic quantities illustrated [40] .

The lag of induction behind the reduction in applied magnetic field shows that for any magnetic measurement, the first concern is prior magnetic history of the material. It can have particular implications for any electromagnetic non-destructive testing technique, as the measurements that are taken can be misrepresentative therefore depending on the type of measurements it is necessary to demagnetise the specimen [30, 35].

2.8 Classes of Permeability

The normal permeability or cyclic permeability is often denoted as permeability *(μ),* and is typically measured as the ratio of B/H, when the material is under the “cyclic

magnetic state" [23]. It is worth noting that for this measurement the material is initially demagnetised by applying a high enough amplitude field to achieve saturation state, then reducing the cycle magnetic field amplitude incrementally to zero [23, 30].

Permeability can be defined in a number of ways such as initial permeability, maximum permeability, incremental and differential permeability. Figure 2.9 illustrates the permeability curve of iron and the permeability curve is represented by plotting the permeability μ against either magnetic field (H) or magnetic flux density (B). In any case, the permeability curve increases from a point on the permeability axis above the origin (the initial permeability is non-zero) to reach a maximum value, called the maximum permeability, and falls off rapidly and then more slowly toward a value of one (not zero). The maximum permeability (μ_{max}) is the largest value of normal permeability gained by varying the amplitude of magnetic field strength, H [63]. The permeability curve may describe the behaviour of a material [30, 39].

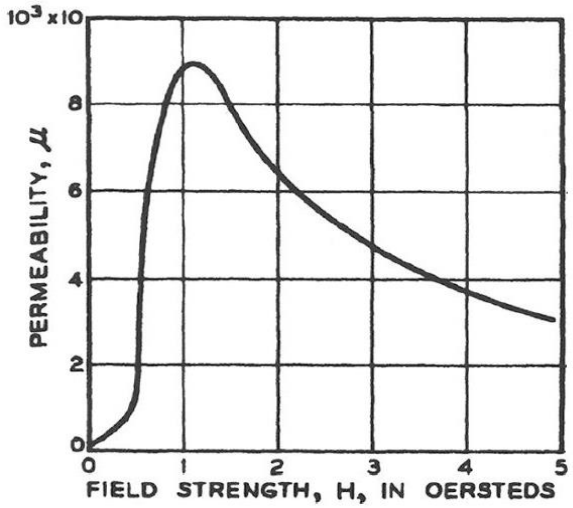

Figure 2.9: Permeability curve of Iron as a function of field, the maximum permeability is the largest value of normal permeability[23].

Figure 2.10 shows the initial permeability of iron, nickel, silicon – iron and Permalloy. The initial permeability is the limit approached by the normal permeability as *H* and *B* are decreased toward zero and initial permeability is usually considered to be the value at very low magnetic field strength [23].

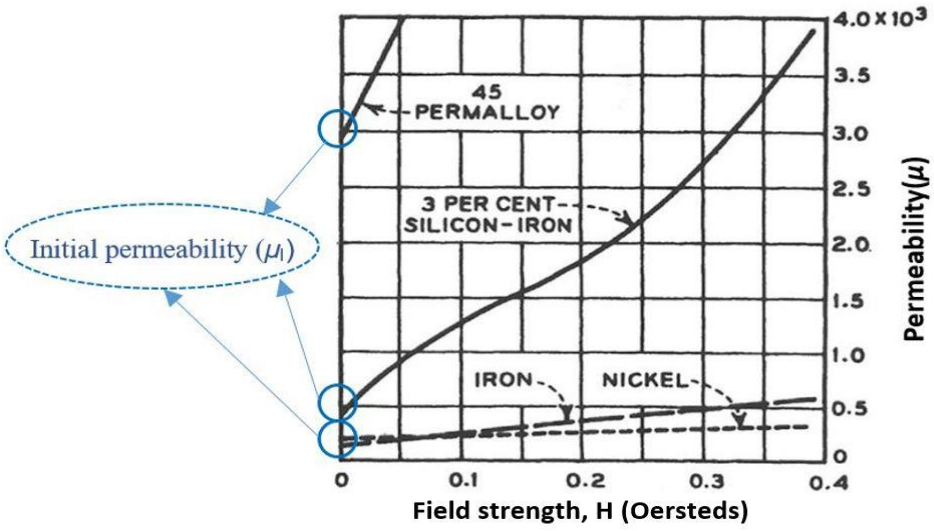

Figure 2.10: Initial permeability of iron, nickel, silicon – iron and Permalloy, the curves showing permeability vs field strength and initial permeability, which is usually considered to be the value at very low magnetic field strength [23].

The next form of permeability is called the incremental permeability (μ_Δ), which is referred to as the permeability measured with a superimposed field. For this permeability a biasing magnetic field is applied, being held constant, and another field is applied and alternated cyclically, making an alternating magnetic flux then the incremental permeability is calculated by Equation 2.7 [23, 35].

$$\mu_{\Delta} = \Delta B / \Delta H \qquad \textit{Equation } 2\text{-}7$$

The incremental permeability is linked to the minor loop hysteresis curve. Basically, three minor loop configurations can be used to derive incremental permeability values; deviations from the major B-H curve, deviations from the initial magnetisation curve and minor loop amplitude sweep deviations [41].

Differential permeability is another form of permeability that occasionally is used. It is simply the slope of the B versus H curve or dB/dH [23].

Finally, the most functional term of permeability is relative permeability, which is very useful in classifying the permeability of one material in comparison with another. Relative permeability considers the permeability of a material for a given field in relation to the magnetic constant, otherwise known as the permeability of free space (μ_0), 12.6 x 10^{-7} T/m. Ferromagnetic materials have relative permeability values of more than one and paramagnetic materials have a relative permeability of close to 1. Therefore, this term of permeability can be used as a scale to compare the magnetic property of materials [40].

2.9 Magnetic Barkhausen Noise (MBN)

The magnetisation process of a polycrystalline ferromagnetic material does not take place continuously and a series of sudden changes occurs causing jumps. These magnetisation jumps are very small and magnification of the magnetisation curve is required in order that the steps can be seen (as shown in Figure 2.11), they can however be heard with the use of a microphone as they produce a crackling noise. These magnetisation jumps can be interpreted as discrete changes in the size or rotation of

ferromagnetic domains. During magnetisation (or demagnetisation), as the domains grow, shrink or rotate in accordance with the applied field, the domain walls become pinned and unpinned as the applied field increases or suddenly rotate. The combination of domain walls overcoming the pinning points and abruptly changing orientation at higher fields causes a release of energy which is called the magnetic Barkhausen noise effect (MBN) [23]. In fact, MBN is the irreversible "jump" of domain walls over local obstacles acting as pinning sites, such as dislocations, grain boundaries, imperfections and inhomogeneities. Therefore, analysis of MBN can give information on the interaction between domain walls and microstructure or stress configurations [42].

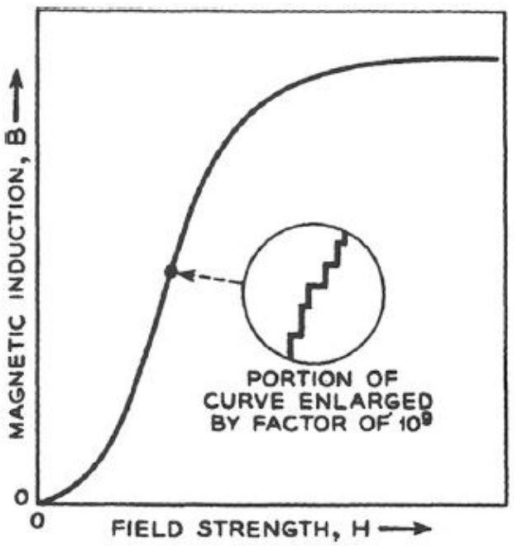

Figure 2.11: The magnetization curve of a ferromagnetic sample is stepped; each step corresponds to a change in the intensity of magnetization [23].

2.10 Effective Factors on Magnetic Properties of Steel

It has been well documented that the magnetic properties of ferromagnetic materials, such as permeability, coercivity, remanence etc are strongly related and dependent on many material characteristics such as, metallurgical structure (e.g. grain size, phase balance and texture), chemical composition, hardness and mechanical stress [43-51]. Therefore, the link and effect of each individual parameter on magnetic properties is significant and can be interesting from a physical point of view, and with regard to possible applications in non-destructive testing and on-line monitoring of material characterisation. In the following sections a summary of the significant factors including grain size, phase balance, temperature, magnetic field and orientation of microstructure that affect permeability will be discussed.

2.10.1 Variation of Magnetic Property with Temperature

Temperature is the most significant factor on magnetisation of ferromagnetic materials. The greatest influence of temperature upon magnetisation for ferromagnetic materials occurs at the Curie temperature (T_c). In steels, with a low applied field, permeability increases with temperature up to the Curie temperature (T_c) and it drops to a value of 1 very quickly when the temperature exceeds the Curie temperature (T_c) and the material changes from ferromagnetic to paramagnetic. At this point the magnetic moments within the material become misaligned and cancel each other out due to a combination of exchange energy and internal thermal energy changes [23]. Figure 2.12 illustrates the effects of temperature on permeability at different applied magnetic field

strengths for iron. It can be observed that when a high applied field is used the effect is reversed and permeability decreases as temperature increases [23].

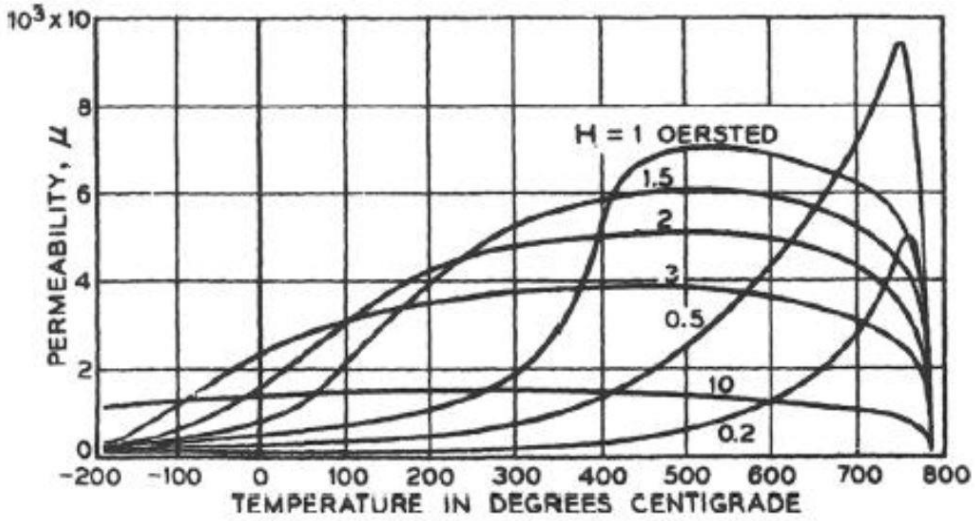

Figure 2.12: The effects of temperature on permeability value for iron at varying constant magnetic field strengths [23].

2.10.2 Variation of Magnetic Property with Grain Size

The magnetic properties of steel are associated with its domain structures (e.g. domain size) and domain wall motion. Magnetic properties are affected by grain size due to the generation of closure domain at the grain boundaries, which creates barriers to the movements of the domains during magnetisation [44, 45, 52-57]. It has been reported that the magnetic domain size is proportional to the square root of grain size in the range of between 0.05 mm and 1.0 mm [44]. A linear trend between inverse ferrite grain size and coercivity, *Hc* has been observed for steel, Figure 2.13 [54].

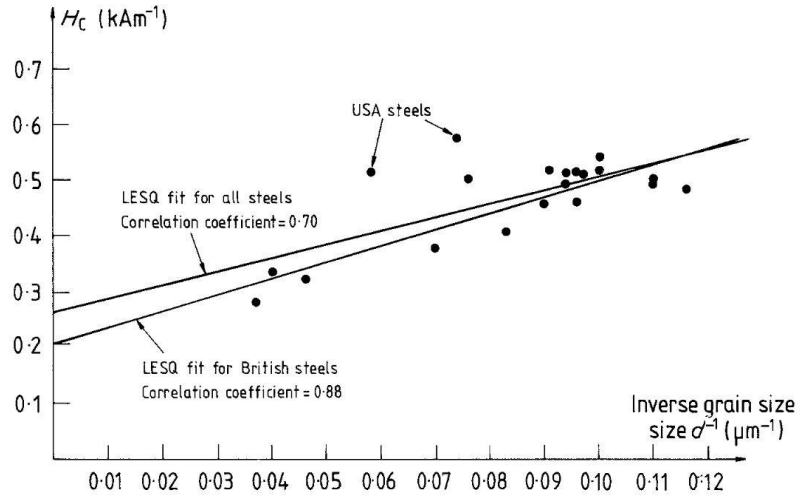

Figure 2.13: Coercive field Hc plotted against inverse ferrite grain size [54].

It has also been reported that there is an increase in the relative permeability value as the ferrite grain size increases from 14 to 52 μm (single phase microstructure of ferrite) [53]. The effect of grain size on the induced magnetic saturation (B_{max}) and changes in the hysteresis curve as a result of variation of grain size are given in Figure 2.14. It can be clearly seen that the induced magnetic saturation decreases with grain size coarsening [41].

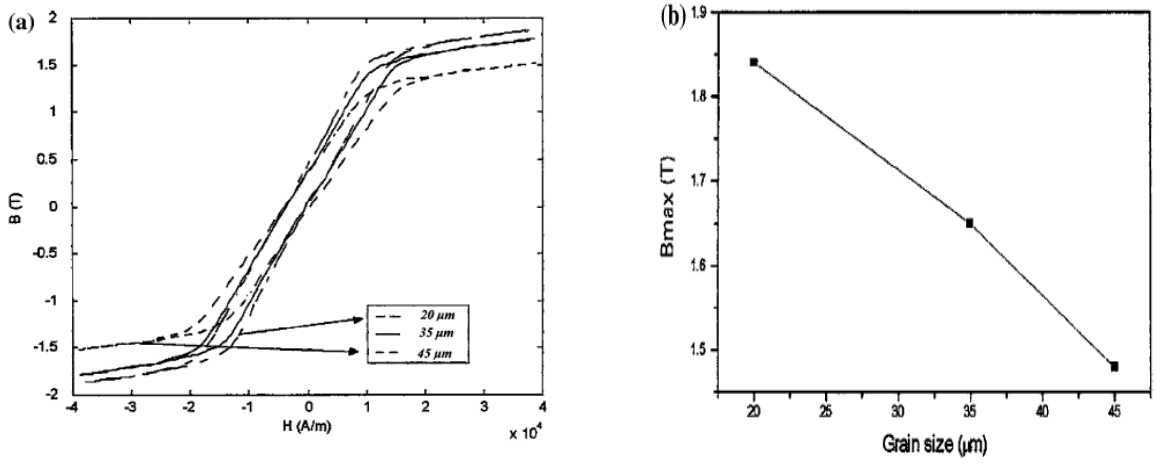

Figure 2.14: (a) Influence of grain size on the magnetic hysteresis curve in AISI1005 steel (b) effect of grain size on the induced magnetic saturation (B_{max}) in AISI1005 steel [43].

Zhou et al. showed that in a low carbon steel heat treated to give grain sizes from 13 to 64 μm each ferrite grain contains a single domain packet and the increase in grain size from 13μm to 64μm results in an increase in the domain packet size and hence an increase in the relative permeability value [22, 55]. However, multiple domain packets per grain were seen for a very large grain size (i.e. 223μm in a pure iron sample), Figure 2.14 [22].

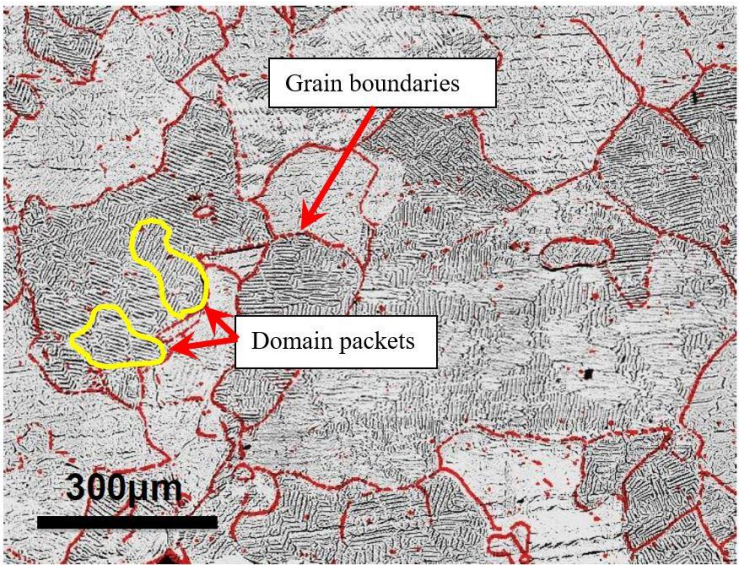

Figure 2.15: Magnetic domain structure of Fe-0.17C (heat treated at 1300 °C for 1 hour), showing ferrite grain boundaries (red) and multiple domain packets per grain (yellow) [22].

2.10.3 Variation of Magnetic Property with Chemical Composition

Chemical composition can affect magnetic properties in steel. Overall, increasing carbon content increases hardness and strength – the effect on magnetic permeability is seen via the change in phase balance rather than as an effect of changing carbon content in solid solution. Si provides some solid solution strengthening but at the levels seen in DP steel (typically < 0.2 wt%) has little effect on permeability [23]. Mn is also a solid solution strengthening element in steels and is typically present in the range 1.8– 2.1 wt% in DP steels. The average grain size decreases as Mn content increases which deteriorates the magnetic losses[58, 59]. Moreover, it is noted that for a given chemical composition, the magnetic properties are generally improved by lowering the sulphur level [23, 59, 60], but all the DP steels considered are commercial grades with

very low sulphur levels, therefore it is not expected that there will be any effect of sulphur for these steels.

2.10.4 Variation of Magnetic Property with Phase Balance

Tanner et al. suggested the coercivity value *Hc*, is a function of ferrite and pearlite fraction. Figure 2.16 shows the pearlite content has clearly a major influence on the coercivity where the coercivity increases with pearlite content. This was stated to be due to the boundaries between cementite lamellae and ferrite within the pearlite grains acting as strong pinning sites and these appear to be about an order of magnitude greater than the sites associated with ferrrite-ferrite boundaries [54]. It can be seen from Figure 2.16 that the effect of increasing pearlite content is particularly significant for fractions from 15 – 20% with the increase in coercivity being significantly less for higher fractions.

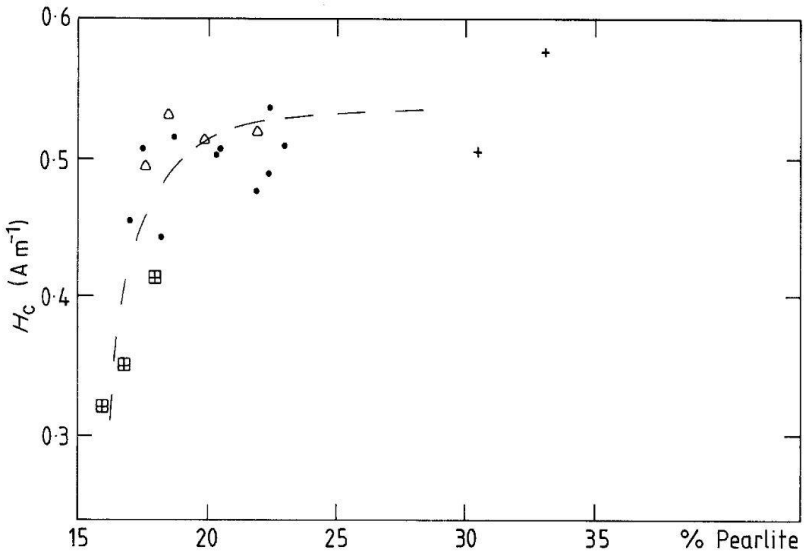

Figure 2.16: Coercivity plotted against pearlite fraction [54].

Zhou et al. [61] established a microstructure-permeability FE model for determining the relative permeability based on actual microstructure and showed the effect of ferrite fraction on the relative permeability for 0.17–0.8 wt %C steels with ferrite–pearlite microstructures with uniform second phase distribution. From Figure 2.17 it can be seen there is an increase in the relative permeability value as the ferrite fraction increases across the full range of ferrite fraction, although the effect of ferrite fraction is small for values greater than abount 85 - 90%.

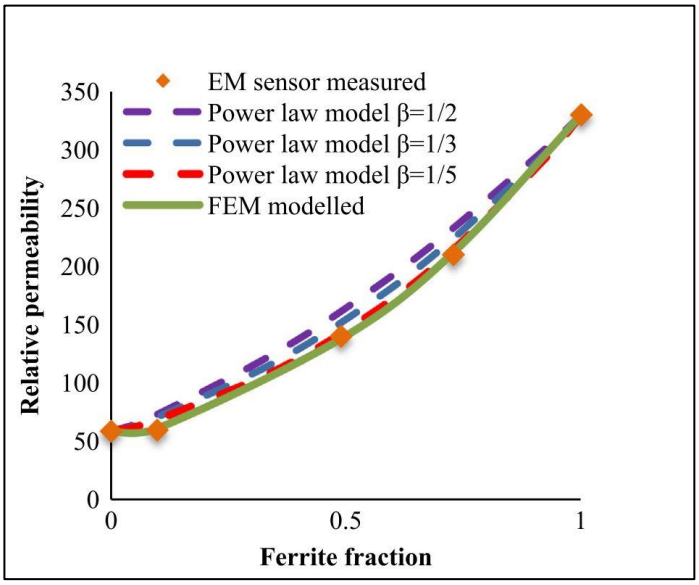

Figure 2.17: Relative permeability change with ferrite fraction in ferrite + pearlite microstructures, there is an increase in the relative permeability value as the ferrite fraction increases [61].

Thompson et al. considered the magnetic properties of ferritic steel as a function of carbon content and showed the maximum relative permeability and remanence decrease with increased carbon content while coercivity increases with increased carbon content (Figure 2.18 and Figure 2.19) [49]. The reason could be explained due to the influence of the fraction of pearlite phase, which has a lower maximum

permeability and initial permeability compared with ferrite. The microstructure for the steels with carbon compositions of 0.44-0.87 wt% C mostly consists of pearlite, which explains their low permeability values since, when the magnetic field is applied then domain wall movement occurs and the magnetic properties will be dominated by the pearlite phase. On the other hand, for the 0.17 wt % C steel which mainly consists of ferrite phase, during the initial magnetisation the majority of domain wall movement occurs within the ferrite grains where they need low field strengths to move, while domain wall movement in the pearlite area occurs at a higher field. Therefore, the magnetic property of the 0.44-0.87 wt %C steel is dominated by pearlite phase and magnetic property of the 0.17-0.44 wt% C steel is dominated by the ferrite phase which has a higher permeability value [49].

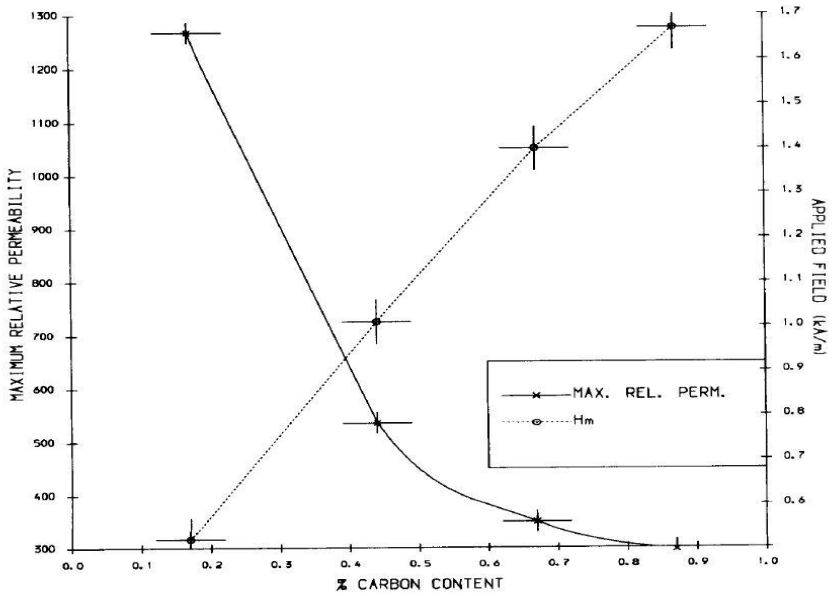

Figure 2.18: Plot of variation of maximum relative permeability and applied field at which this occurs with carbon content in ferrite- pearlite steels [49]

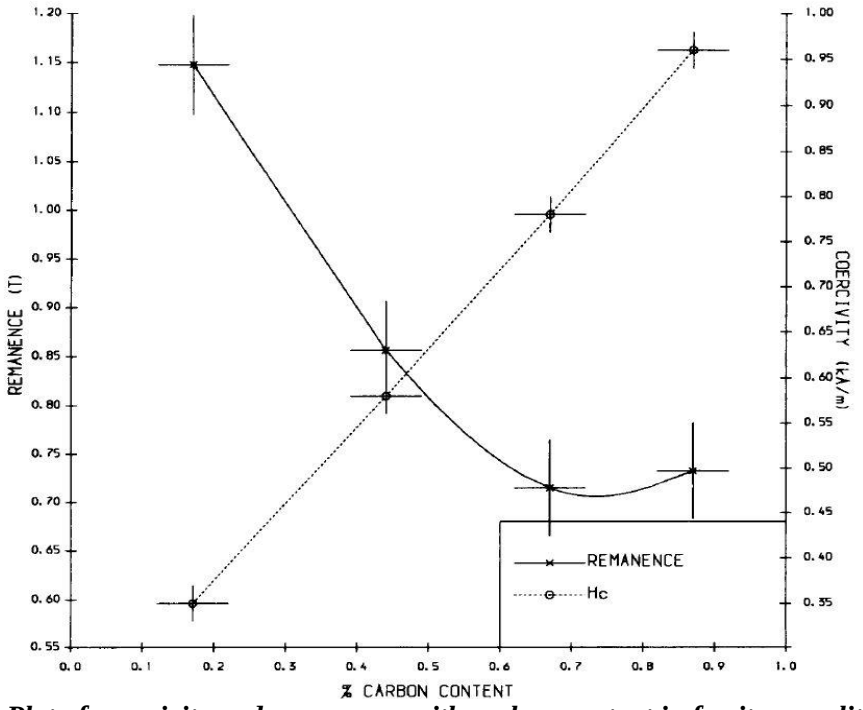

Figure 2.19: Plot of coercivity and remanence with carbon content in ferrite- pearlite steels [49].

2.10.4.1 Phase Type - Ferrite, Pearlite, Martensite

Materials with different phases in steel (such as ferrite, pearlite, martensite etc.) offer diverse permeability values. For instance, for a fully ferritic structure only the grain boundaries have a major influence on the domain wall motion under an applied field but there are many more pinning sites for domain wall motion inside a pearlite grain compared with ferrite. In martensitic microstructures there can be a large density of dislocations which can decrease the mean free path for domain wall motion, hence the coercivity value of these samples shows an increasing order of ferrite < pearlite < martensite and the order for permeability is martensite < pearlite < ferrite [62]. The differences between permeability values for these phases can be also observed from the B-H loops for ferrite, pearlite and martensite as illustrated in Figure 2.20 [62]. It has been reported that permeability decreases (as a result of the more effective domain

wall motion pinning effect) with an increase in cementite lamellae thickness and a decrease in inter lamellar spacing [62].

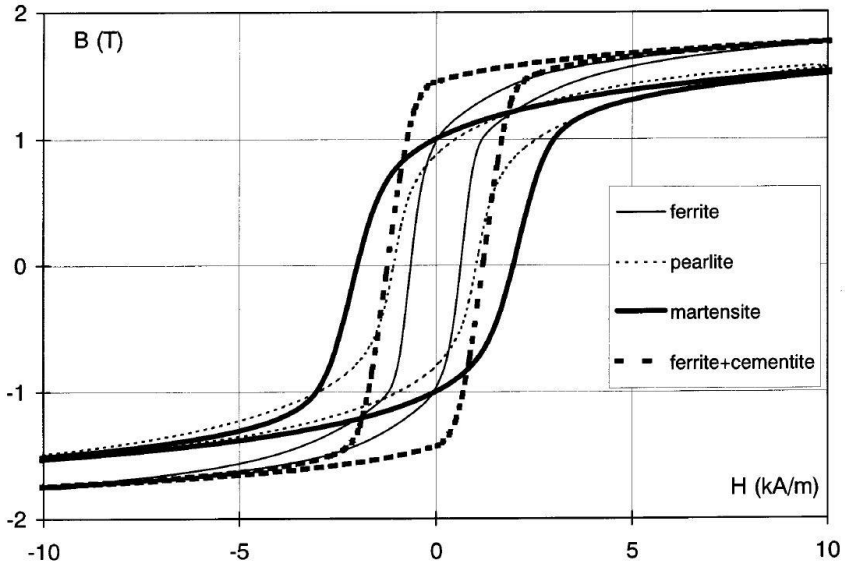

Figure 2.20: Hysteresis loops B versus H for ferrite, pearlite, martensite and ferrite + cementite. The hysteresis loops report the highest coercivity value order is ferrite < pearlite < ferrite + cementite < martensite and the highest permeability (steepest slope dB/dH) value for ferrite and the lowest permeability value for martensite [62].

2.10.4.2 Phase Distribution

Second phase may affect the magnetic property and this effect can be due to the amount of second phase or/and can be related to the distribution of the second phase. It means that, besides the second phase balance, the morphology of the second phase microstructure also has an effect on magnetic property [63].

Work completed by Zhou [64] also found that there is a significant difference in permeability values from the direction of the field with respect to the orientation of any second phase banding in the microstructure, as shown in Figure 2.21.

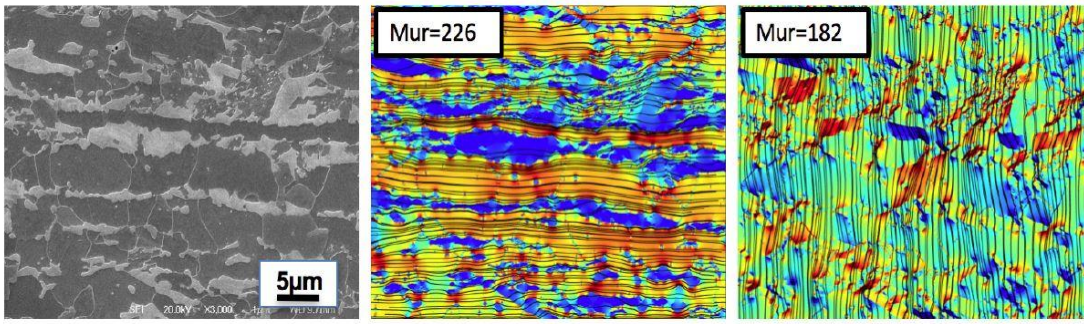

Figure 2.21: The modelled effective permeability (Mur) results and flux distribution in a DP800 steel microstructure. Left: SEM image showing phase distribution of ferrite (dark) and martensite (bright); middle: modelled magnetic flux distribution when horizontal and, right, vertical magnetic fields are applied[64].

As well as the above mentioned factors, the role of precipitates in steel needs to be considered as an effective parameter affecting the magnetic property since precipitates can act as pinning points. It has been shown that there is a significant drop in coercivity for steel after tempering which can be attributed to the recovery of dislocations, coarsening of the martensitic laths and also coarsening of precipitates [41].

Papaelias et al [65] studied the effects of ferrite distribution, contiguity and orientation upon impedance response. Simulations on random ferrite distributions showed that impedance response follows a linear relationship with ferrite volume fraction when it does not exceed 20% of the total volume fraction. Above volume fraction of 20%, whereas ferrite grains start connecting with each other, the electromagnetic field is

affected more by the increased contiguity of ferrite forming a favourable ferromagnetic path which shows a higher impedance signal.

2.10.5 Variation of Magnetic Property with Crystallographic Orientation

Magnetic properties in single crystals of iron (and of other magnetic materials) depend on the direction in which they are measured. For instance, for a single crystal of iron (BCC crystal structure) containing about 3.8% silicon, the measured permeability in the three principal directions are seen as [100] highest, [110] intermediate and [111] lowest (Figure 2.22). It means for this material there is a crystallographic direction in which magnetisation is easiest and saturation is achieved at the lowest magnetic field. The easiest magnetisation direction for nickel (FCC crystal structure) is [111] and the hardest crystallographic direction is [110].

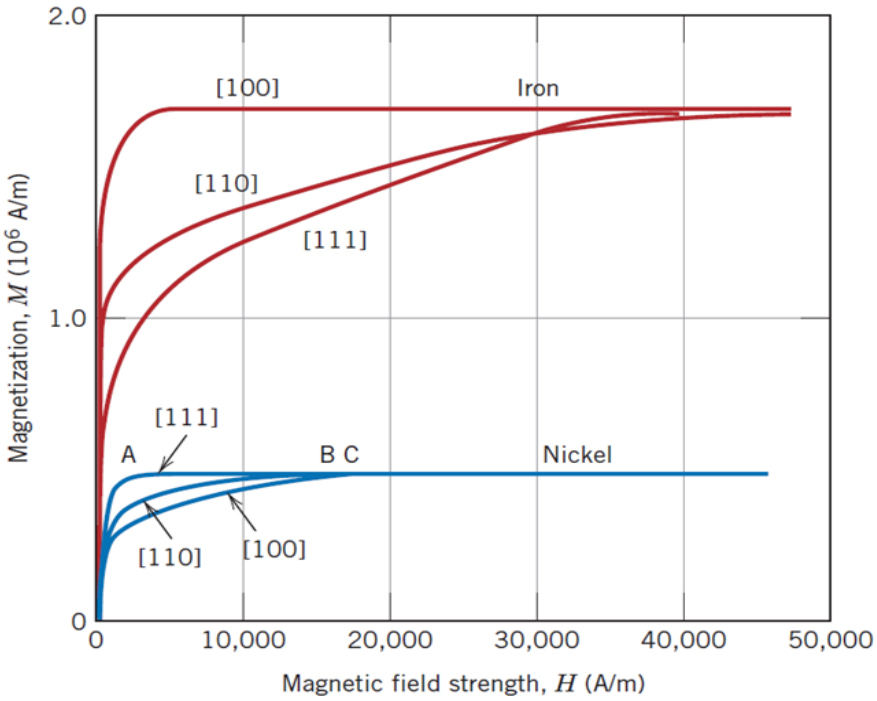

Figure 2.22: Dependence of permeability on crystallographic direction in iron containing 3.8% silicon (red) and nickel (blue) [29].

Figure 2.23 illustrates BH loops measured for a 3% Grain Oriented Si Steel (GOSS) sample at four different directions in terms of applied field including; transverse direction (TD), rolling direction (RD), 45^{o} to the rolling direction, 54^{o} to the rolling direction. The highest flux density is recorded in the RD sample meaning that RD is the most easily magnetised direction hence highest permeability is seen in this direction while the sample measured with orientation 54^{o} to RD showed the lowest flux density for the same applied field, hence 54^{o} to RD is the hardest direction to magnetise [38].

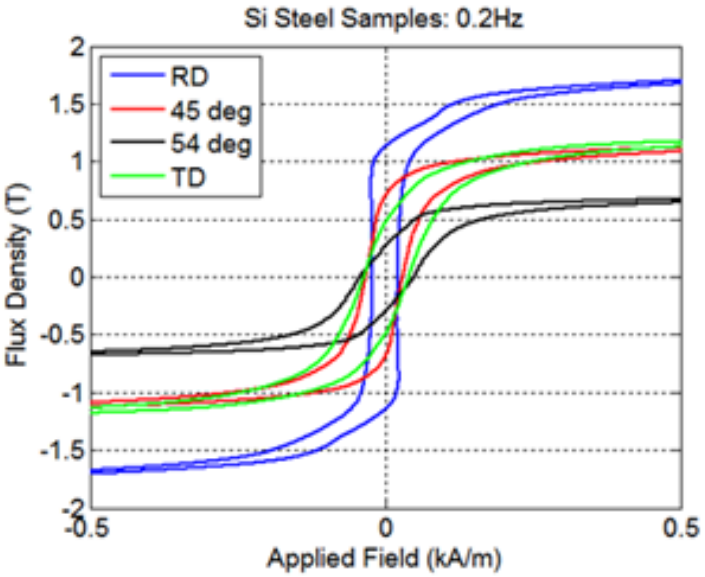

Figure 2.23: Magnetic hysteresis loops recorded for 3%Si Steel samples in four different applied field directions into the samples including, transverse direction (TD), rolling direction (RD), 45^o to rolling direction, 54^o rolling direction [38].

2.10.6 Variation of Magnetic Property with Strain/Strain

It has been shown that the initial permeability and the maximum relative permeability decrease with an increase in plastic deformation [66]. This is believed to be due to the formation of dislocations and the increased number of pinning sites for domain wall movement [50]. The plot of maximum relative permeability and initial permeability with plastic deformation are illustrated in Figure 2.24 and Figure 2.25 respectively.

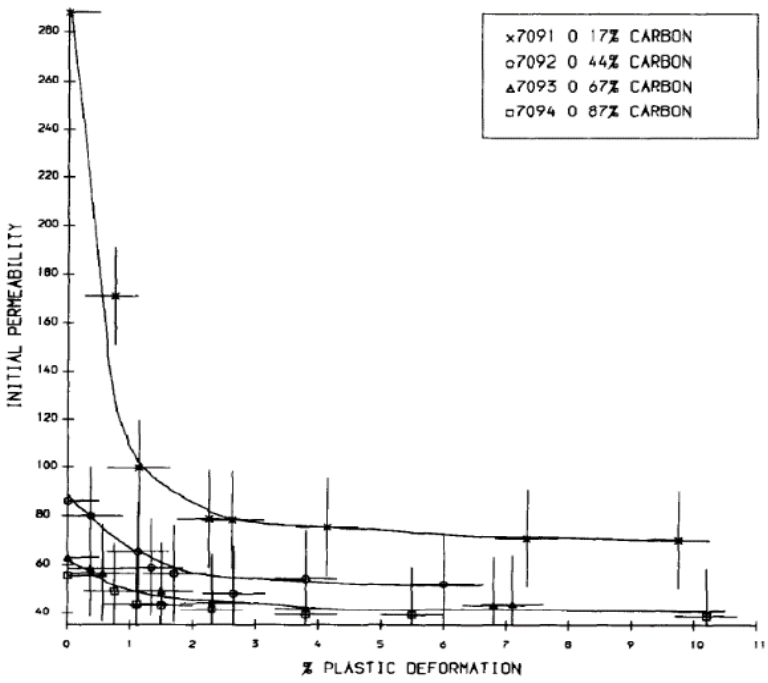

Figure 2.24: Plot of initial permeability with plastic deformation in pearlite- ferrite steels [50].

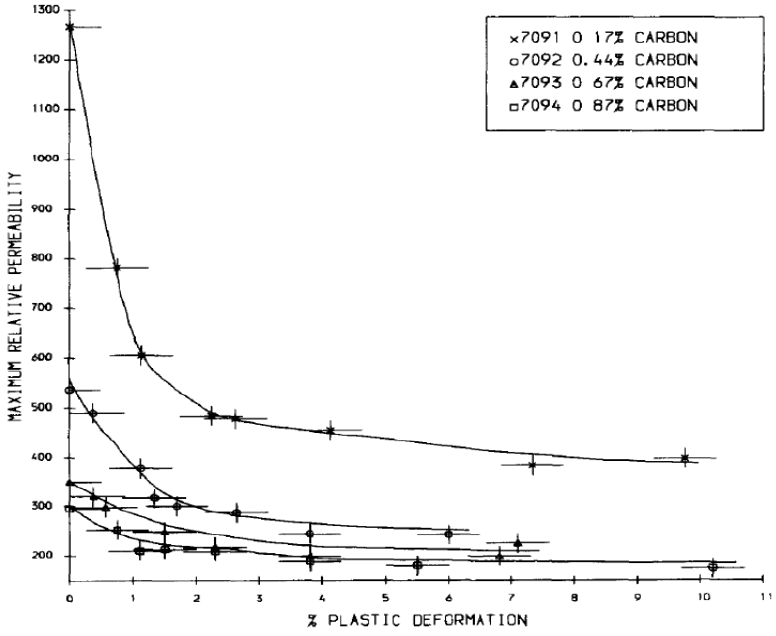

Figure 2.25: Plot of maximum relative permeability with plastic deformation in pearlite ferrite steels[50]

Sipeky and Ivanyi [67] looked at the hysteresis loops under different applied stress in silicon steel. It has been concluded that applied tensile stress increased coercivity, permeability and the gradient of hysteresis curves and consequently decreased the energy loss under the same applied tensile stress, as shown in Figure 2.26.

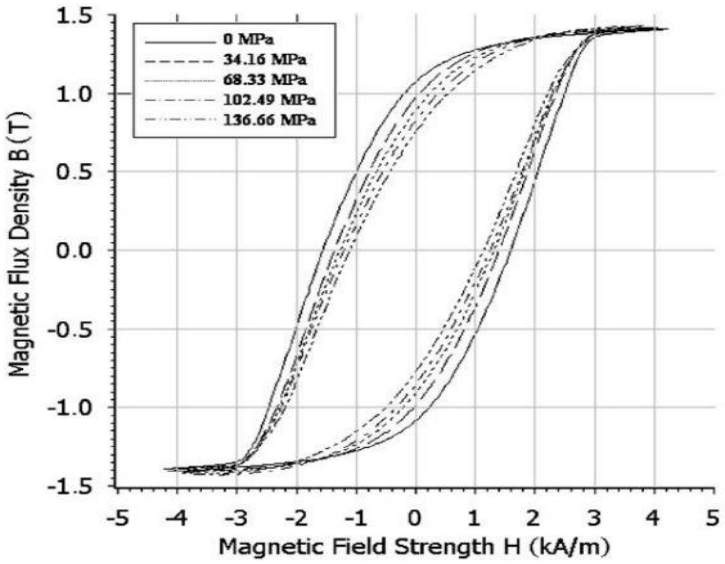

Figure 2.26: Hysteresis loops versus the stress (0MPa to 136.66MPa) at 10 Hz measurement frequency in GO silicon steel

Similar results were obtained by Kwun and Burkhart [45] in an investigation in ferritic stainless steel to see the effects of tensile stress and compressive stresses on the magnetic property. The measurements showed that the hysteresis loop shapes were significantly changed by the application of tensile and compressive stresses as illustrated in Figure 2.27. Moreover, the hysteresis loop shapes showed compressive stress decreased magnetic induction (*B*) and that tensile stress increased the magnetic induction (*B*).

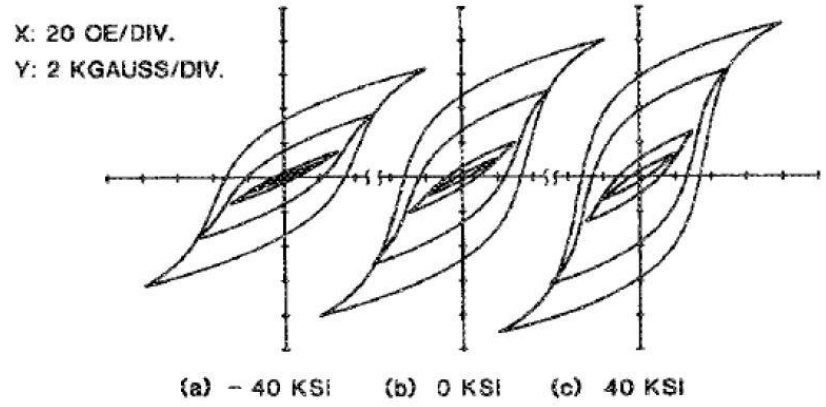

Figure 2.27: Effect of stress on the magnetic hysteresis loops for AISI 410 ferritic stainless steel in both compression and tension (1 KSI = 6 MPa)

Residual stresses are the stresses present in a material which is free from an external load. These stresses are present in many assembled structures and manufactured components, although their effects are often not evident until the components or the structures are subjected to external loads or exposed to an adverse environment. The residual stresses are superposed upon loading stresses, thus the determination and control of residual stresses resulting from the intentional or unintentional thermal and mechanical loading of steels during their production or manufacturing process, as well as during their lifetime, is a challenge for both the relevant industries and the scientific community. Magnetic properties result directly from the movement of domain walls and the original domain configuration. In reality, solids are typically somewhat magnetically anisotropic. The magnetisation varies with direction depending on the domain configuration. This anisotropy is influenced by, stress induced anisotropy (magnetostrictive anisotropy), crystalline texture, magnetic annealing and non-uniform plastic deformation [68-70]. This gives rise to a macroscopic easy axis, or direction of easy magnetisation. For a polycrystalline sample with a single easy axis an excess population of 180 ° domain walls may be considered to be aligned in the easy axis

direction, while the remaining 180 ° domains walls are isotropically oriented [71]. The EM sensor is sensitive to changes of both microstructure and applied stress. Therefore, EM signal can be converted to residual stress values by using an appropriate calibration curve if the microstructure remains constant (or is known and an appropriate model is developed). For the DP steels considered in the work presented no residual stress is expected as the samples are thin sheets in the as-received condition (either hot rolled or cold rolled and annealed). The effect of applied stress has been considered in parallel work, for example [38] where sensors used in-line for inspection of strip under line tension were being considered and no significant effect of stress is anticipated.

2.10.7 Variation of Magnetic Property with Applied field

The effect of applied field on magnetic permeability has been investigated [50, 72]. Figure 2.28 illustrates the permeability values in ferrite + pearlite microstructure steel, where the pearlite percentages varying from around 20% to 100%, as a function of applied field [49]. At low applied field reversible magnetisation dominates, as the applied field increases the irreversible component is introduced and the gradient of the curve increases. These plots show a smooth curve with a peak near the coercive force. The increased pinning, seen in the microstructures with higher amounts of pearlite, results in a lower relative permeability and reduced gradient of the initial magnetisation curve. The decrease in the peak permeability and broadening of the curve is attributed to saturation [66].

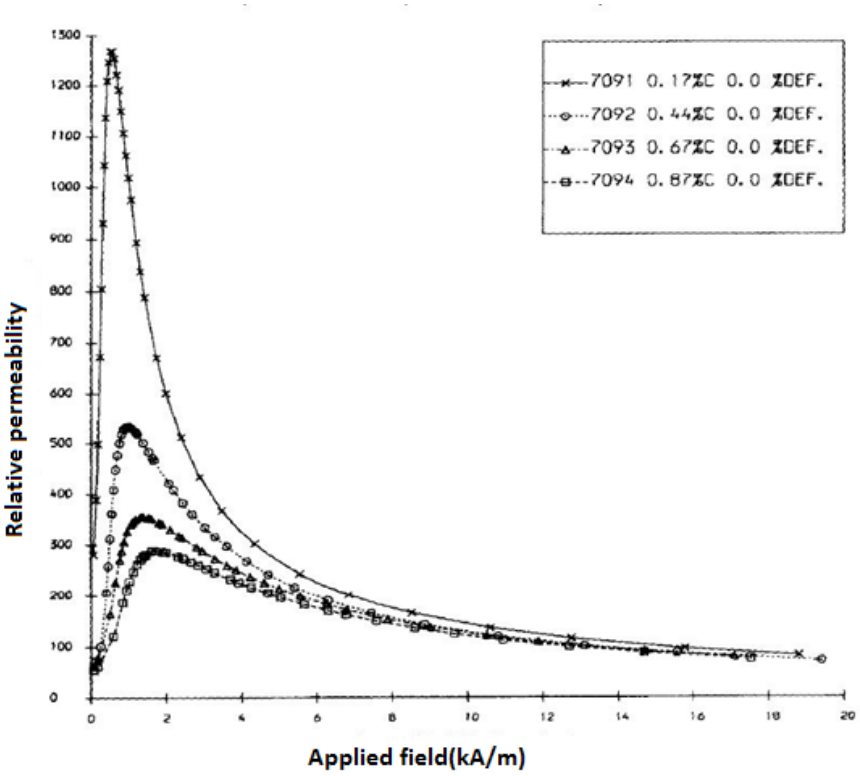

Figure 2.28: Permeability values of pearlite fractions varying from 0.19 to 100% as a function of applied field [50]

2.10.8 Variation of Magnetic Property with other microstructural parameters

Non-magnetic inclusions and non-magnetic intra-granular precipitates influence permeability by pinning domain walls [73-75] due to the surface tension effect, and the effect of internal magnetic poles [74]. It has been found that the coercive force depends both on the total volume fraction of inclusions and the state of dispersion. For a given composition of alloy, for particles both much larger (which typically have low number density) and much smaller (which may have high number density but will have a low

pinning force) than the thickness of the domain wall, the net contribution to the coercive force is small [74]. In addition, the maximum effect on coercive force (i.e. the strongest pinning) occurs for particles of size about 120 nm in ferrite phase in carbon steels.

2.11 Summary

This chapter covered some important fundamental theories of magnetism and magnetic properties of materials. Following that, the effective factors on magnetic property were analysed. It was explained that the permeability of steel is affected by intrinsic parameters such as microstructural features and/or extrinsic parameters such as applied field.

3 Fundamental EM Sensor

3.1 Maxwell's Equations

The fundamental electromagnetism relationships rely on Maxwell's equations. These equations describe how electric charges and electric currents create electric and magnetic fields. Moreover, they describe how a magnetic field can generate an electric field and vice versa. Maxwell's equations consist of Gauss's law, Gauss's law for magnetism, Ampere's circuital law and Faraday's law of induction. Gauss's law signifies that electric charges are the source for the electric field; Gauss's law for magnetism indicates that magnetic monopoles do not exist; Faraday's law signifies how an electric field is produced by a time changing magnetic field; and finally Ampere's circuital law indicates the reverse process. These four partial differential forms of Maxwell's equations are listed below [76-78];

Gauss' Law:	$\nabla . \bar{E} = \rho/\varepsilon_0$	*Equation 3-1*
Gauss' Law for magnetism	$\nabla . \bar{B} = 0$	*Equation 3-2*

Faraday's Law of induction:

$$\nabla \times \bar{E} = -\frac{\partial \bar{B}}{\partial t}$$ *Equation 3-3*

Ampere's circuital Law:

$$\nabla \times \bar{B} = \mu_0 I_D + \mu_0 \varepsilon \frac{\partial \bar{E}}{\partial t}$$ *Equation 3-4*

Where E presents electric field intensity, ρ is the free charge density, ε is permittivity, μ_0 is permeability and I_D stands for current density. In addition, the relationship between electric field *(E)*, magnetic field *(B)*, magnetic field strength *(H)* and electric displacement *(D)* are presented by constitutive equations below:

$$\bar{B} = \mu_0 \mu_r H$$ *Equation 3-5*

$$\bar{I}_D = \sigma \bar{E}$$ *Equation 3-6*

$$\bar{D} = \varepsilon \bar{E}$$ *Equation 3-7*

where the symbols of μ, σ and ε denote the permeability, conductivity and electromagnetic constant permittivity of a material respectively [76, 78].

3.2 Inductance

Inductance for a straight wire with length *l* is calculated by Equation (3.8) as shown in Figure 3.1 [79].

Figure 3.1: Inductance for a straight wire with length l and diameter of 2r, is calculated by L=200l (ln (2l/r)-1) x10^{-19} [79]

$$L = 200l\ (\ln (2l/r)-1)\ \times 10^{-19} \qquad \text{Equation 3-8}$$

Where *I* is the current (in Amp) and *r* the radius of the wire (in mm).

For a straight very long wire, Figure 3.2, the magnetic field at point *p* is measured by [79];

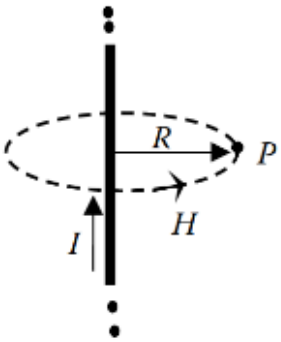

Figure 3.2: Magnetic flux density and magnetic field at point p with R distance from a straight very long wire can be expressed by $B=\frac{\mu.\mu_r I}{2\pi R}$ ***and*** $H=\frac{I}{2\pi R}$

$$H = \frac{I}{2\pi R} \qquad \textit{Equation 3-9}$$

and magnetic flux density is calculated by;

$$B = \frac{\mu.\mu r I}{2\pi R} \qquad \textit{Equation 3-10}$$

Where *I* is the current (in Amp) and *R* is the distance from point p to the wire (in mm)

Inductance for infinite cylindrical coil helix is calculated by (Figure 3.3) [79];

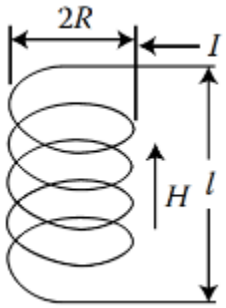

Figure 3.3: Infinite cylindrical coil helix with diameter of 2R [79].

$$L = \frac{N^2 \mu A}{l} \qquad \textit{Equation 3-11}$$

$$H = NI \textit{ (for } R << l \qquad \textit{Equation 3-12}$$

where A_{coil} is the area of the coil(m^2) and N is the number of turns in the coil.

According to Faraday's law when the magnetic field that flows through a conductor changes, a current or voltage is induced in the conductor. This phenomenon is called the self-induced inductance, which is opposite to the original flux change (i.e. negative sign) [22-23]. Self-induced inductance is indicated by Equation 3.13 [80];

$$L = \frac{N_1 \ \varphi}{I} \qquad \textit{Equation 3-13}$$

Where N_1 is the number of turns in the coil and φ is the flux in Wb and I is current in A.

If two multi turn coils are kept close to each other, with a varying magnetic field due to varying current flowing through one, a voltage is generated in the other one. This process is called the mutual inductance and it is achieved by Equation 3.14 [80].

$$M_L = \frac{N_2 \ \varphi}{I} \qquad \textit{Equation 3-14}$$

Where M_L in Wb/Amp and N_2 is the number of turns in the second coil.

The mutual inductance is related to the relative permeability of the sample and can be simplified by Equation 3.15;

$$M_L = \frac{N_2\ \varphi}{I} = \frac{N_2\ BA}{I} = \frac{A\,N_1 N_2 \mu_0 \mu_r}{l} \qquad \textit{Equation 3-15}$$

Where M_L is mutual inductance in Wb/Amp, N_1 is the number of turns in the first coil N_2 is the number of turns in the second coil [79, 81].

3.3 Impedance

Impedance stands for all forms of opposition to electron flow, including reactance and resistance, where reactance is inertia against the motion of electrons and resistance is friction against the motion of electrons. Resistance and reactance are measured in the unit of ohm (Ω) and mathematically symbolised by the letter *"R"* and *"X"* respectively. The complex quantity of impedance is presented by two parts; the first part is *"R",* the real part of resistance and the second part is the imaginary part. Impedance is measured in the unit of ohm (Ω) and mathematically symbolised by the letter *"Z"[81]*.

$$Z = R + jX \qquad \textit{Equation 3-16}$$

Imaginary impedance is defined as the impedance 90 degrees out of phase or leading with the driving current. Inductive reactance interprets into a positive imaginary impedance (the impedance value +90º). In electromagnetic sensors, imaginary

impedance relates the induced voltage in the sensing coil and real impedance represents the losses in the EM sensor [79, 81].

The impedance for a circuit with inductor and capacitor is calculated as Equation 3.17 [23];

$$Z_{totall} = Z_R + Z_L + Z_C \qquad \textit{Equation 3-17}$$

So for a circuit without an inductor and capacitor the impedance is purely real as in Equation 3.18 [81];

$$Z_R = R \qquad \textit{Equation 3-18}$$

Ideal capacitors and inductors have purely imaginary impedance as in Equation 3.19 and 3.20 respectively [81];

$$Z_c = \frac{\mathbf{1}}{\boldsymbol{j}\omega \boldsymbol{c}} \qquad \textit{Equation 3-19}$$

$$Z_L = \boldsymbol{j}\omega L \qquad \textit{Equation 3-20}$$

where $\omega = 2\pi f$

Inductance is calculated as Equation 3.21 [81];

$$L = \frac{\boldsymbol{Z_L}}{\boldsymbol{j}\omega} \qquad \textit{Equation 3-21}$$

3.4 Eddy Current Theory

The tendency of magnetic flux (or current) to become distributed throughout the cross section of a conductor is affected by two independent phenomena known as proximity effect and skin effect [23, 32]. Foucault current or Eddy current theory is based on the fundamental *EM* theories provided in section 3.2. The basic principle for this phenomenon is Faraday's law. When the magnetic flux in a conducting medium changes with time, an electromotive force is generated in the plane at right angles to the direction in which the flux is varying, and there is a resulting flow of current within the material. These eddy currents depend on the resistivity and permeability of the specimen, frequency and the geometry of the specimen [23]. The eddy current effect prevents the field from penetrating to the interior of the material. Therefore, the magnetic induction drops from the surface toward the interior. The eddy currents cause an increase in the resistance of the coil. In addition, the eddy currents generate a magnetic field and change the inductive reactance of the coil [78, 79]. The principles of eddy current generation are schematically illustrated in Figure 3.4.

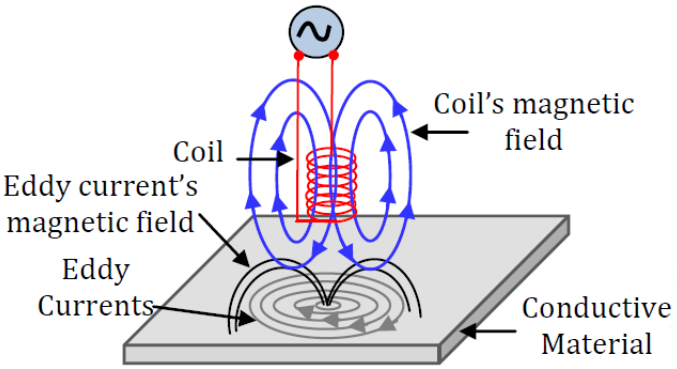

Figure 3.4:Typical eddy current generation [79].

The skin effect is the tendency of magnetic flux and current to become distributed throughout the cross section of a conductor such that the flux, or current, density in a thin layer on the surface of the conductor is much more pronounced Figure 3.5.

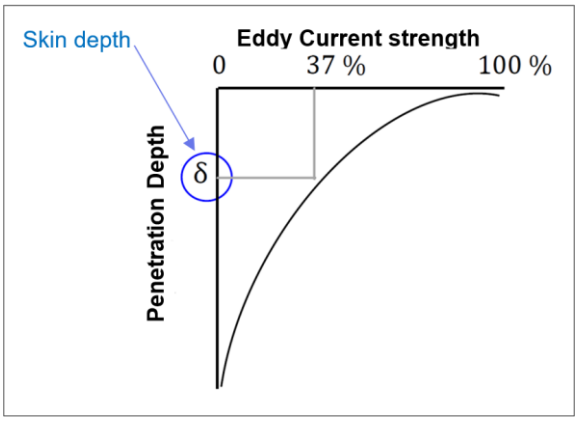

Figure 3.5: Skin depth illustration, in the skin effect the largest amount of current density can be seen at the surface of the conductor and current density decreases by increasing the depth. The eddy current density near the surface of the conductor is

much greater than the inside the conductor which is called "skin depth", defined as the distance over which the electromagnetic wave falls to 1/e or 37% of its original value.

The skin effect is calculated by equation 3.22 and 3.23;

$$\Delta_s = \sqrt{\frac{2\rho}{\omega\mu}} \qquad \textit{Equation 3-22}$$

$$\Delta_s = \sqrt{\frac{\rho}{\pi f \mu_0 \mu_r}} \qquad \textit{Equation 3-23}$$

where $\omega=2\pi f$, f is the AC excitation frequency in *Hz,* ρ is the resistivity of the conductor,

μ is absolute magnetic permeability ($\mu = \mu_0 \mu_r$) and $e = 2.718$.

3.5 Frequency Dependence of Permeability

Magnetic permeability measurement as a function of frequency is challenging as the signal is affected by many factors, such as the electric conductivity of the material, the eddy current effect, dimensions and shape of the sample. A study by Bowler has been done to characterise metal plates by means of model-based, broadband, four-point potential drop measurement technique [82] . The study has shown that the real and

imaginary parts of the permeability (μ) of a steel sample (alloy 1018 - low-carbon steel) are complex and it can be a function of frequency, as illustrated in Figure 3.6.

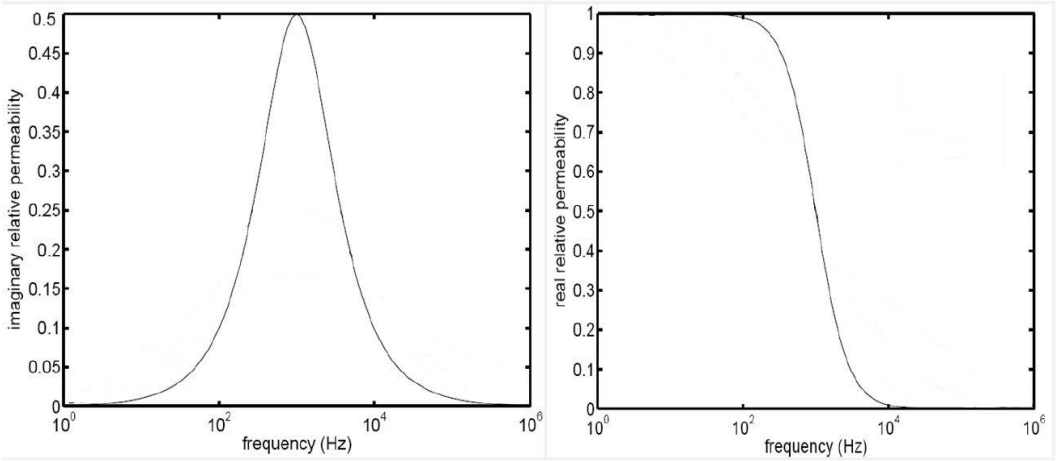

Figure 3.6: Real and imaginary parts of relative permeability as a function of frequency [82].

3.6 EM sensor function

Figure 3.7 shows different laboratory EM sensors in term of geometry. Cylindrical EM sensors (air cored/ferrite cored) have been designed for rod and bar samples where the samples are placed within the cylindrical sensor body. U-shaped EM sensors (or H-shaped) are basically used for flat surfaces (sheet samples). EM sensors consist of an excitation coil and sensing coil. The EM sensor's excitation coil is driven by an AC voltage and induces an alternating current magnetic field into the sample. The sensing coils pick up changes in the magnetic field caused by the test sample. The EM sensor

can be operated at frequencies from 1Hz to 1MHz and measures inductance (real inductance and imaginary inductance).

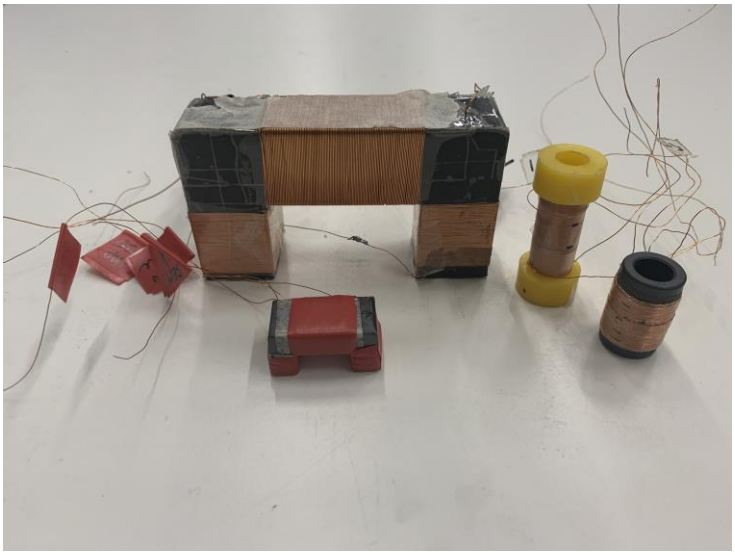

Figure 3.7: Different geometry cylindrical and U-shaped multi frequency EM sensors, including U-shaped ferrite core, cylindrical air-cored and cylindrical ferrite cored.

Figure 3.8 illustrates a typical EM sensor response curve that has been operated at frequencies from 10Hz to 100 kHz for a DP1000 sample. The EM sensor is sensitive to magnetic permeability and electrical resistivity of the material being tested. At low frequency the eddy currents in the sample are very weak; the contribution to the inductance change is mainly from the magnetisation of the sample and therefore the real inductance measured is related to the sample permeability. As the frequency is increased, the effect of the eddy currents becomes more dominant, i.e. the inductance reading is affected by the samples resistivity.

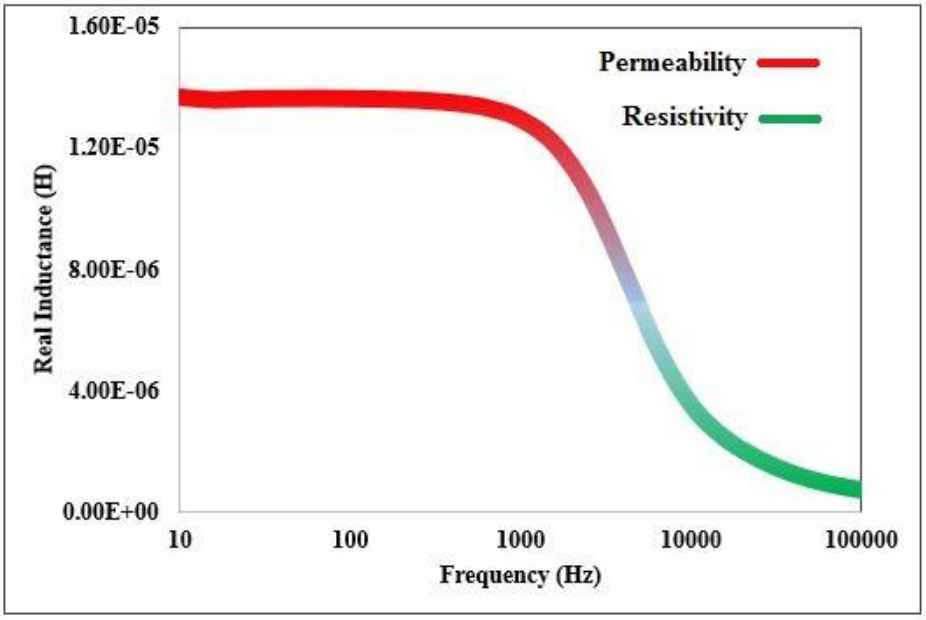

Figure 3.8: Typical EM sensor multi frequency measurement and dominant materials parameter affecting the curve.

It is worth mentioning that permeability is a physical property of material whereas inductance is a physical property of a coil that describes how a magnetic field is generated when an electrical current is sent through material. The measured real inductance from the EM sensor is sensitive to both changes in sample geometry and to changes in the relative permeability and resistivity of the steel, with the low frequency inductance values being directly related to the permeability. As the frequency is increased, the effect of the eddy currents becomes more dominant, i.e. the inductance reading is affected by the samples resistivity. There are known relationships between magnetic properties (for example coercivity or permeability) and mechanical properties (hardness or strength). Therefore the low frequency EM signal can be directly correlated to the mechanical properties for samples of constant thickness. However, the sensor signal cannot be correlated to strength directly if different thickness samples are assessed unless a calibration curve to account for thickness is

generated – using a model to determine permeability from a given sensor and sample thickness avoids the need for lots of calibration samples.

3.7 EM Sensor and microstructure-magnetic property models

Building a model facilitates the design of the sensor and sample set-up, the sensor and sample interaction, the effect and the significance of changes in each materials property on the EM sensor signal.

The model can be carried out in order to generate frequency-domain responses of the sensor/sample in term of real inductance between the excitation coil and sensing coils and later can be utilised to determine the relative permeability of the samples by fitting with experimental.

Magnetic permeability – microstructure model has been used to determine the relative permeability of steel based on actual microstructure where the model shows the effects of grain size and phase balance on permeability.

3.8 Summary

The fundamental EM sensor relationship including Maxwell's equations, inductance and impedance were discussed. It has been explained that a typical multi frequency

EM sensor is sensitive to electrical conductivity (resistivity) and permeability of the material being tested where at low frequency the inductance corresponds to permeability of the sample as the effect of eddy currents are negligible.

4 Methods of steel microstructure characterisation

This chapter provides a basic introduction to the most commonly used methods of microstructural characterisation to observe and interpret the microstructure of metals and steels. The whole range of techniques from optical microscopy, electron microscopy, ultrasonic and thermal analysis are briefly explained, followed by X-ray and ultrasonic technique. The basic principles for each technique and interpretation of microstructural features are explained.

Finally, magnetic techniques are presented and will be explained on the basis of the fundamental magnetic properties discussed in Chapter 2, to allow correlations to microstructural features for characterisation of steel. Moreover, existing commercial EM sensors for characterisation of steel will be introduced at the end of the chapter.

4.1 Conventional Methods

4.1.1 Optical Microscopy

The optical microscope is a commonly used tool for the characterisation of steel. In this method, the light is incident on the sample and a magnified image is generated by a combined action of eyepiece and objective lenses [83]. Meticulous surface preparations are required to reveal the needed details of the microstructure. For this aim the specimen surface must first be ground and polished to a smooth and mirror like finish (1 micron or ¼ micron surface finish) followed by chemical etching if necessary as chemical reactivity of the grains of some single-phase materials depends on crystallographic orientation, then in a polycrystalline specimen, etching characteristics vary from grain to grain [84]. This results in a different reflectivity of different regions of microstructure that makes a contrast in the image [83].

The maximum magnifications achieved in this type of microscope are in the range of 1000-2000X and many microstructural features of common interest can be observed and quantified such as determination of grain sizes/distribution, shapes, amounts of the different phases in multi-phase systems and precipitates (larger than 0.2 micron).

The maximum resolution achieved by optical microscopy is limited by the wavelength of light, it means the maximum resolution is around 200 nm. Some structural elements (e.g. dispersoids, fine second-phase precipitate particles) possess much smaller dimensions, therefore more powerful microscopes are required in order to observe these items (Figure 4.1) [29].

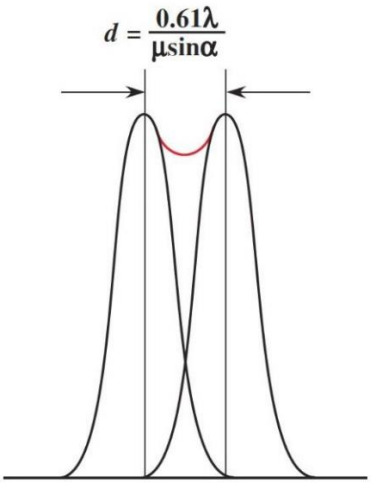

Figure 4.1: The maximum resolution (minimum d) is typically about one-half of the wavelength. The limit of resolution for an optical microscope which uses visible radiation (λ=300–700 nm) is about 200 nm [29].

4.1.2 Scanning Electron Microscopy

The scanning electron microscope provides the microscopist with higher resolution than optical microscopy. In this method, the surface of a specimen to be assessed is scanned with an electron beam, which is generated by heating a tungsten filament (or lanthanum hexaboride filament) and the reflected (or backscattered) beam of electrons is collected and then displayed at the same scanning rate on a cathode ray tube (CRT). The electron beam interacts with the specimen and generates a variety of signals, including backscattered electrons, secondary electrons, characteristic X-rays, Auger electrons, and cathode luminescence (Figure 4.2). These different signals can be used to obtain valuable information about the microstructure of the sample;

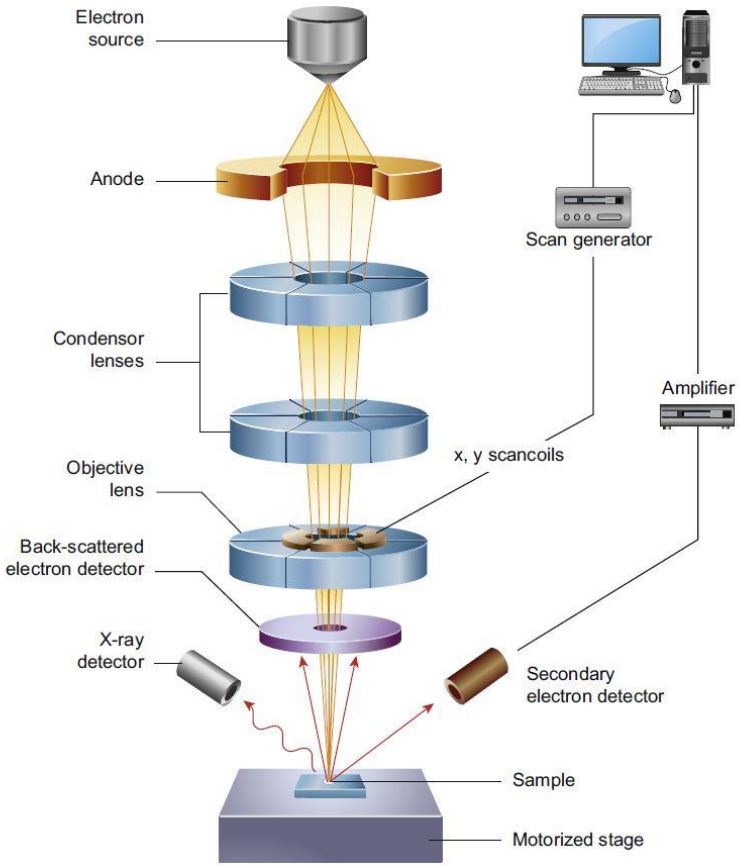

Figure 4.2 : Schematic diagram of the core components of an SEM microscope [85].

4.1.2.1 Secondary electrons

These are produced by interaction between the primary electrons in the electron beam and the loosely bound electrons in the atoms of the specimen. Secondary electron imaging technique can be used for examining microstructures, usually in combination with chemical analysis using X-ray signals.

4.1.2.2 Backscattered electrons

Backscattered electrons are formed by multiple small-angle or single large-angle scattering events that mostly depends on the atomic numbers of the elements. In this technique, particles and phases with a higher average atomic number are indicated as

bright regions because a large portion of primary electrons are backscattered. Therefore, backscattered electron imaging may be used to distinguish between particles and phases with different average atomic numbers.

4.1.2.3 Characteristic X-rays

In scanning electron microscopy when the primary electron beam has sufficient energy to knock out electrons from atoms, the X-rays generated from the sample may be employed to determine the chemistry of the specimen using either energy dispersive spectroscopy (EDS) or wavelength dispersive spectroscopy (WDS) where the intensity of the excited X-radiation is collected as a function of the wavelength. Moreover, the X-ray generated from the sample can produce an elemental map (or X-ray dot image) showing the distribution of different elements in the specimen [86]. The morphological data from secondary electron images with compositional information from EDS provides compositional mapping of the chemical components in the microstructure.

Analysing electron backscatter diffraction (EBSD) provides quantitative microstructural information about the crystallographic nature of specimen. It reveals texture, grain boundary, grain size, grain orientation and phase identity of the specimen.

4.1.3 Transmission Electron Microscopy

Transmission electron microscopy (TEM) is a microscopy technique in which a high energy electron beam is transmitted through a sample to form an image. In this method contrast in the image is formed by differences in beam scattering. The specimen size

for TEM analysis is normally required to be a 3mm disc and must be prepared in the form of a very thin foil (typically less than 100 nm in thickness) as solid materials are highly absorptive to electron beams. The thin film is obtained by either conventional electro polishing methods (for conducting samples like metals/alloys), ion milling (for non-conducting samples) or focussed ion beam technique. The specimen preparation for TEM analysis can be challenging and time consuming. The transmitted beam may be used to obtain the crystal structure and microstructural information.

4.1.4 High-Temperature Microscopy

High temperature microscopy is essential for monitoring and in-situ characterisation of microstructural changes that happen at high temperature with wide applications in different areas of materials science. High Temperature Confocal Scanning Laser Microscopy (HT-CSLM) is used to observe in situ and in real-time metallurgical reactions and transformations at high temperatures (up to 1700^{o}C).

In this technique, a laser is scanned across the specimen, focused at a particular depth. Light from the specimen passes through a small aperture (pinhole) which selects only light which contributes to an in focus image. Figure 4.3 shows a schematic representation of the furnace chamber for a high temperature confocal scanning laser microscope. The sample is inserted into the top half of the furnace chamber where the atmosphere is controlled to avoid oxidation of the sample at high temperature [87]

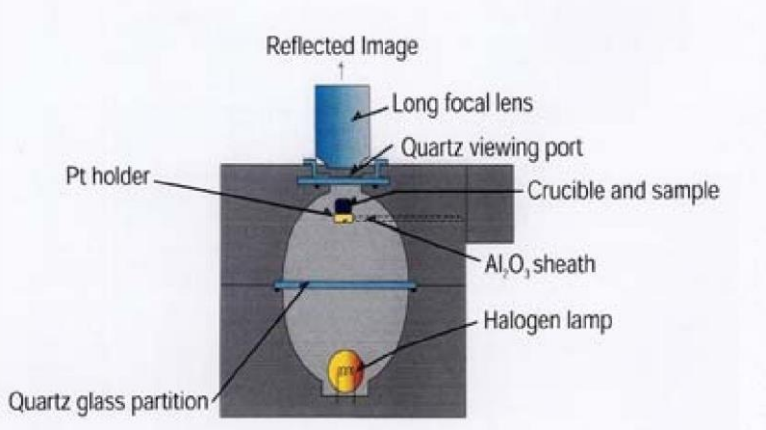

Figure 4.3: Schematic representation of the LSCM chamber[87]

4.1.5 3D Atom Probe Microscopy (3DAP)

Three-dimensional atom probe (3DAP) is used to assess compositional variations on a very fine scale. Such studies are difficult or not possible using other techniques (e.g. X-ray diffraction or TEM). For example, investigation on Al coatings deposited on a 304 stainless steel substrate revealed a cubic phase (α-ferrite phase) with a chemical composition of predominantly Fe, Cr, Ni. This result could not have been obtained from other analysis techniques such as X-ray diffraction and TEM [88, 89].

4.1.6 Thermal Analysis

In thermal analysis, the properties of materials are investigated based on temperature variations. Several types of thermal methods are in use and examples include coefficients of thermal expansion, specific heat capacities, melting and solidification

temperatures or enthalpies and characteristic thermal effects are some of the areas of high interest in metallurgical applications.

One of the most common thermal analysis techniques employed for phase transitions in steel is dilatometry. In this method the coefficient of thermal expansion is precisely measured. In other words, dilatometry utilizes the variation in volume associated with nearly all transitions and measures the change of length of a sample as it is heated up and cooled down at a fixed rate. Dilatometry technique has served to estimate the fraction of constituent phases and gives the phase fraction as a function of temperature and time, by which the transformation kinetics can be evaluated as well [90-93]. Dilatometric method has been used for quantifying the austenite to ferrite/pearlite transformation [91, 92]. In situ studies of reaustenitisation in a low carbon micro alloyed steel have been carried out by dilatometry [94].

Jun-Yun et al. used a dilatometric analysis to estimate the volume fraction of ferrite / martensite in dual phase steel (as shown in Figure 4.4). Furthermore, it was shown that dilatometry can provide a history of phase fraction along the given thermal cycles, which can be helpful to investigate the transformation kinetics or to design thermal process to obtain optimal microstructure [95].

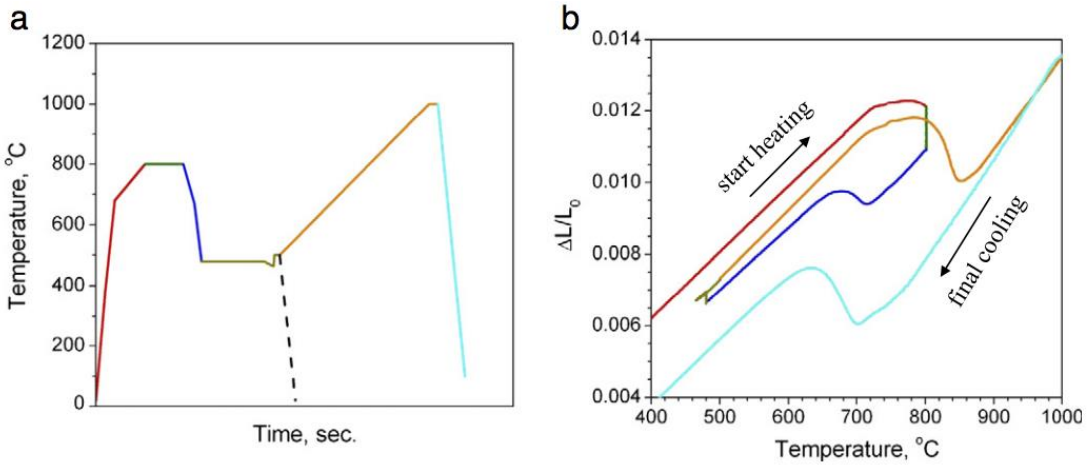

Figure 4.4: An example of dilatometric experiment to estimate the martensitic volume fraction in steel: (a) used thermal cycle and (b) an example of corresponding dilatation curve (a portion of dilatation curve can be linked to corresponding stage in the heat cycle by the same colour of line) [95].

4.2 NDT Techniques for Steel Characterisation

4.2.1 X-ray

X-rays are high-energy electromagnetic waves with a wavelength between 10^{-3} and 10^{1} nm. When a beam of X-rays impinges on a solid material, some parts of the beam will be diffracted by the electrons associated with each atom or ion that is in the beams path. It is possible to determine the molecular or atomic structure of the material by measuring the pattern and spacing of the diffracted X-rays beam since the grouping of electrons affecting the diffraction within the measured structure will provide a specific signature (diffraction pattern). This signature is analysed to determine the mean atomic spacing and disorder in a single crystal or polycrystalline structure. Basically, the experimental technique based on X-rays employed in material science and engineering may be categorised into three main classes [96]. In terms of qualitative and quantitative chemical analysis, X-ray fluorescence spectroscopy is extensively used [86, 96]. X-ray radiography is used as an imaging technique to show internal structure due to the variation in intensity of absorption [86].

The X-ray diffraction (XRD) method can be either a reflective technique or a transmission technique which offers a precise study of the structure of crystalline phases [96]. It obtains information based on the ability of crystals to diffract X-rays in a characteristic manner. The principle of XRD is based on the diffraction of X-rays by periodic atomic planes and the angle or energy-resolved detection of the diffracted signal [96]. The geometrical expression of XRD technique can be clarified by Bragg's law. Equation (4.1) quantifies Bragg's law and Figure 4.5 gives the details about geometrical condition for diffraction and the determination of Bragg's law [96].

$$n\lambda = 2d_{hkl}\sin\theta \qquad \text{Equation 4-1}$$

In Equation 4.1, n is the number of wavelength, λ is the wavelength of the incident beam (in nm), d_{hkl} is inter planar spacing and θ is the angle of incident beam to the targeted solid [96].

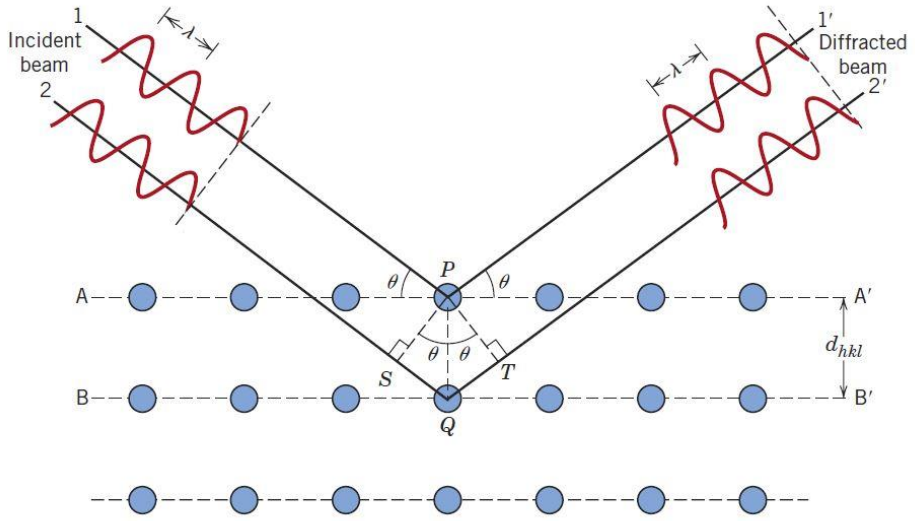

Figure 4.5:Schematic geometrical condition for diffraction and the determination of Bragg's law[29].

In the XRD technique three parameters including the peak intensity, the peak position and the peak shape are significant to interpret. The peak intensity gives information about quantitative phase analyses, texture and crystal structure. Chemical composition, space group and lattice parameters can be identified by the position of the peak. Finally, crystallite size can be investigated by the peak shape [86, 96]. The phase fractions and lattice parameters of martensite/ferrite, austenite, $M_{23}C_6$ and M_2X have been monitored by in situ X-ray diffraction technique during tempering of a martensitic stainless steel [97]. From Figure 4.6 (a) it can be clearly seen that there is transformation of martensite (with two peaks) into ferrite (single peak) with their (101)/(11 0) reflections during heat treatment alongside the presence of austenite with its (111) reflection. The precipitates are not observed in this plot but they can be seen in Figure 4.6 (b), in six clear diffraction peaks from M_2X to $M_{23}C_6$ [97]. In addition, the X-ray diffraction procedure can be employed to measure the microstructural phase balance [97-103] or steel crystallographic texture [86, 97, 102].

(a)

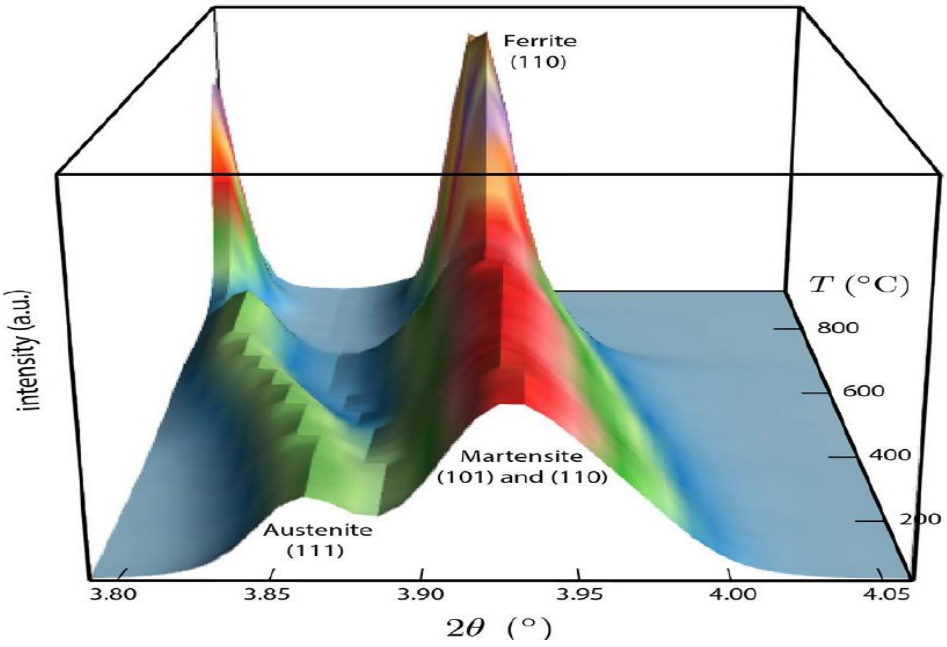

(b)

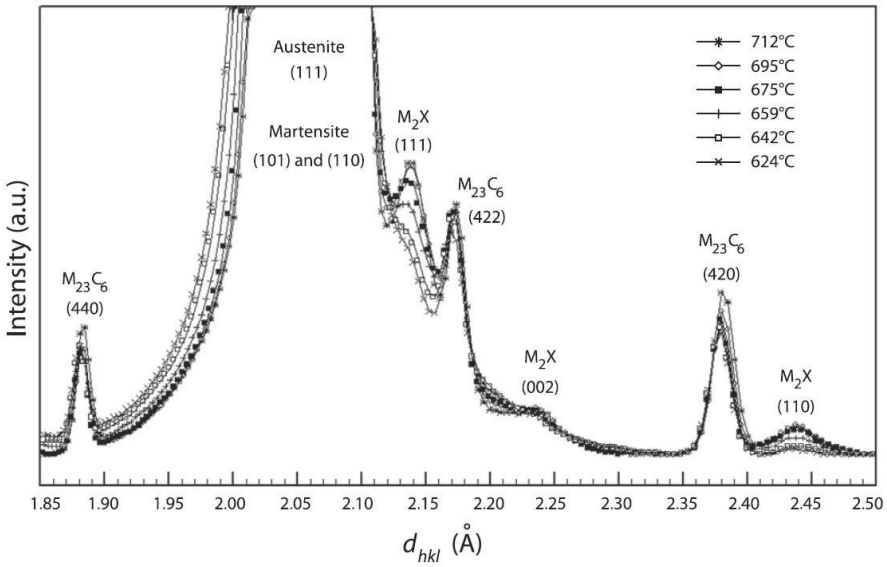

Figure 4.6: (a) X-ray diffraction procedure can be employed to determine the transformation of martensite (two peaks) into ferrite (single peak) with their (101)/(110) reflections alongside the presence of austenite with its (111) reflection. (b) The precipitates that form are characterised in six clear diffraction peaks fromM_2X to $M_{23}C_6$ [27].

The method has been reported to be successful and widely used which is relatively unaffected by environmental issues such as dust. On the other hand, most analytical X-

ray diffraction measurements are lab based and samples are usually required to be very small size (less than a 10mm cube). In addition, X-rays are generated during the measurements technique which may have enough power (i.e. radiation dose) to cause radiation burns (ionisation) [104], therefore this technique requires specific shielding to prevent exposure of workers to stray X-rays generated during measurement. The X-rays technique is a relatively expensive method [104, 105].

4.2.2 Ultrasonic Testing

Ultrasonic non-destructive technique uses high frequency sound waves (above 20 KHz) to conduct examinations of materials [106]. This technique functions by introducing transmit ultrasonic pulses into the specimen under inspection; the pulses are reflected from the back surface of the sample [107]. Figure 4.7 illustrates an operation of a UT system in pulse-echo mode. The pitch-catch technique is used when the material being tested has a high attenuation coefficient, the amplitude of echo waves are not large enough to give clear reflections for evaluation. In this technique, two transducers are located in line on opposite sides of the samples, one acting as the transmitting and the other as the receiving probe [108].

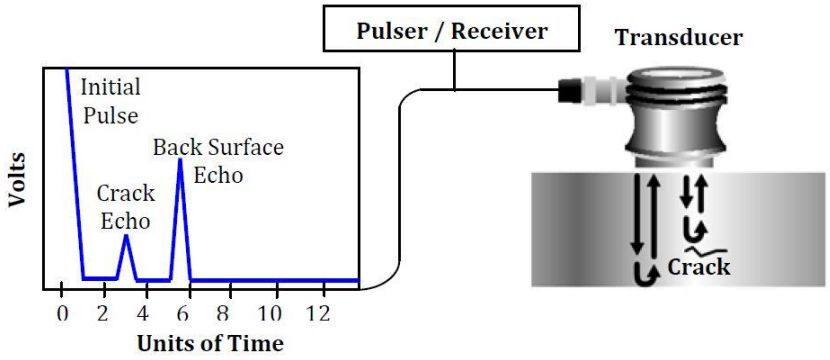

Figure 4.7: Operation of a pulse-echo UT system [109]

The features of the wave such as the amplitude of the reflection and the time taken for the reflected pulse to be received are affected by the sample's microstructural characteristics and dimensions [107]. In term of methods for generating and detecting, many different ultrasonic measurements exist; including basic ultrasonic testing, electromagnetic acoustic transducers (EMAT), electromagnetic acoustic resonance (EMAR) and laser ultrasonics [106, 107, 110]. Propagation of sound waves, loss of amplitude (or attenuation) and analysis of backscattered signals are affected by microstructural parameters (e.g. grain size, composition and crystallographic texture) or defects (e.g. inclusion or crack) [106, 107, 110-117].

The ultrasonic pulse-echo technique can be used to differentiate between different amounts of cold working in stainless steel, since a more deformed structure introduces a greater amount of dislocation density through the material and gives a slower sound velocity [114].

The thickness of a hardened surface layer was characterised by ultrasonic techniques. From Figure 4.8 (a) it can be observed for induction-hardened components, the transition from the coarse-grained base material to fine-grained surface layer is abrupt. In this event the microstructure changes within a small transition zone (one mm) from

martensite, near the surface, to the ferrite/ pearlite state of the parent material. An ultrasonic pulse is applied into the sample and the sound waves propagate within the hardened layer without any significant scattering but noticeable scattering appears at the transition zone (Figure 4.8) [107, 116].

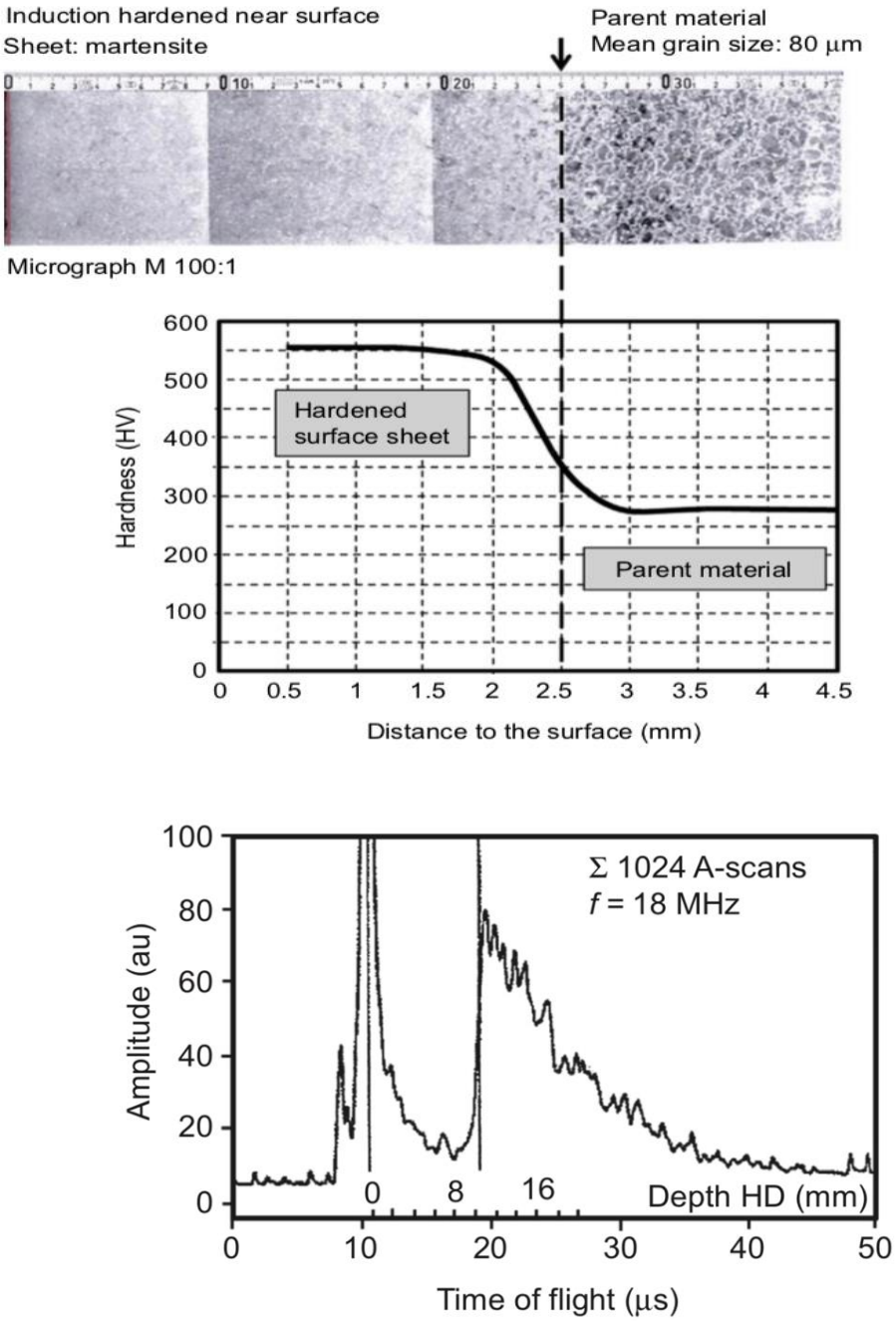

Figure 4.8: (a) Micrographs of the transition zone at induction-hardened component, hardness distribution, (b) An ultrasonic pulse is coupled into the sample Typical

backscattering signals at the transition zone from hardened surface layer to the base metal [116].

Recrystallisation in austenitic AISI 316 stainless steel was studied using laser ultrasound [111]. It was observed that there is a nearly linear relationship between velocity and measured recrystallised fraction that results when the texture change happens uniformly with time during the recrystallisation process as the velocity of ultrasonic waves is strongly affected by the elastic property which is dependent on the crystallographic texture, while attenuation of the waves is dependent on the grain size and dislocation density, Figure 4.9 [111].

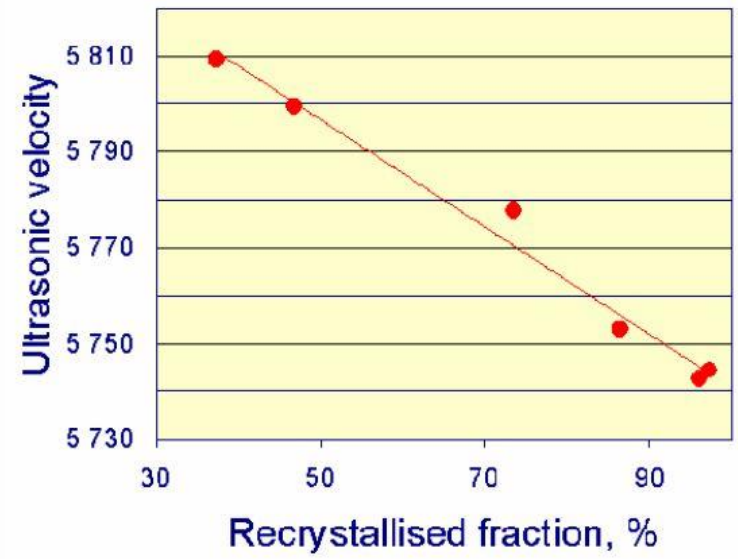

Figure 4.9: Velocity as function of measured recrystallised fraction for 316 austenitic stainless steel at room temperature, there is nearly linear relationship between velocity and measured recrystallised fraction [111].

Ultrasonic techniques have been used for determination of grain size [106, 107, 110, 113, 117]. Figure 4.10 indicates the grain size value measured by ultrasonic technique (d_{US}) in comparison to the grain size measured by metallographic method (d_{met}). It has been reported that the ultrasonic velocity decreases with decreasing grain size in maraging steels [113] and electromagnetic acoustic resonance (EMAR) has been used to detect the mean grain size of dual phase steel plate [110].

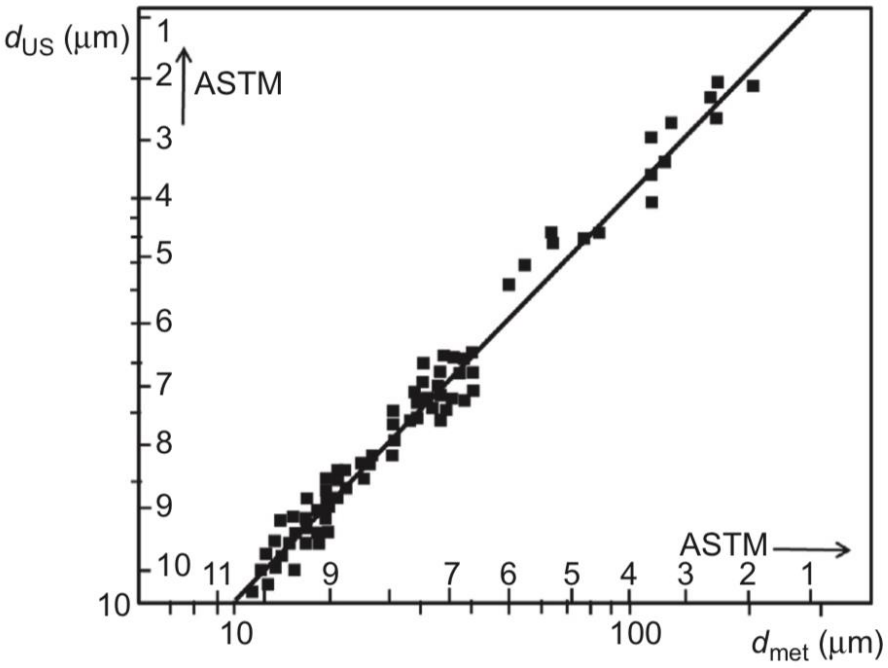

Figure 4.10: Comparison of average grain size measurements made by ultrasonic method (d_{US}) and grain size measurements made by optical microscopy (d_{met}). There is good agreement between the ultrasonic measurement and grain size estimated by microscopy [113]

Freitas [115] used ultrasonic measurement to identify ferrite, pearlite and martensite. In that experiment the lowest value of ultrasonic velocity was observed for the

martensitic microstructure in relation to the other microstructures (Figure 4.11). In addition, from Figure 4.12, it can be seen that martensite was the most attenuating microstructure and ferrite–pearlite with larger pearlite interlamellar spacing was the least [115]. The lowest ultrasonic velocity and the highest value of ultrasonic attenuation verified for martensitic microstructure can be explained by the great amount of internal tension from crystal lattice distortions [112, 115]. The results point out that whilst martensite can be differentiated from pearlite / ferrite + pearlite it appears to be difficult to separate ferrite from ferrite + pearlite or pearlite from ferrite + pearlite as there are variations for ferrite + pearlite depending on the phase fraction that means there is not a clear relationship. There have been no reports on the use of ultrasonic technique use for dual phase steel characterisation.

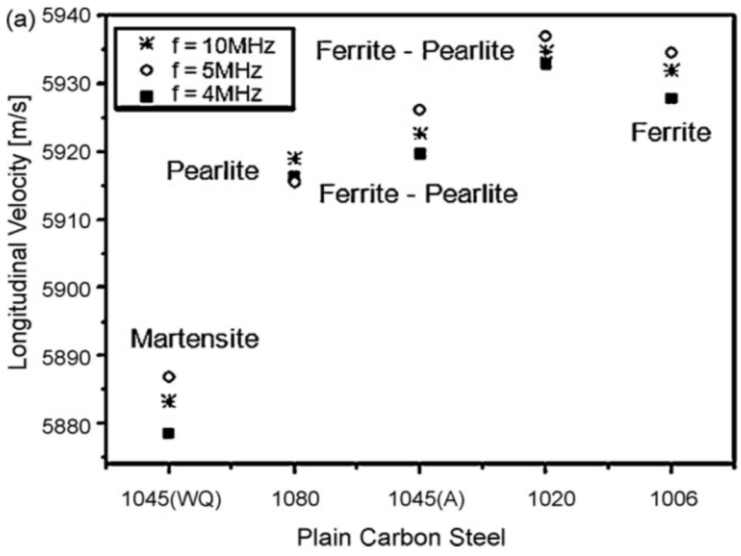

Figure 4.11: Average ultrasonic velocity measurements for longitudinal waves with 4, 5 and 10 MHz of frequency for AISI 1045 annealed (A), quenched in water (WQ), 1080, 1020 and 1006. The lowest value of ultrasonic velocity was observed for the martensite in relation to the other microstructures [115].

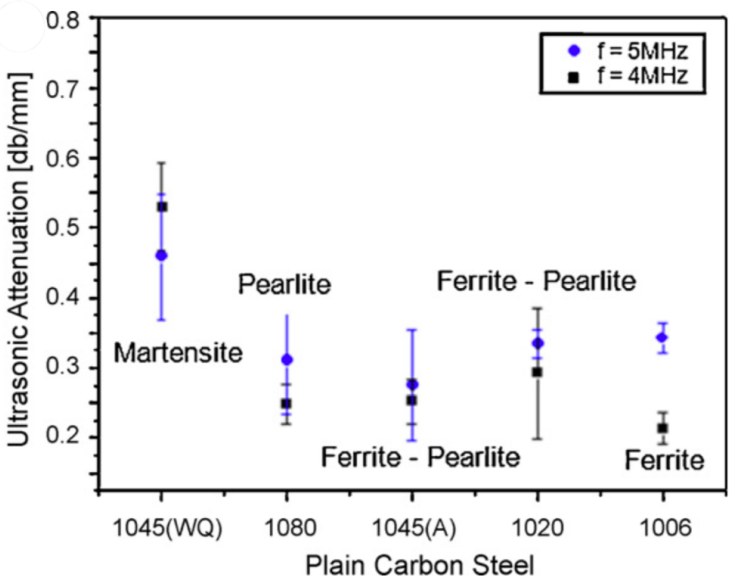

Figure 4.12: Average ultrasonic attenuation measurements for longitudinal waves with 4, 5 and 10 MHz of frequency for AISI 1045 annealed (A), quenched in water (WQ), 1080, 1020 and 1006. The highest value of ultrasonic attenuation was observed for the martensite in relation to the other microstructures [115]

4.2.3 Magnetic Techniques

A large portion of structural components are made of ferromagnetic steel. The mechanical properties of steel are affected by the microstructure, texture and residual stress state. With the understanding of ferromagnetic properties and magnetic theory, the interaction between lattice imperfections and Bloch walls is explained. Relying on this principle, various magnetic techniques for non destructive evaluation have been introduced. Out of all available methods, magnetic hysteresis, magnetic Barkhausen noise, incremental permeability, upper harmonics, and dynamic magnetostriction are very promising methods for materials characterisation.

The principles of magnetic properties were discussed in Chapter 2. The following section explains how microstructure can be correlated to measured magnetic parameters through the hysteresis B-H loop (coercivity and permeability etc.) and Barkhausen effect. Initially, lab based techniques are presented followed by commercial techniques for characterisation of steel.

4.2.3.1 Lab based Technique

4.2.3.1.1 Magnetic hysteresis

Characteristic relationships between magnetic induction (B) and magnetic field strength (H) are observed for ferromagnetic materials. Values derived from the major hysteresis loop, such as coercivity, permeability, saturation magnetisation and remanence, can be used to quantify the magnetic hardness of a material, which in turn is indicative of material hardness or mechanical property [49, 50, 54]. In addition to

these major loop properties, information can also be derived from small minor loop deviations from the major loop or initial magnetisation curve.

Takahashi et al. [118, 119] analysed the minor hysteresis loops of cold rolled low carbon steel in connection with the rolling reduction. From Figure 4.13, it is clearly seen that the cold rolling process decreases the magnetisation. This is believed to be due to the fact that dislocations produced by cold rolling act as obstacles to the Bloch wall displacement. In addition Figure 4.13 illustrates the magnetisation process before the saturation can be divided conveniently into three stages; initially a linear increase of magnetisation with *H* then sharply increases in the second stage and finally shows a gradual increase with *H* [118].

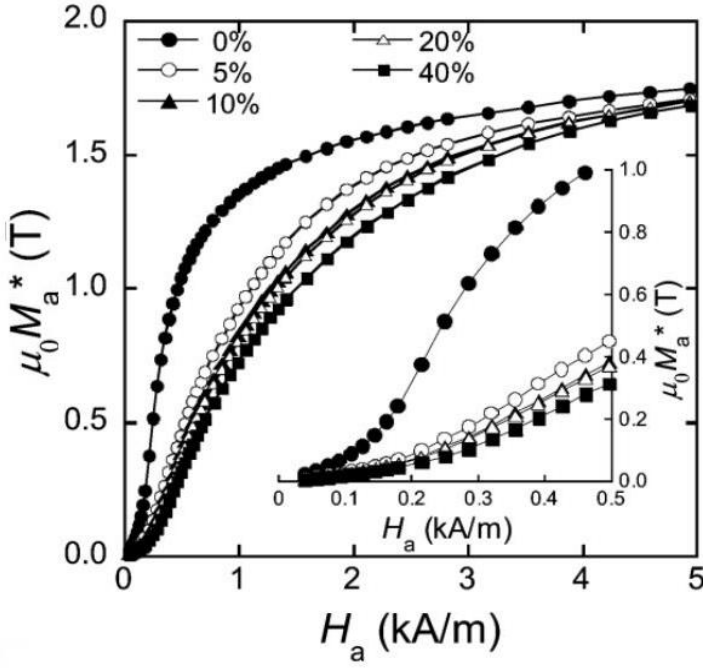

Figure 4.13: Minor-loop magnetisation as functions of H before and after cold rolling in low carbon steel, each data point represents the value of magnetisation (M_a) for each minor loop measured with H_a [118].

Magnetic hysteresis loop measurements have been used to study changes of minor loops during creep in power plant steels (Cr–Mo alloy steels) [41, 72, 120]. Since, creep damage is associated with microstructural changes due to the formation of Cr-rich carbide precipitates, coarsening of martensite laths into broader ferrite laths, formation of an equiaxed ferrite grain structure with grain growth, and cavities etc., as well as changes in distribution and density of dislocations. These defects act as effective pinning points for magnetic domain walls and will disturb their movement. Consequently, it results in changes of magnetic properties during creep (shown in Figure 4.14).

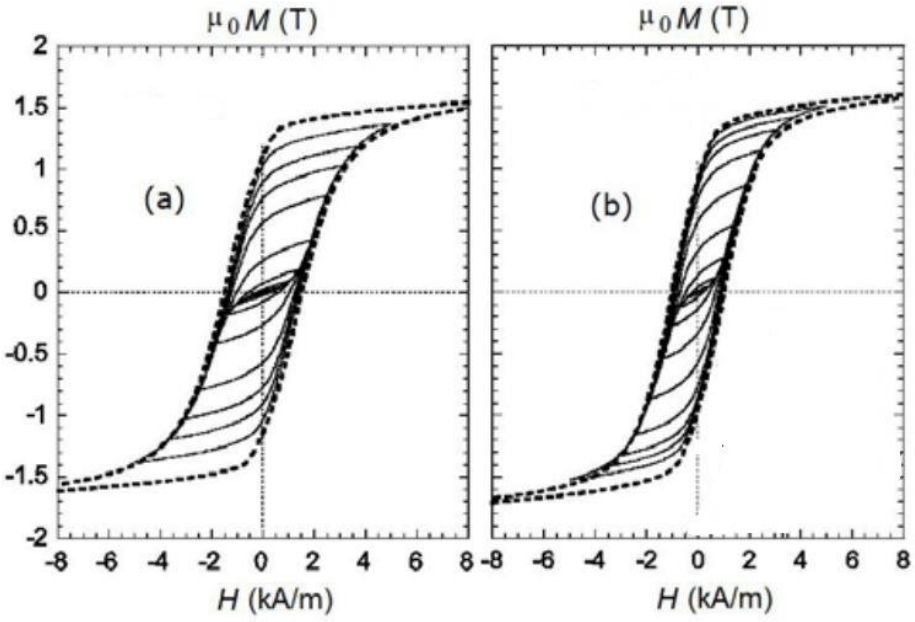

Figure 4.14: A set of minor hysteresis loops of 1Cr-0.5Mo-0.25V ferritic steel, (a) measured before and (b) after creep tests (at 923 K under tensile stress of 25 MPa). The decrease of the coercive field during creep is observed. The dotted lines correspond to the major loop [120].

The surface decarburisation layer of steel was quantitatively and non destructively investigated by magnetic hysteresis [121]. High silicon 54SiCr6 spring steel was annealed in air at 800° C for 1, 4, 8 and 20h in order to obtain different decarburisation layers. Figure 4.15 illustrates the hysteresis loops for these samples, compared with the usual sigmoid shape, the loops become more and more bulged with annealing time in air and the coercive field value decreases [121].

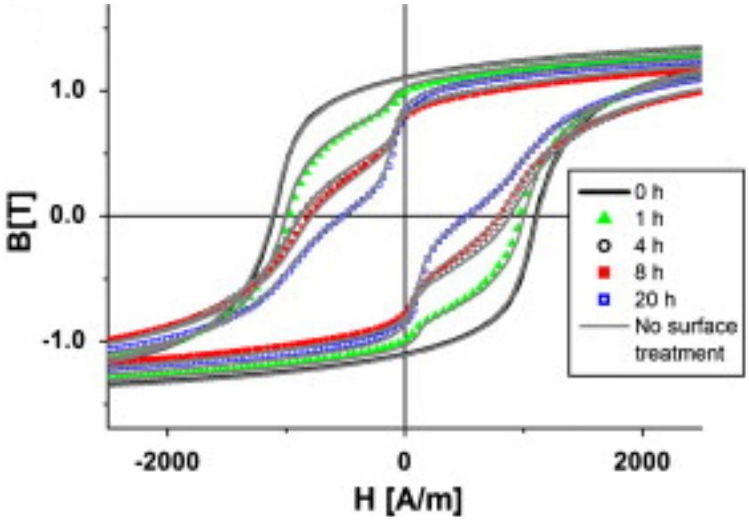

Figure 4.15: Hysteresis loops measured for high silicon 54SiCr6 spring steel samples annealed in air at 800º C for 1, 4, 8 and 20h in order to obtain different decarburisation layer [121].

A study completed by Gurrachaga et al. [122] showed that coercivity is sensitive to recovery and recrystallisation with coercivity dropping as the amount of time for recovery increases. That study showed that as recrystallisation takes place at higher temperatures the drop in coercivity is more significant than for recovery, Figure 4.16.

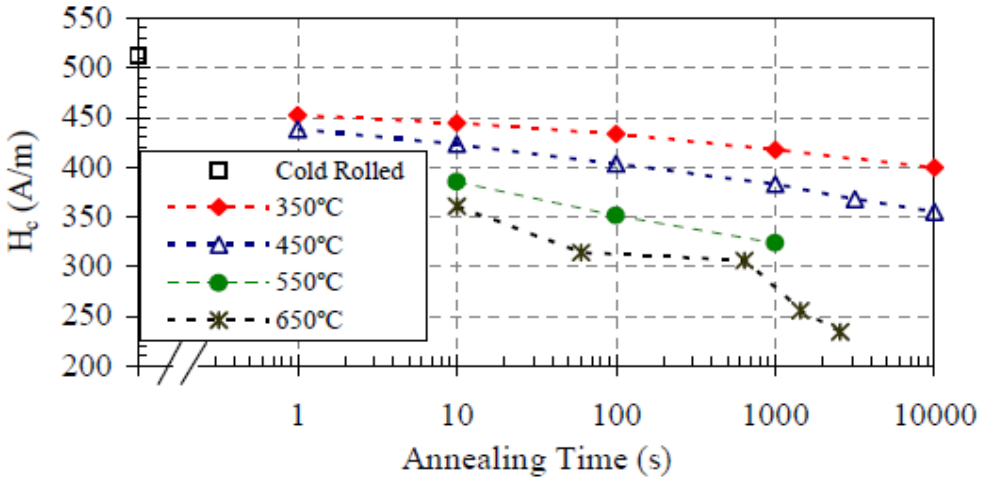

Figure 4.16: Evolution of coercivity as a function of annealing time for different temperatures in IF steels. The decrease in coercivity for the 650°C annealed sample after 1000s was due to the onset of recrystallisation [122].

It has been shown that the coercivity can be correlated to the microstructural features such as grain size and texture [44, 52, 54], carbon content [54], dislocation density [53] and phase changes in steels [52].

A study completed by Petryshynets et al. [52], (as shown in Figure 4.17) on electrical steel showed that there is an inverse relationship between grain size and coercivity (in agreement with Landgraf et al. [56] and Lukin et al. [123]) at room temperature and they used the relationship to suggest that it is possible to estimate grain size in electrical steels using coercivity measurements during steel manufacturing, although the study does not mention any practical solution of taking coercivity measurements on moving steel at high temperature.

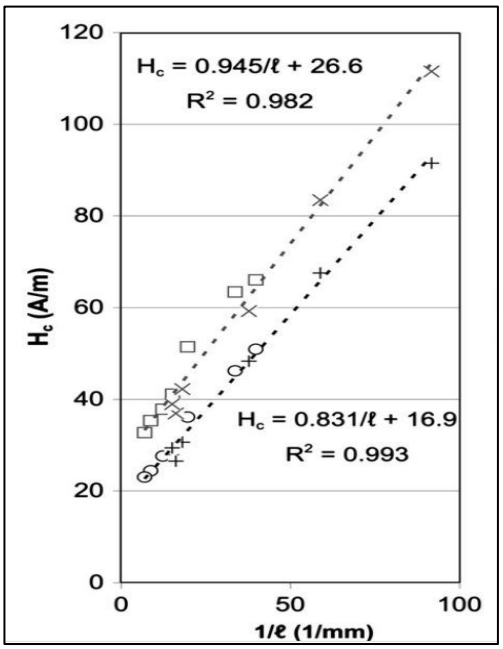

Figure 4.17: Linear inverse proportionality between the coercive field and grain size (measured through the intercept method) in electrical steel where there was no other microstructural change [52].

Coercivity measurements have been used to examine the mechanical properties of steels. It has been observed [41, 72, 124] that the coercivity, as magnetic hardness, can indicate the hardness in alloy steel (as shown in Figure 4.18), which is similar to the reported general trend that coercivity increases with hardness [49, 54, 125]. Tanner et al. [54] established a correlation between coercivity measurements and tensile strength in high tensile strength steels.

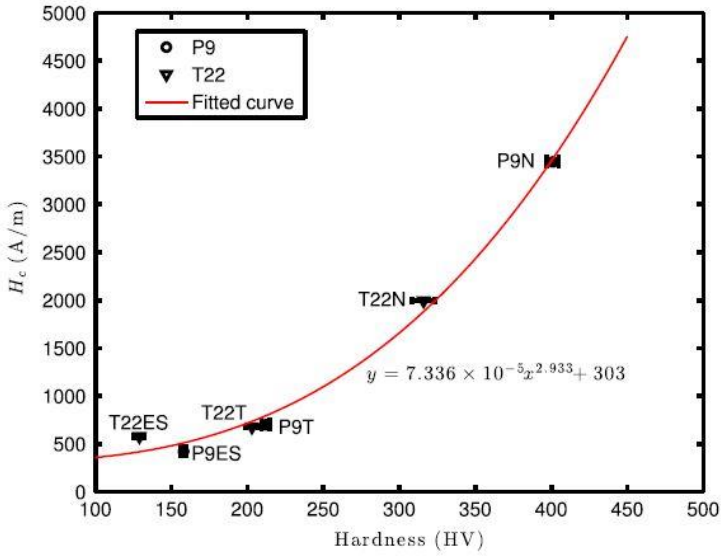

Figure 4.18:The coercivity, Hc as a function of the Vickers hardness for P9 and T22 (power station steels), Suffixes N as normalised, T as normalised and tempered and ES as ex-service [41].

Similar results were obtained by Martinez et al. [126] who revealed an almost linear relationship between the coercivity and both the martensite volume fraction and the mechanical properties for a set of samples with different volume fraction of martensite (martensite from 3% to 100%), Figure 4.19.

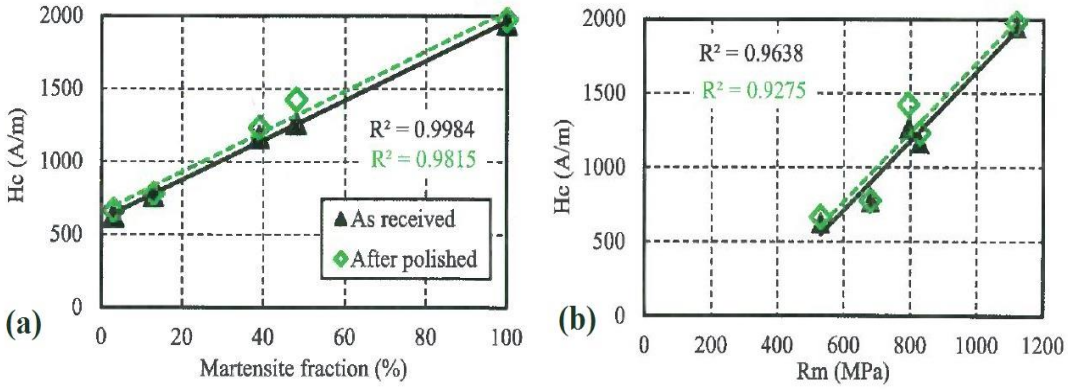

Figure 4.19: Coercivity as a function of the martensite fraction (a) and tensile strength (b) in samples with 3% to 100% martensite [126].

Rumiche et al. [127] established an electromagnetic sensor consisting of a primary excitation coil that magnetises the steel samples, a secondary coil wound on the test sample senses changes of magnetic flux, and an array of three Hall sensors to read the magnetic field (Figure 4.20). The value of the coercivity, saturation and retentivity were determined on cylindrical rods of four different structural steels, AISI 1010, 1018, 1045, and AISI 1045 - high manganese/stress proof. It was observed that the induced magnetic saturation and coercivity measured with the EM sensor can be reliably correlated to percent of ferrite, grain size, and hardness of the steel. The data reported concluded that the carbon content of the steels affected the magnetic behaviour and the increase in the amount of iron carbide (cementite) reduced their magnetisation potential.

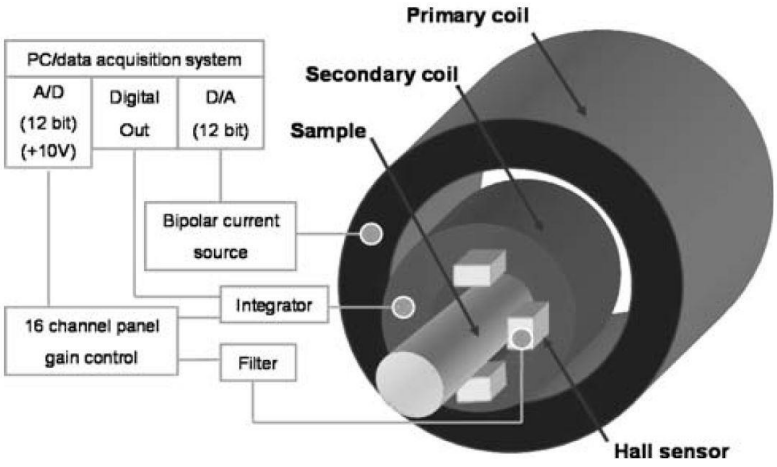

Figure 4.20: Schematic of the electromagnetic sensor and measuring system [127].

4.2.3.1.2 Magnetic Barkhausen Noise (MBN)

The degree and amount of Barkhausen noise that is produced during magnetisation of a sample is linked to the type and density of pinning points, therefore, MBN theoretically can be a good indication to measure different microstructural characteristics of a material. However, use of Barkhausen noise in this way is in reality difficult due to the stochastic nature of domain wall movement and the inclusion of competing types of pinning points within a sample. MBN technique needs a magnetic yoke (excitation coil), Hall sensor, pick up coil and signal amplification equipment (as shown in Figure 4.21) [42, 128].

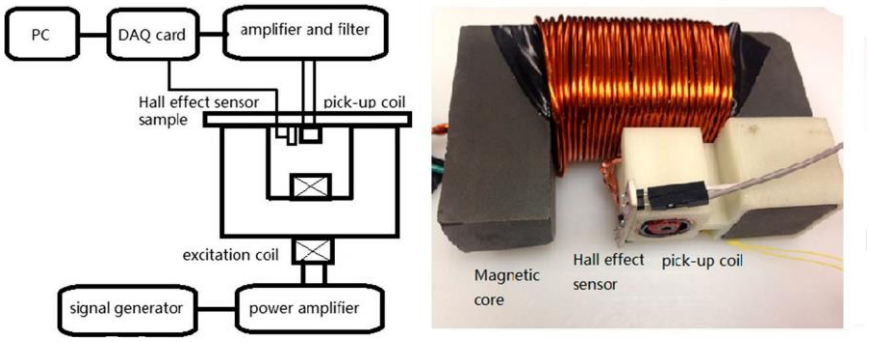

Figure 4.21: Schematic and image of the experimental set up for MBN measurement [128].

Sorsa et al. used a magnetic yoke to excite the magnetic field and established a MBN measurement system for evaluating fatigue damage based on the MBN amplitude in low-carbon structural steel [129].

Wilson et al. [72, 130] used a lab-based closed magnetic circuit measurement system and a field deployable device to work on microstructural changes in power station pipes in different states of degradation. That work showed the MBN peak position is indicative of the hardness of the samples. It is apparent from Figure 4.22 that although the MBN profile peaks do not exactly correspond to the coercive force, they do follow the trend in H_C which in turn is indicative of material hardness [72].

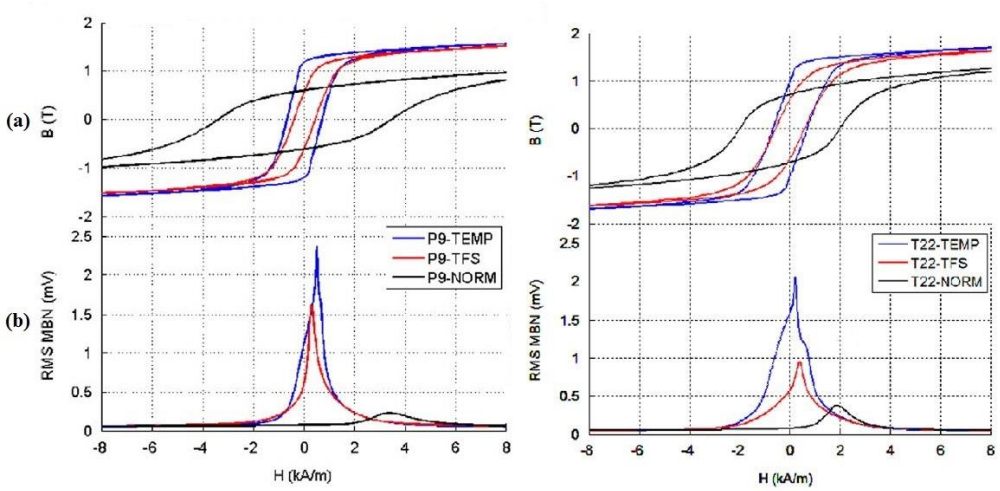

Figure 4.22 : BH loops (a) and corresponding MBN profiles for P9 and T22 (alloy steel seamless pipes/tube for high temperature service), (b), the MBN profile peaks do not exactly correspond to the coercive force but they do follow the trend in H_C , suffixes TEMP as tempered, TFS as taken from service and NORM as normalised [72].

MBN measurement techniques have been used to investigate variations in grain size, where the intensity of MBN signal is related to the number of grain boundaries, smaller grained samples have more grain boundaries (pinning sites) and give a larger MBN signal response.

Sample composition and phase change also have effects on MBN measurement, it has been reported that the presence of impurity segregation, precipitates and different phases cause variations in Barkhausen noise [131].

Magnetic properties of ferrite–martensite dual-phase steels were evaluated using Barkhausen noise and correlated with their microstructural changes. Different percentages of martensite (from 17% to 89%) and ferrite grain size numbers (from 9.47 to 11.12 in ASTM number) have been correlated to the MBN signal. From Figure 4.23 (a) it is apparent that as the martensite fractions in the DP steels increase, number of pinning sites and corresponding unpinning events increase which led to an increase in the MBN signals. In addition, the MBN signals increase with decreasing the grain size (i.e. increasing ASTM grain size number), Figure 4.23 (b), which is related to the higher grain boundary density in smaller ferrite grain [132].

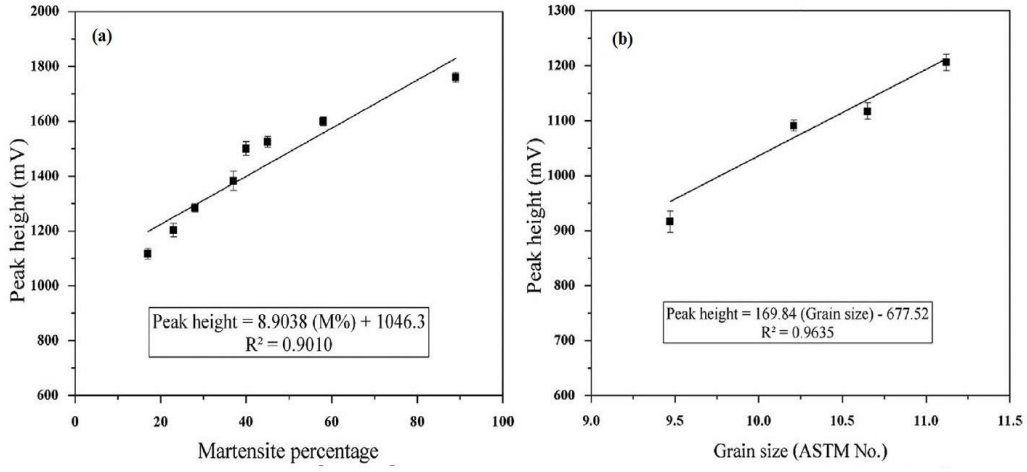

Figure 4.23:MBN signal as a function of martensite phase percentage (same grain size) (a), the ASTM ferrite grain size number with the fixed martensite percentage (i.e.17%)(b) in dual phase steel samples [132] .

Martinez et.al [126] used different proportions of ferrite and martensite produced in the laboratory to investigate the sensitivity of parameters derived from the application of magnetic hysteresis loops and Barkhausen noise. Due to the large effect of a decarburised surface layer on the overall MBN signal, the technique could not be validated for as heat treated samples or on-line measurements. However, in absence of decarburisation, the MBN signal can be related with both the tensile strength and the martensite content in dual phase steel, shown in Figure 4.24.

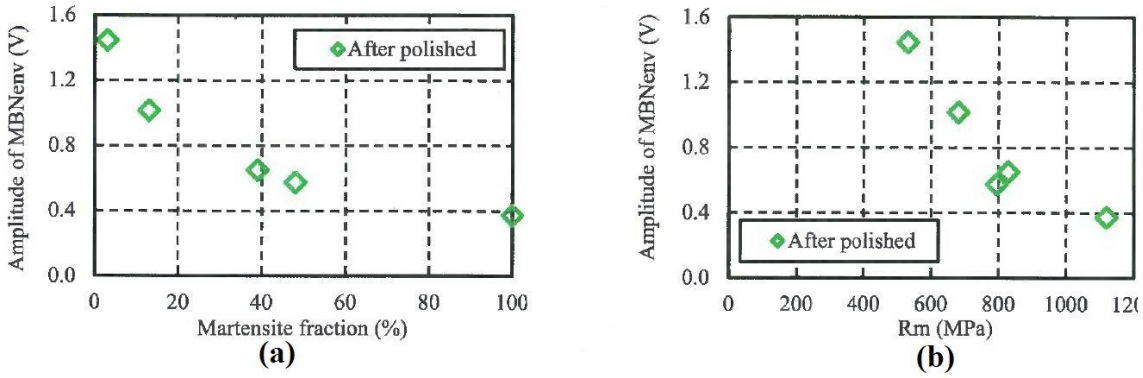

Figure 4.24: Amplitude of the MBN as a function of the tensile test (left) and martensite fraction (right) in DP steel samples [126].

MBN method is most effective when there is no lift off between the MBN pick up coil and the sample, therefore a reasonable amount of surface preparation is required. Any oxide or rust should be removed before MBN measurement. This technique can be operated as non-contact measurement, however careful calibration for lift off is required as even small variations in lift-off can have significant effects on the magnetisation amplitude and consequently on MBN signal [131].

A major drawback of MBN technique is that it needs high magnetic fields that causes significant magnetisation of the specimen therefore without demagnetisation the results

are not easily repeatable [131]. The technique is also often carried out at high frequency, making it most sensitive to surface / near surface microstructures. Therefore surface feature (such as geometry, oxide, decarburisation) have a dominant effect. Currently it is not possible to model or predict MBN quantitatively for a given microstructure.

4.2.3.1.3 Permeability based Techniques

Zhu et al. proposed a H-shaped electromagnetic sensor (EM) based on eddy current methods composed of five coils, one generation coil, and four coils as sensing pick-coils and showed that typical decarburisation layers of a rail sample can be distinguished as the sensor exploits the increase in relative permeability in the surface layers of the steel due to decarburisation [133, 134].

Work completed by Dickinson et al. [21] described a design and operation to analyse phase transformations in hot strip steel using EM instrument. Figure 4.25 shows changes in the measured impedance versus temperature. As can be observed for the low carbon steel sample, the curve displays a steep rise at the Curie temperature T_C, which is the point where the material becomes ferromagnetic, therefore, here the sensor is detecting the paramagnetic to ferromagnetic transformation. The curve for the medium carbon and high carbon steel, containing more carbon (0.44 and 0.68 wt. %, respectively), are expected to transform to a mixed ferrite and pearlite microstructure. Therefore, the curves display a steep rise (as the same as the low carbon sample) but a second transformation at the eutectoid temperature occurs. The work concluded that

differences in the measured impedance can be used to discriminate between steels of varying carbon composition.

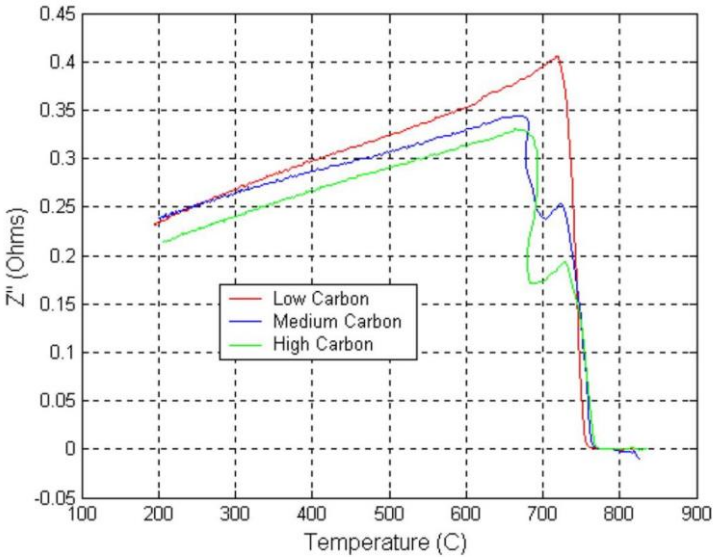

Figure 4.25: Changes in the measured impedance at 12.5 kHz versus temperature for the low carbon, medium carbon and high carbon steel [21].

Thompson et al. [49] looked at the permeability of ferritic steel as function of carbon content and showed the initial permeability and maximum relative permeability decrease with increased carbon content. Similar results were obtained by Zhou et al. [22] for relative permeability, Figure 4.26.

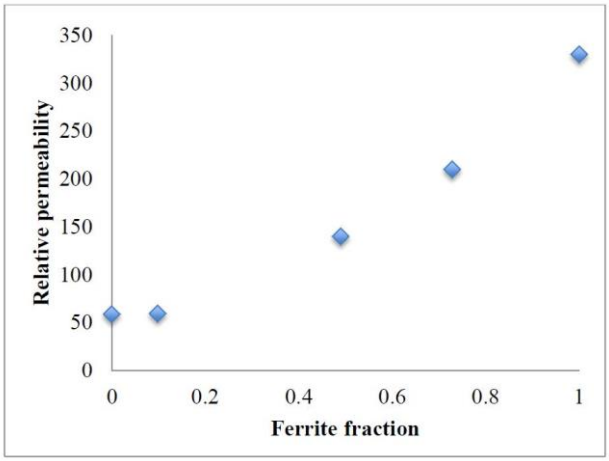

Figure 4.26: Plot of relative permeability measurements for pure iron, 0.17C, 0.38C, 0.53C and 0.8C steel samples against ferrite fraction [22].

Haldane et al [14] used a multi-frequency electromagnetic sensor to measure the impedance and inductance of samples containing varying fractions of ferromagnetic phase over a range of frequencies (100 Hz to 1 MHz). It was observed that the impedance values are approximately linearly related to ferrite fraction for random microstructures up to about 40% ferrite. The study also revealed a relationship between the zero crossing frequency (i.e., the frequency at which the inductance is zero) and ferrite percentage, Figure 4.27.

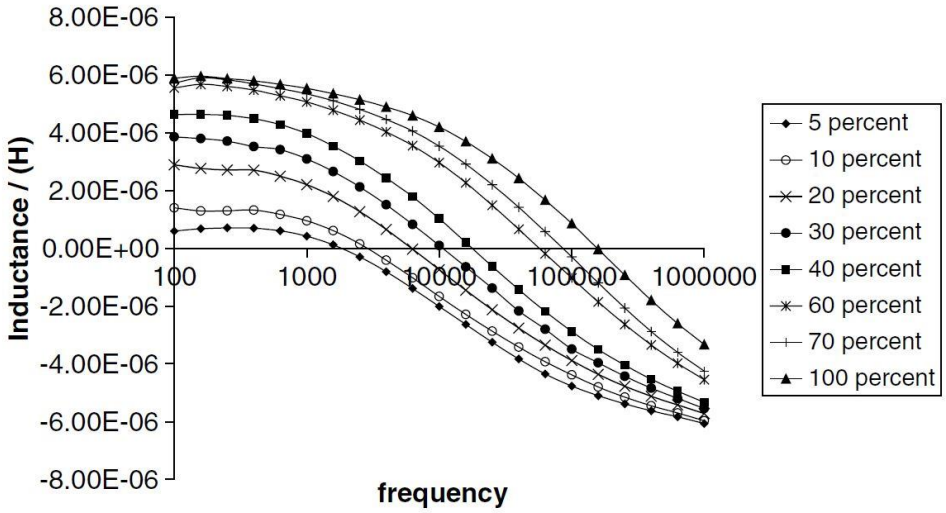

Figure 4.27: Inductance values versus frequency for the HIP_{ped} samples (listed by nominal ferrite percentage [14].

Permeability measurements have been used to investigate changes in mechanical properties of steels. A study completed by Tanner et al. on pearlitic steels suggested an hyperbolic variation of the initial permeability value with tensile strength, Figure 4.28 [54]. This is believed to be due to the boundaries between cementite lamellae and ferrite within the pearlite grains acting as strong pinning sites and these appear to be about an order of magnitude greater than the sites associated with ferrite-ferrite boundaries [36].

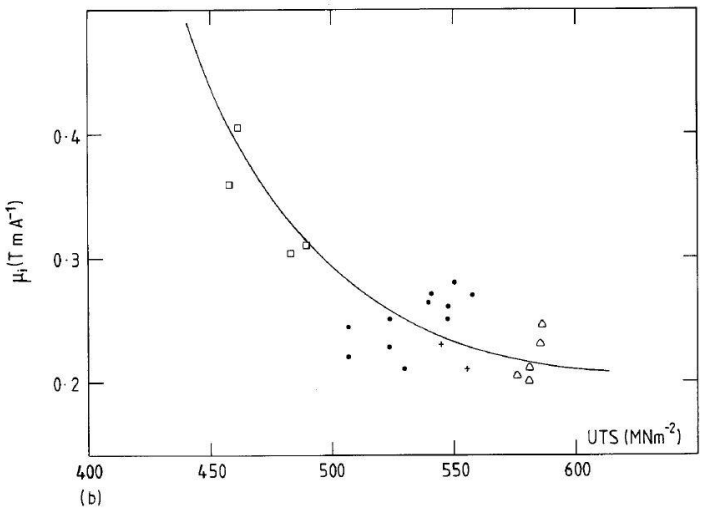

Figure 4.28: Variation of ultimate tensile stress (UTS) with initial permeability in pearlitic steels [54].

Hao et al. showed the ability of a multi frequency EM sensor to measure the ferrite fraction from 0% to 100% in austenite-ferrite steel microstructures. It was indicated that the real inductance value at low frequency (10Hz) increases with ferrite percentage. This is because at low frequency (plateau region) real inductance is related to the relative permeability of the sample, shown in Figure 4.29 [63].

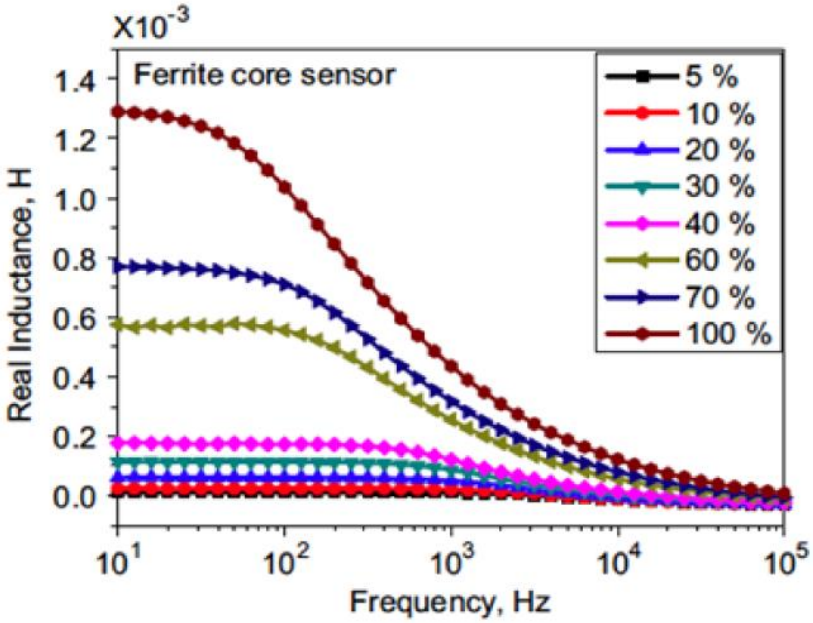

Figure 4.29: Real inductance versus frequency at ferrite fraction of 5%-100% in ferrite + austenite steels[63].

Ghanei et al. showed the potential of using an eddy current method to measure the percentage of martensite in heat-treated DP steels. Furthermore, the technique was used for the prediction of mechanical properties of DP steel [135]. The work reported for constant thickness samples and a frequency of 250Hz, which was chosen by regression analysis to be the optimum frequency for impedance output correlation to strength, Figure 4.30.

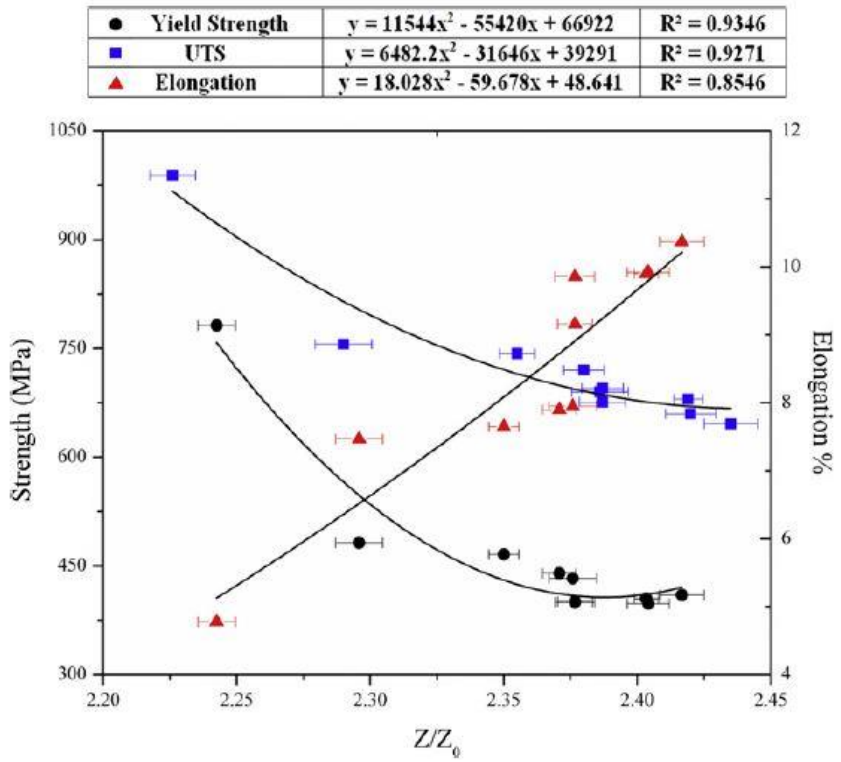

Figure 4.30:Relation between the tensile properties of different DP steel with normalized impedance [135].

4.2.3.2 Commercial EM sensors

EM sensor systems have been developed or commercialised in order to use in industry for characterisation of steel. Commercial EM sensors have been used for phase transformation, evaluating/monitoring microstructure, mechanical properties (tensile strength, hardness etc). The following section introduces different commercial techniques used for non-destructive characterisation of steel and the main features will be explained.

4.2.3.2.1 EMspec^{TM} System

EM sensor systems have been developed to operate in the run out table after hot rolling of strip steel, with three systems having been installed in Tata Steel's IJmuiden hot strip mill (EMspec^{TM}). The sensor works at low magnetic field and has been designed to sit in-between the rollers of the hot strip mill's run out table and monitor phase transformation as the hot steel passes over the run out table during the cooling process. The distance between the sensor and the sample being tested is approximately 40 mm (lift off) and the sensor measures phase angle changes. It has successfully demonstrated that EMspec^{TM} is able to quantitatively measure phase transformation in an accurate and consistent manner as long as it is well calibrated, Figure 4.31.

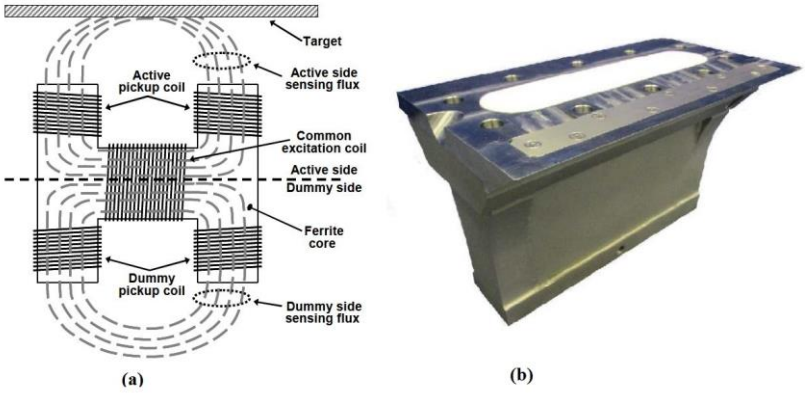

Figure 4.31: Electromagnetic sensor for monitoring the phase transformation. The inductance sensor head consists of ferrite yoke, excitation coil and pick up coils (a) It is assembled in a water- filled steel house with a ceramic window (b)[136].

4.2.3.2.2 IMPOC measurement

Impulse Magnetic Process Online Controller (IMPOC) is based on a magnetisation and read back principle using two identical sensors, arranged on the upper and underside of the strip sample as illustrated in Figure 4.32. The amount of residual magnetisation in the sample is used in a mathematical model to determine the material properties of the specimen. The running strip is magnetised periodically by the two magnetising coils up to saturation point and the gradient of residual magnetic field strength on both sides of the steel strip is measured by highly sensitive magnetic field probes.

The mechanical properties of the steel strip (i.e. yield strength and tensile strength) can then be assigned to this gradient via empirical correlations. The IMPOC system is capable of measuring steel strip passing at a high speed of 900 m/s although the effect of lift off between the sensor head and the surface of the material being measured needs to be considered. This is taken into account by having a sensor on both sides of the

strip and balancing the sensor outputs [137]. IMPOC systems are now used in pickling lines, continuous annealing lines (near the accumulator / strip exit point operating at ambient, not high, temperature) and hot dip galvanising lines. IMPOC measurements are sensitive to change in the grain size, recrystallisation state and different cooling conditions in the hot strip mill. IMPOC measurement has been done to investigate the skin pass effect on DP steel but it showed an inconsistent relationship between magnetic measurement and skin pass level [138].

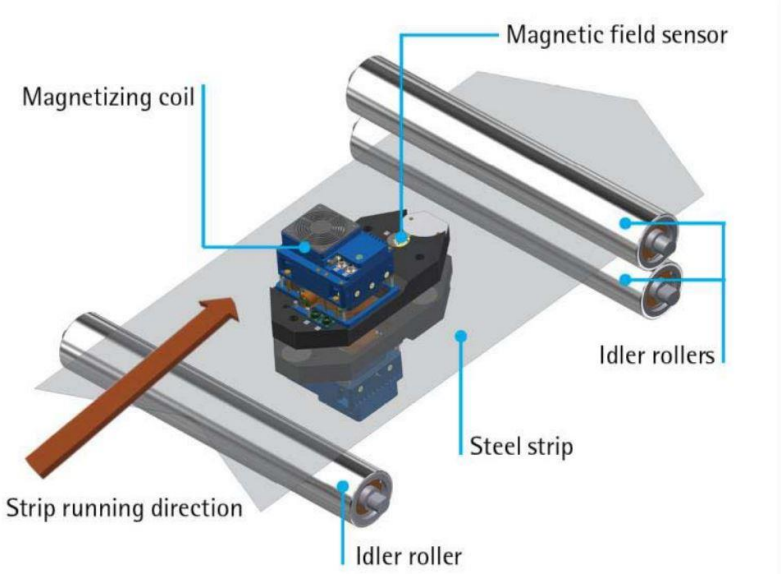

Figure 4.32: Schematic diagram of IMPOC operating principle [137].

4.2.3.2.3 HACOM system

Harmonic Analysis Coil Online Measuring (HACOM) system has been developed to measure changes in microstructural parameters. It is a type of magnetic hysteresis loop measurement. HACOM uses sinusoidal magnetisation of the sample at a low flux

density far from saturation employed at four frequencies between 20 Hz and 5 kHz. The magnetisation of the sample runs through hysteresis loops and the magnetic hysteresis induces field changes into receiving coils. An FFT (Fast Fourier Transform) is performed to gain the harmonic spectrum. HACOM provides non-destructive determination of direction-dependent mechanical material properties such as tensile strength, yield strength, strain hardening and anisotropy. For instance, HACOM has been employed to analyse cold rolling in three different steels including; IF steel, micro-alloyed (MA) and dual phase steel (DP). Figure 4.33 shows a plot of the real and imaginary signal components from the HACOM system and it can be observed from the plots that for IF and DP steels the HACOM signal decreases monotonically with increasing percentage elongation [137].

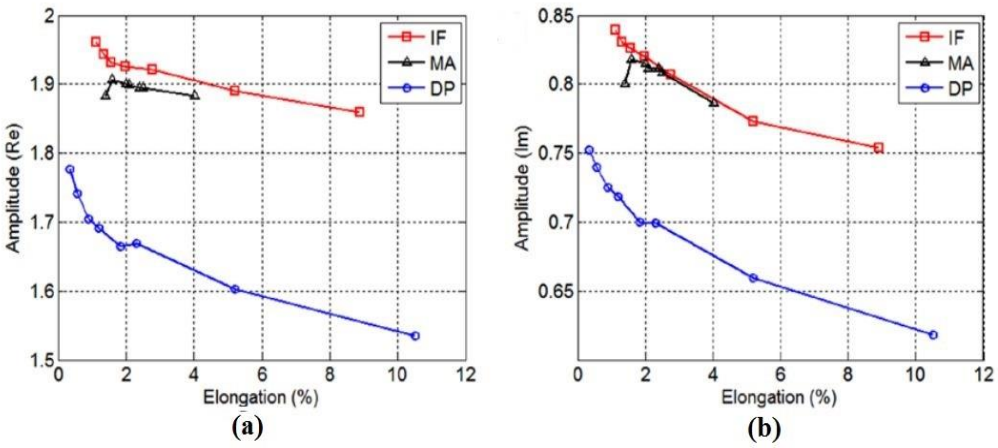

Figure 4.33: Plots of the real (a) and imaginary (b) signal components from the HACOM system measurement for IF steel, micro-alloyed (MA) and dual phase steel (DP) [137].

A major disadvantage of HACOM measurement system is that it is extremely sensitive to external electromagnetic noise, lift off and the residual stress state of the material.

Therefore two sensor heads were used to eliminate the effect of lift off by reading the mean value of the two sensors. It seems due to the amount of disruption required to place the equipment within the line, the interpretation of signals from HACOM for industrial application for on-line measurement is very challenging.

4.2.3.2.4 (3MA)

Micro-Magnetic Multi-parameter Microstructure and Stress Analyser (3MA) system consists of a power supply for magnetisation, and an analog part with different potential modules to measure various micro-magnetic parameters such as; Barkhausen noise, permeability and magnetic field strength. The 3MA technique has been used to determine surface and subsurface hardness, tensile, yield strength, residual stress etc. Figure 4.34 shows a comparison between the non-destructively predicted yield strength and tensile strength values by 3MA technique and the destructively determined values for high strength steel[139] .

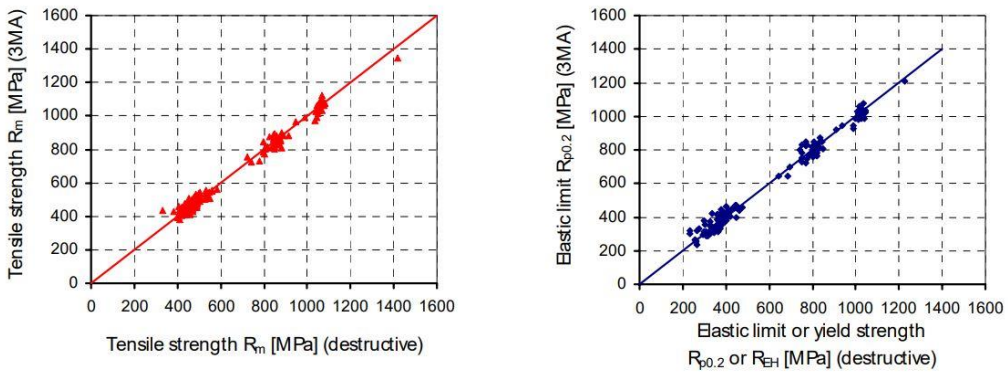

Figure 4.34: Non-destructively predicted tensile and yield strengths as a function of the destructively determined results in high strength steel [139].

Major concern about this technique is that the best results could be achieved if individual calibration functions were used for each steel producer, each steel grade and each plate thickness and also a clean surface is required before operating the sensor.

4.2.3.3 Magnetic Technique Modelling

The development of dedicated simulation tools, which treat the underlying electromagnetic problem, can offer quantitative answers to some issues regarding experimental process which may serve as a valuable support towards the improvement of sensor and enhancement the technique measurement. For instance, the determined values by the IMPOC-system (Impulse Magnetic Process Online Controller) can be influenced by material thickness, strip speed and other measurement conditions. Although these sensitive parameters can partly be compensated using different calibration procedures, which is time consuming and labour-intensive. The construction of an accurate, physics-based model of the technique (i.e. sample/instrument) will accelerate the calibration of the IMPOC and the interpretation of the data. The real IMPOC instrument magnetisation coils have a 3D geometry but a 2D model of the IMPOC system gave sufficient results for demonstrating the general trends, allowing to investigate the effect of the speed (coil movement) and average gradient of remanent magnetic field strength. The 2D model is very beneficial in terms of reduction of the computational burden compared with 3D.

Figure 4.35 depicts two different snapshots of the field profile inside the plate at two different characteristic times, before the excitation peak (Figure 4.35 a) and during the relaxation time (Figure 4.35 b) [140].

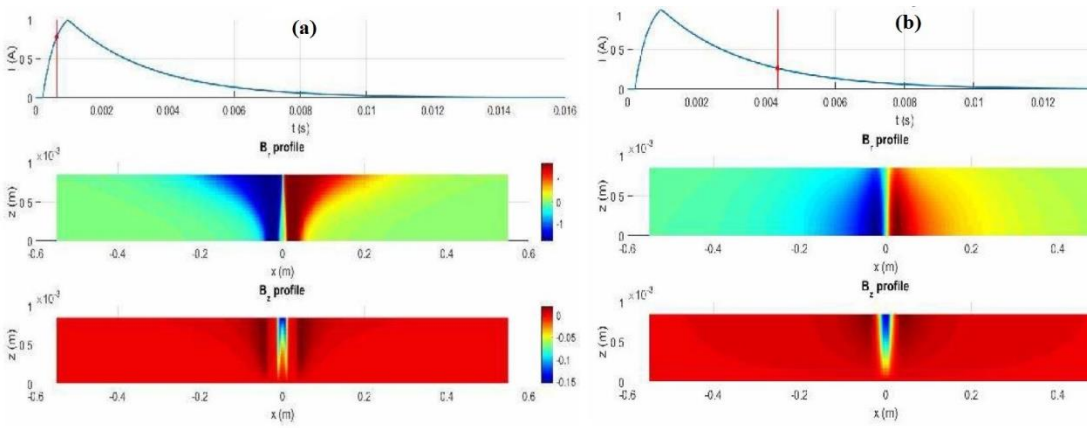

Figure 4.35: The field profile inside the sample at two characteristic times, before the excitation peak (a) and during the relaxation time (b) [140].

A measuring system for detecting phase transitions during heat treatment based on impedance measurements was developed and put to operation in a hot strip mill as shown in Figure 4.36. Parameters including; signal amplitudes, phases and some of the disturbing influences can be studied by simulation work. The modelling for the generalised multi-frequency response of the system was mainly based on the 3D finite element method (FEM) using a commercial simulation package, Maxwell 3D.

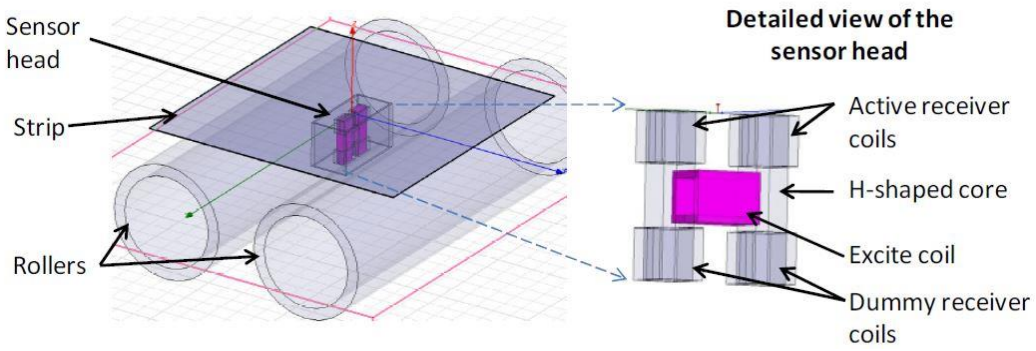

Figure 4.36: A typical model of an H-shaped sensor placed between two rollers, with the hot strip on the top [138].

Zhou et al [64] studied the effect of phase fraction (in ferrite - austenite and ferrite – pearlite steels) and the influence of the second phase distribution on the low field relative permeability were modelled using a 3D finite element (FE) microstructure – EM model using COMSOL Multiphysics. The modelled results showed that the effect of low ferrite volume fractions (e.g. 30% ferrite fraction) on the relative permeability values for microstructures with ferrite-pearlite is more significant than for ferrite - austenite microstructures. This is due to the fact that and at room temperature pearlite is ferromagnetic whereas austenite is paramagnetic, when the ferrite fraction is low (ferrite grains are isolated) the magnetic flux can more readily pass through pearlitic regions between the preferred ferrite regions.

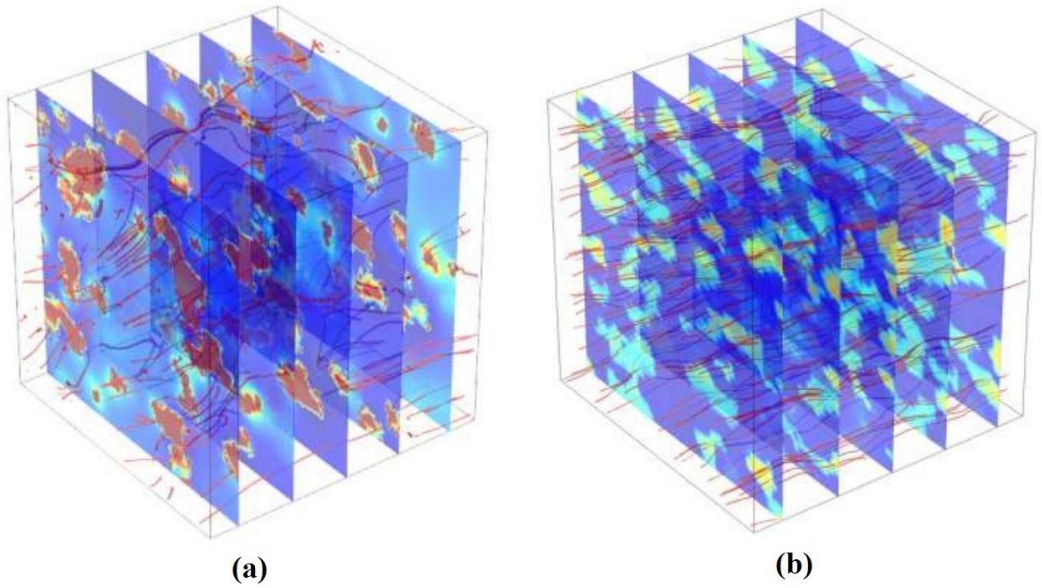

Figure 4.37: FE modelled results of magnetic flux distribution for microstructures in ferrite-austenite phase balance with 30% ferrite (a) and for microstructures in ferrite –pearlite with 30% ferrite (b) Stream lines illustrate magnetic flux density [64]

That work was carried to consider the effect of grain size on the low field relative permeability for single and dual phase microstructures [55]. It can be seen from Figure 4.38, there is an increase in the relative permeability value as the ferrite grain size increases from 14 to 52 µm for an extra low carbon steel sample and 13 to 64 µm for a 0.17wt%C steel sample.

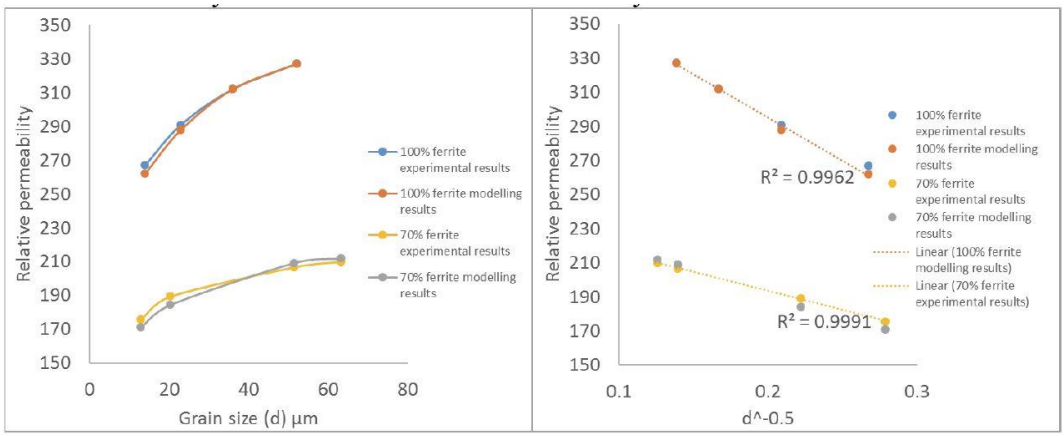

Figure 4.38: FEM modelled and experimental determined low field relative permeability plot with grain size (a), inverse square root of the grain (b)[55].

A model has been developed by Shen et al. [141] for the EMspec^{TM} sensor system using the measured zero crossing frequency (i.e., the frequency at which the inductance is zero) to obtain the permeability at any (known) temperature, which can then be used to determine the microstructure (phase fraction), mimicking the real-time monitoring of phase transformation of steel product, as shown in Figure 4.39.

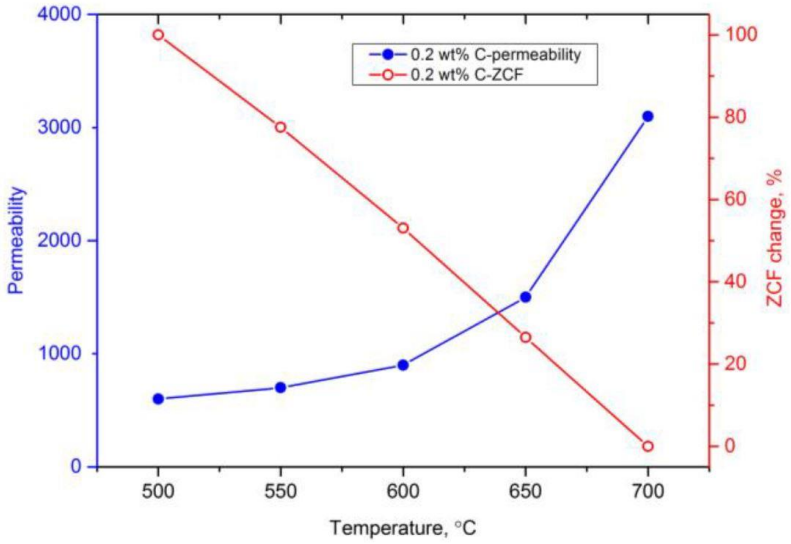

Figure 4.39: Modelled zero crossing frequency (ZCF) with permeability for 0.2 wt% carbon steel against temperature [141].

4.3 Summary

In this chapter, the main techniques for steel characterisation have been introduced. A variety of techniques can be used to characterise microstructure. The conventional methods to obtain phase and grain size information are destructive, and time consuming, as they require a small piece of material to be removed.

Whilst the UT technique can operate at a significant standoff but the technique requires high degree of surface preparation and laser safety requirements for LUS. The X-rays technique provides information on a range of scales from atomic to through thickness but significant health and safety protocols have to be in place for the system to be used and correlations to mechanical properties have not yet been made. Electromagnetic (EM) methods have a high potential for material characterisation.

Different application of MBN measurements were presented for characterisation of steel. The MBN signal can be correlated to the mechanical property of a sample. MBN technique is strongly influenced by the surface of the specimen since MBN is often carried out at high frequencies, for low frequency systems it can measure up to depths of 1.5 mm depending on the material. A relatively high field is required to obtain the MBN signal.

Hysteresis loops are sensitive to microstructural features such as phase, grain size, dislocations, precipitates, stress and etc. The clear disadvantage of such technique includes; high power requirements to magnetise sample limiting practical application and the prior magnetic history can affect results if the initial magnetisation curve is being assessed.

Multi frequency EM sensors have been used at low field strength and operating at different frequencies. They can be designed for different sizes and geometries and it is possible to operated with lift off (although this needs to be calibrated). A variety of electromagnetic (EM) sensors have been developed or commercialised for evaluating/monitoring microstructure and/or mechanical properties. EM sensors have been shown to be able to monitor the transformation from austenite to ferrite, below the Curie temperature, and to distinguish between samples with mixed microstructures (ferrite + austenite; ferrite + pearlite; ferrite + martensite) across the whole range of ferrite percentage

EM sensors can be used to characterise austenite and ferrite fraction in hot strip mills (EMspec^{TM}) system and for statistical correlations to mechanical properties, IMPOC and HACOM systems in cold strip mills.

EM sensors have been employed for characterising a limited number of heat treated and commercial DP600, DP800 and DP1000 samples and demonstrated that a clear, qualitative relationship between sensor signal and tensile strength/martensite fraction can be obtained. The work has been done for a constant thickness and the effect of sample thickness was not assessed.

Magnetic techniques can be simulated (2D/ 3D) in order to facilitate the design and answer to some issues regarding experimental process.

5 Materials and experimental procedure

5.1 Materials

5.1.1 Heat treated DP600 steel

Laboratory heat-treated dual phase (DP) steels were used to investigate the correlation between ferrite/martensite fraction and EM sensor signal for samples with constant thickness. Samples of heat treated dual phase (DP600) steels with a carbon content of about 0.17 wt.% were supplied by Tata Steel Europe in various heat treated conditions, prepared by an intercritical annealing heat treatment to generate different ferrite-martensite phase fractions (full compositions of the heat treated DP steel has not been included for commercial reasons as it is a production grade but it fits the DP600 grade specification.

The samples were austenitised and held at intercritical temperatures ranging between A_{C1} and A_{C3} from 650°C to 800°C in 50°C steps then water quenched for the austenite to form martensite. Table 5.1 shows the form of the dual phase steel samples and their thermal history/heat treatment conditions.

Table 5-1: Laboratory heat-treated dual steel samples and heat treatment conditions.

Sample	Heat treatment conditions
DP600-650	DP600 strip steel (1.4 mm thickness) intercritical annealed at 650 °C for 1 hour followed by water quench.
DP600-675	DP600 strip steel (1.4 mm thickness) intercritical annealed at 675°C for 1 hour followed by water quench.
DP600-700	DP600 strip steel (1.4 mm thickness) intercritical annealed at 700 °C for 1 hour followed by water quench.
DP600-725	DP600 strip steel (1.4 mm thickness) intercritical annealed at 725 °C for 1 hour followed by water quench.
DP600-750	DP600 strip steel (1.4 mm thickness) intercritical annealed at 750 °C for 1 hour followed by water quench.
DP600-800	DP600 strip steel (1.4 mm thickness) intercritical annealed at 800 °C for 1 hour followed by water quench.

5.1.2 Commercial DP steel

In order to study the effect of phase balance (i.e. ferrite/martensite fraction) on EM sensor measurements for varying thickness strip samples, different commercial grade dual phase steels with a variety of thicknesses were used (supplied by Tata Steel Europe from the Port Talbot and IJmuiden strip mills).

The steels contained 0.075 -0.23 wt% C and 1.1– 2.9 wt% Mn, the amount of these elements generally increasing with increasing strength (i.e. higher for DP1000 than DP800 than DP600). Additions of Ti and Nb are also used to achieve strength levels of DP800 and above. The DP800 and DP1000 grades have higher carbon content than DP600 grades. The DP600GL, DP800GL and DP1000GL have, nominally, the same composition as the DP600, DP800 and DP1000 grades respectively and were supplied with a galvanised layer approximately 50μm thick. The chemical composition for the commercial DP samples are given in Table 5.2 (full compositions of the commercial DP steels have not been included for commercial reasons but fit within the DP600, DP800 and DP1000 specifications). The grade of DP steels and their dimension details are given in Table 5.3.

Table 5-2: Chemical composition for the commercial DP samples, all in wt%.

DP Grade	C	Si	Mn	P	S	Al	Nb+Ti
DP600	0.07- 0.12	0.06-0.5	1.8-2.1	0.02-0.08	0.005-0.015	0.040-1	0.02-01
DP800	0.12-0.18	0.24-0.8	1.8-2.06	0.008-0.07	0.004-0.015	0.04 -2	0.05-0.15
DP1000	0.15-0.23	0.04-0.1	2-2.1	0.01-0.04	0.001-0.1	0.04-1	0.05-0.15

Table 5-3: Hot rolled and cold rolled DP steels and their dimensions

Sample	Type	Thickness (mm)	Dimensions (mm)
DP600 CR	Cold Rolled	1	1000 x 570
DP600 CRGL	Cold Rolled	1	1000 x 570
DP600 CR	Cold Rolled	1.4	1000 x 570
DP600 CR	Cold Rolled	1.5	1216 x 1000
DP600 HR	Hot Rolled	4	210 x 300
DP800 CR	Cold Rolled	0.95	1250 x 1000
DP800 CR	Cold Rolled	1.6	1000 x 570
DP800 CRGL	Cold Rolled	1.6	210 x 335
DP800 CR-A	Cold Rolled	2	1000 x 570
DP800 CR-B	Cold Rolled	2	1178 x 1000
DP1000 CR	Cold Rolled	1	1225 x 1000
DP1000 CRGL	Cold Rolled	1.2	210 x 335
DP1000 CR	Cold Rolled	1.6	1260 x 1000

*HR=Hot-rolled, CR=Cold-rolled, GL=Galvanized

5.2 Sample Preparation, Experimental Equipment and Methods

5.2.1 Metallography, Sample Mounting, Grinding, Polishing and Etching

Samples of approximately 300mm×80mm were cut in the appropriate direction (rolling direction and transverse direction). The sections were mounted in conductive Bakelite, followed by grinding with grit papers with increasing levels of refinement and fine polishing of the surface to a 0.05μm finish. The DP steel samples were etched using Nital 2% etchant.

5.2.2 Microscopy

Sample microstructures were viewed using a Nikon ECLIPSE LV150N optical microscope. Images were recorded using Axiovision 4 software, which was on a dedicated PC linked to a camera on the microscope.

5.2.3 Phase Quantification

Ferrite/martensite phase balance for each sample was evaluated by using Image J analysis software. In order to find out the phase balance (e.g. ferrite/martensite fraction), optical images of the microstructure were converted to black and white through image J software. Typically, 10 images for each grade were selected, quantified and the average fraction of each phase was calculated Figure 5.1.

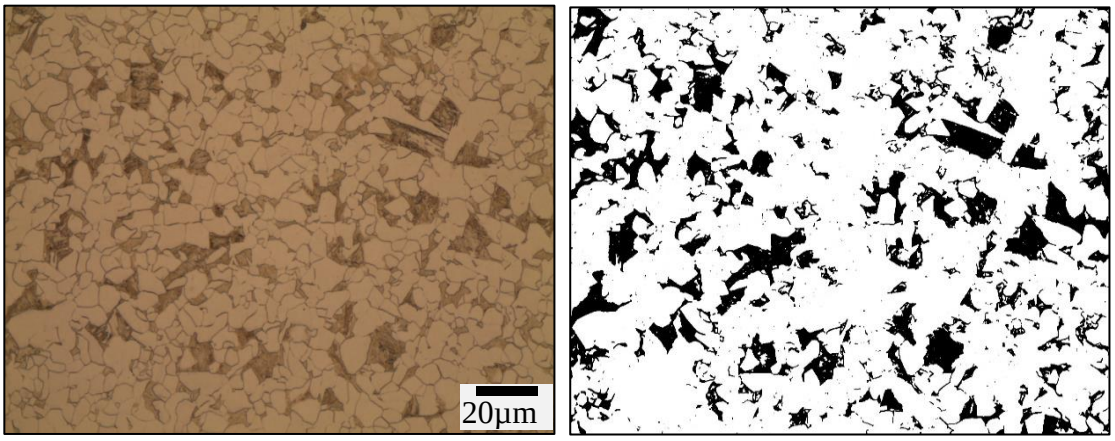

Figure 5.1: The optical micrograph of a DP 600 sample 4mm (left) and processed black/white image (binarised) microstructure by using Image J software (right).

5.3 Grain size measurement

In order to measure the ferrite grain size, the mean linear intercept method was used on the optical micrographs taken at a magnification of 1000× in different directions across the desired area (a minimum of 5 lines per micrograph). The number of grain boundaries along each test line was counted. Three images were used for each sample to obtain the average grain size [142].

5.4 Hardness measurement

Hardness was measured as per ASTM E92-17 standard, on the polished samples by a TUKON 1102 Vickers micro hardness machine with a 500g load. The hardness value for each sample was obtained by taking the average of ten measurements spaced with

a distance of more than three hardness diameters to avoid overlapping stress field on the results [143].

5.5 Tensile strength

Flat tensile specimens of 80mm gauge length and 20mm gauge width were prepared as per ASTM E8M standard; tensile tests were conducted using a Static Instron 100kN testing machine at a strain rate of $0.002s^{-1}$ and stress-strain plots were obtained for each sample. Four repeated tensile tests were carried out for each DP steel [144].

5.6 Electrical resistivity measurement

Electrical resistivity measurements were carried out on the strip samples (4.95×50mm with varying thicknesses of 1mm to 4mm) and rod samples (4.95mm diameter and 50 mm length) using a conventional four point DC method with a CROPICO MICROHMMETER type DO5000 with a resolution of 100 nano-ohm. Each resistivity value was determined by taking the average of eight measurements.

5.7 Magnetic field measurement

In order to determine the magnetic field value both experimental and modelling studies have been carried out. A gauss meter GM08 was used to measure the strength of the magnetic field generated by the EM sensor. The magnetic field through the sample/sensor was determined by FE COMSOL modelling (e.g. point evaluation, surface evaluation etc.) using a cylindrical sensor and U-shaped sensor model, these models are described in Section 6.2.2.4 Chapter 6.

5.8 EM Sensors measurements

Two types of EM sensor were used; a U-shaped EM sensor, which is ideal for strip or plate samples, and a cylindrical EM sensor (air cored/ferrite cored) for rod or strip samples. U-shaped EM sensors are placed onto the surface of a test sample whereas samples are placed within the cylindrical sensor body and are typically rod shaped, but strip samples can also be tested (and modelled).

The U type EM sensor design is formed of a U shaped ferrite core (sourced from Magdev Ltd.) The sensor consists of one generating coil with 100 turns of 0.20 mm insulated copper wire and two sensing coils with 86 turns of 0.16mm insulated copper wire which were wound on a ferritic U-shaped core with a bridge of 100mm, leg lengths and thickness of 56mm and 25mm respectively (Figure 5.2).

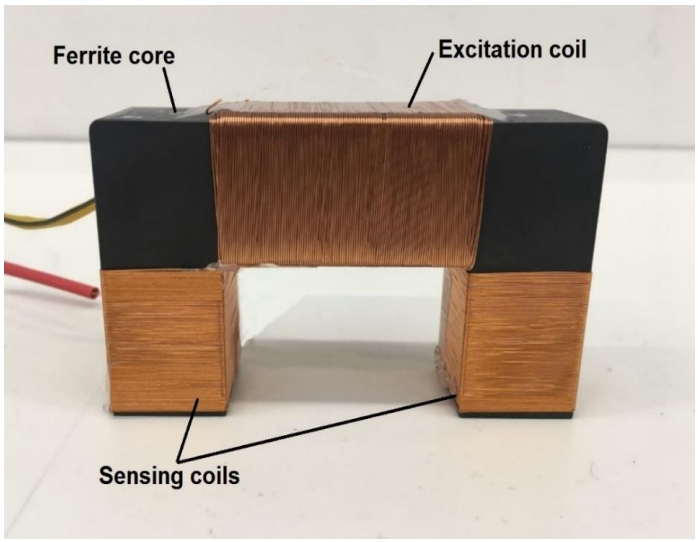

Figure 5.2 : U shaped sensor with bridge=100mm, legs= 56mm and thickness of 25mm. The sensor consists of one generating coil with 100 turns and two sensing coils with 86 turns each

The EM sensor's sensing coil and exciting coils are driven using an Impedance Analyser Solartron (SL 1260 A) with an AC voltage of 3V at frequencies from 10 Hz to 10 kHz.

The excitation coil induces an alternating current magnetic field into the sample. The flux sensing coils pick up changes in the magnetic field caused by the test sample [21]. The cylindrical sensors in this project have exciting and sensing coils wound around cylindrical formers of different sizes, as shown in Figure 5.3.

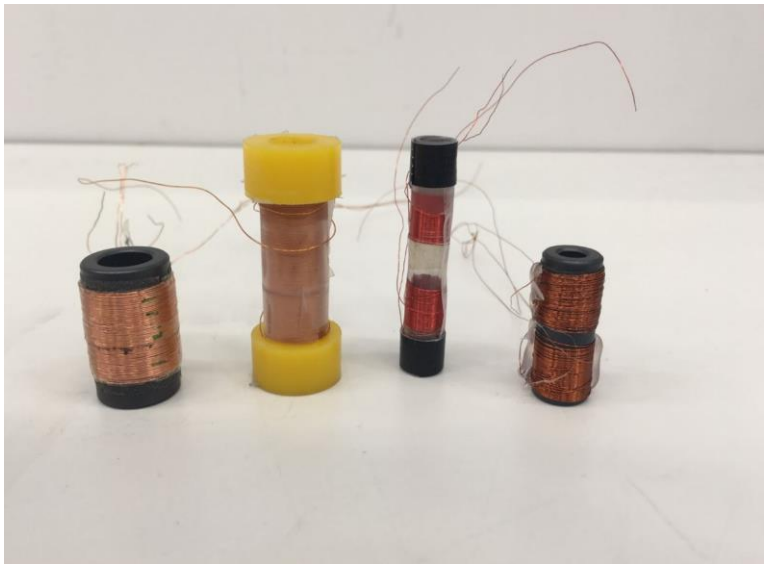

Figure 5.3: Different types of cylindrical sensors (Air-cored and ferrite cored cylindrical EM sensor).

Samples for cylindrical EM sensor testing (strip shape with 4.95mm width and 50mm length and cylindrical shape with 4.95mm diameter and 50mm length) were cut by Electric Discharge Machining (EDM) from as received samples.

As discussed in Section 3.6 Chapter 3, an EM sensor measures inductance, which at low frequency can be related to the relative permeability of the sample. The EM sensor

responds to materials of different permeability showing different amplitudes of inductance. It is worth stating that the EM sensor signal (i.e. inductance) is strongly influenced by the thickness / diameter of the specimen. This is discussed in detail in Chapter 7.

The EM sensor signal is also affected by proximity to the edges of the sample (edge effect) and any gap between the sensor and the sample (lift off).

The magnitude of the U shape EM sensor responses decreases as lift off increases and decreases when it gets closer to the edge of the sample. The minimum size for edge effects to be ignored was determined for the sensor using a large strip taking measurements progressively closer to the edge. The initial tests were done to determine the edge effect distance, which is different for different sensor geometries. It was found that the signal values stabilise at a distance of $100 \pm 2mm$ from the edge of the sample for the parallel orientation and $25 \pm 1mm$ for the perpendicular orientation of the sensor (Figure 5.4).

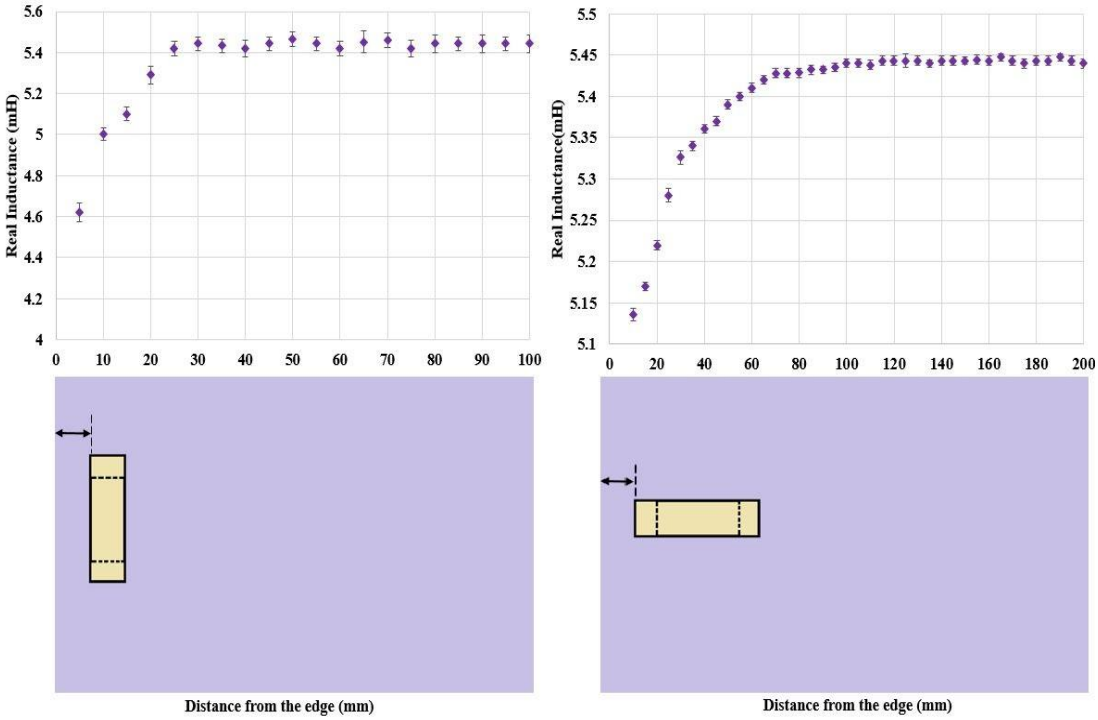

Figure 5.4: Schematic diagram of U-shape sensor orientation to find out the edge effect, signal values stabilise at a distance of 100mm from the edge of the sample for the parallel orientation(right graph) and 25mm from the edge of the sample for the perpendicular orientation (left graph) in DP1000CR with 1.6mm thickness.

A minimum sample size was determined where the edge effects (parallel and perpendicular) and sensor's dimension were considered. Therefore, for this work a size of 300mm x 80mm was determined for strip samples to use for EM sensor measurement.

It is worth mentioning that to increase the consistency of the EM measurement and results, the EM sensor should be operated at the same condition for all measurement tests, as other factors were found to affect the sensor results. For instance, Figure 5.5 indicates that there is an effect of surface curvature (convex/concave shape) on the

value of inductance. For the U-shaped sensor, the magnetic field concentration between the two legs is higher than the outer side (Figure 5.6), therefore for a convex shape, the legs touch the sample and induce more field into the sample, whilst for a concave shape, the outer edges contact, or are closer, to the sample. For the EM sensor measurements reported the samples used had no observable curvature.

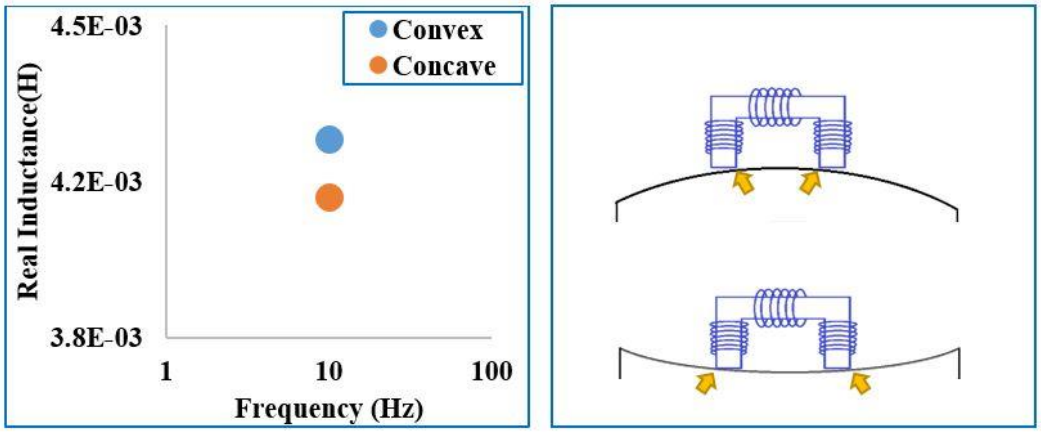

Figure 5.5: The effect of convex and concave surface on EM signal for the U-shaped sensor.

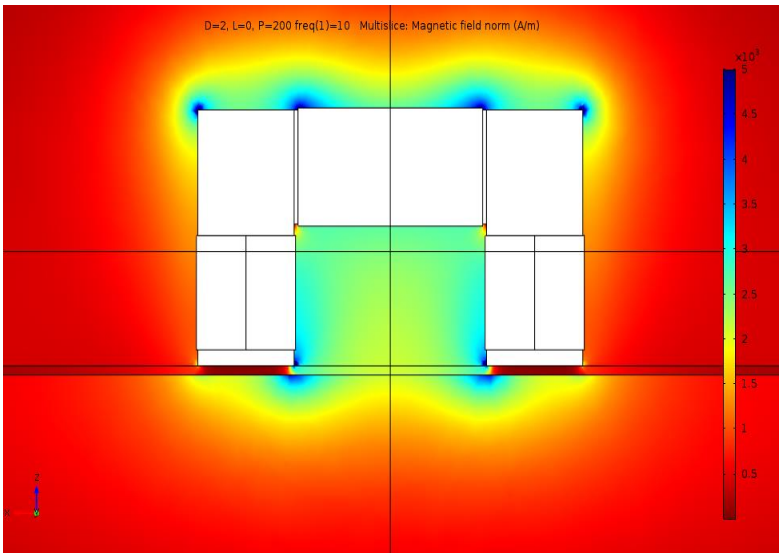

Figure 5.6: Magnetic field distribution in FE modeling of U-shaped sensor, the magnetic field concentration between the two legs is higher than outside the sensor feet.

The EM measurements were carried out for the heat treated DP600 samples and the commercial DP steel samples using the U shaped electromagnetic sensor on strip samples.

EM sensor measurements were made with the sensor oriented parallel and perpendicular to the rolling direction of the strip samples. Each sample was examined with five repeat tests with zero lift-off (the distance between the sensor and the sample). The average real inductance values and standard deviation were recorded. The U-shaped sensor induces electromagnetic fields into the test sample with the depth of the sample being effectively measured by the sensor (the 'skin depth') being affected by the permeability and resistivity of the sample, frequency of applied field and the sensor design.

5.9 BH loop measurement

Values derived from the major BH loop, such as permeability, coercivity and hysteresis loss can be used to measure the magnetic hardness of the material [41, 78]. In addition, minor loop deviations from the major loop or from the initial magnetisation curve can provide deeper insight into the magnetisation, which in turn, is indicative of the material properties [145].

In order to measure the magnetic properties of the DP steels, a lab-based closed magnetic circuit measurement system, developed at the University of Manchester was employed, as shown in Figure 5.7 [72]. This technique involves the measurement of magnetic flux density (*B*) in reaction to an applied field *(H).* A current with low frequency time varying signal was applied to the excitation coils wrapped around the silicon steel core. The strip samples were fitted into the slot in the core to maximise coupling between the core and the sample. The axial applied field (*H)* and the flux density of the induced field *(B)* were measured.

The flux density of the induced field *(B*) was recorded through a 40-turn encircling coil of 0.20mm insulated copper wire and the axial applied field *(H)* was measured using a Hall sensor with sensitivity of 0.16 mV/mA.mT, developed by the University of Manchester [72]. For each DP steel grade tested, five rectangular samples were prepared with the length of 49.34 ± 0.6 mm and width 4.99 ± 0.7mm (the sample thickness was the same as the supplied strip sheet).

It is worth stating that the sample cross section should be determined for the B-H measurement. Therefore, for the measured magnetic parameters (e.g. coercivity) the effect of thickness has been included to ensure the material property is reported. This

is different to the EM sensor measurement where the inductance value is affected by thickness.

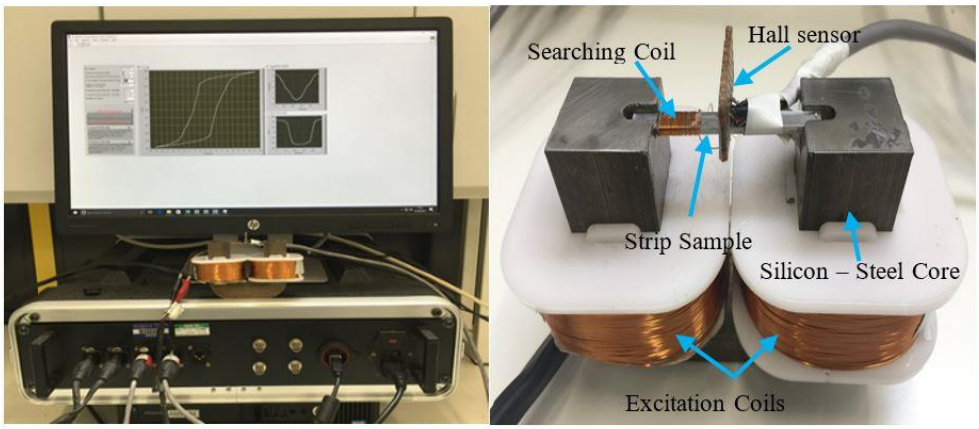

(a)

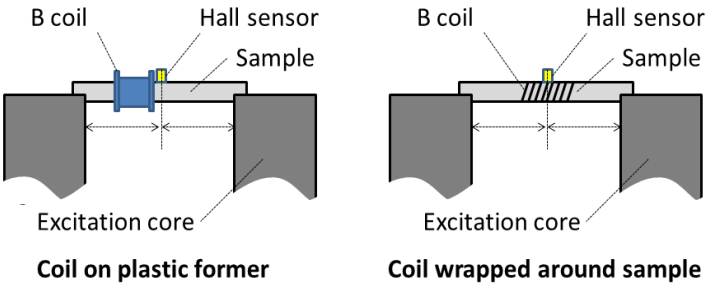

(b)

Figure 5.7: (a) BH measurement system, developed at the University of Manchester, to measure BH hysteresis loops and magnetic properties (b) A schematic arrangement of the coil to calculate magnetic flux density (B) coil wrapped around a strip sample and coil in plastic former for rod sample

5.9.1 Major loops B-H hysteresis

For the major loops, a 1Hz sinusoidal excitation is used and 9 cycles were recorded and averaged. The B-H curves exhibit the micromagnetic properties of steels including permeability, remanence, coercivity and saturation magnetisation, which are affected by different microstructural parameters (discussed in Section 2.7 Chapter 2).

5.9.2 Minor loops BH hysteresis

Minor loop hysteresis means any excursion for which either the range of magnetisation or the range of magnetic field is not symmetric about zero [146, 147].

For the minor loops, a 1 Hz sinusoidal excitation was used to generate the minor loops. The incremental permeability (μ_{Δ}) is obtained from the minor loops by calculating the ratio of the variation in flux density (ΔB) and the corresponding change in the applied field (ΔH), scaled with respect to the permeability of free space (μ_0); presented in Equation 5.1;

$$\mu_{\Delta} = \frac{\mathbf{1}}{\boldsymbol{\mu_0}} \cdot \frac{\boldsymbol{\Delta B}}{\boldsymbol{\Delta H}} \qquad \textit{Equation 5-1}$$

Three types of minor loop configurations were used to derive incremental permeability values; the minor loop deviations from the initial magnetisation curve (μ_{Ic}); the minor loop deviations from the main *B-H* loop (μ_{BH}) and the minor loop deviations from amplitude sweep μ_{i}), as shown in Figure 5.8.

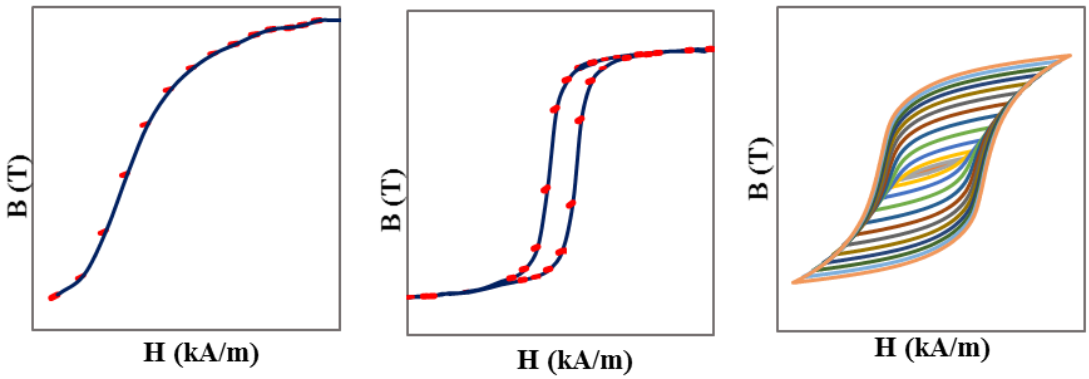

(a) (b) (c)

Figure 5.8: Derivation of incremental permeability curves from minor loops; (a) minor loop deviations from initial magnetisation curve (μ_{Ic}); minor loop deviations from B-H loop (μ_{BH}) and minor loop amplitude sweep (μ_i).

Three different minor loops configurations were employed to see the consistency in the permeability behaviour between different measurements techniques, which can indicate the underlying domain processes are similar in the three methods [41, 147, 148].

In the minor loop deviations, firstly the sample was demagnetised by the application of a full scale 1 *Hz* sinusoidal excitation. In this case the applied field was gradually reduced in amplitude to zero. The applied field was then increased to a pre-determined *H* value and several minor loop cycles recorded.

5.10 FE modelling

5.10.1 EM sensor FE modelling

In order to determine the low magnetic field permeability of the DP samples from the cylindrical and U-shaped EM sensors and investigate the effect of the low magnetic field strength on the permeability value, FE modelling work was carried out. In this work 'low field' refers to the applied magnetic field *H* being less than about 50±4 (*A/m*) for the cylindrical sensor and for the U-shaped sensor about 250-450 (*A/m*) which reflects the fact that a relatively low magnetic field is induced by the EM sensors used in this work (discussed in Section 6.2.2.4 Chapter 6).

A two-dimensional *(2D)* axial symmetry FE and a three-dimensional *(3D)* sensor output model developed using COMSOL Multi-physics in the AC/DC mode for the cylindrical samples and the strip samples were used respectively [149]. In this work established models (developed and verified within parallel projects within the research group at WMG and therefore described elsewhere [55, 64, 141, 150]) were used with modifications for the sensor and sample geometries tested within this project.

The COMSOL modelling approach is based on solving the Maxwell equations and in the model boundary conditions of the magnetic field, the perfect magnetic conductor and the magnetic insulation were used [51, 134, 151]. The geometry and details of the sensor/sample were set to be the same as the experimental set up.

The effect of sensor design was achieved by analysing the simulation results of each completed model where the most desirable configuration is the one that shows the highest signal and allows easy identification of the different samples.

5.10.2 Modelling of Magnetic Microstructure

A previously developed FE model using COMSOL Multi Physics software [22] was carried out for determining the low field relative permeability of a two phase microstructure (ferrite + martensite) based on the actual microstructure (phase balance and distribution). In this model low field relative permeability of the individual phases (ferrite and martensite) was used for the commercial DP steels.

6 Microstructures and magnetic properties of DP steels

In this chapter, properties of DP steels in term of microstructure, mechanical properties and magnetic properties will be investigated.

In the first part, the microstructure, phase balance (ferrite-martensite) and hardness value for the laboratory heat-treated dual phase (DP) steels will be studied, followed by measuring the magnetic properties. A discussion regarding a link between the magnetic properties and mechanical properties will be given for the heat treated DP steels.

In the second part, microstructural parameters, including the ferrite-martensite phase balance and the ferrite grain size in the commercial DP steels (hot rolled and cold rolled) are presented, followed by the mechanical properties (hardness and tensile strength).

The next part of the chapter will concentrate on discussing the magnetic properties using lab based approaches to determine permeability of the commercial DP steels (discussed in Section 5.9.2 Chapter 5), followed by the effective microstructural parameters including the effect of ferrite fraction and ferrite grain size on the incremental permeability of the commercial DP steels will be explained.

Later, the FE modelling for the two EM sensors (U-shaped and cylindrical shape) to determine the applied field and the relevant 'low field' relative permeability of samples

from the EM sensor signal will be presented, followed by an FE model for determining the low field relative permeability of a two phase microstructure.

A comparison between these methods for determining low field relative permeability will be presented and, finally, the effect of magnetic field strength on the incremental permeability of the commercial DP steels will be discussed.

6.1 Heat treated DP samples

6.1.1 Microstructure and mechanical properties

The optical microstructure images of DP600-650, DP600-675, DP600-700, DP600-725, DP600-750 and DP600-800 samples using magnification of 500x are shown in Figure 6.1 to Figure 6.6. As can be seen the microstructures of the heat treated dual phase steels consist of a ferrite matrix (lighter) containing a second phase in the form of islands (darker). It can be seen that the second phase (martensite, bainite and tempered martensite) is randomly distributed in the ferrite matrix.

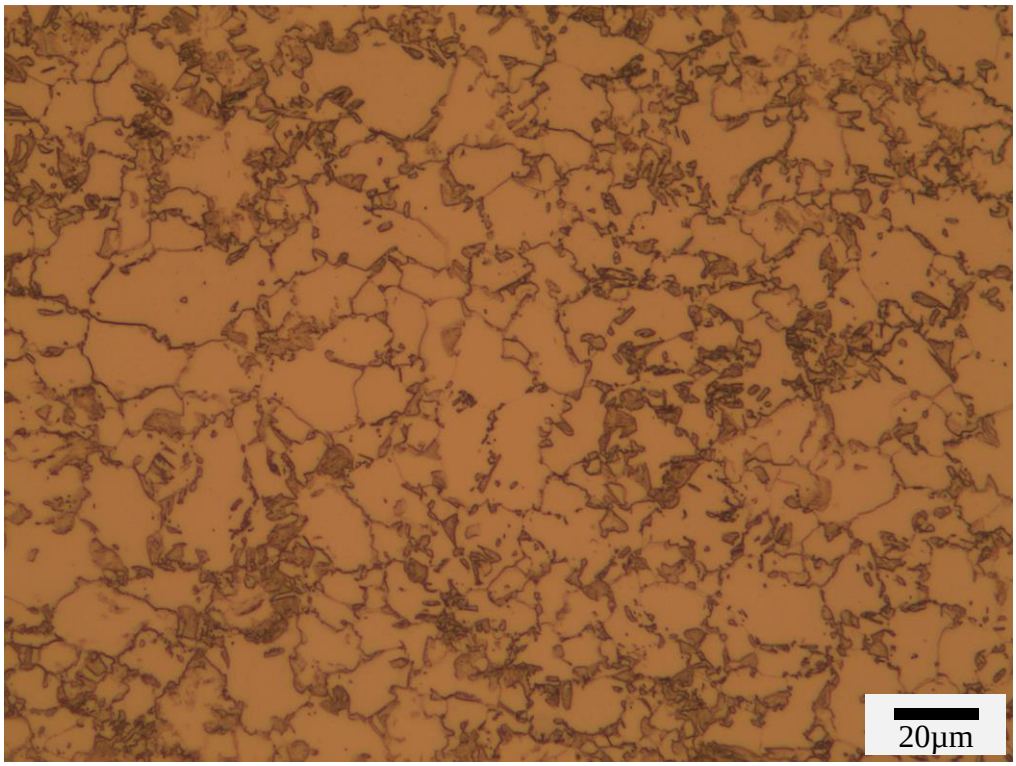

Figure 6.1: Optical microstructure of heat treated DP600-650 at x500 magnification

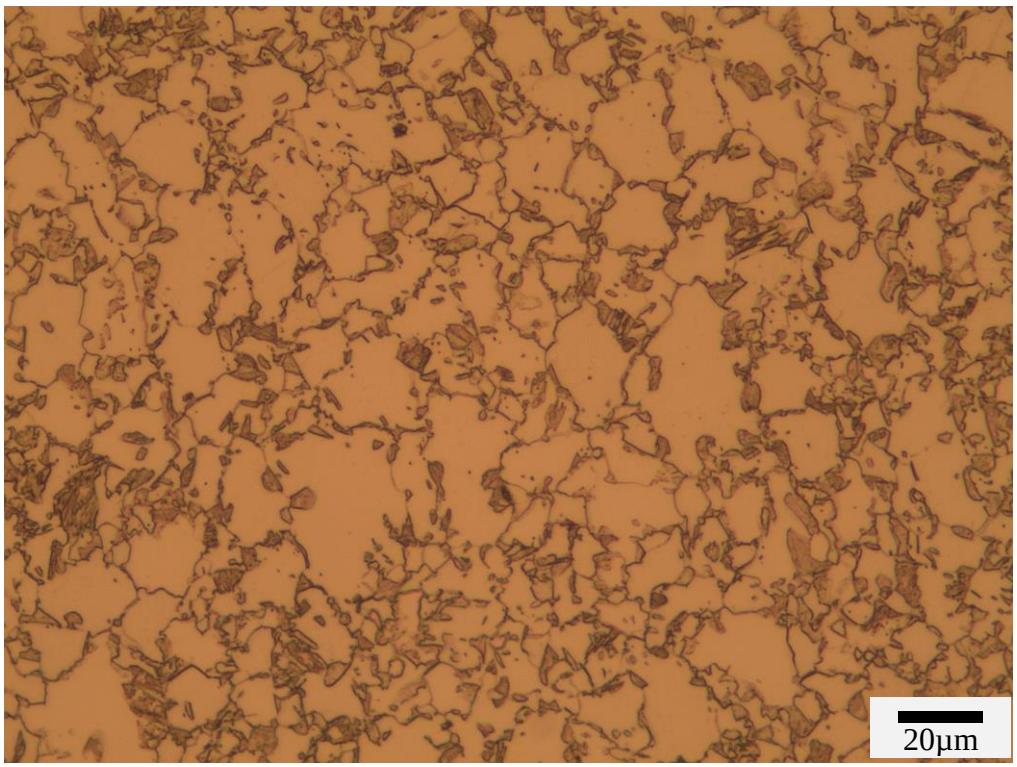

Figure 6.2: Optical microstructure of heat treated DP600-675 at x500 magnification

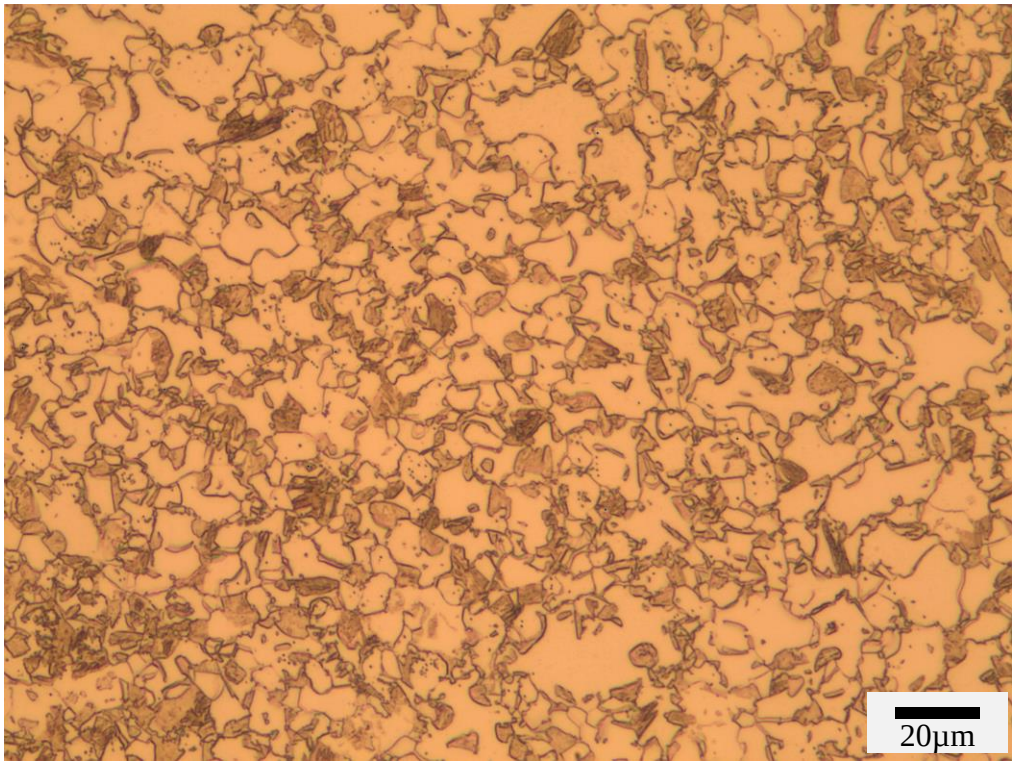

Figure 6.3: Optical microstructure of heat treated DP600-700 at x500 magnification

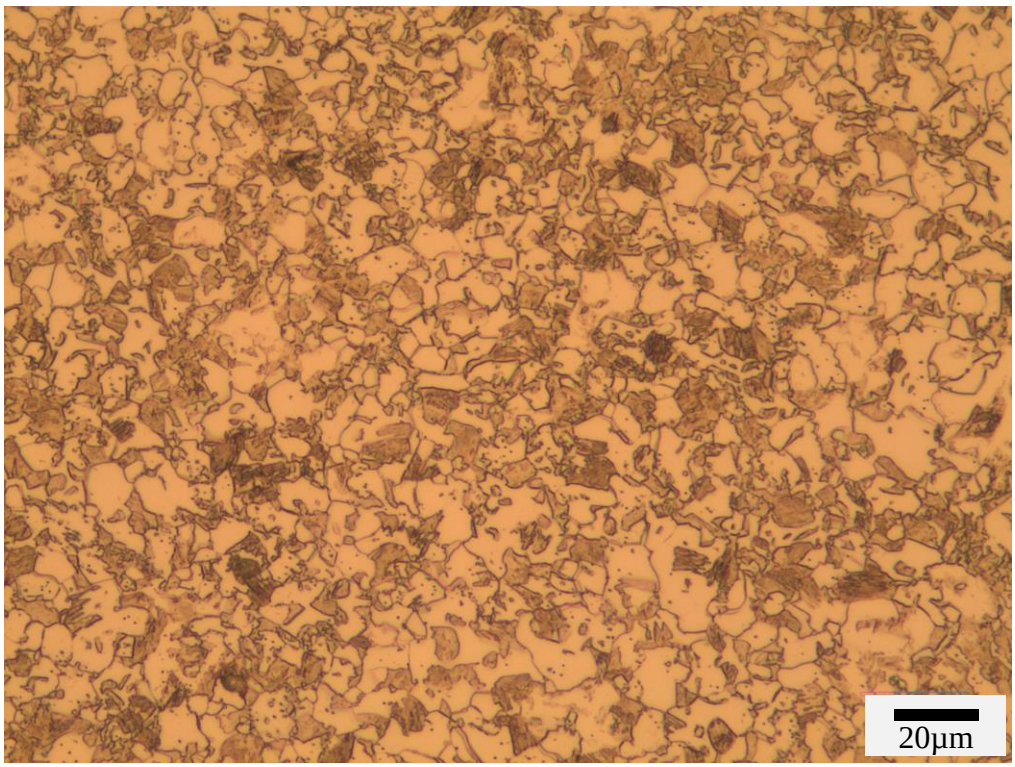

Figure 6.4: Optical microstructure of heat treated DP600-725 at x500 magnification

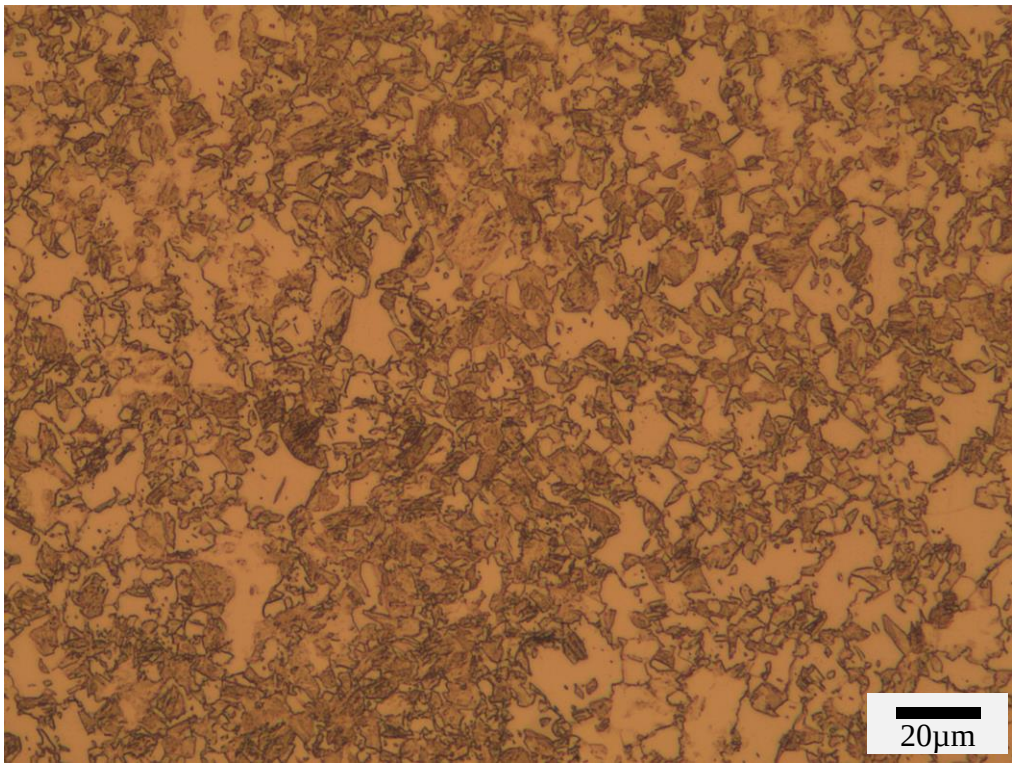

Figure 6.5: Optical microstructure of heat treated DP600-750 at x500 magnification

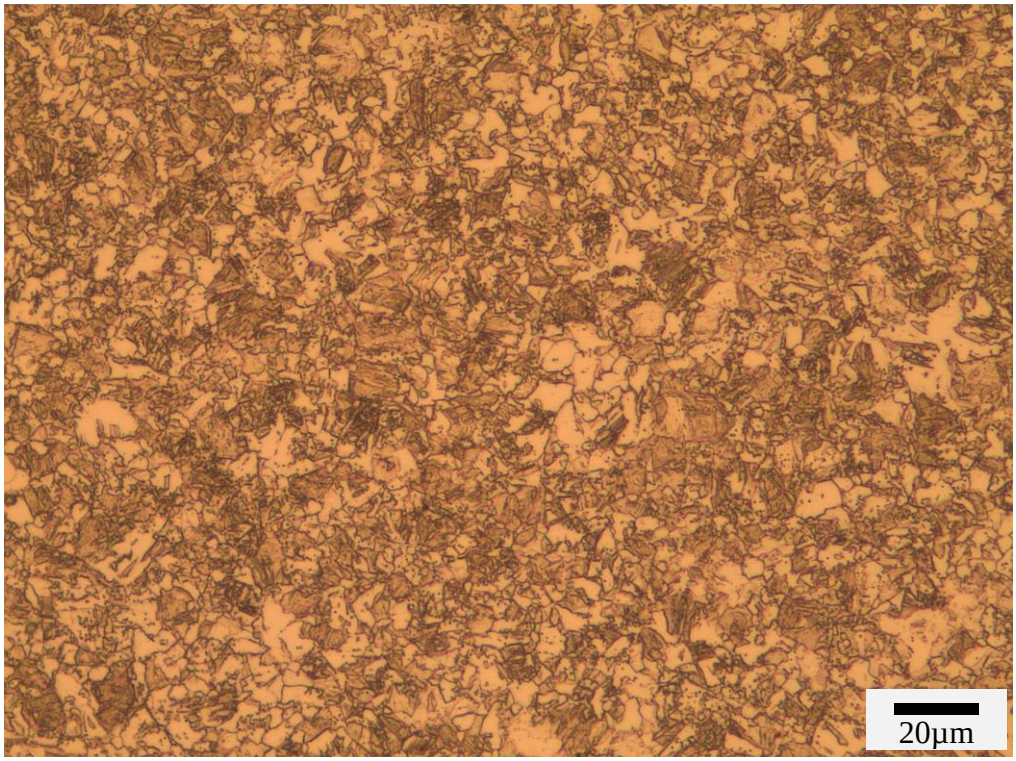

Figure 6.6: Optical microstructure of heat treated DP600-800 at x500 magnification

The phase balance of DP600-650, DP600-675, DP600-700, DP600-725, DP600-750 and DP600-800 samples are given in Figure 6.7. Different heat treatment conditions give a different range of ferrite from around 35% to 70% ferrite.

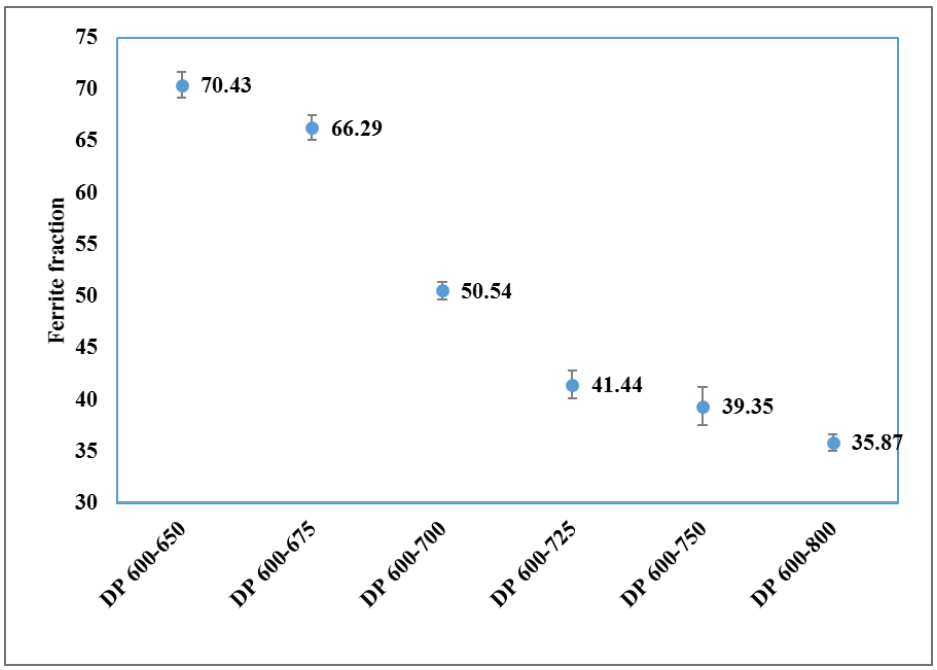

Figure 6.7: Plot of ferrite fraction for different grade of heat treated DP600 samples

Figure 6.8 shows the relationship between the phase fraction and hardness. The decrease in hardness with increasing volume fraction of ferrite for DP steels is well known and widely documented [2, 152, 153]. This is in agreement with the results where a clear decrease in the hardness with an increase in ferrite fraction is observed for the heat-treated DP grades which is related to the lower martensite/bainite fraction. Ferrite is a single phase and thus does not have many obstacles to dislocations, other than grain boundaries, and is thus a soft microstructure. The hardness in untempered martensite comes due to the role of carbon atoms trapped in octahedral interstitial sites with the displacement of iron atoms and volume expansion. Martensite's microstructure consists of a highly strained, meta-stabilized body centered tetragonal (BCT) form of ferrite supersaturated with carbon. There are a lot of shear deformations in martensite because of this strain. This results in martensite having significant amounts of dislocations, which prevent additional dislocations forming and in turn

increase the hardness [1]. Autotempering can occur in low carbon martensite structures, due to the relatively high Ms temperature, which reduces the amount of carbon trapped in solid solution, which reduces hardness, but also results in the formation of fine carbide precipitates which mitigates this loss in hardness.

Bainite consists of laths which would have an inhomogeneous distribution of dislocations across its lath thickness (upper bainite and lower bainte). The density of dislocations in bainite/tempered martensite compared to martensite is less hence strength is lower than martensite. The carbides present in bainite (inter-lath for upper bainite and inter-lath and intra-lath for lower bainite) provide strengthening, although their larger size than for autotempered martensite means their strengthening contribution is less.

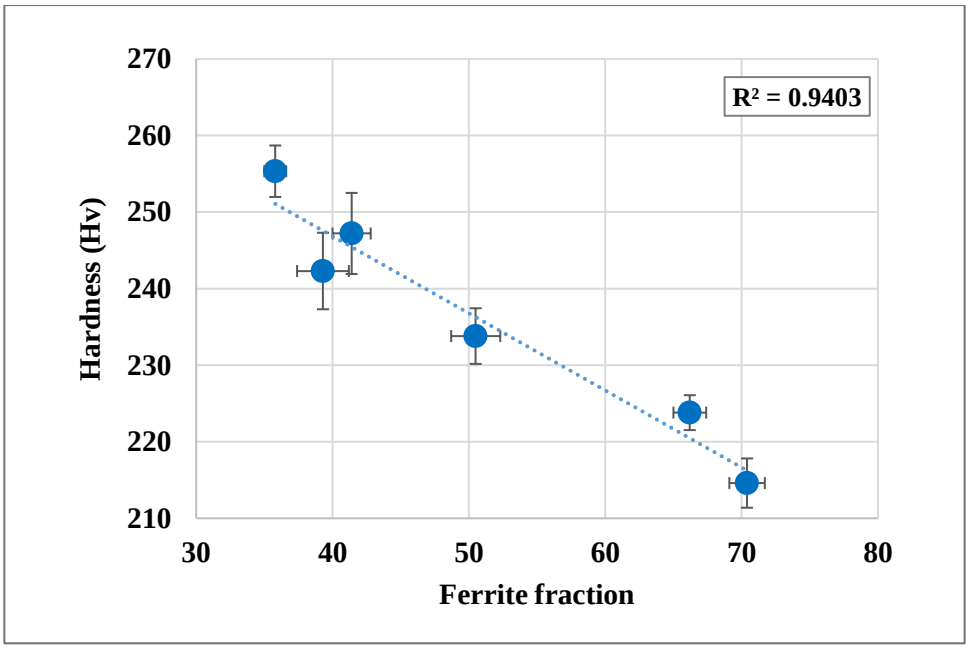

Figure 6.8: Hardness value versus ferrite fraction for heat-treated DP steels

The trend between hardness and ferrite fraction follows a linear relationship for the heat treated DP samples. The trend stems mostly from the composite effect due to the presence of hard particles in a soft matrix. The correlation coefficient for the best fit equation is R^2= 0.9403.

6.1.2 Magnetic property of heat treated DP steel

Major hysteresis loops were used in order to measure magnetic properties of the heat treated DP steel samples. The setup for such measurement has previously been presented in Section 5.9.1, Chapter 5. Figure 6.9 shows the major loops and the initial magnetisation curves for the heat treated DP steel samples. As it can be seen from Figure 6.9 the different samples shows different B-H curves.

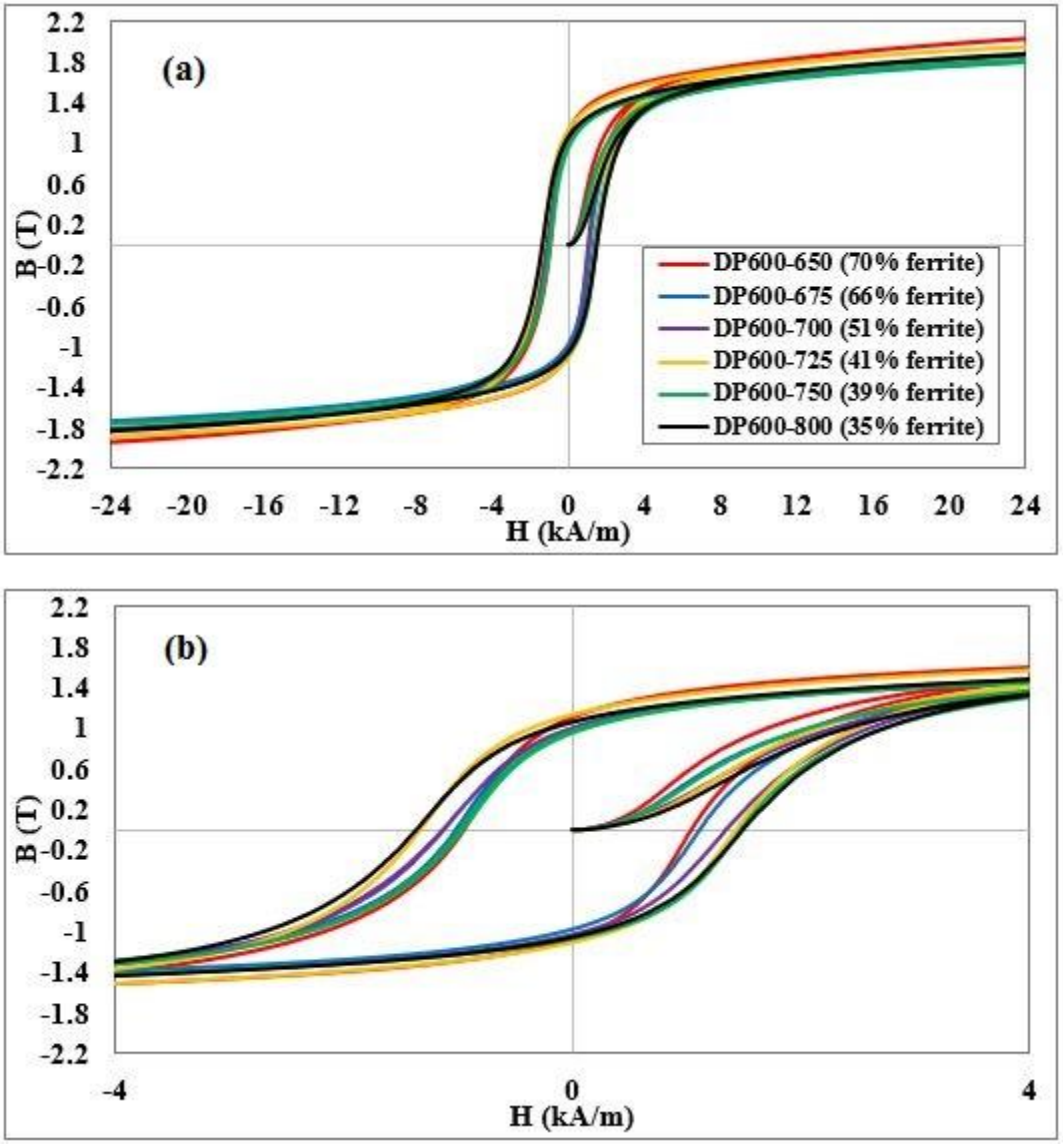

Figure 6.9: Major loops and initial magnetisation curves for the heat treated DP steel samples (a) in full scale and (b) for H between -4 kA/m and 4kA/m.

Figure 6.10 shows the measured coecivity against ferrite fraction. As can be seen the sample with lowest volume fraction of ferrite shows the highest value of coercivity.

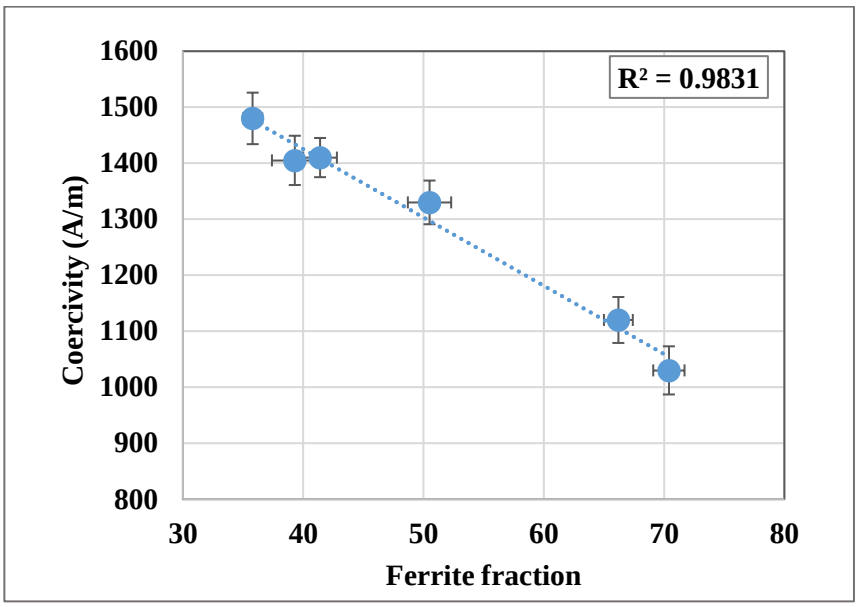

Figure 6.10: Coercivity as a function of ferrite fraction for heat treated DP steel samples.

As can be clearly seen, there is an approximately linear decrease in coercivity with ferrite fraction. Figure 6.11 presents the relationship between coercivity and hardness for the heat treated DP steels.

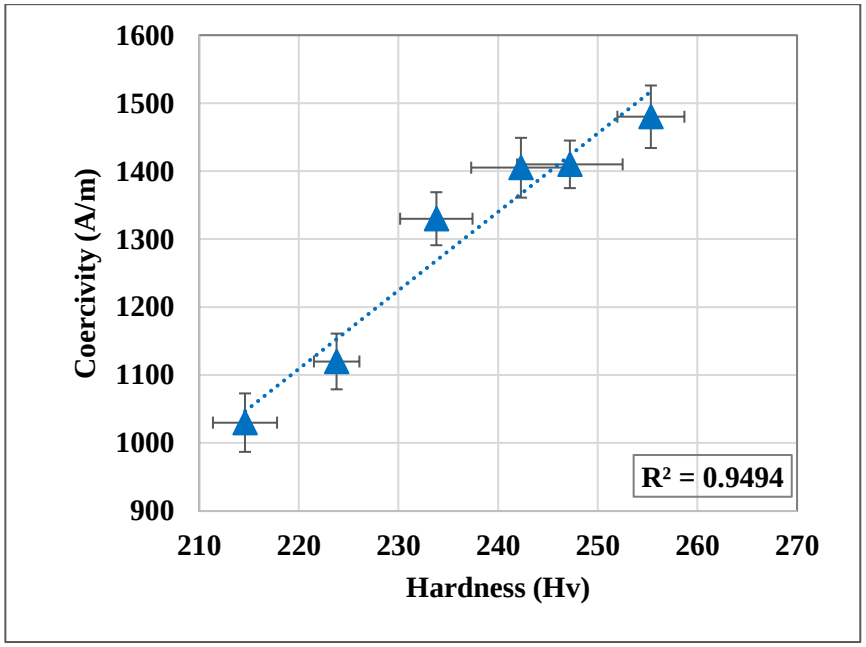

Figure 6.11: Coercivity as a function of Hardness for heat treated DP steel samples

It is known that magnetic hysteresis is a phenomenon caused primarily by interactions between the magnetization process and lattice imperfections. Berkowitz et al. [154] reported the theoretical consideration about magnetisation and indicated that the coercivity H_c is proportional to the square root of the density of lattice defects. Later Vicena [53] showed among the defects controlling the magnetisation processes, that the dislocations play a leading role. Therefore, coercivity decreases with decreasing dislocation density.

The high coercivity value for samples with higher martensite (bainite/tempered martensite) can be ascribed to the density of dislocations (and other domain pinning points such as carbides and lath boundaries) within the microstructure. The martensite phase consists of laths in which the dislocation density is very high (i.e. the dislocation density in martensite is $10^{17}/m^2$ and for tempered martensite is around $10^{14}/m^2$ [155, 156]). Therefore, the high density of dislocations gives rise to stress fields around the dislocation lines, by which magnetic domains are pinned. In this regard, the high coercivity in martensite is believed to be due to the stress field due to dislocations in martensite laths.

6.2 Commercial DP steels

6.2.1 Microstructure and mechanical property

The microstructure of the commercial DP600, DP800 and DP1000 are shown in Figure 6.12 to Figure 6.24. As can be seen, the microstructure of commercial DP steels consists of a ferrite matrix containing a second phase in the form of islands (martensite, bainite and/or tempered martensite) [157].

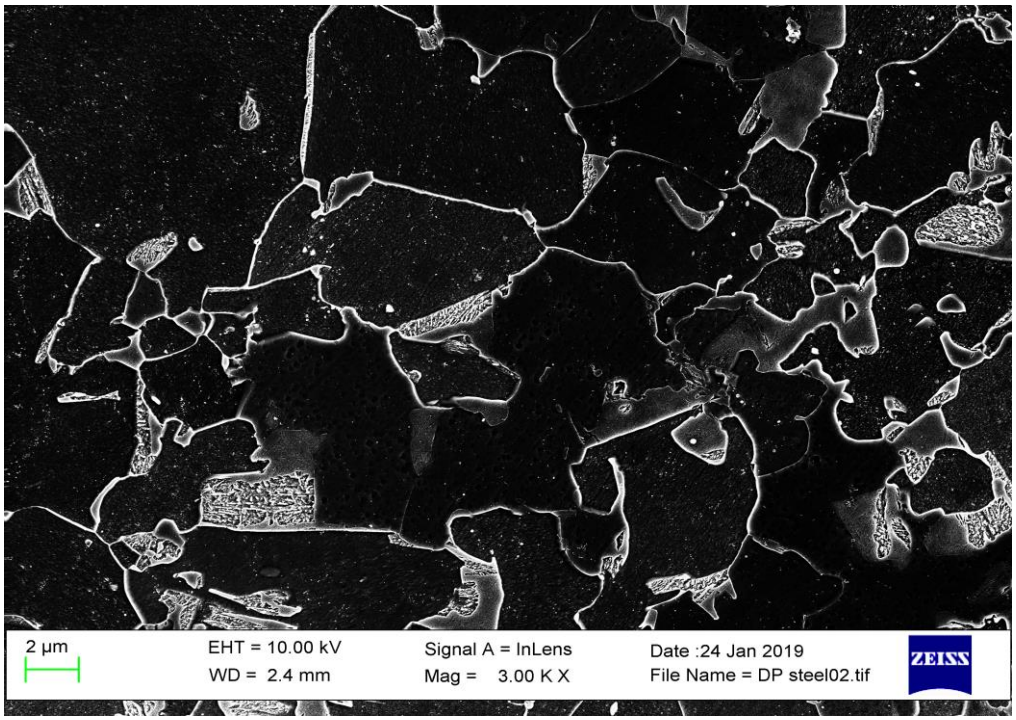

Figure 6.12:SEM image of the DP600CR 1mm GL

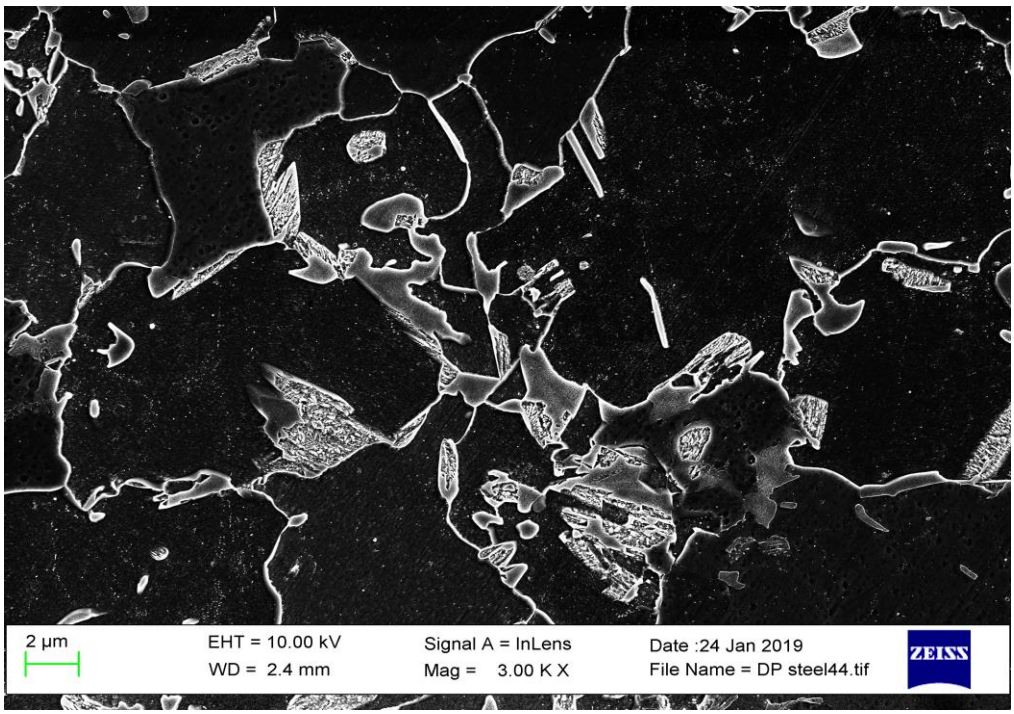

Figure 6.13:SEM image of the DP600CR 1mm

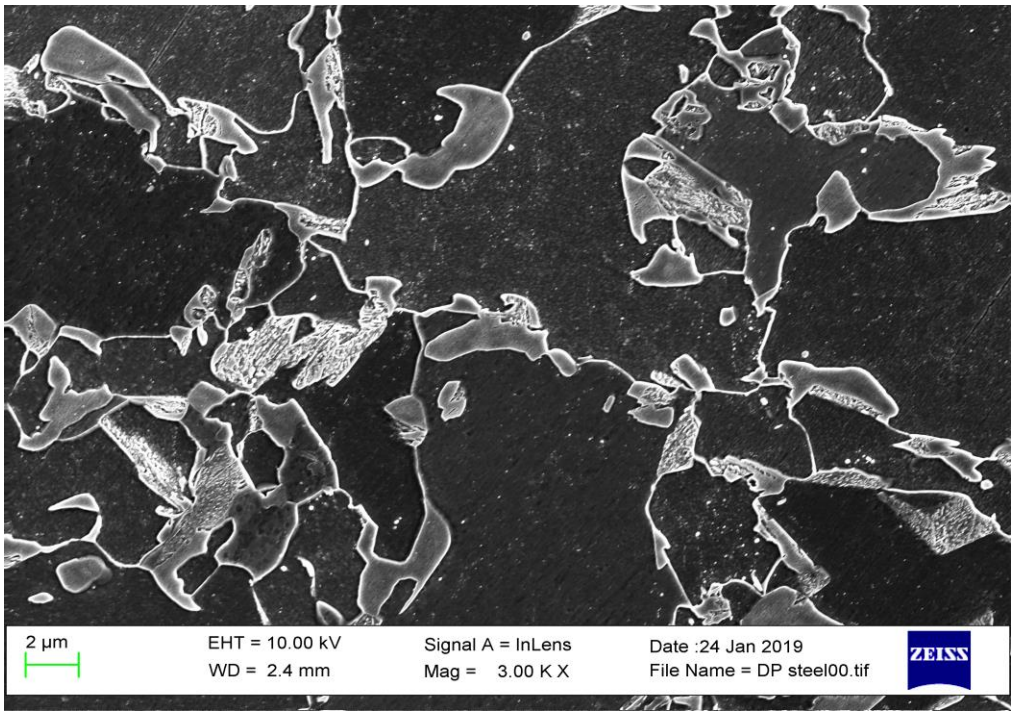

Figure 6.14:SEM image of the DP600CR 1.4mm

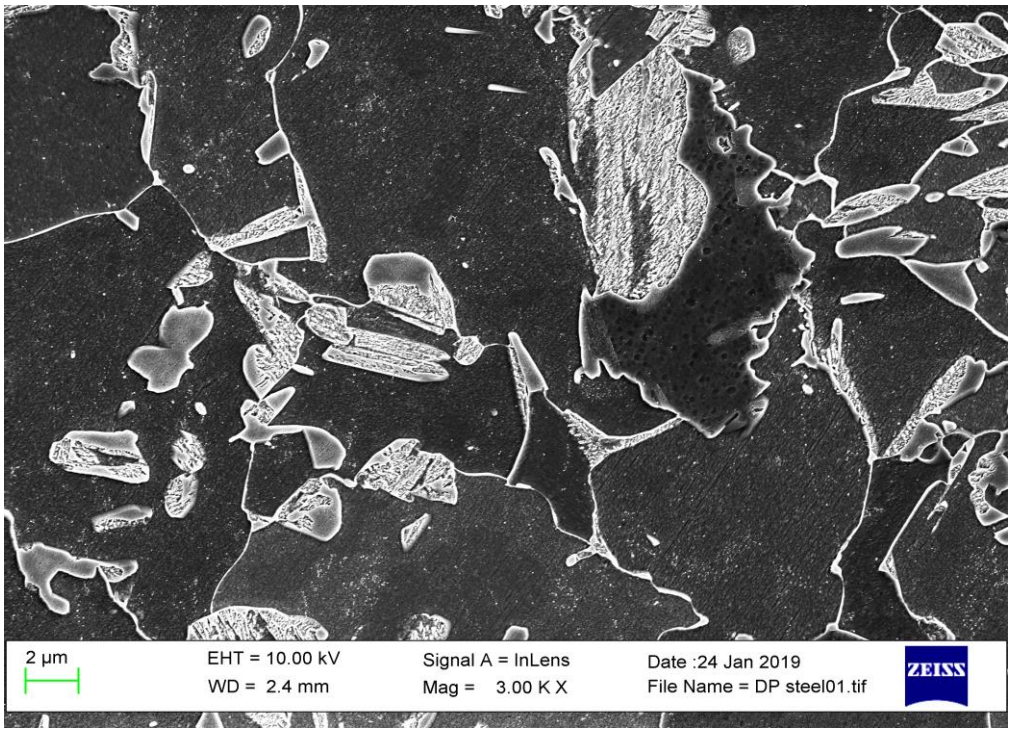

Figure 6.15:SEM image of the DP600CR 1.5mm

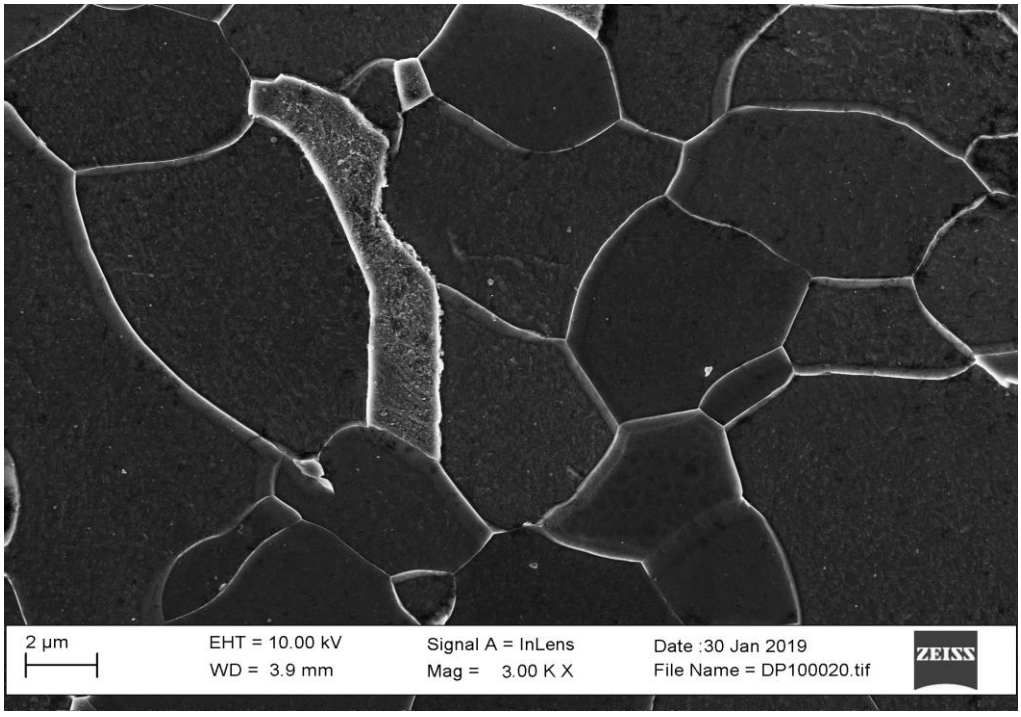

Figure 6.16:SEM image of the DP600HR 4mm

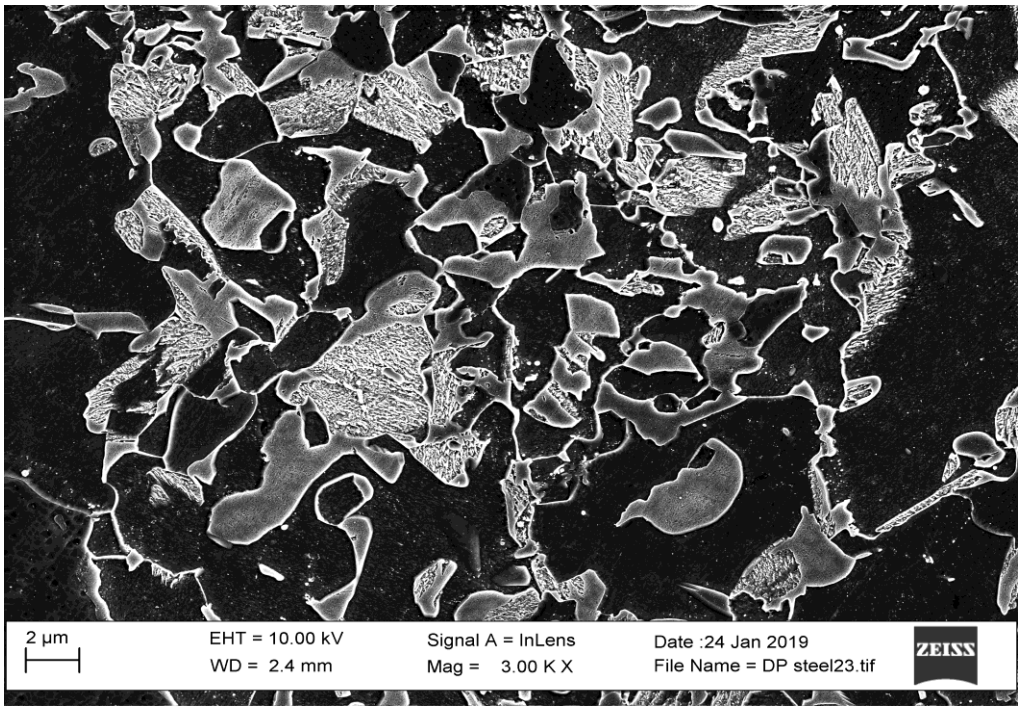

Figure 6.17:SEM image of the DP800CR 0.95mm

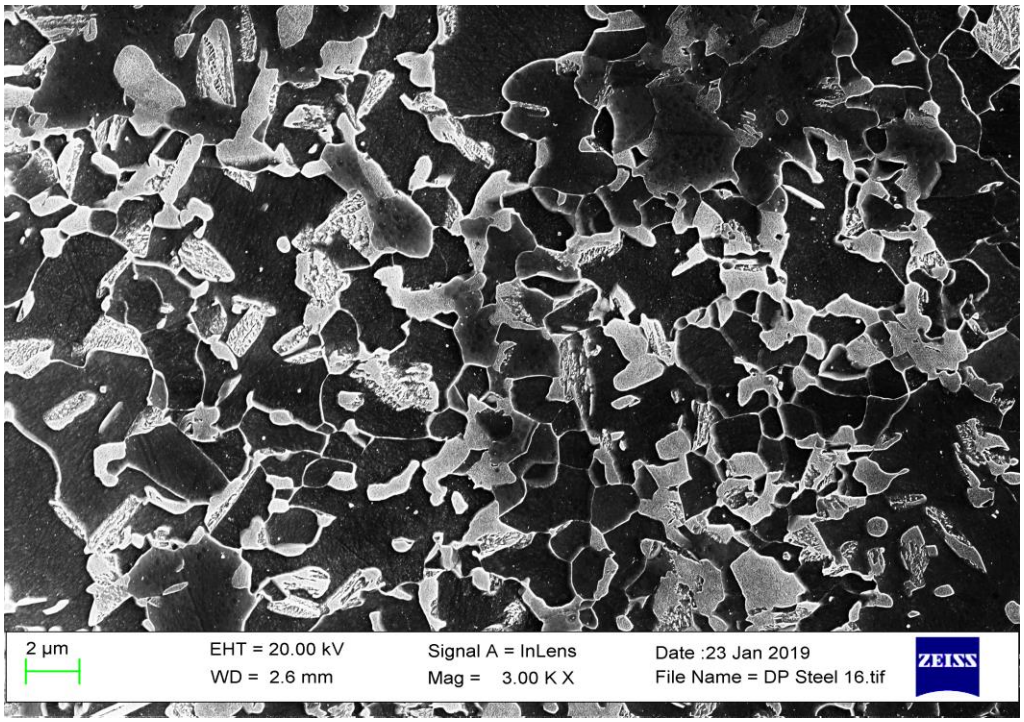

Figure 6.18:SEM image of the DP800CR 1.6mm

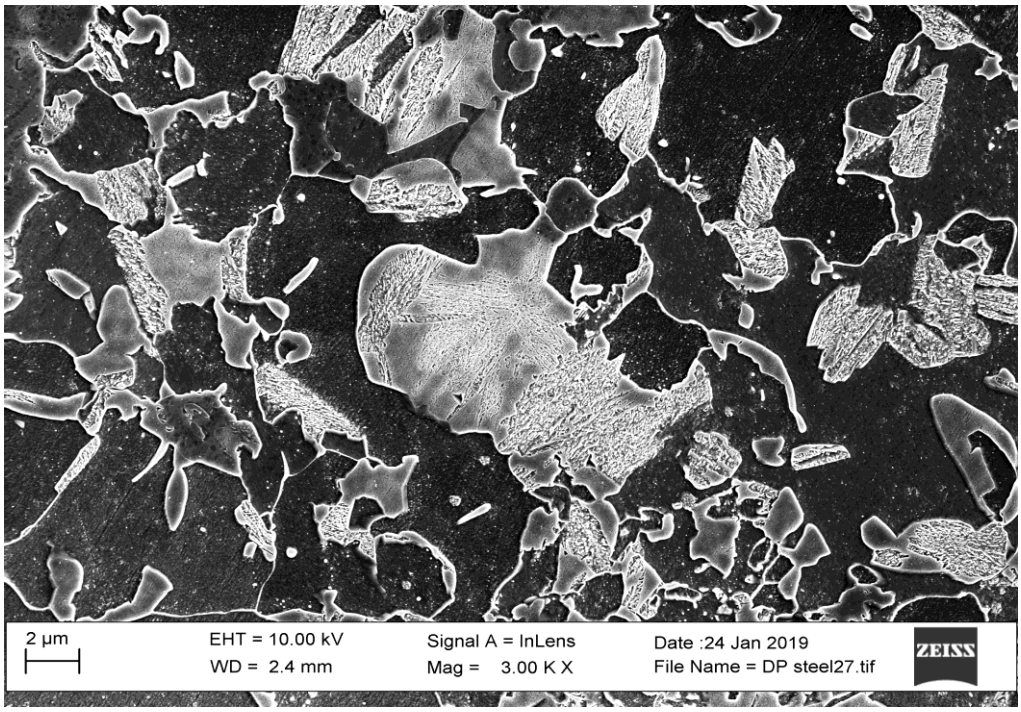

Figure 6.19:SEM image of the DP800CR 1.6mmGL

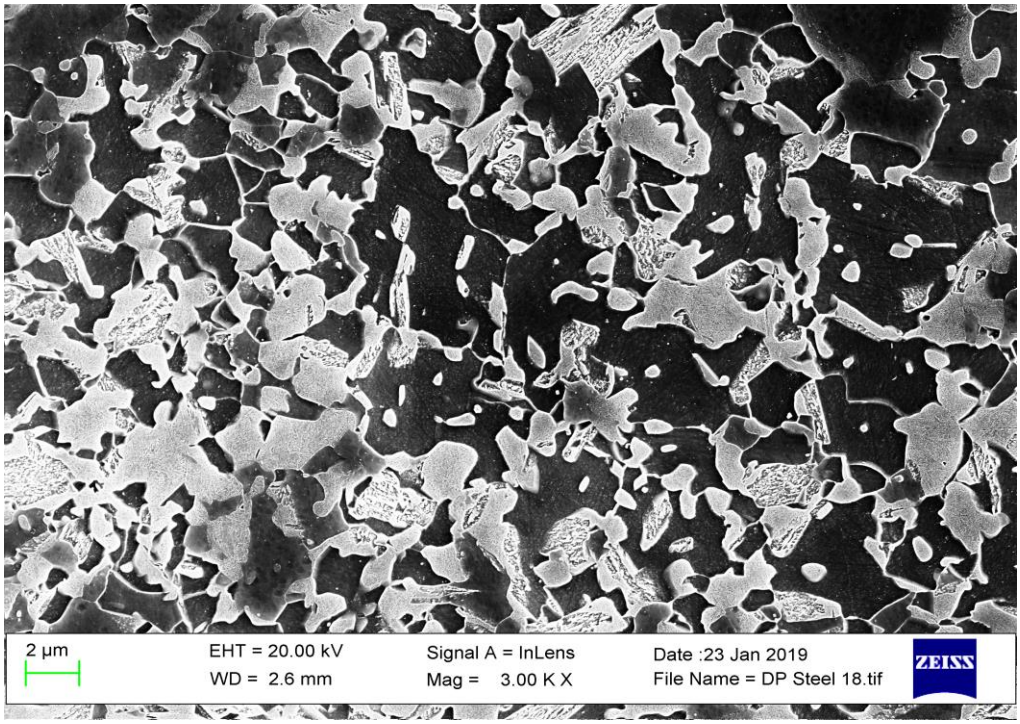

Figure 6.20:SEM image of the DP800CR 2mm A

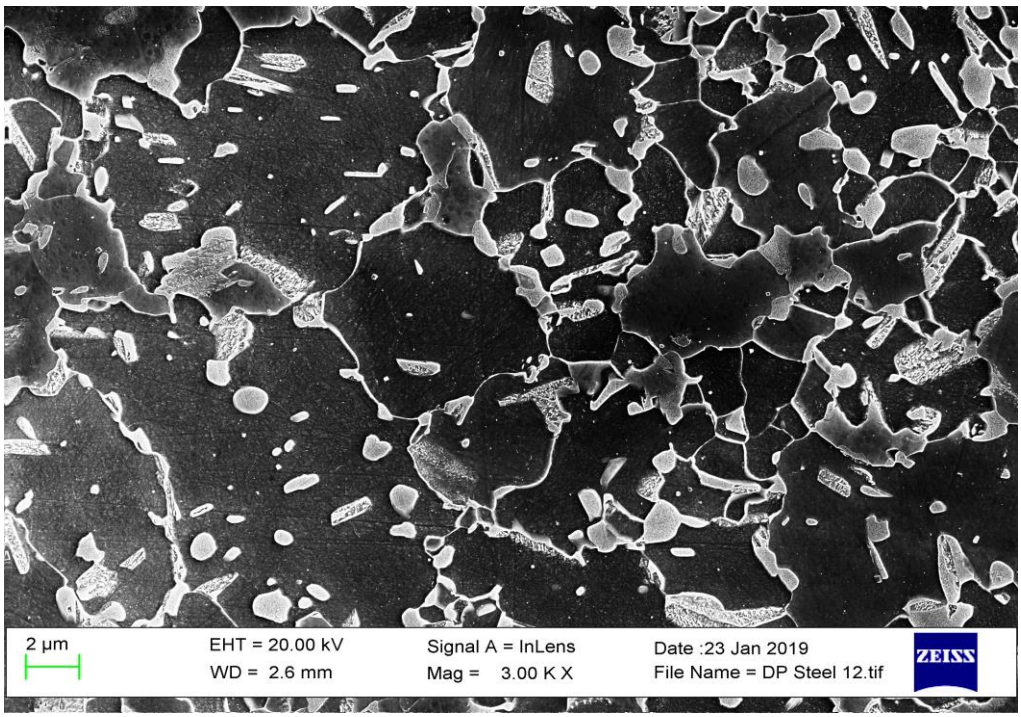

Figure 6.21:SEM image of the DP800CR 2mm B

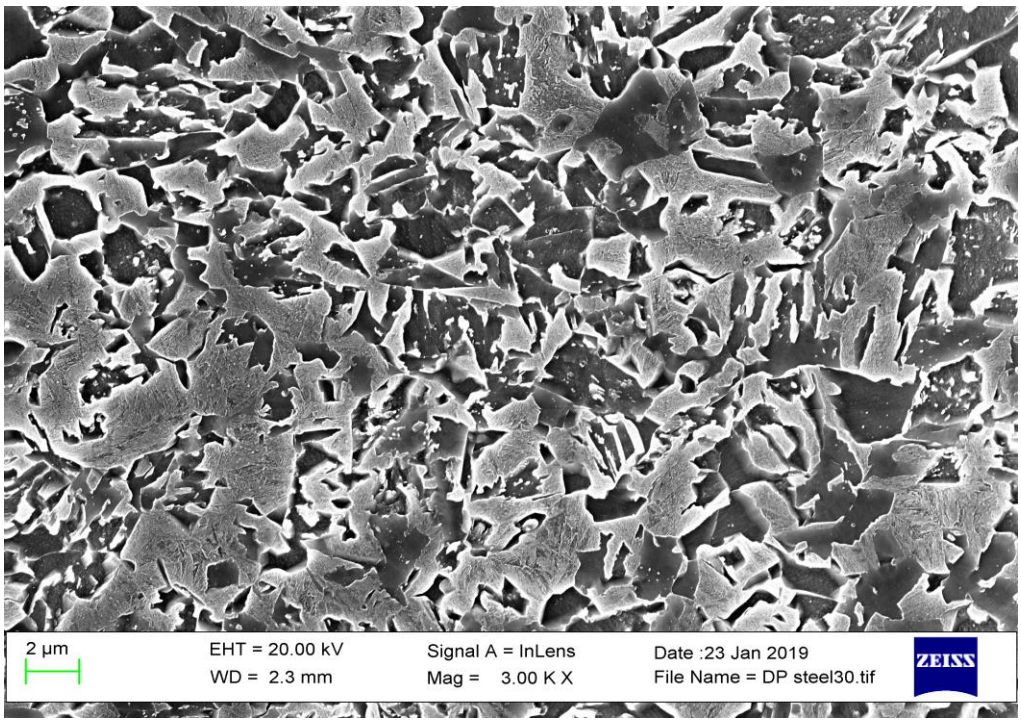

Figure 6.22:SEM image of the DP1000CR 1mm

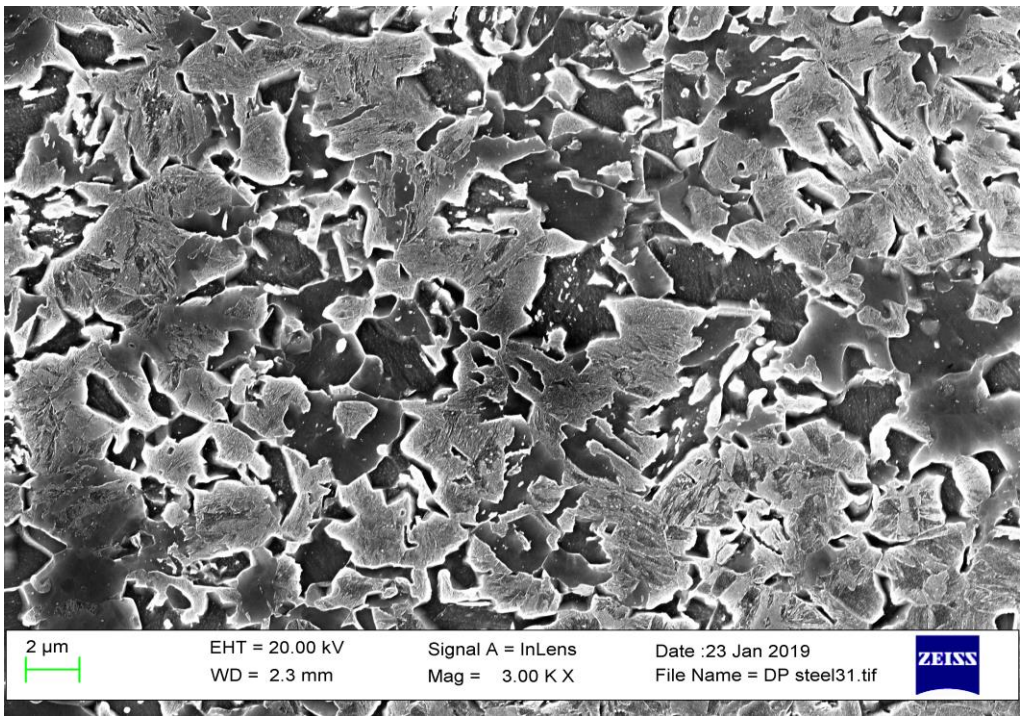

Figure 6.23:SEM image of the DP1000CR 1.2mmGL

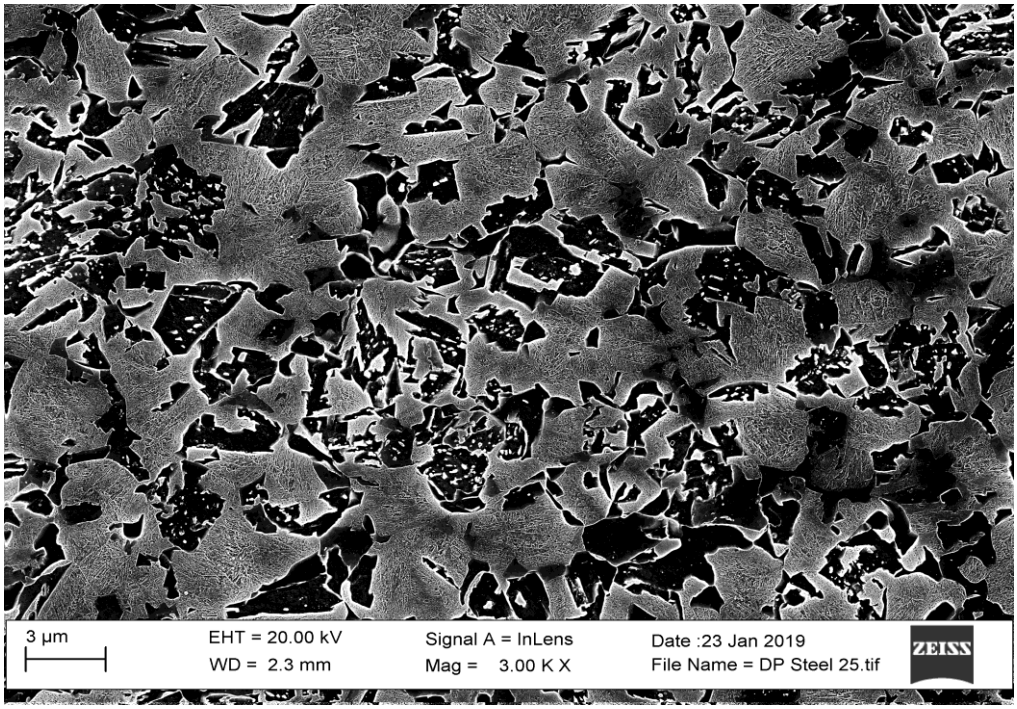

Figure 6.24:SEM image of the DP1000CR 1.6mm

The ferrite fraction for the DP 600 samples is around 74-79%, for DP 800 is 49-65% and for DP 1000 is less than 42%. The DP600HR 4mm sample is a hot rolled DP steel (experienced less refinement than for cold rolled and annealed samples) so its microstructure consists of larger ferrite grain size (10μm) compared to the other DP600 steels (ferrite grain size of 6 to 7μm). It is worth mentioning that the DP800 strips came from different mills and hence experienced different processing conditions, which can give different grain sizes. Table 6.1 provides a summary of the ferrite fraction, Vickers hardness measurement and ferrite grain size for the commercial DP steel samples.

Table 6-1: Summary of the ferrite fraction, hardness and grain size of commercial DP steels.

Sample	Ferrite fraction	Ferrite grain size (μm)	Hardness (Hv)	UTS (MPa)
DP600CR 1mm	73±2	7±3	194±2	684±19
DP600CR 1mm GL	76±2	6±2	190±3	657±25
DP600CR 1.4mm	72±3	7±3	205±5	656±11
DP600CR 1.5mm	74±2	7±2	189±3	669±17
DP600HR 4mm	79±3	10±4	185±4	646±30
DP800CR 0.95mm	58±3	6±3	234±5	762±41
DP800CR 1.6mmGL	51±2	5±2	240±4	824±36
DP600CR 1.6mm	59±3	3±1	245±4	803±14
DP800CR 2mmA	49±3	5±1	245±2	827±15
DP800CR 2mmB	65±2	3±2	255±5	863±38
DP1000CR 1mm	39±3	3±1	322±6	1074±10
DP1000CR 1.2mmGL	42±2	3±1	318±5	1026±15
DP1000CR 1.6mm	42±2	4±2	317±7	1023±20

HR=Hot-rolled, CR=Cold-rolled, Gl=Galvanized

Figure 6.25 shows the relationship between the phase fraction and hardness in the commercial DP steels. There is a clear decrease in the hardness value with an increase in ferrite fraction which is related to the lower martensite (tempered martensite/ bainite) fraction as discussed earlier. In addition, from Figure 6.25 it can be seen that there is a lot more scatter for the DP800 grades than the other steels which will be explained in the following section.

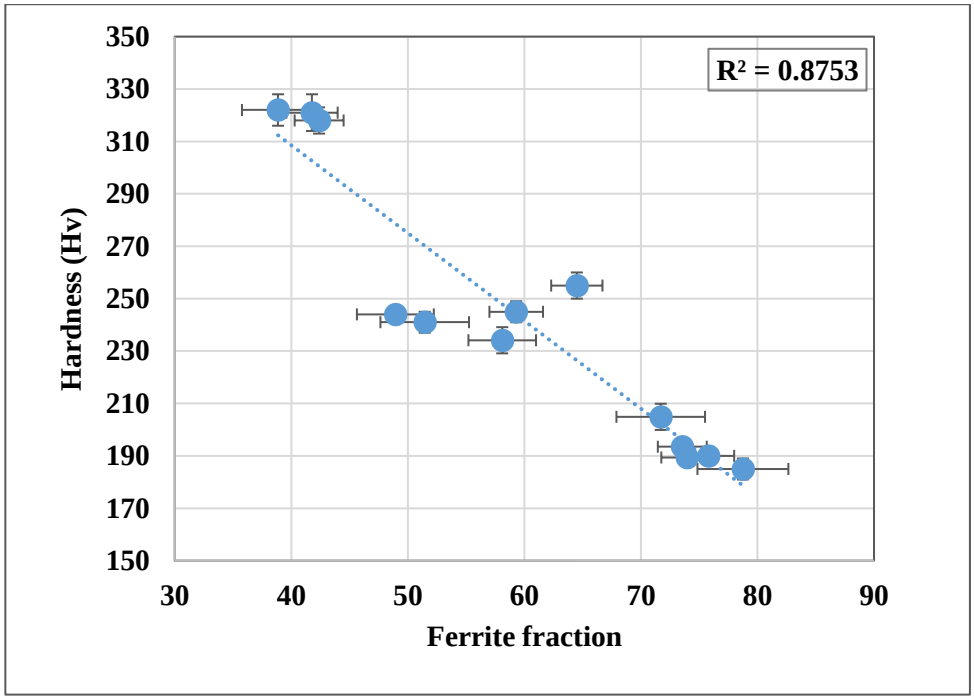

Figure 6.25: Hardness measurement of the commercial DP steels as a function of ferrite fraction

The decrease in tensile strength with increasing volume fraction of ferrite for DP steels is well known and widely documented [2, 152, 153] and consistent with the observed trend for hardness, Figure 6-25. This is in agreement with the results shown in Figure

6.26. There is a clear decrease in the tensile strength with an increase in ferrite fraction for DP grades, which is related to the lower martensite (or bainite) fraction.

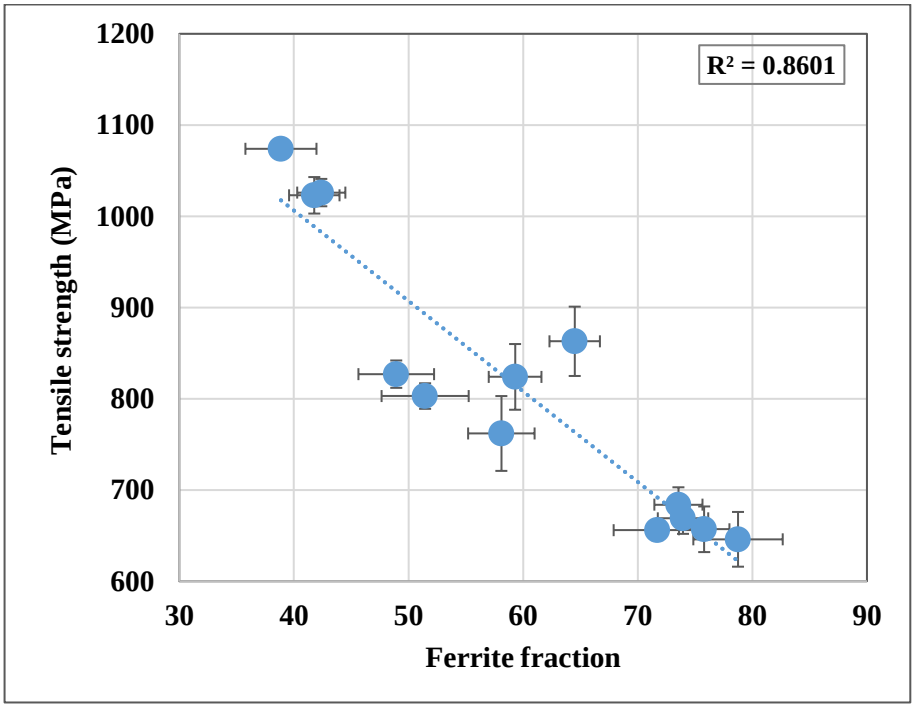

Figure 6.26: Ultimate tensile strength as a function of ferrite fraction for the commercial DP600, DP800 and DP1000 steel samples; the DP800 samples show more scatter in their relationship, where the higher than expected tensile strength is due to samples with a smaller grain size (3µm compared to 5µm).

The trend between tensile strength and ferrite fraction follows an approximately linear relationship for the DP samples. The trend stems mostly from the composite effect due to the presence of hard particles in a soft matrix. The trend obeys the law of mixtures, which is in agreement with the literature [4, 158, 159]. The correlation coefficient for the best fit equation is only $R^2 = 0.8581$. Therefore, ferrite fraction alone is not a good indicator of grade type or tensile strength. In addition, from Figure 6.26 it can be observed that there is a lot more scatter for the DP800 grades than the other steels.

To determine the cause of the scatter, a closer examination of their microstructures was carried out and, in particular, the ferrite grain size was investigated. It was found that the scatter can be related to the difference in grain size between the samples, with the samples above the best fit line having a finer grain size than those below the best fit line. The approximately linear relationship between strength and ferrite fraction holds well if the ferrite grain size does not alter between samples, however if ferrite grain size varies then this also needs to be taken into account

The relationship for the observed dependence of the tensile strength on the volume fraction of ferrite and the ferrite grain size will take into account both the phase balance (rule of mixtures, *Equation 6-1*) and Hall-Petch relationship (*Equation* 6-2) for the ferrite:

$$\sigma_U = \sigma_{Um} V_m + \sigma_{Uf} V_f \qquad \textit{Equation 6-1}$$

where, σ_U is tensile strength of dual phase steel, V_f fraction of ferrite, and V_m fraction of martensite , σ_{Um} and σ_{Uf} are tensile strength of martensite and ferrite respectively.

$$\boldsymbol{\sigma = \sigma_0 + k d_f^{(-1/2)}} \qquad \textit{Equation 6-2}$$

where σ_0 and K are material constants and d is ferrite grain size.

It should be noted that for DP1000 material any effect of ferrite grain size variation will be less significant on strength as the ferrite fraction is low (approximately 40% ferrite).

6.2.2 Magnetic property of commercial DP steels

6.2.2.1 Major B-H Loop for commercial DP steel

The setup for such measurement has previously been presented (Section 5.9.1, Chapter 5) and was used to generate major loops for the commercial DP steels. Figure 6.27 shows the major loops and the initial magnetisation curves for the commercial DP steels. As it can be seen from Figure 6.27 the different commercial DP steel samples produce different B-H curves.

As shown in Figure 6.27 and Figure 6.28 the DP 1000 samples (which have a higher volume fraction of martensite) show the largest coercivity values. The coercivity value is the field strength required to bring the sample to zero magnetic induction which reflects the magnetic hardness of the material [62]. As the microstructure of DP 1000 is predominantly martensitic with a high dislocation density as well as a larger number of lath boundaries and carbides, therefore, higher fields are required for demagnetisation and it exhibits the greatest coercivity value among these grades of DP steels, which in turn is indicative of material hardness. The coercivity values of DP 800 and DP600 show a reduction in comparison to the DP1000 due to their having more volume fraction of ferrite rather than martensite (or bainite) fraction.

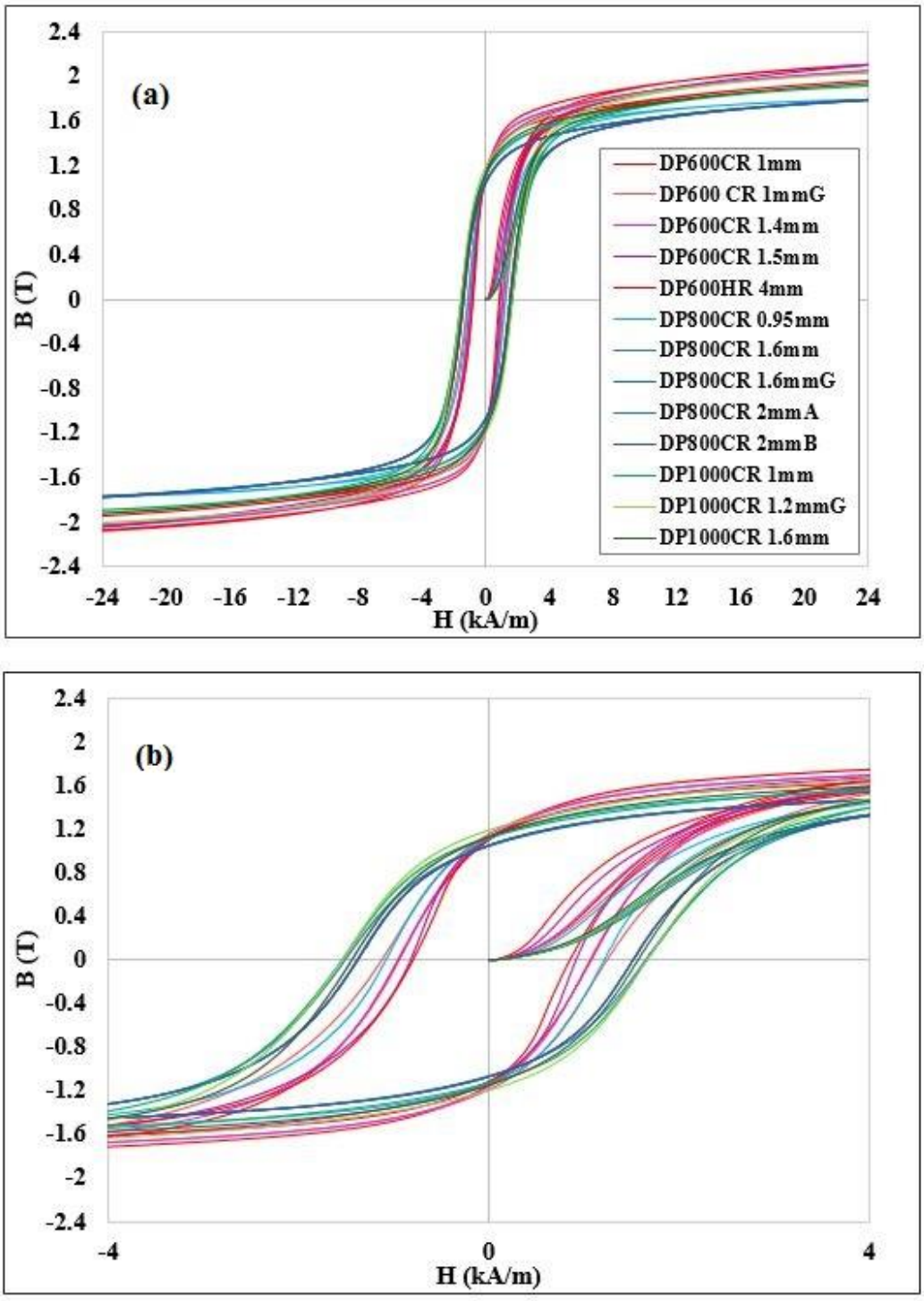

Figure 6.27: Major loops and initial magnetisation curves for the commercial DP steel samples (a) in full scale and (b) for H between -4 kA/m and 4kA/m.

In martensite there can be a large density of dislocations as well as having a fine lath structure with carbides, which can decrease the mean free path for domain wall motion, hence the coercivity value of these samples shows an increasing order of DP600 < DP800 < DP1000. Moreover, from Figure 6.28 it can be seen that there is a lot more scatter for the DP800 grades than the other steels. This is related to the fact that the ferrite grain size affects the magnetic properties in low carbon steel as the grain boundaries act as effective pinning points to magnetic domain movement [49, 50, 160]. Therefore, smaller ferrite grain size means more grain boundaries hence more pinning points resulting in higher coercivity.

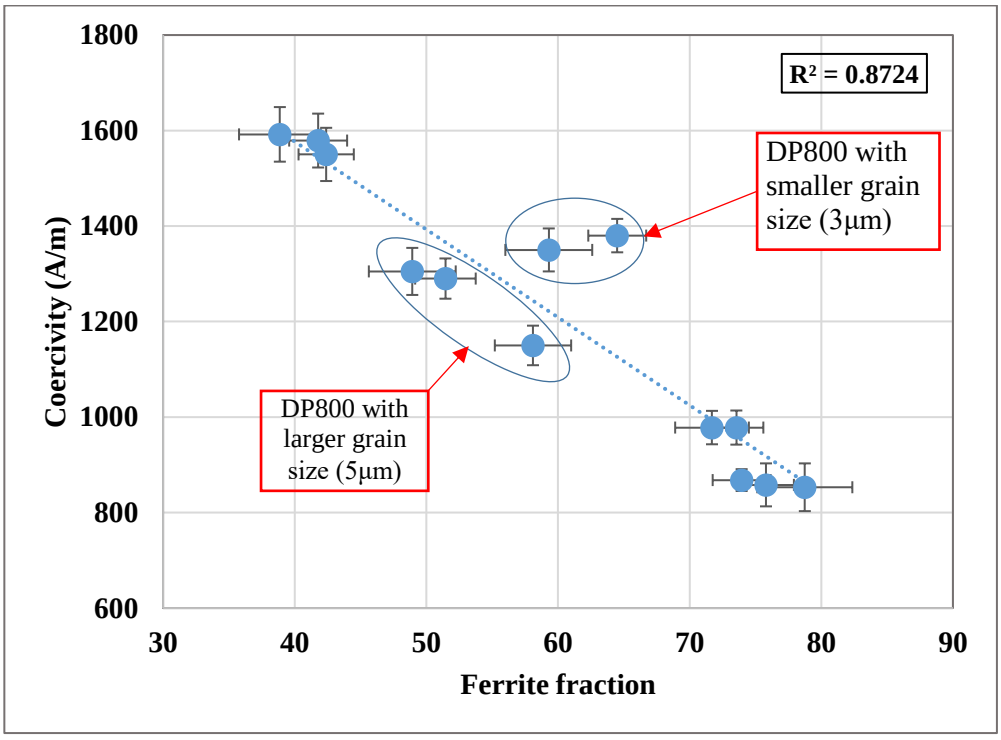

Figure 6.28: Coercivity values as a function of ferrite fraction for the commercial DP steel samples.

An excellent relationship between coercivity and mechanical properties (hardness and tensile strength) for the commercial DP steels are presented in Figure 6.29 and 6.30. As can be clearly seen, the coercivity values show a strong correlation with the tensile strength and hardness for the DP grades (an approximately linear decrease in coercivity with higher tensile strength and hardness). The correlation coefficient for the best fit equations are $R^2_{Hv} = 0.9258$ and $R^2_{UTS} = 0.9333$ for the hardness and the tensile strength respectively, suggesting, coercivity as a potential magnetic parameter for quantitatively assessing mechanical properties and discriminating phases. The commercial IMPOC and HACOM systems for steel assessment produce signals that are more closely related to the coercivity as they use a high magnetic field and there are empirical relationships between signals from these systems and strength for DP (and other grade) steels, as discussed in Chapter 4. These systems are used on-line during steel processing (cold strip mills / galvanising lines) and apply a large magnetic field making them less suitable for easy deployment in a lab setting for assessment of strip samples.

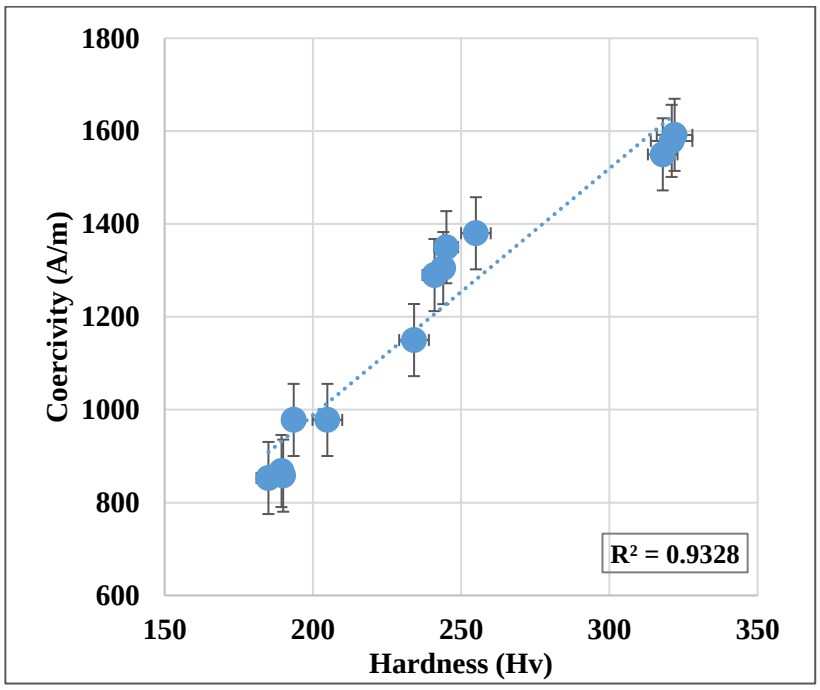

Figure 6.29: Coercivity values as a function of hardness for the commercial DP steel samples.

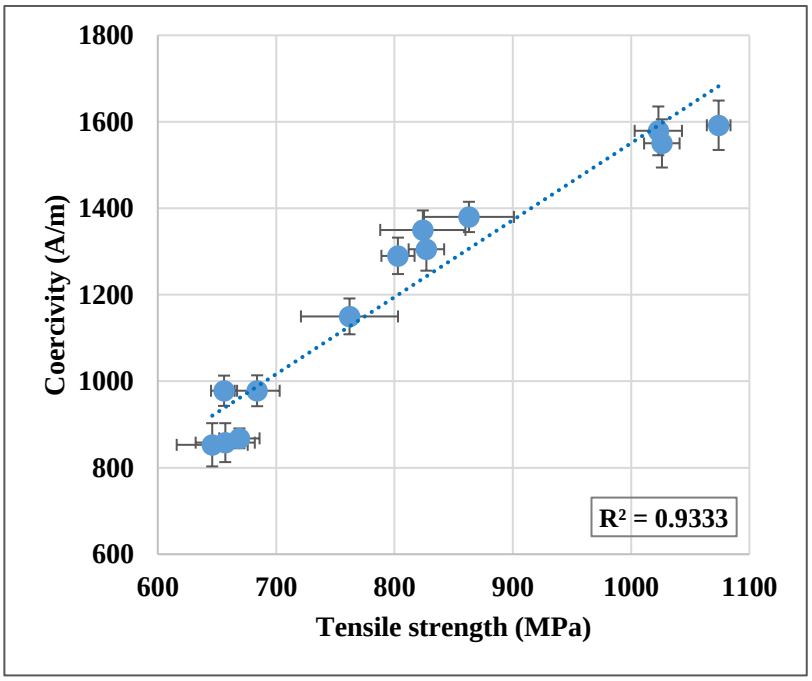

Figure 6.30: Coercivity values as a function of tensile strength for the commercial DP steel samples.

6.2.2.2 Minor B-H loops

6.2.2.2.1 Incremental permeability from initial magnetisation

Figure 6.31 (a) shows the evolution of the minor loop as deviations from the initial magnetisation curve for the commercial DP 600 1.4mm sample. In this plot the origin of the first minor loop corresponds to the demagnetised state where *H* and *B* are equal to zero.

The magnetisation of the sample in this condition, and for this applied magnetic field, can be described by the Raleigh Law [129]. Therefore, in this region, magnetisation is a combination of reversible and irreversible components, resulting in a loop enclosing a relatively large area, as shown in Figure 6.31 (b). As the applied field increases, the initial magnetisation curve approaches saturation, domain walls are swept away by field pressure and the dominant magnetisation can be described as the progressive alignment of the field against anisotropy and the rotation of the domains happen from their magnetic easy axes towards the direction of the applied field [161] therefore, resulting in a closed up loop, with a much smaller variation in *B* for a given applied field, as shown in Figure 6.31(e) .

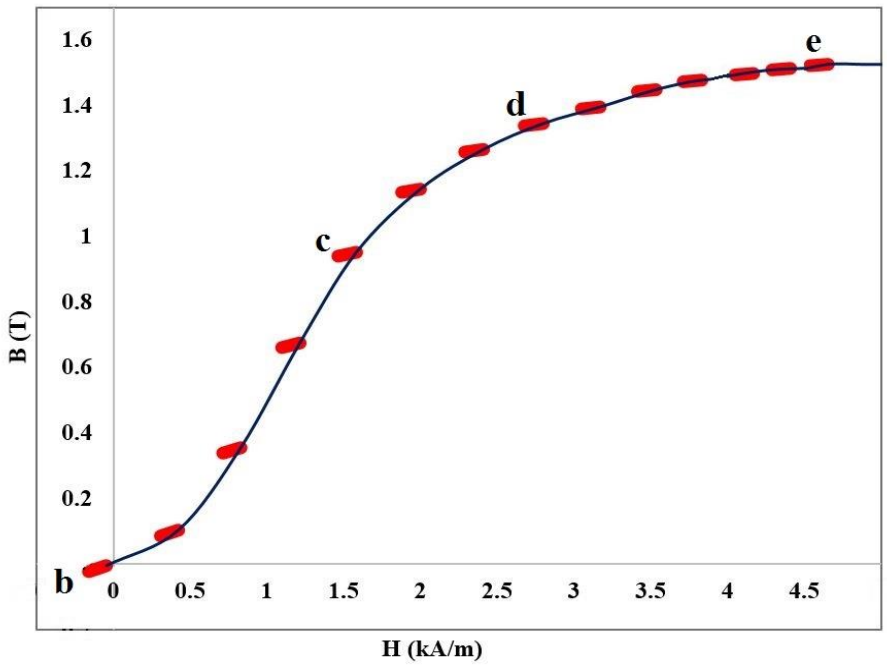

(a)

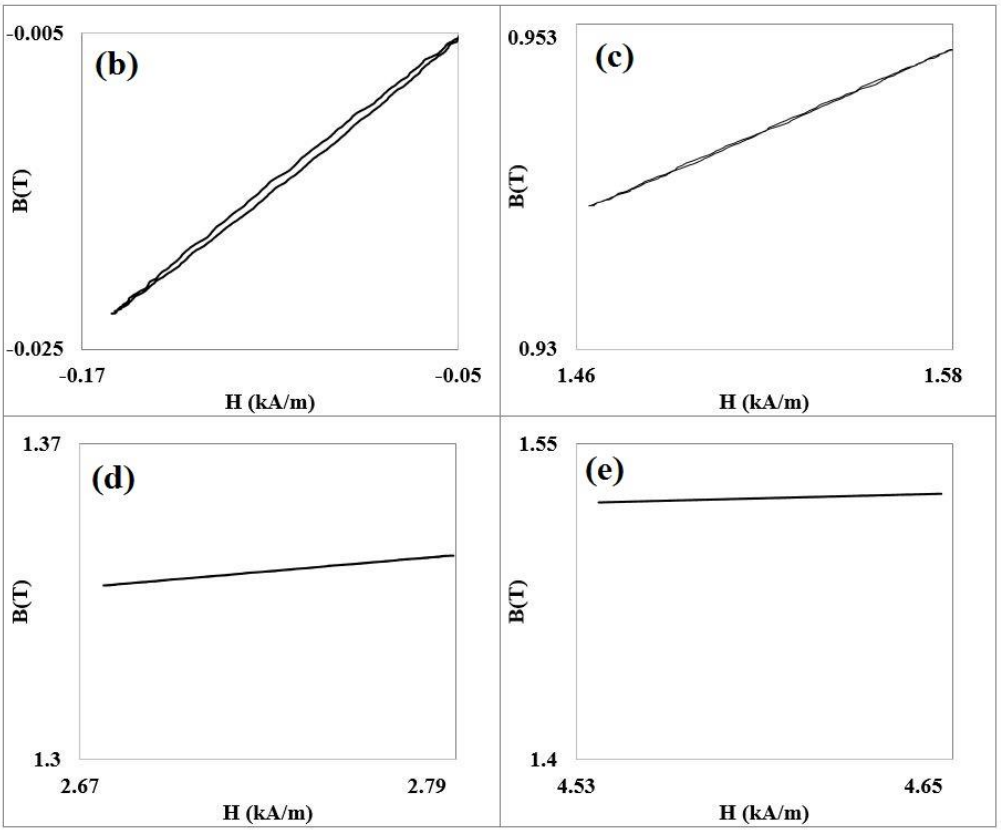

Figure 6.31: Presents the initial magnetisation curve (a) and a series of minor loops deviations from initial magnetisation curve for the commercial DP600 1.4mm sample

Figure 6.32 shows the incremental permeability as a function of applied field for three commercial DP samples. It is apparent from Figure 6.32 that the maximum incremental permeability value corresponds to a value of *H* where the domain walls have the greatest degree of freedom to move. There is a sharp decrease in permeability (μ_{IC}) with increasing magnetic field (*H),* along with near convergence in permeability values for the commercial DP600, DP800 and DP1000 samples. The convergence can be observed for these samples where saturation is approached and contributions from domain wall pinning sites are reduced, giving way to reversible domain rotation effects [41]. Moreover, it is apparent from Figure 6.32 that the DP600 sample exhibits much more variation in μ_{IC} whereas DP1000 sample shows a much smaller variation for increasing *H*. This is believed to be due to the greater area fraction of martensite and associated high dislocation density which results in heavy domain wall pinning in the DP1000 sample.

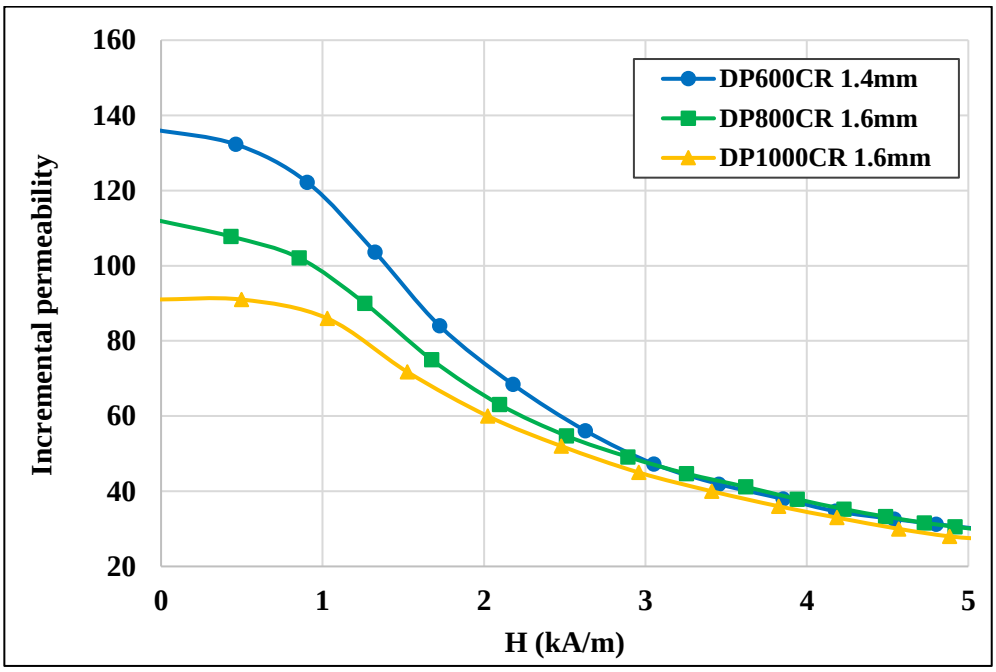

Figure 6.32: Incremental permeability values for minor loop deviations from the initial magnetisation curve as a function of field for the commercial DP600 CR 1.4mm, DP 800 CR 1.6mm and DP1000 CR 1.6mm.

The incremental permeability measurements at *H=0* (deviations from the initial magnetisation curve) for the commercial DP steel samples are given in Table 6.2.

Table 6-2: The incremental permeability measurements deviations from the initial magnetisation curve for the commercial DP steel samples

Sample	μ_{IC}
DP600CR 1mm	142±3
DP600CR 1mmGl	141±3
DP600CR 1.4mm	137±3
DP600CR 1.5mm	136±3
DP600HR 4mm	177±4
DP800CR 0.95mm	126±3
DP800CR 1.6mm	112±3
DP800CR 1.6mmGl	115±3
DP800CR 2mmA	112±3
DP800CR 2mmB	109±2
DP1000CR 1mm	94±3
DP1000CR1.2mmGl	95±2
DP1000CR 1.6mm	92±3

Figure 6.33 shows a strong effect of ferrite fraction on the permeability, as has been seen previously [22]. Moreover, Figure 6.33 reveals that the correlation coefficient for the best fit line is low (R^2 =0.8581) as the effect of grain size on permeability is not taken into account. It can be seen that the two DP800 samples with the smaller ferrite grain size (3μm) show lower permeability values than the other DP800 samples (grain size of 5-6 μm) and the DP 600 4mm with a larger ferrite grain size (10μm), shows higher permeability values than the other DP600 samples (ferrite grain size of 6-7 μm) indicating that ferrite grain size has a significant effect on the magnetic property (permeability) in these steels as well as ferrite fraction [19, 55]. This is due to the ferrite grain size affecting the magnetic properties in low carbon steel as the grain boundaries act as effective pinning points to magnetic domain movement [49, 50, 160]. Therefore,

not only ferrite fraction but also the ferrite grain size influences the permeability in the commercial DP steels.

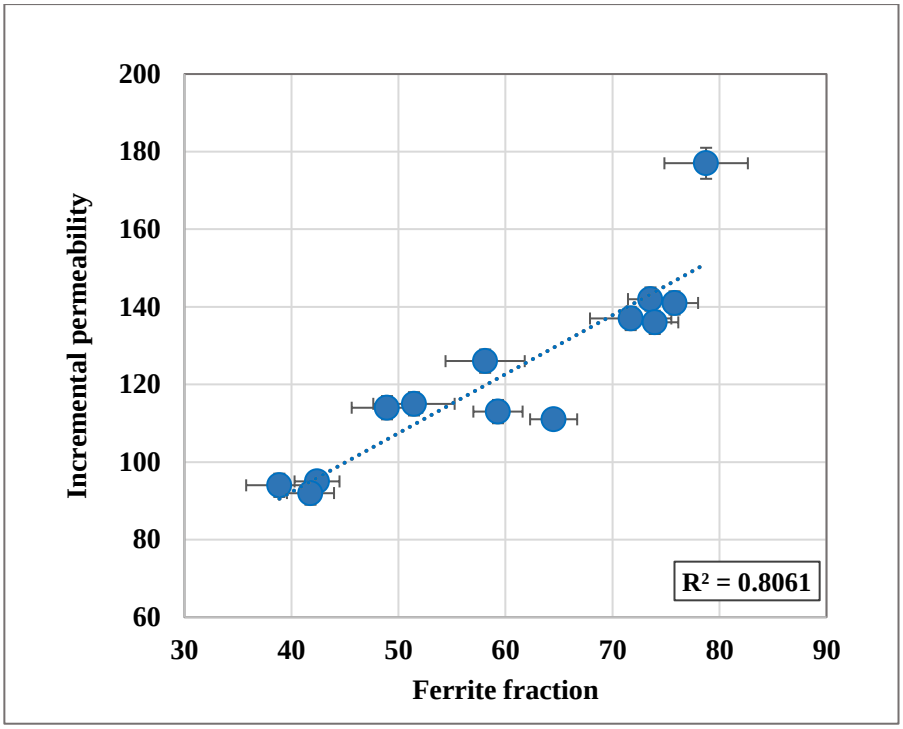

Figure 6.33: Incremental permeability values deviations from the initial magnetisation curve as a function of ferrite fraction for the commercial DP steel samples.

6.2.2.2.2 Incremental permeability from main BH loops

In domain processes during a minor loop, the amplitude field plays a predominant role as it predetermines the domain structure [41]. Predetermined amplitude field required for minor loop processing which is basically lower than saturation field value. For instance, the magnetic field required to be applied into the sample to achieve saturation for the DP600 CR 1.6mm is around 26 kA/m and in this work 50% of this field (i.e.13 kA/m) was used to process minor loop.

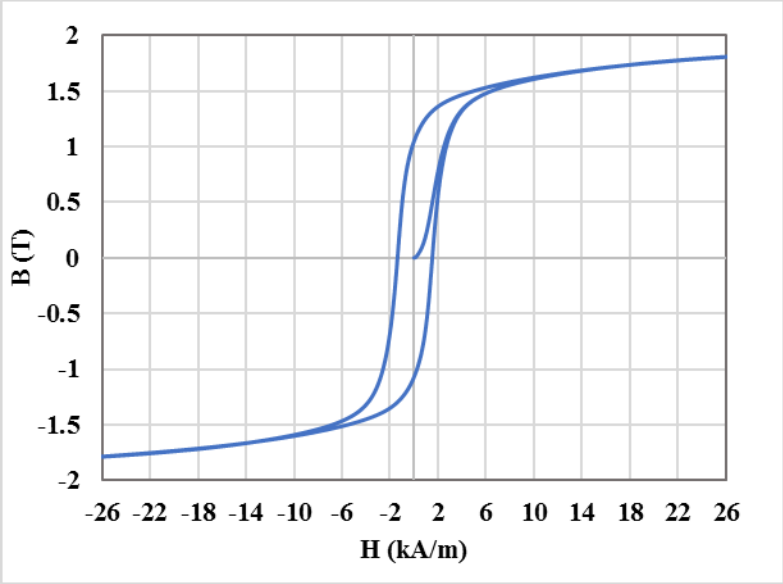

Figure 6.34: Full BH hysteresis loop for the DP800 CR 1.6mm

Figure 6.35 (a) represents the minor loop deviations from the main B-H loop for the commercial DP800CR 1.6mm. In Figure 6.35 (b), the incremental permeability as a function of applied field can be observed. It is worth stating that each peak corresponds to one half of the major *B-H* loop (descending and ascending field sweeps), Figure 6.35(c-h). The maximum incremental permeability value at the peak of the curve for

the upper half of the major loop (μ_{BHU}) and the lower half of the major loop (μ_{BHL}) correspond to a H value where $B = 0$ and it occurs close to the coercivity where domain walls have the greatest degree of freedom to move [148].

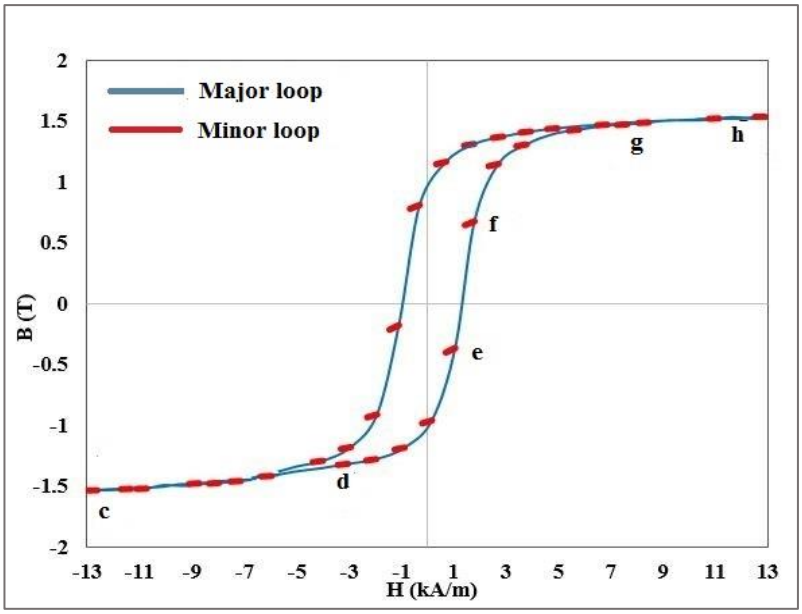

(a)

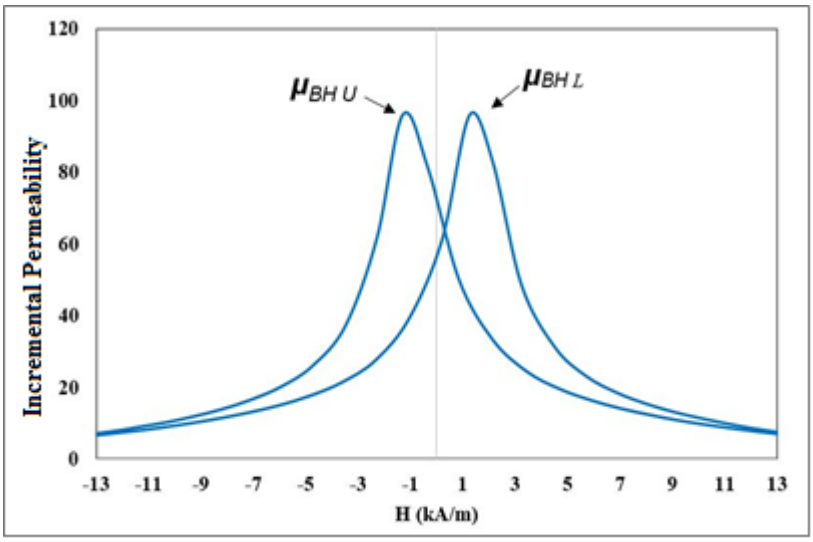

(b)

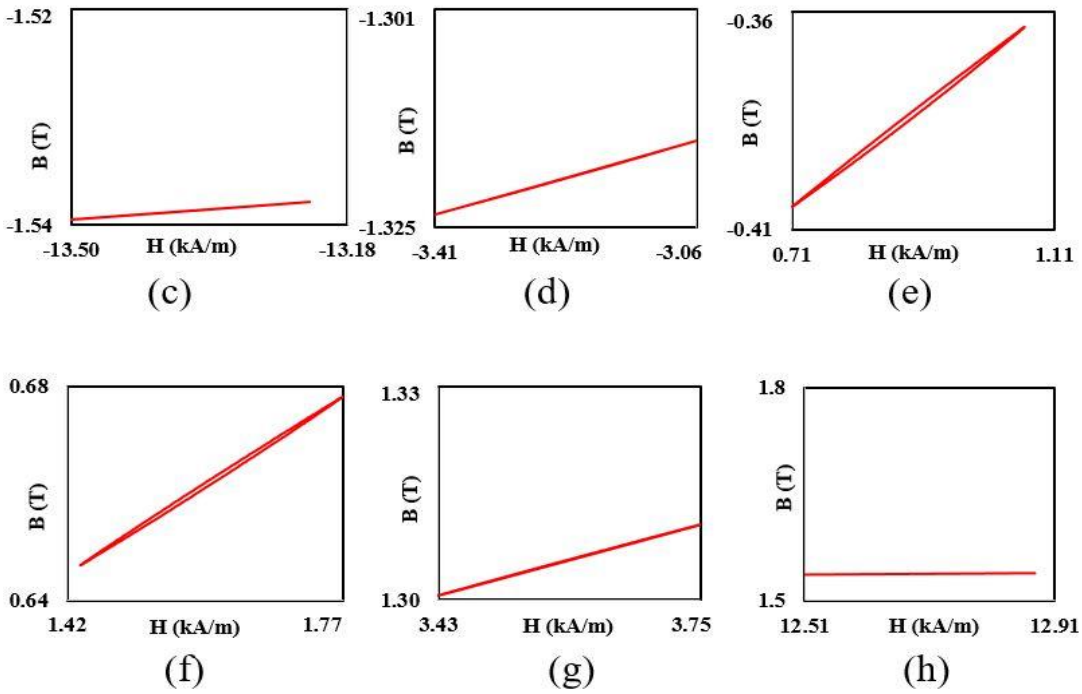

Figure 6.35: (a) Major loop and minor loops for the commercial DP800CR 1.6mm sample with the amplitudes ranging from -13(kA/m) to +13 (kA/m), (b) Incremental permeability values derived from the BH loop, the maximum incremental permeability from the upper half of the major loop(μ_{BHU}) and the maximum incremental permeability from the lower half of the major loop (μ_{BHL}) correspond to the coercive force,(c-h) a series of minor loops deviations from the lower half of major loop.

Figure 6.36 illustrates a comparison between the incremental permeability of the DP600CR1.4mm, DP800CR1.6 and the DP1000CR1.6mm samples. As can be seen, each sample shows two peaks. For the DP600CR 1.4mm sample these peaks are closer together than the peaks in the DP800CR1.6mm and the DP1000CR 1.6mm samples. The peak for the DP600CR1.4mm samples is narrower and shifted to a lower H value, which is expected due to the higher volume fraction of ferrite since easier reverse domain formation and domain wall motion takes place at a lower applied field [49, 62].

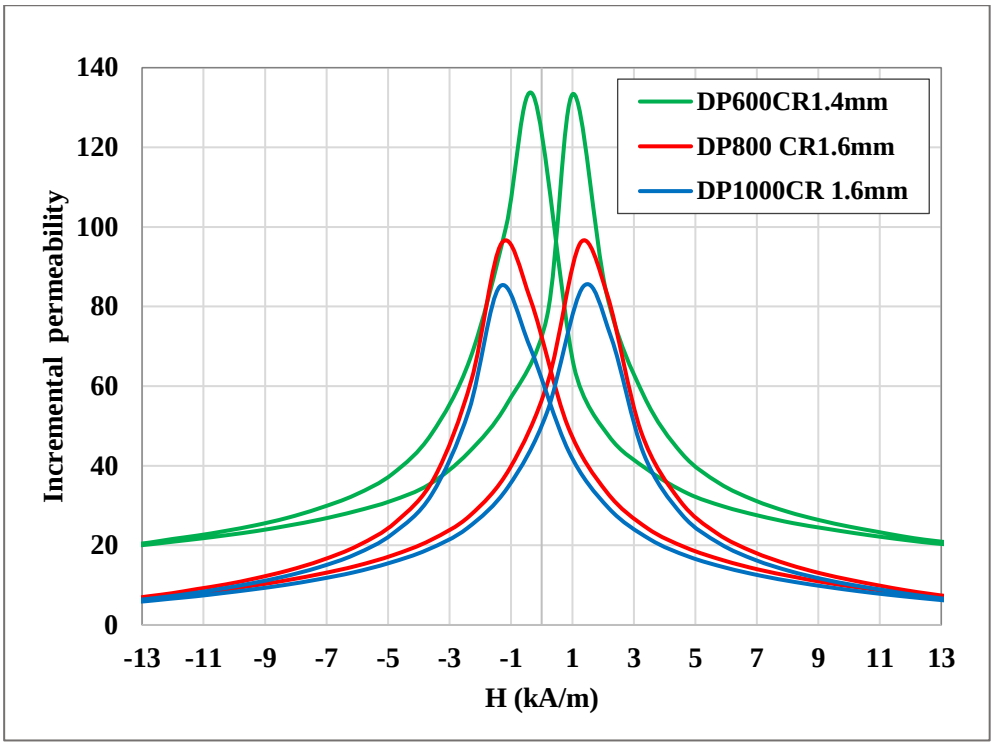

Figure 6.36: Incremental permeability values derived from the major loop with the amplitudes ranging from -13kA/m to +13(kA/m) for the commercial DP600CR 1.4mm, DP800CR 1.6mm and DP1000CR 1.6mm samples

The maximum incremental permeability measurements deviations from the major loop for the commercial DP steel samples are given in Table 6.3.

Table 6-3: The incremental permeability measurements deviations from the major loop for the commercial DP steel samples

Sample	μ_{BH}
DP600CR 1mm	136±3
DP600CR 1mmGl	135 ±4
DP600CR 1.4mm	133±3
DP600CR 1.5mm	140±3
DP600HR 4mm	176±4
DP800CR 0.95mm	120±3
DP800CR 1.6mm	100±4
DP800CR 1.6mmGl	105±2
DP800CR 2mmA	107±2
DP800CR 2mmB	101±3
DP1000CR 1mm	84±2
DP1000CR1.2mmGl	85±3
DP1000CR 1.6mm	86±2

It can be seen that the incremental permeability values (deviations from the major B-H loop) are close to the values of the incremental permeability (deviations from the initial magnetisation curve) where the incremental permeability of these samples shows an increasing order of DP 1000 < DP800 < DP600. From Figure 6.37, the effect of the ferrite grain size and ferrite fraction on the value of incremental permeability can be observed. The results indicate a notable difference in the permeability value between the DP600HR 4mm sample and the rest of the DP600 samples which is related to the average ferrite grain size of these samples (the average ferrite grain size of 10μm for the DP600HR 4mm and 6-7μm for the rest of the DP600 samples). The effect of ferrite grain size also can be observed in the DP800 CR 1.6mm and DP800CR2mm B samples.

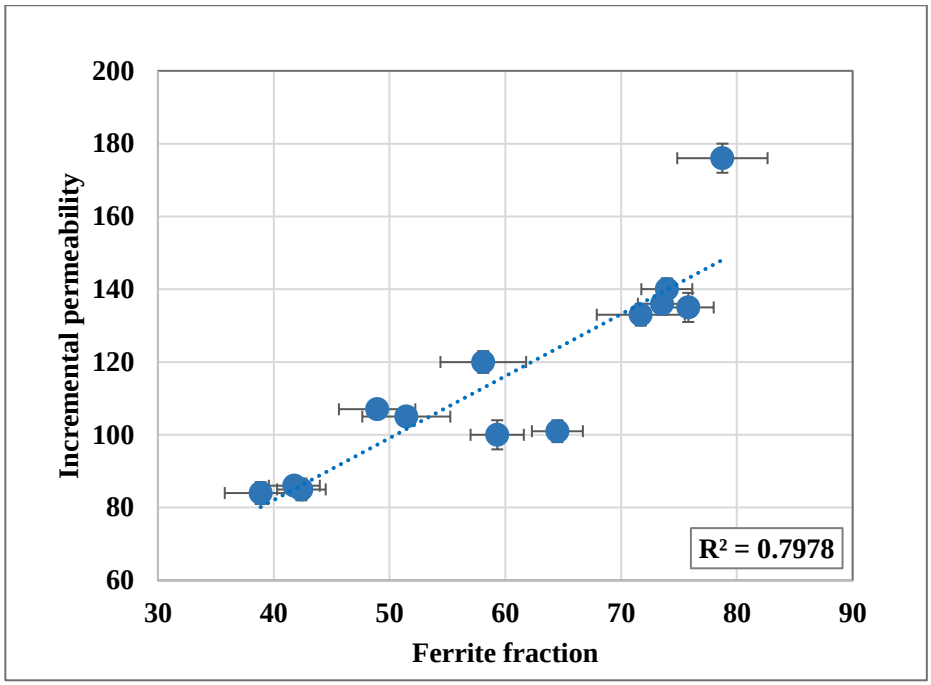

Figure 6.37: Incremental permeability values deviations from the major B-H loop as a function of ferrite fraction for the commercial DP steel samples.

Figure 6.38 shows a comparison between the incremental permeability curves for the initial magnetisation and the major B-H loop for the commercial DP600 1.4mm sample. It is apparent that the incremental permeability curves for initial magnetisation and major *B-H* loop have different values when H=0. This is believed to be due to the random domain distribution of the demagnetised sample in the major BH loop where the demagnetisation process occurs with residual magnetisation, compared with the initial magnetisation curve with greater variation in *B* for a given *H* field and higher permeability value.

It is clear that although the incremental permeability curves for initial magnetisation and major B-H loop have different values at *H=0*, they converge at the coercive field (H_C).

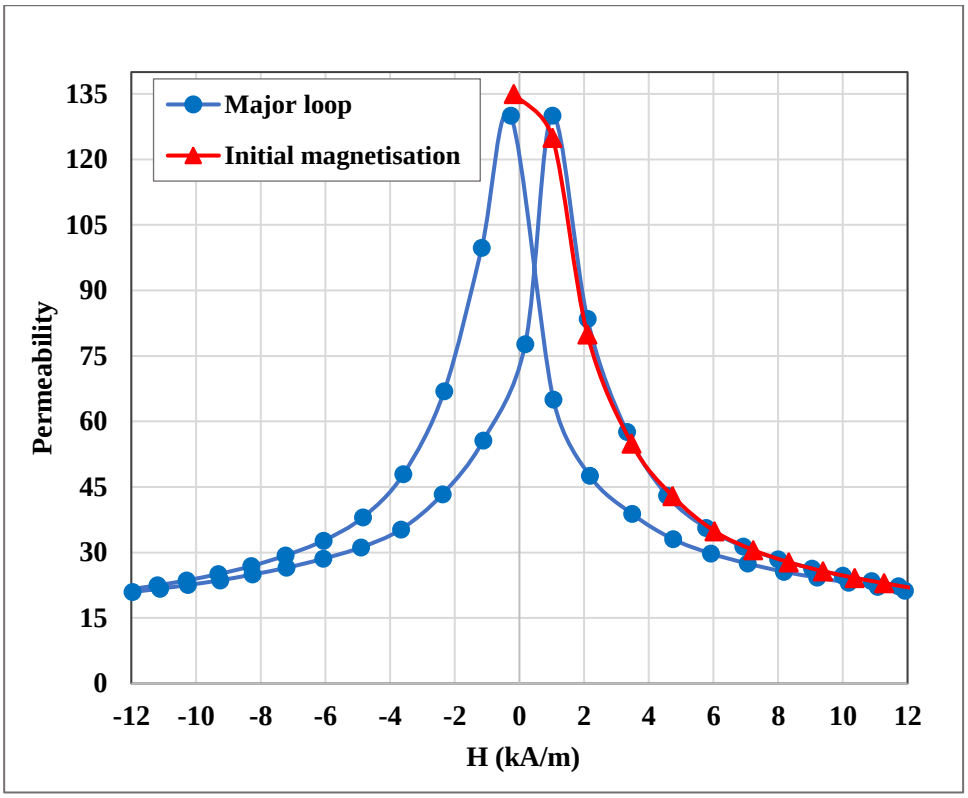

Figure 6.38: Comparison between incremental permeability curves for initial magnetisation and major B-H loop for the commercial DP600 1.4mm, although the incremental permeability curves for initial magnetisation and major B-H loop have different values at H=0 (higher permeability value for initial magnetisation) they converge at the coercive field (H_C)

6.2.2.2.3 Incremental permeability from amplitude sweep

Figure 6.39 presents a series of minor loops with the different amplitudes ranging from approximately 138 A/m to 2 kA/m for the DP600CR 1.4mm sample. The shape of the minor loops varies with the amplitude where at a small amplitude it is a lenticular shape which changes into a sigmoid shape at a higher amplitude as shown in Figure 6.39(b), Figure 6.39(c) and Figure 6.39(d). The gradient of the loop is physically interpreted as the incremental permeability.

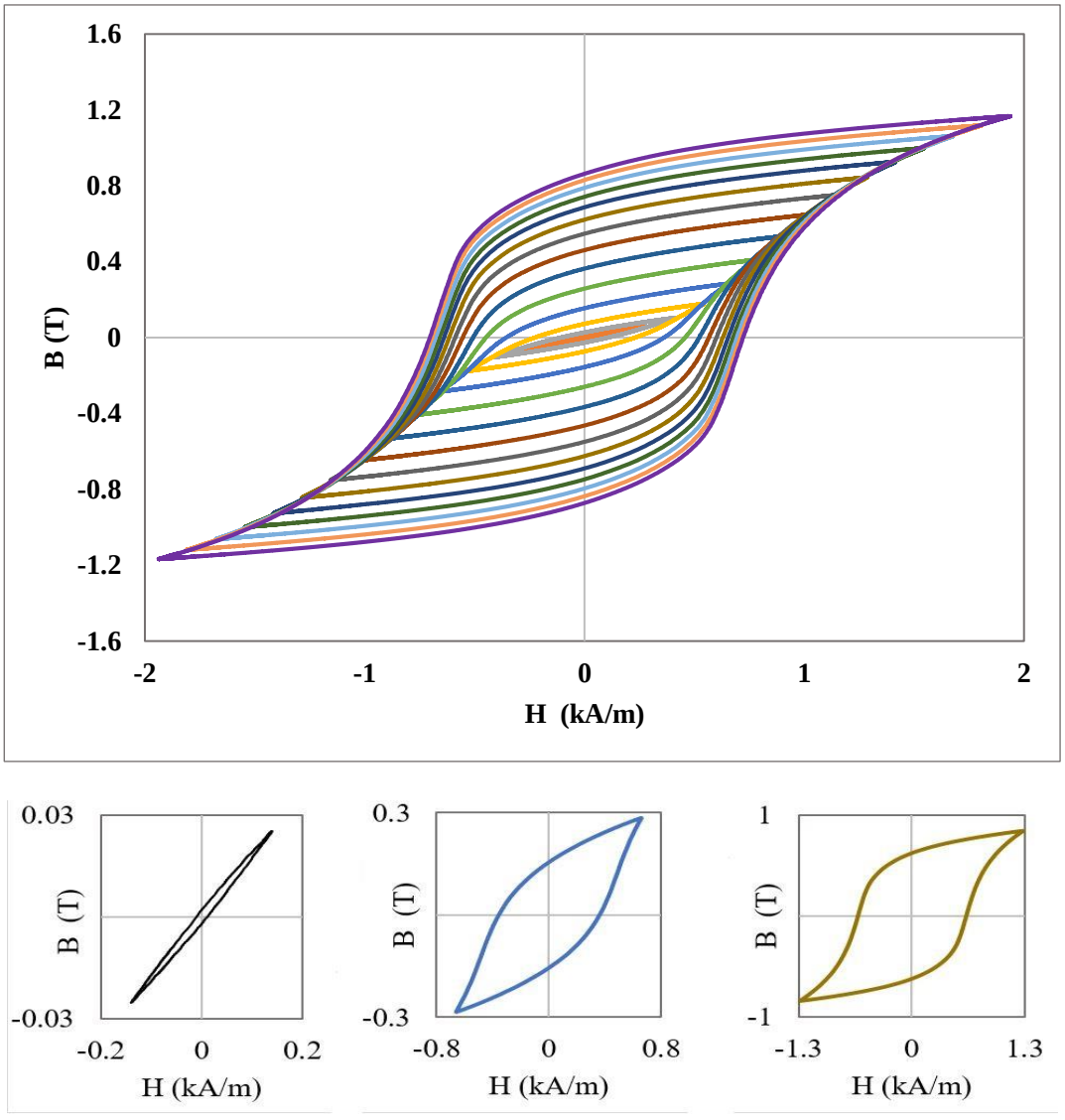

Figure 6.39: A series of minor loops with the amplitudes ranging from 140 A/m to 2(kA/m) for the DP600CR 1.4mm.sample

The resultant incremental permeability curves for minor loop deviations from the minor loop amplitude are presented in Figure 6.40. As it is apparent from the plot, with an increase in the minor loop amplitude, the permeability (μ_i) also increases to reach a peak and then drops. At low minor loop amplitudes, the reversible magnetisation component dominates; as the minor loop amplitude increases, the irreversible component is introduced and the gradient of the minor loop increases, as a greater ΔB is generated for a given change in H. Incremental permeability deviations from the minor loop amplitude will be fully explained in Section 6.2.3 in this chapter.

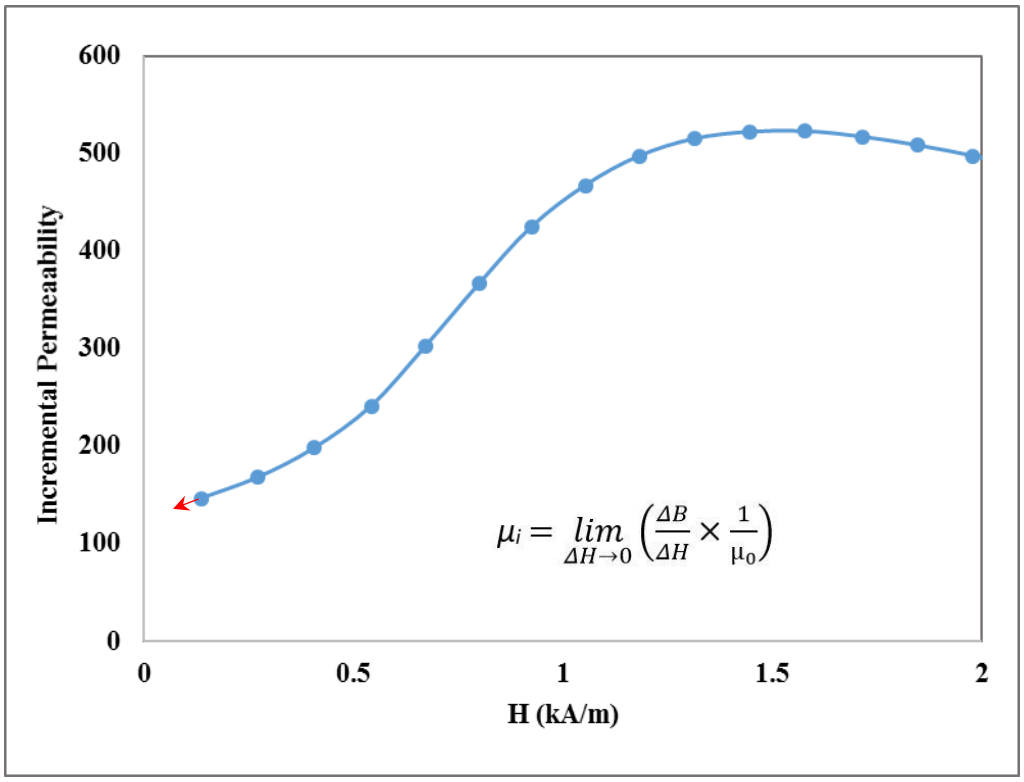

Figure 6.40: Incremental permeability values derived from minor loop amplitude sweeps as a function of applied field for the commercial DP600CR1.4mm sample, initial permeability is extrapolated if the minor loop amplitude could be made to equal zero

Equation 6.3 indicates that the incremental permeability can be employed to extrapolate to a value for initial permeability *(μ_i)* if the minor loop amplitude could be made to equal zero.

$$\mu_i = \lim_{\Delta H \to 0} \left(\frac{\Delta B}{\Delta H} \times \frac{1}{\mu_0} \right) \qquad \textit{Equation 6-3}$$

The initial permeability *(μ_i)* values derived from minor loop amplitude sweeps for the commercial DP steel samples are given in Table 6.4. The results indicate that the values of the initial permeability are slightly higher than the incremental permeability deviations from the initial magnetisation curve and from the major B-H loop. Figure 6.41 shows the measured initial permeability as a function of ferrite faction for the commercial DP steels. The effect of ferrite fraction and ferrite grain size on the permeability can be observed.

Table 6-4: Initial permeability measurements derived from minor loop amplitude sweep for the commercial DP steel samples

Sample	μ_i
DP600CR 1mm	152±4
DP600CR 1mmGl	150±3
DP600CR 1.4mm	147±4
DP600CR 1.5mm	149±3
DP600HR 4mm	180±3
DP800CR 0.95mm	127±3
DP800CR 1.6mm	109±2
DP800CR 1.6mmGl	114±3
DP800CR 2mmA	115±2
DP800CR 2mmB	111±3
DP1000CR 1mm	90±3
DP1000CR1.2mmGl	92±3
DP1000CR 1.6mm	92±4

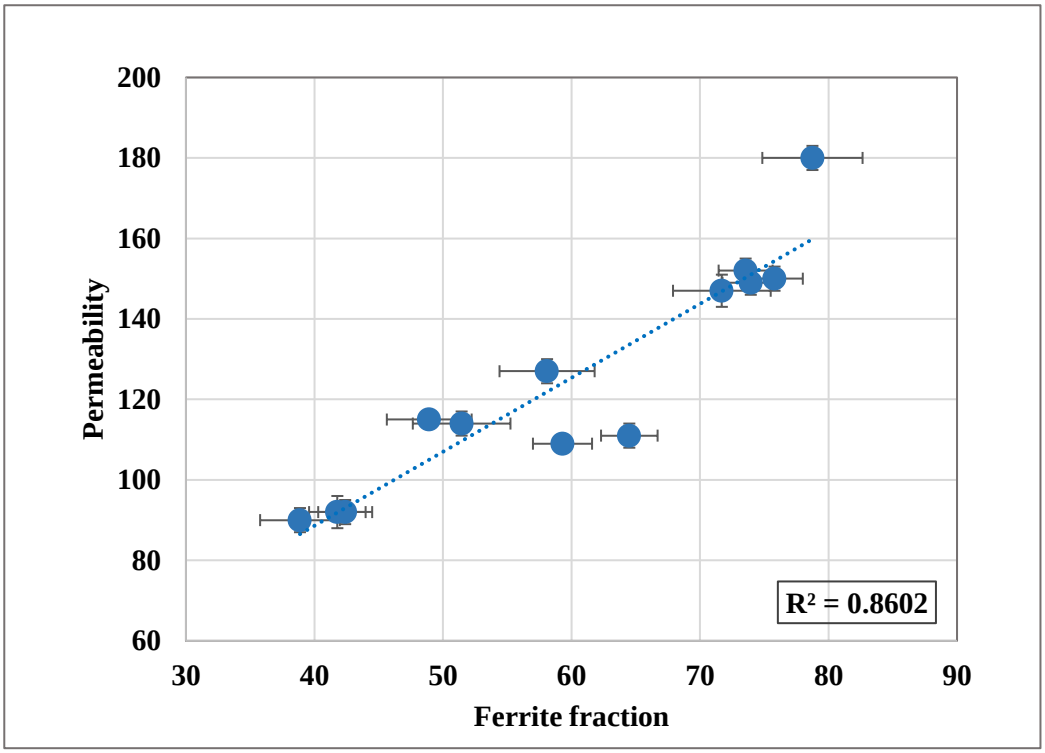

Figure 6.41:Initial permeability values derived from minor loop amplitude sweeps as a function of ferrite fraction for the commercial DP steel samples

It is worth mentioning that when there is more than one type of microstructural feature present, their effects on permeability cannot be separated. Besides the effect of phase fraction and ferrite grain size, others parameters such as precipitates, chemical composition differences and inclusions are less significant (in DP steels) and can be placed as second order influences after phase fraction and ferrite grain size for DP steel samples.

The most frequent size range of inclusion (Figure 6.42) for DP samples is between 3 to 12 µm and the number density is low (typically less than 25±3 μm^2 / mm^2). By comparing the typically inclusion content in DP steels with Figure 6.43, it can be judged that inclusions in DP steels will not have a significant effect for magnetic

permeability. In addition all the DP steels have been produced using consistent steel processing (chemistry and inclusion control) meaning that there is unlikely to be significant differences in inclusion content between the DP steels.

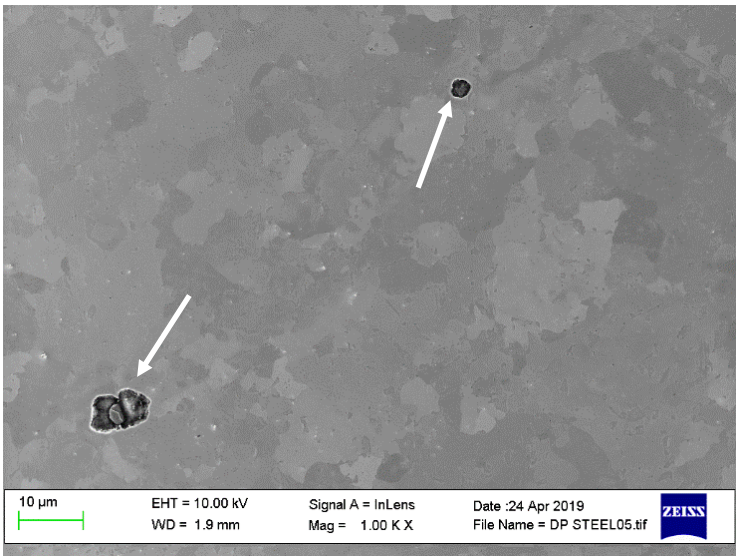

Figure 6.42: SEM micrograph of the DP600 1.4mm showing distribution of inclusions. A low number density of inclusions was observed with this micrograph being selected to show inclusion rather than being representative of the general microstructure.

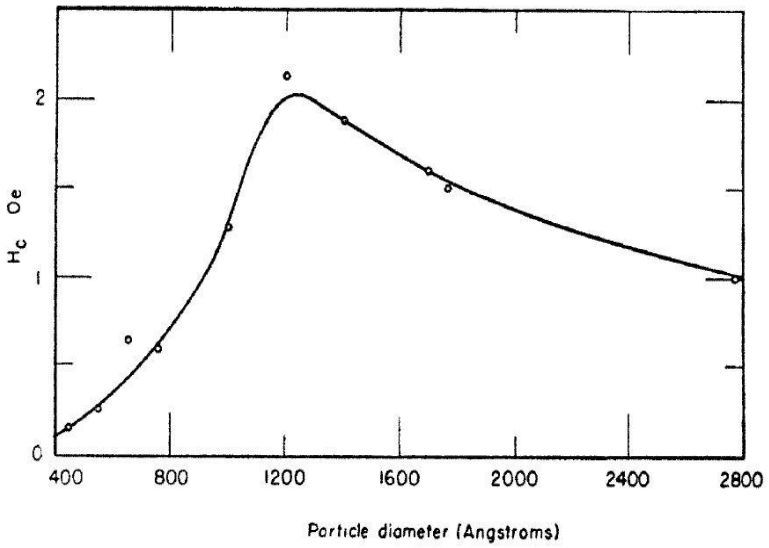

Figure 6.43: Coercive force as a function of particle size in iron [74]

6.2.2.3 Summary

Three types of minor loop configurations including; minor loop deviations from the initial magnetisation curve, major BH loop and minor loop amplitude sweeps have been used to investigate the permeability of commercial DP steel samples.

Figure 6.44 shows a comparison between the measured incremental permeability values. It can be seen that, although the permeability values are not precisely the same for the three sets of measurements, similar trends for the samples can be observed. In addition, in all three measurements, the effect of phase fraction and ferrite grain size on permeability can be observed.

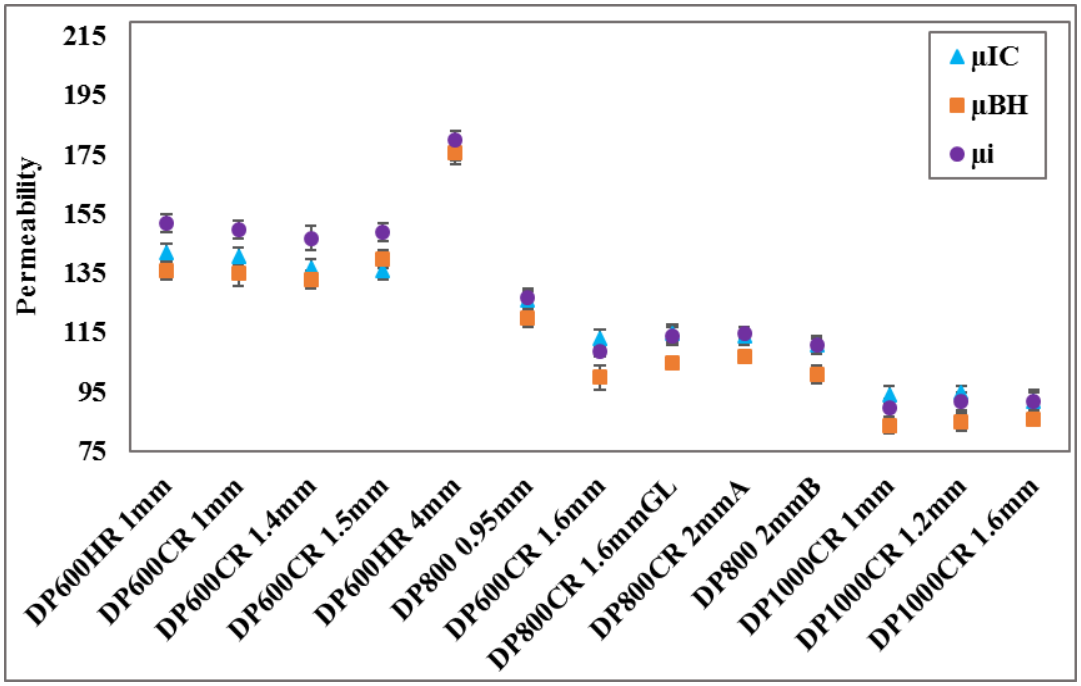

Figure 6.44: Comparison of incremental permeability values; derived from initial magnetisation curve (μ_{IC}), incremental permeability values derived from BH loop (μ_{BH}) and incremental permeability values derived from minor loop amplitude sweep (μ_i) for the commercial DP steels

The BH technique, i.e. major loop and minor loops, both involve the measurement of magnetic flux density *B* in response to an applied field *H*, however, the interaction between magnetic domains and material microstructure can be different.

In general, the minor loop response to a small applied field is predominantly reversible; corresponding to bowing of domain walls and domain rotation at higher major loop offsets [23, 72]. In contrast, the major BH loop response consists of a combination of reversible and irreversible components [23]; irreversible magnetisation from domain walls overcoming pinning features such as grain boundaries and dislocations and in term of reversible, magnetisation from domain wall motion and rotation of magnetic domains [72].

6.2.2.4 Modelling of the EM sensor output using FE method

A least square fitting method was used for the EM sensor to determine the relative permeability values of the samples by fitting the modelled real inductance with the experimental measured one through Comsol. The cylindrical sensor is discussed first with initial fitting used to calibrate the cylindrical sensor for rod samples with known permeability, then the 2D model was converted into a 3D FE cylindrical sensor model for strip samples to allow the determination of the permeability of the DP steels. Finally, the U-shaped sensor was modelled to investigate the effect of microstructure on EM signals and to determine the relative permeability of any strip sheet thicknesses using the easily deployable sensor.

6.2.2.4.1 Cylindrical air - cored sensor

A cylindrical air – cored sensor was selected initially in order to determine the relative permeability of samples using a sensor that is easily modelled and would show the effect of changes in the DP steel microstructure on the EM sensor signal. Since the low field relative permeability values of DP grade samples are expected to be relatively close to each other (i.e. from 115 - 216) based on literature reports [22], compared with 0.17 wt% C and 0.87 wt% C with permeability of 288 and 56 respectively, [49] a large series of FE models for different potential cylindrical air-cored sensor geometries were run (for a given sample size) to ensure that sufficient signal differentiation could be obtained. The initial model geometry was based on previous work, reported in ref [22, 162], where the sensor model was fitted and verified for pure iron and fully pearlite samples. Initially a two-dimensional (2D) axial symmetry FE cylindrical sensor model developed using COMSOL software was used for the calibration rod samples.

As can be seen from Figure 6.45, different configurations such as; position of excitation coil, sensing coil, number of turns and the thickness of wire, affect the signal [163].

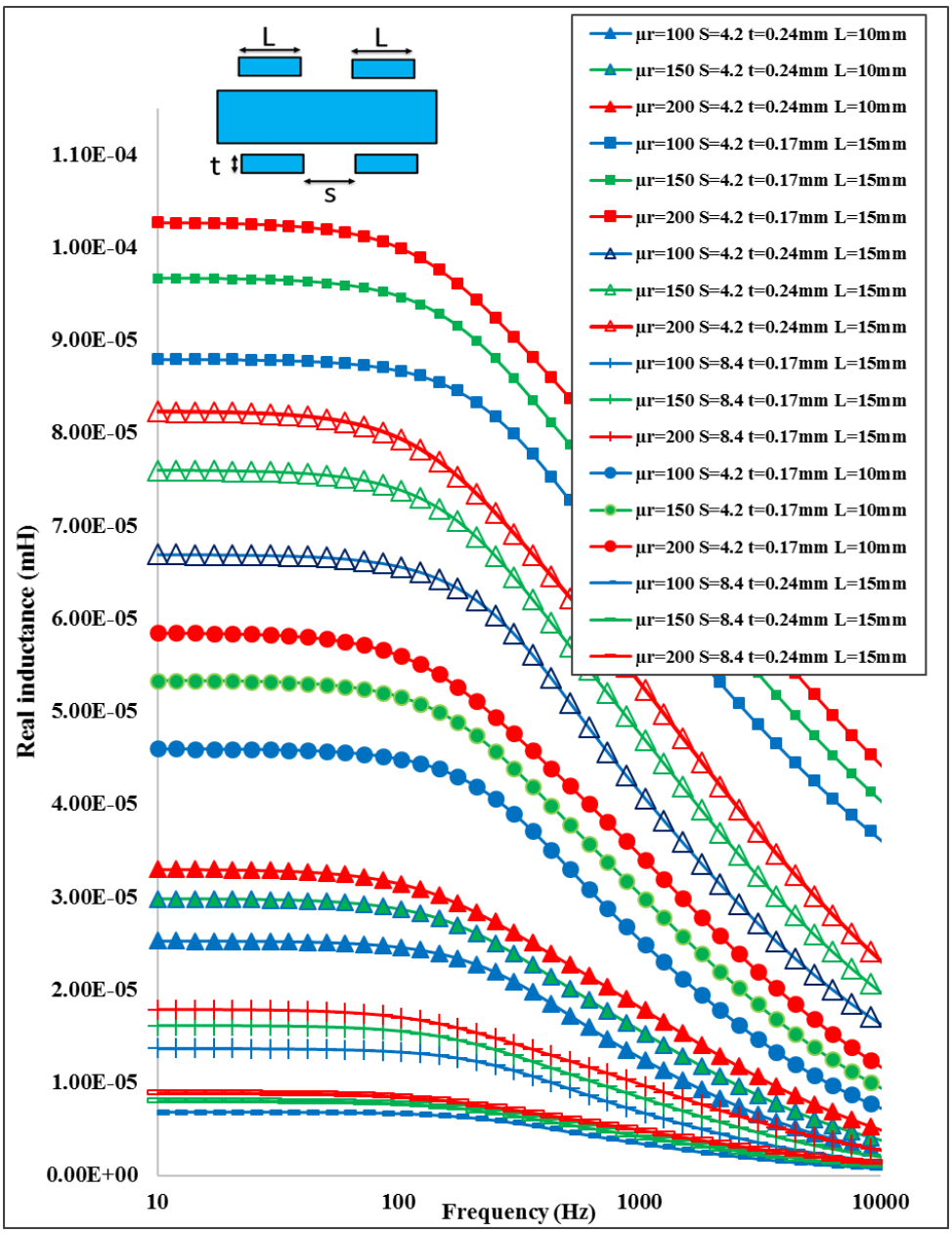

Figure 6.45: Plots of model results for the different cylindrical configurations such as length and position of exciting coil, sensing coil (L= length of the exciting and sensing coil, S = separation between exciting and sensing coil), the thickness of wire (t) in order to find the most desirable configuration for the air-cored cylindrical sensor. The simulations are for a constant sample size (rod of diameter 4.95mm and length 50mm, with different relative permeability values (μr of 100 to 200) and resistivity values (210nΩm).

It is worth stating that a sample size of 50 mm by 4.95mm, same as the sample size used for the B-H machine, was used in order to compare the results. Consequently, a length of 50mm was chosen for the cylindrical sensor. In term of the diameter for the cylindrical sensor, since the maximum thickness of the commercial DP steels used in this work was 4mm and considering a 4.95 mm width for strip samples then a minimum internal diameter of 6.4 mm was required. The best configuration from the sensor geometries trialled, and considering practical limitations in terms of the number of turns that could be wound onto a cylindrical former, was reached with the following characteristics; two identical coils arranged with their axis aligned, one as excitation coil and the other as sensing coil, the cylindrical air cored sensor with outer diameter of 8.4mm, length of 50mm, copper wire of 0.17mm in diameter, the equal number of 88 turns (15mm length) for the excitation coil and for the sensing coil, the distance between sensing coil and excitation coil 4.2 mm (Figure 6.46).

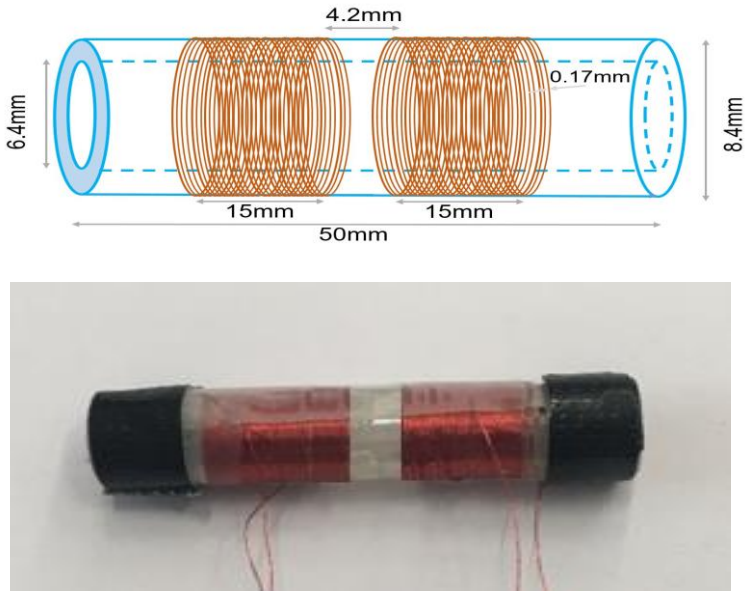

Figure 6.46:The preferred geometry of the coil for the cylindrical sensor from the models (a), and constructed cylindrical air cored sensor (b)

Once the cylindrical sensor was built, Figure 6.44, a two-dimensional (2D) axial symmetry FE sensor model was developed in COMSOL taking full account of the final sensor geometry and the sample in order to determine the relative permeability [49, 164]. The magnetic field produced by a multi-frequency EM sensor acts on a ferromagnetic target in two modes; first it tends to magnetize the sample, which increases the coil's inductance. Second, the alternating current magnetic field also induces eddy currents in the sample, which tend to oppose the driving current and reduce the coil's inductance [14]. At a low frequency, the eddy currents in the sample are very weak; the contribution to the inductance change is mainly from the magnetisation of the sample and therefore the real inductance measured is related to the sample permeability. As the frequency is increased, the effect of the eddy currents becomes more dominant. Therefore, the real inductance versus frequency plot for the EM sensor has a plateau in inductance value at low frequency (1Hz -10Hz) in the region where the signal is independent of the electrical resistivity but dependent on the relative permeability of the sample. Therefore, the low field relative permeability value is determined from the experimental EM sensor measurement in that region.

An extremely fine physics controlled mesh was applied to the entire sensor geometry with refined mesh to the sample geometry to make sure the FE model of the cylindrical air-cored sensor is no longer mesh dependent. The exterior boundaries were set as magnetic insulation and the interior boundaries were set as continuity. The 2D cylindrical sensor complete mesh consists of 28699 domain elements and 983 boundary elements, as shown in Figure 6.47.

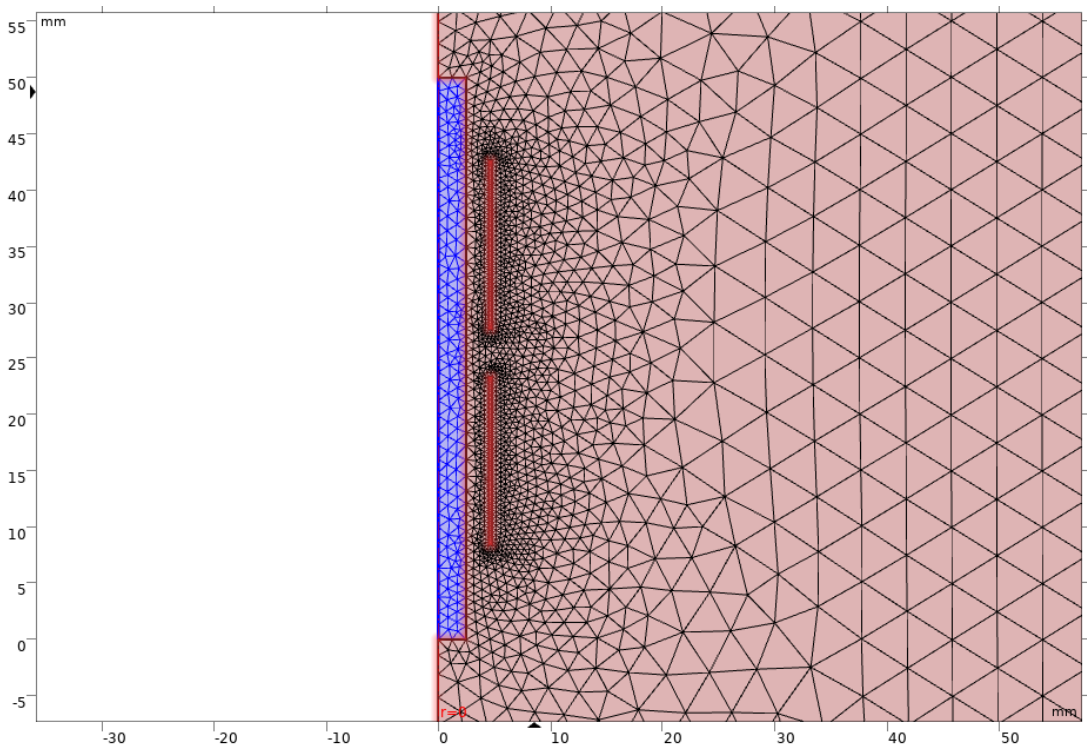

Figure 6.47: Meshing view of the 2D symmetrical FE model for the cylindrical sensor and sample.

The average magnetic field generated by the cylindrical EM sensor for a 0.17 wt.%C steel rod (ferrite + pearlite microstructure), predicted by the model and measured using a Gauss meter is 50 ±4 A/m. The magnetic field required to be applied into the sample to achieve saturation for a pure iron and a 0.17 wt.%C steel is > 10 kA/m [165] and > 25 kA/m (Figure 6.48) respectively.

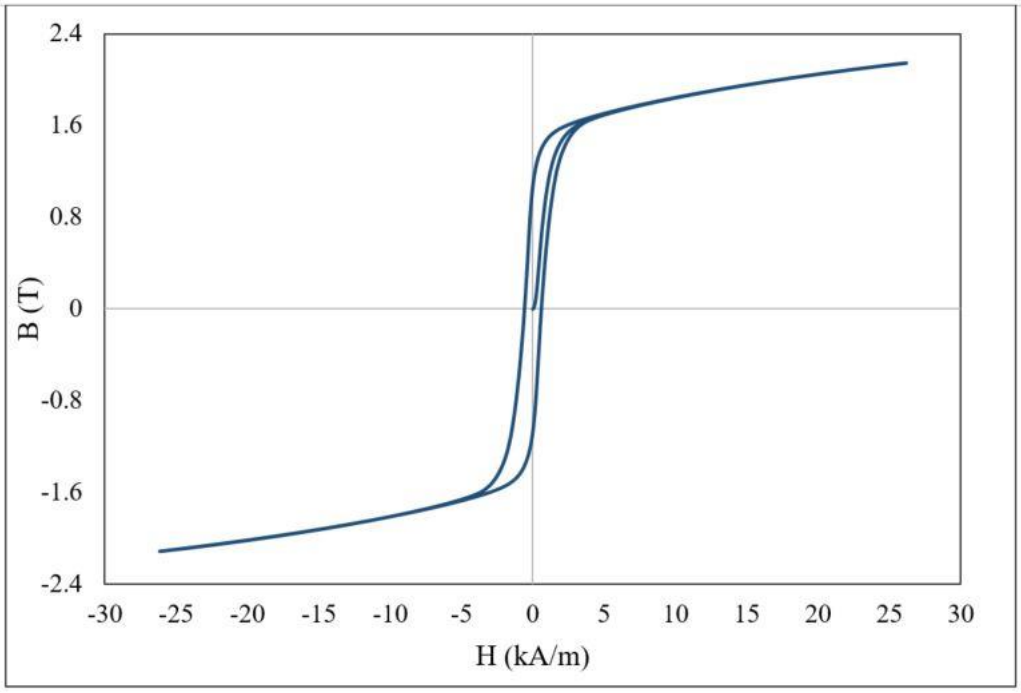

Figure 6.48: BH curve for a 0.17wt % C steel where the magnetic field applied into the sample to achieve saturation is > 25 kA/m

Therefore, the applied magnetic field to the sample in the cylindrical sensor is a very low field which corresponds to the Rayleigh region (i.e. very low field) where the permeability in this region can be described as the initial permeability [119]. The relative permeability values, determined by fitting the experimental EM sensor results with the FE model, for a 99.99% pure iron, 0.17 wt% C steel and 0.8 wt% C, are 350, 300 and 60 respectively. The results agree well (within 7.5%) with Thompson et al. [49] who reported the initial relative permeability of 0.17 wt% C and 0.87 wt% C for carbon steel as being 285 and 56 and L. Zhou et al. [22] who used a similar cylindrical sensor and reported the values as being 290 and 58.6.

The two-dimensional (2D) axial symmetry FE model was extended into a three dimension (3D) FE model in the AC/DC module for the DP strip samples, shown in

Figure 6.49. The modelling results were compared to the measured results for inductance to fit the resistivity and permeability in a least squared sense for the cylindrical- air cored sensor. Initially it was accomplished for samples with known permeability and resistivity values to account for minor differences between the model and experimental set up. The resistivity values of the samples were taken from the experimental measurements (presented in Section 5.6). The experimental measurement and modelling results are in good agreement, shown in Figure 6.50.

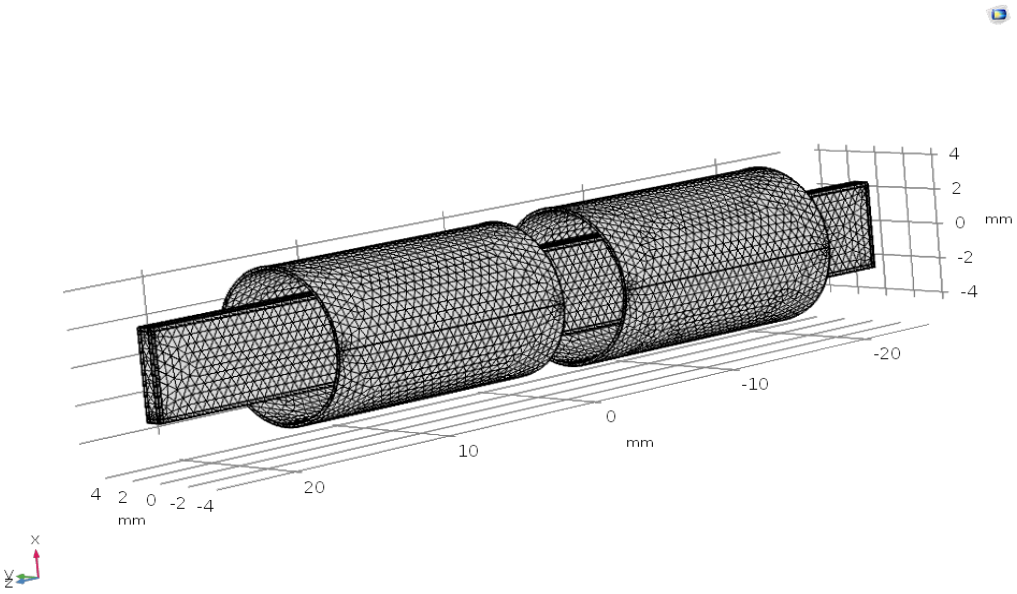

Figure 6.49: Meshing view of the 3D FE model for the cylindrical sensor and the strip sample, the fine mesh close to the sample surface can be seen

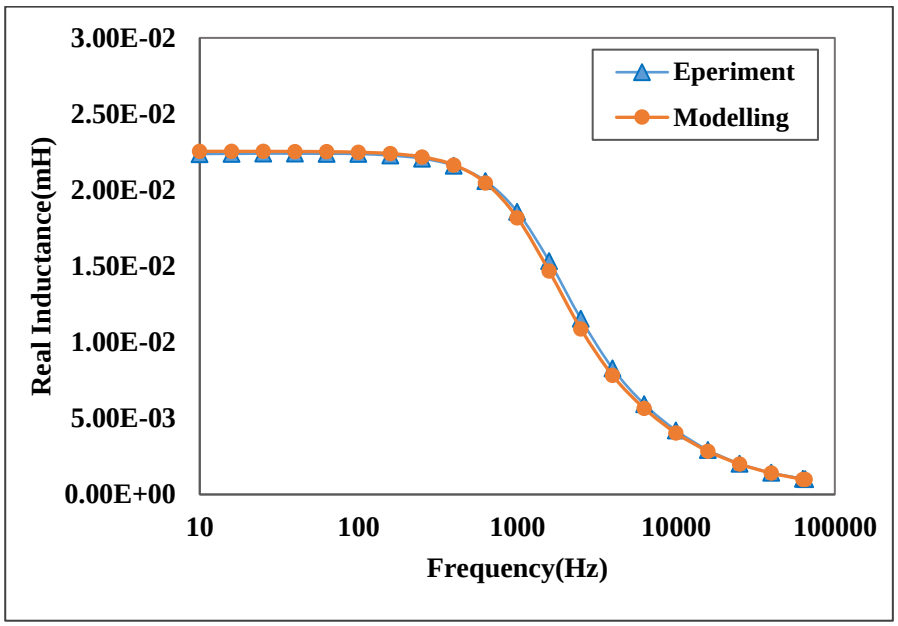

Figure 6.50: Comparison of the experimental measurement with modelling results for the DP1000CR 1.6mm, the experimental measurement and modelling results are in good agreement.

Table 6.5 lists the fitted relative permeability values for the commercial DP steels using the cylindrical air cored sensor. As it was earlier discussed, the applied magnetic field for the cylindrical EM sensor used in this work corresponds to Rayleigh region (the field is about 50±4 A/m) therefore, the low field relative permeability is determined using the cylindrical sensor.

Table 6-5: Electrical resistivity and fitted low field relative permeability values for commercial DP steels using the cylindrical sensor.

Sample	Electrical resistivity (10^{-7} Ω.m)	Fitted relative permeability
DP600CR 1mm	2.435 ± 0.007	120±2
DP600CR 1mmGl	2.455 ± 0.008	121±2
DP600CR 1.4mm	2.438 ± 0.008	120±3
DP600CR 1.5mm	2.524 ± 0.005	118±2
DP600HR 4mm	1.998 ± 0.006	155±5
DP800CR 0.95mm	2.695 ± 0.005	112±2
DP800CR 1.6mm	2.727 ± .009	104±3
DP800CR 1.6mmGl	2.684 ± 0.016	106±3
DP800CR 2mmA	2.701 ± 0.005	105±3
DP800CR 2mmB	2.725 ± 0.008	102±3
DP1000CR 1mm	2.739 ± 0.007	98±2
DP1000CR1.2mmGl	2.818 ± 0.016	95±2
DP1000CR 1.6mm	2.786 ± 0.009	96±3

By comparing the magnetic permeability values presented in Table 6-5 and Figure 6.51, it can be seen that the DP600 samples, with lower martensite/bainite fraction distributed within ferrite, have a higher magnetic permeability value. There is a notable difference in the inferred permeability values between the DP600HR 4mm and the rest of the DP600 samples which is related to the average ferrite grain size of these samples (the average ferrite grain size of 10μm for the DP600HR 4mm and 6-7μm for the rest of the DP600 samples). The DP 1000 samples with larger amounts of martensite/bainite produce a lower magnetic permeability value. In addition, there is a

lot of scatter for the permeability value with ferrite fraction (the correlation coefficient for the best fit equation is very low, $R^2 = 0.6355$).

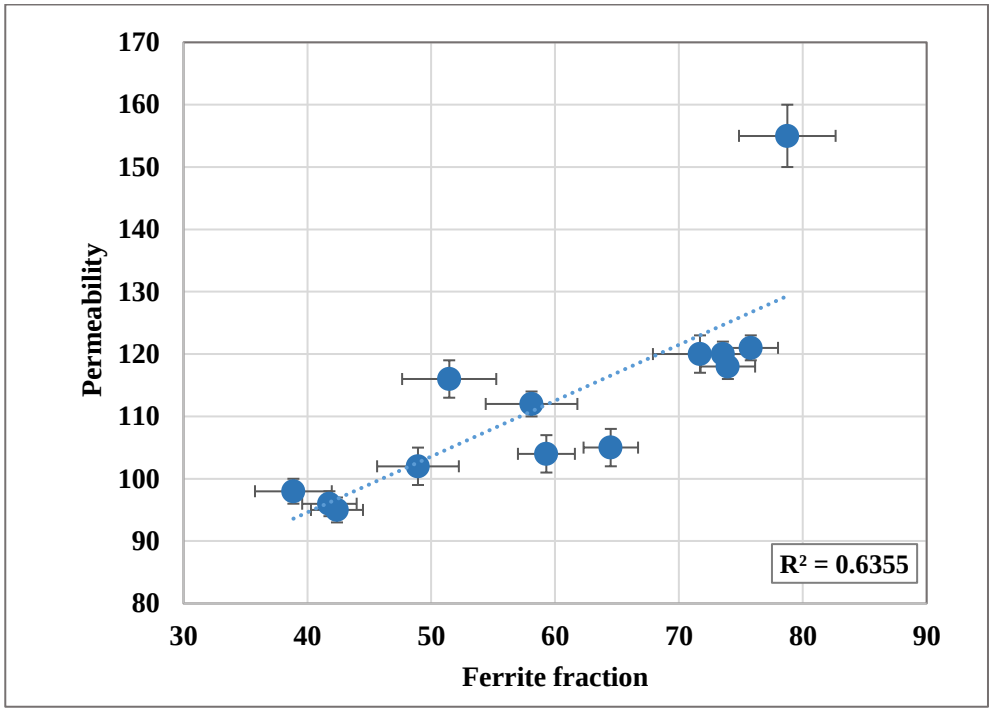

Figure 6.51: Low field relative permeability values (using the cylindrical sensor-sample FE model) against the ferrite fraction.

6.2.2.4.2 U-shaped EM sensor

The modelling work for the U-shaped sensor was carried out using COMSOL Multi-physics software using the three dimension FEM (3D) mode in the AC/DC model [149] to study the relationships between sensor signals (real inductance) and relative permeability of the strip steel sample using a sensor that is easily deployable for use on industrial strip samples. The model is similar to that reported in ref [150].

The U-shaped sensor consists of one excitation coil with 100 turns and two sensing coils with 86 turns with a bridge of 100mm, leg lengths and thickness of 56mm and 25mm respectively. The geometry and details of the sensor/sample were set to be the same as the experimental set up.

It is worth mentioning that the process of optimisation to select a suitable EM sensor was carried out using smaller U-shaped sensors (with a bridge of 10mm and 30mm) to measure the inductance. Full details of the process will be presented in Section 7.1 Chapter 7.

The FEM (3D) model of the U-shaped sensor consists of a U-shaped block representing the ferrite core of the sensor, an excitation coil and two sensing coils, as shown in Figure 6.52. A block of the steel sample with zero lift-off is placed under the sensor feet. The physics of magnetic fields was used in the model and the multi-turn coil feature was assigned to the excitation and sensing coils. Frequency domain (10Hz – 65 kHz), coil geometry of 100 turns for the excitation coil and 86 turns for the sensing coils were assigned to the study.

The mesh elements for the model is about 1.3 million where extra fine physics controlled mesh was applied to the entire sensor geometry with refined mesh to the sample geometry and sensing coil domains.

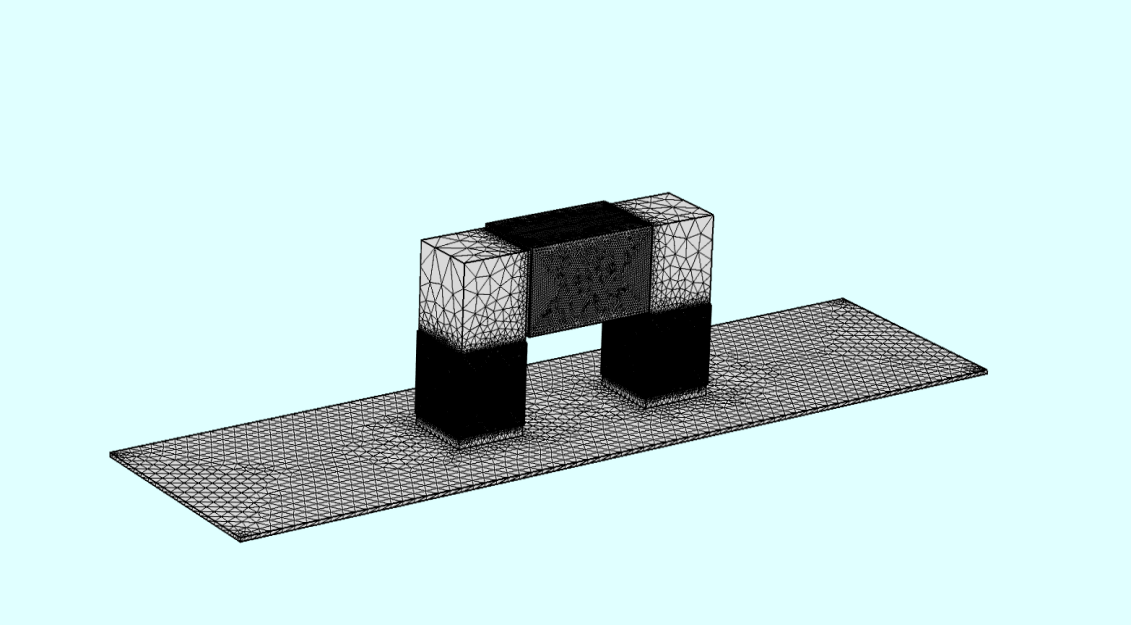

Figure 6.52: Meshing view of the 3D FEM model for the cylindrical sensor and the strip sample.

Initial calibration of the model was carried out by fitting the sensor model to sensor measurements for samples (e.g. 0.17 wt% C plate used as a calibration sample) of known relative permeability and resistivity to account for minor differences between the model and experimental system. The model was then used to determine the relative permeability (using the low frequency signal which is unaffected by eddy currents and hence resistivity) from the measured sensor signal for the samples of interest.

It is worth mentioning that the applied magnetic field for the U-shaped EM sensor used in this work corresponds to Rayleigh region (the field is 250±11 A/m, determined from the sensor sample model (Figure 6.53) and Gauss meter readings. Table 6.6 lists the fitted low field relative permeability values of the commercial DP steels using the U-shaped sensor.

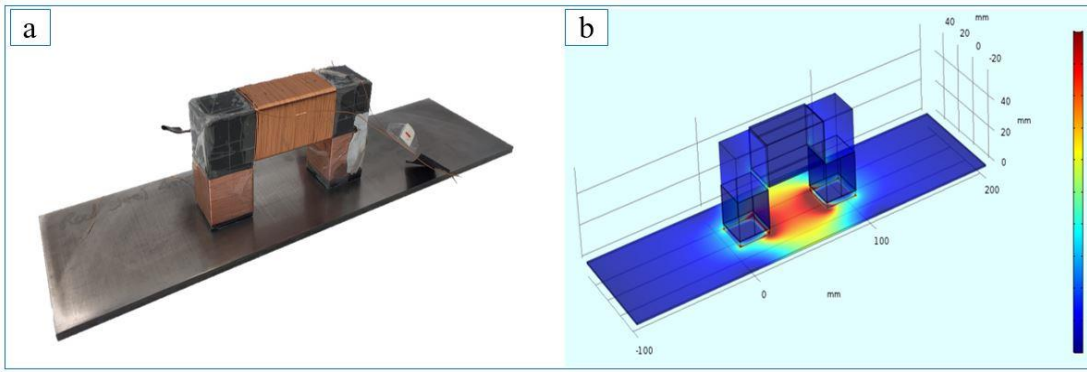

Figure 6.53: U-shaped EM sensor on the strip sample (a) and U-shaped 3D FE model to estimate the low field permeability of specimens where the colour scale represents the magnetic flux intensity (b).

Table 6-6: Electrical resistivity and fitted relative permeability values for commercial DP steels using U-shaped sensor

Sample	Electrical resistivity (10^{-7} Ω.m)	Fitted low field relative permeability (U-Shaped sensor)
DP600CR 1mm	2.435 ± 0.007	150±3
DP600CR 1mmGl	2.455 ± 0.008	154±2
DP600CR 1.4mm	2.438 ± 0.008	146±3
DP600CR 1.5mm	2.524 ± 0.005	147±2
DP600HR 4mm	1.998 ± 0.006	177±3
DP800CR 0.95mm	2.695 ± 0.005	130±2
DP800CR 1.6mm	2.727 ± .009	120±3
DP800CR 1.6mmGl	2.684 ± 0.016	125±3
DP800CR 2mmA	2.701 ± 0.005	122±3
DP800CR 2mmB	2.725 ± 0.008	118±4
DP1000CR 1mm	2.739 ± 0.007	108±2
DP1000CR1.2mmGl	2.818 ± 0.016	110±2
DP1000CR 1.6mm	2.786 ± 0.009	110±3

By comparing the inferred permeability values using the U-shaped sensor and the inferred permeability values using the cylindrical sensor, it can be observed that the U-shaped sensor determined a higher value of permeability for the commercial DP steel samples although similar trends for the samples can be observed, as shown in Figure 6.54. This discrepancy will be considered in Section 6.2.3 Chapter 6 and Section 7.2.1 Chapter 7.

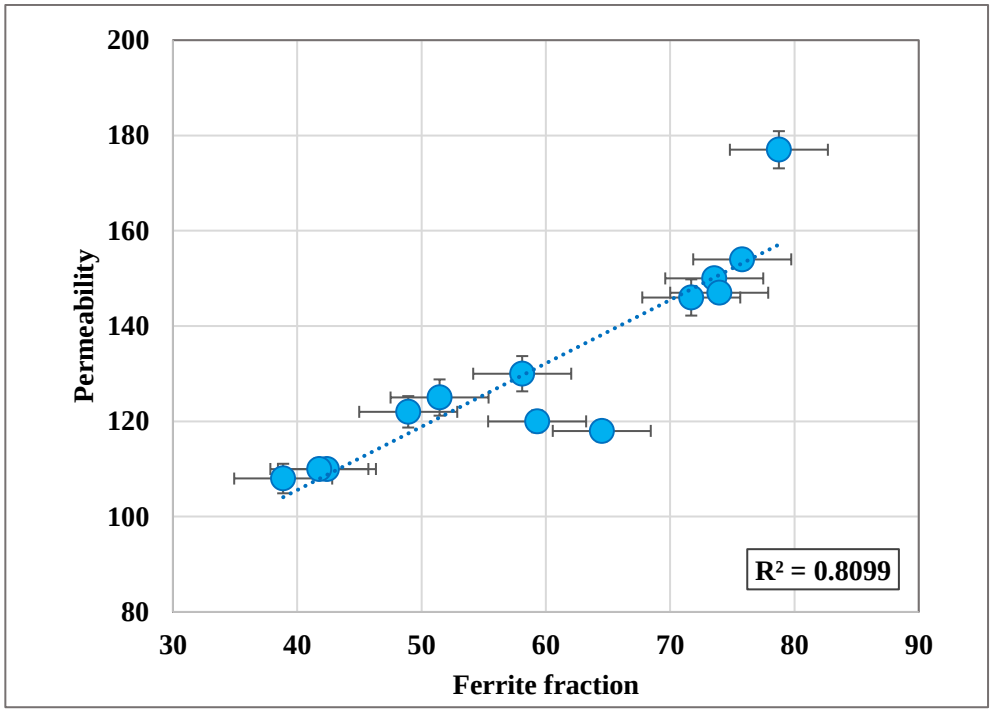

Figure 6.54: Determined low field permeability values (using the U-shaped sensor-sample FE model) against the ferrite fraction.

6.2.2.4.3 FE Modelling of Magnetic Microstructure

The optical microstructures from the DP steels were used in order to predict their relative permeability using a previously developed magnetic permeability – microstructure model for different phase balances that takes into account phase distribution. The description of the FE model using COMSOL Multi Physics software can be found in [63, 164]. In the model the microstructure of dual phase steel was assumed to be ferrite and martensite and the relative permeability values of ferrite and martensite were assigned as 320 and 56 respectively [49, 164]. Optical micrographs taken from the samples were converted to black-white binary images to represent the ferrite and martensite (note that any bainite present will be classified as martensite in the black and white images). The black-white images were imported into COMSOL using the built-in "image import function".

The sample was put into a uniform horizontal magnetic field with a magnetic potential of 1 (top) and 0 (bottom). In order to eliminate the demagnetising field and generate a uniform magnetisation the left and right boundaries of the sample were set as electric insulation [164]. The relative permeability can be calculated by dividing the magnetic flux flowing through the sample by the average magnetic field (H_{ave}) inside the sample. As can be clearly seen from Figure 6.55, in the sample with the higher volume fraction of ferrite, the magnetic flux can more readily pass through the microstructure region, whereas the martensitic is less favourable [61]. Therefore, FE modelling of magnetic microstructure can predict the permeability of any dual phase steel based on the phase fraction and distribution within the microstructure.

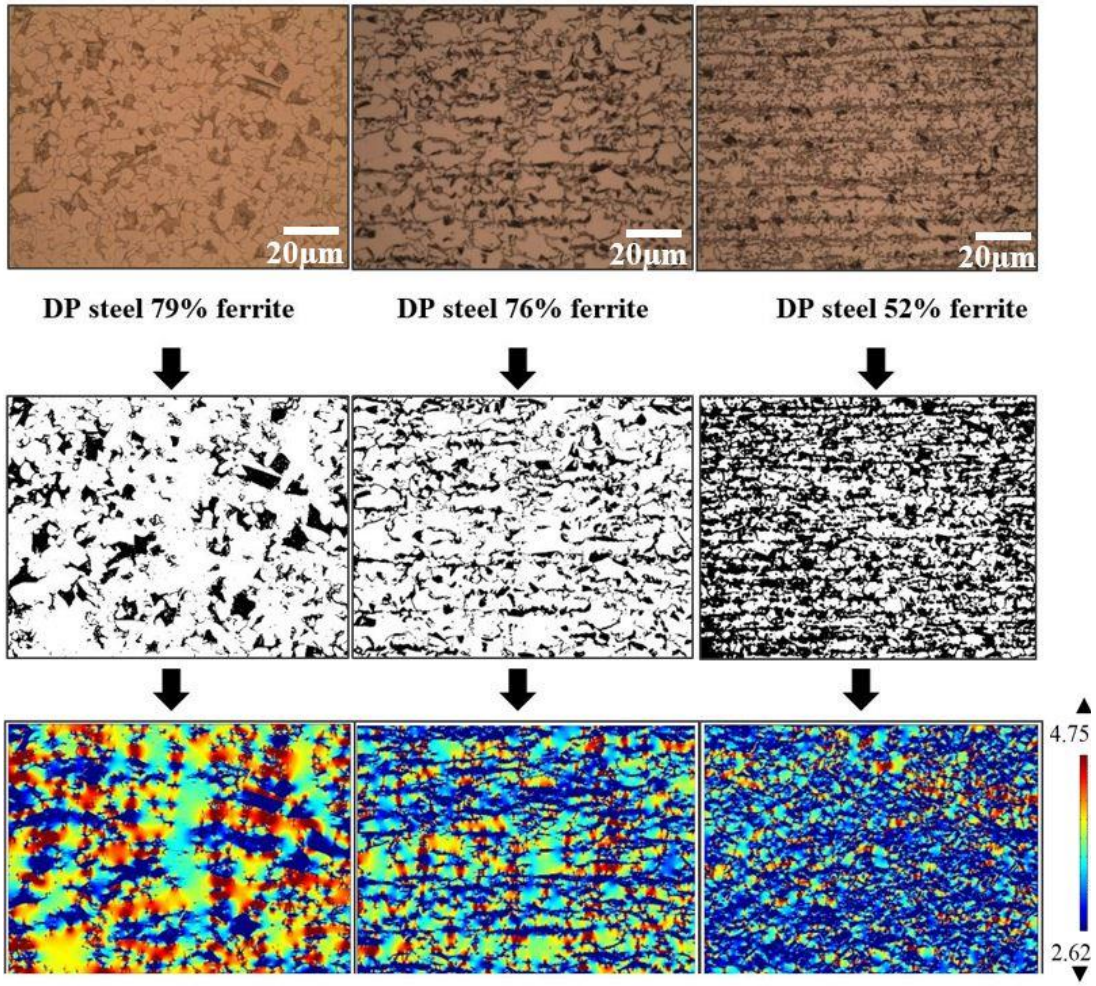

Figure 6.55: Optical micrographs of DP steel samples with different volume fraction of ferrite/martensite, which were converted to black-white binary images, the black-white images were imported into COMSOL. The sample containing the higher ferrite fraction shows the higher flux density, it can also be seen that the flux density is higher in the ferrite regions than in the martensite regions.

FE modelling of magnetic microstructure was used to predict the low field permeability of the commercial DP steels and the results are given in Table 6.7.

Table 6-7 : The permeability values derived from the magnetic microstructure FE model for the commercial DP steel samples

Sample	Magnetic Microstructure FE Model
DP600CR 1mm	206±8
DP600CR 1mmGl	210±9
DP600CR 1.4mm	203±8
DP600CR 1.5mm	211±3
DP600HR 4mm	229±13
DP800CR 0.95mm	159±3
DP800CR 1.6mm	146±15
DP800CR 1.6mmGl	127±8
DP800CR 2mmA	128±3
DP800CR 2mmB	174±8
DP1000CR 1mm	112±8
DP1000CR1.2mmGl	117±4
DP1000CR 1.6mm	116±5

The model shows an approximately linear relationship between the ferrite fraction and permeability indicating a significant effect of ferrite fraction on the permeability of the commercial DP steels however, as the ferrite grain size varies then this also needs to be taken into account. For instance, there is remarkable consistency in permeability value with ferrite fraction and ferrite grain size between the measurements by different techniques in this study but the DP800 CR 1.6mm and DP800 CR2 mm B with the smaller ferrite grain size ($3\mu m$) have shown high permeability values compared to the incremental permeability values, discussed in the previous sections. On the other hand, the permeability value of the DP600HR4mm sample is not a lot higher compared to the other DP600 steels (discussed earlier value measurements), therefore, it can be attributed to grain size.

Moreover, Figure 6.56 reveals that the correlation coefficient for the best fit line is high (R^2 =0.9754) as the effect of grain size on permeability is not taken into account. A new microstructure model taking account phase balance and grain size has recently been developed [55] and could be used to consider grain size in the DP steels in the future but was outside the scope/timescale of this project.

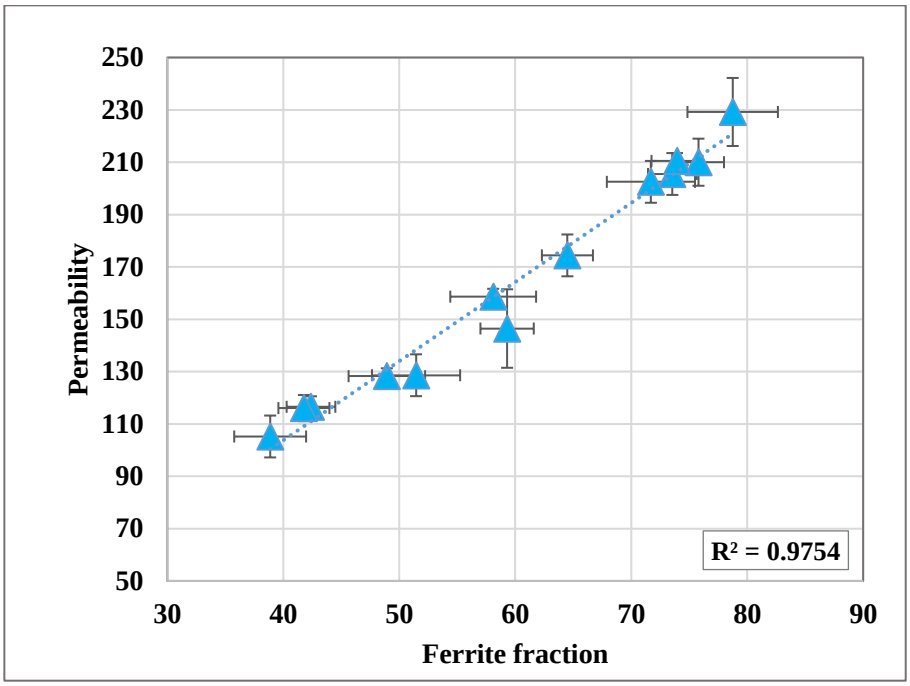

Figure 6.56: Relative permeability obtained from FE modelling of magnetic microstructure as a function of ferrite fraction for the commercial DP steel samples.

6.2.3 Effect of magnetic field on permeability

In Section 6.2.2.2 the three types of minor loop configurations employed to derive incremental permeability values were discussed; deviations from the initial

magnetisation curve *(μ_{IC})*, deviations from the major B-H curve *(μ_{BH})* and minor loop amplitude sweep *(μ_i)*.

There has been a lot of reports on empirical relationships between major and/or minor loop measurements and mechanical properties such as tensile strength and hardness [49, 50, 54] or use of major/minor loop assessment as inspection of cold rolling [118, 119], changes of magnetic minor hysteresis loops during creep [120], but there have been few reports on detailed correlation between the measured magnetic properties from major/minor hysteresis loops and microstructural parameters or interaction of microstructural features with domain processes for given applied fields. Liu et al. introduced a non-destructive way of selecting microstructural features of interest by minor loop measurements at a selected range of applied fields and explained the fundamental mechanism in terms of relevant domain processes [41].

It is very interesting to study the relationship between microstructural parameters, such as phase fraction or average grain size, and corresponding major/minor loop behaviour in DP steel. The BH system used in this work is able to apply a magnetic field *(H)* of any selected range of amplitude, within a specified power limit, and measure the applied field *(H)* and the induced magnetic field *(B)*. Therefore, the relationship between minor loop features and microstructural changes in commercial DP steel samples can be investigated. Figure 6.57 gives a plot of the incremental permeability and magnetic induction as a function of field for the DP600CR 1.4mm sample.

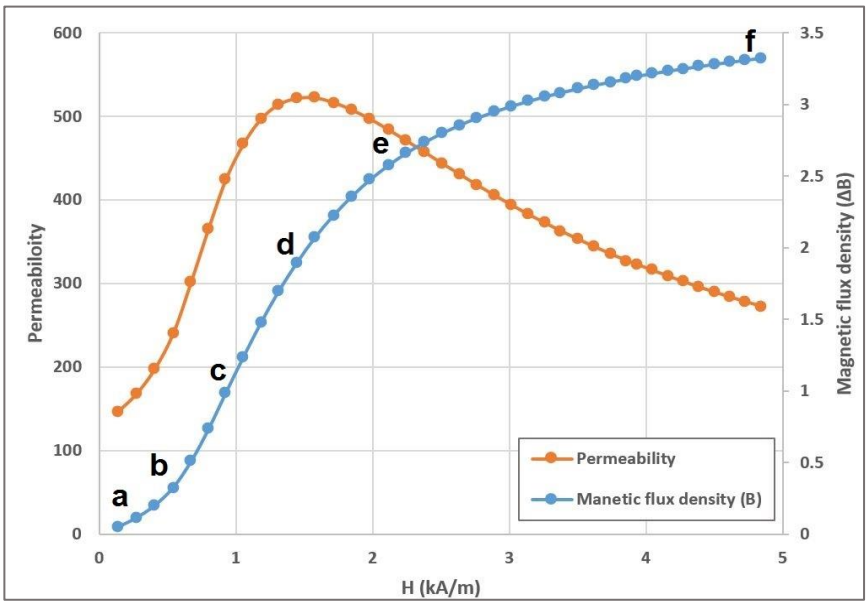
Permeabiloity
Magnetic flux density (ΔB)
H (kA/m)
Permeability
Manetic flux density (B)
a
b
c
d
e
f

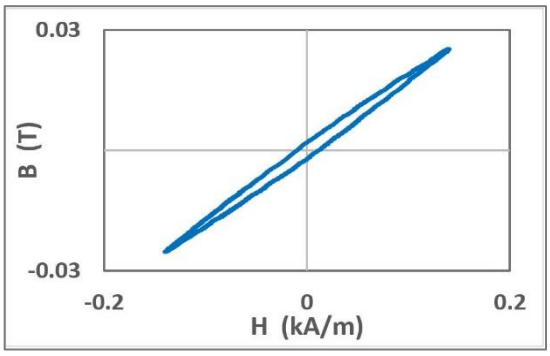
B (T)
H (kA/m)

(a)

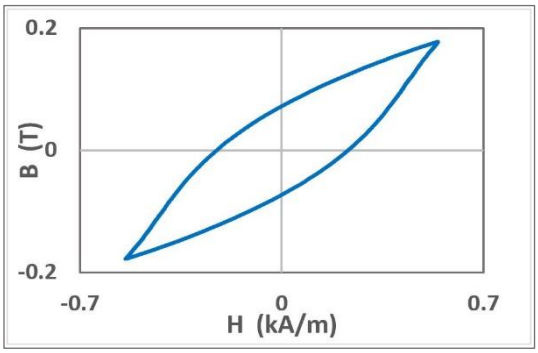
B (T)
H (kA/m)

(b)

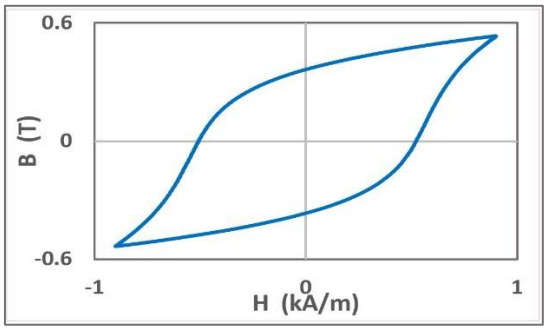
B (T)
H (kA/m)

(c)

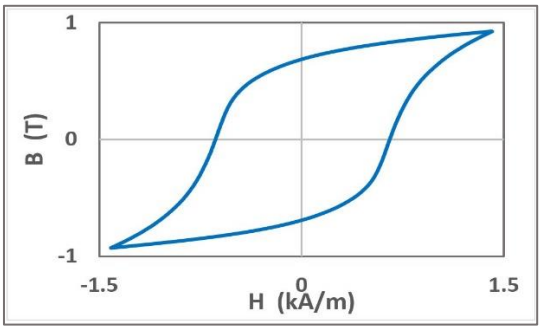
B (T)
H (kA/m)

(d)

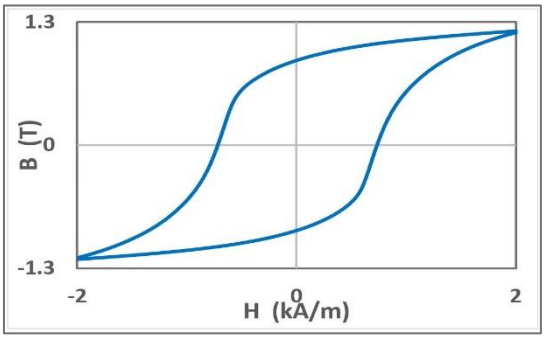
B (T)
H (kA/m)

(e)

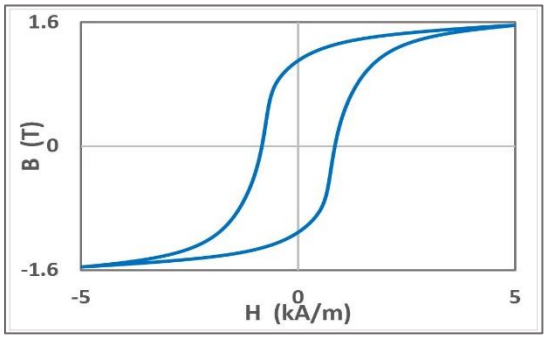
B (T)
H (kA/m)

(f)

Figure 6.57: Incremental permeability as a function of applied field and the minor loops corresponding to different magnetic flux densities.

It can be clearly observed from Figure 6.57 that the magnetic field amplitude and magnetic flux density constantly increase and the maximum variation in induction (Δ_B) is obtained at a field of 1400*A/m*. It is worth stating that the applied field constantly increases by around 200A/m in each step of measurement. Moreover, the incremental permeability increases with the field amplitude until reaching a maximum incremental permeability value of 522 at a field of 1400A/m and then drops.

This measurement was carried out for the all DP steel samples and Figure 6.58 shows the resultant incremental permeability as a function of applied field for the commercial DP steel samples.

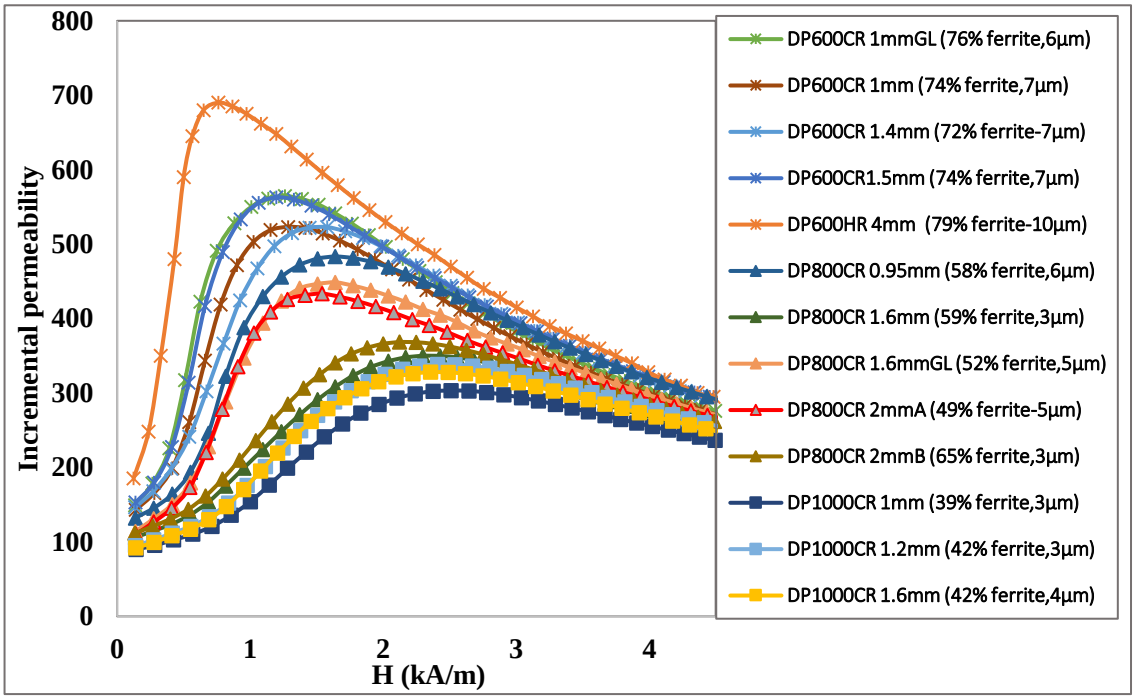

Figure 6.58: Incremental permeability as a function of applied field for the commercial DP steel samples

It can be observed from Figure 6.58, the curves follow a similar profile pattern, where the incremental permeability values for all the samples increase with the applied field amplitude until reaching a maximum value at a certain applied field amplitude (i.e. very close to the coercivity values) and then drop at higher applied field amplitude and converge to a similar permeability value. The initial gradient and the peak position for the samples are different and would allow them to be distinguished from each other.

The DP 600 samples show narrow peaks with high gradient, shifting the peaks to the right with lower gradients for DP 800 samples and further shifting to the right with broad profiles for the DP 1000 samples can be observed.

The principal assumptions of the hysteresis mechanism models of Kersten [166], Becker and Doring [167], and Kondorsky [168] is that the domain walls are rigid and planar in the demagnetised state since they do not experience any net force tending to move them therefore there is no reason for bending. It is worth clarifying that when the domain walls bend while being held on two pinning sites this results in a reversible change in magnetisation process. It continues until domain walls either encounter another nearby pinning features or it has expanded sufficiently to enable de-pinning and break away from the present pinning sites and moves discontinuously [166-168].

Three factors determine the amount of domain wall bending. Two of these factors are intrinsic and dependent on the properties of the material. The first one is the strength of the pinning sites and the second parameter is the domain wall surface energy [146, 147]. Differences between the surface energy and the pinning energy may result such that the domain walls will undergo more/less bending before breaking away from the sites. The third factor is extrinsic and depends on the magnetic field *H* [32, 146, 147]. Sufficient driving force provided by the applied field is required to give a domain wall potential to move and overcome the pinning sites. The energy is influenced by the

number density of domains, which is in turn affected by a number of microstructural features such as phase fraction, grain size, dislocation density and precipitates. If we assume f_{pin} is the minimum applied field H required to enable a domain wall to just overcome the pinning site of a microstructural feature [41] then it is apparent that one can characterise the microstructural feature distribution by correlating it with f_{pin} distribution [41]. The mean free path to domain wall motion is determined by the spacing between the effective pinning features and hence incremental permeability for a given applied field, H_a.

The predominant domain processes for small field ($f_{pin} > H_a$) *is* 180° domain walls oscillating between the microstructural features that are effectively pinning [41, 146, 147]. It is expected that for a given amplitude increment ΔH_a the number of depinned sites proportionally increases [41]. The microstructural features will be passed through by the domain walls with ($f_{pin} < H_a$). The broad and lower peak of the DP1000 samples indicate a broad distribution of f_{pin} , which in turn is associated with an expectedly broad spatial distribution of pinning features including martensitic lath boundaries (made of dislocation networks). The peak for the DP800 samples narrows and shifts to a lower H value. It is believed that this is due to the lower density of dislocations. Further shifting to the left for the DP600 samples can be attributed to a significant increase in the mean free path due to the higher ferrite fraction in DP600 which decreases f_{pin} hence lowering the H value giving a higher permeability.

The incremental permeability curves for all samples after reaching the maximum value, drop and converge to a lower value of permeability at high applied field amplitudes. Therefore, the convergence is the point at which saturation is approached and contributions from domain wall pinning sites are reduced, giving way to reversible domain rotation effects [146].

6.2.3.1 Effect of microstructural features on incremental permeability

It has been shown that the magnetic permeability is affected by microstructural features such as phase fraction, grain size, distribution of phase, precipitates etc. [55, 57, 164, 169, 170]. Among these microstructural features, phase fraction and grain size are particularly important factors in influencing the magnetic permeability values of DP steels [169].

The incremental permeability values measured through minor loop amplitude sweeps, make it possible to study the microstructural features of interest by examination of minor loop measurements at a selected range of applied fields. In addition, it would be interesting to see the effect of grain size on permeability and compare this parameter with phase fraction (i.e. ferrite fraction) as both affect magnetic permeability in DP steel.

Figure 6.59 shows the incremental permeability of the DP600 steel samples as a function of applied field. The main purpose of this comparison is to investigate the effect of grain size for the samples with almost similar range of ferrite fraction (72-79%). There is a notable difference in grain size between the DP600 4mm sample (average ferrite grain size of 10 μm) and the rest of the DP 600 samples (average ferrite grain size of 6-7 μm). From Figure 6.59 it is apparent that the DP600 4mm shows higher permeability value than the other steels and that this appears to be more related to the ferrite grain size rather than ferrite fraction: the DP600 CR 1 and DP600 CR1.5 mm samples have a range in amount of ferrite (72 - 76% ferrite) but show similar incremental permeability values whilst the DP600 4mm sample has only a little more ferrite (79% ferrite) but shows a significantly higher incremental permeability peak.

It is known that the ferrite grain size affects the magnetic properties in low carbon steel as the grain boundaries act as effective pinning points to magnetic domain movement [49, 50, 160].

On the other hand, dislocation density in martensite/bainite (e.g. martensitic lath boundaries) can be regarded as point pinning features in DP steel. Martensite lath boundaries are typically low angle and would have less strong pinning sites than ferrite with high angle boundaries. Therefore, increasing ferrite grain size means less effective boundaries, which corresponds to less strong pinning sites.

Therefore, for this range of ferrite fraction (72-79%) and range of ferrite grain size (6-10 μm), the effect of ferrite grain boundaries on permeability is more significant than the effect of ferrite/martensite fraction.

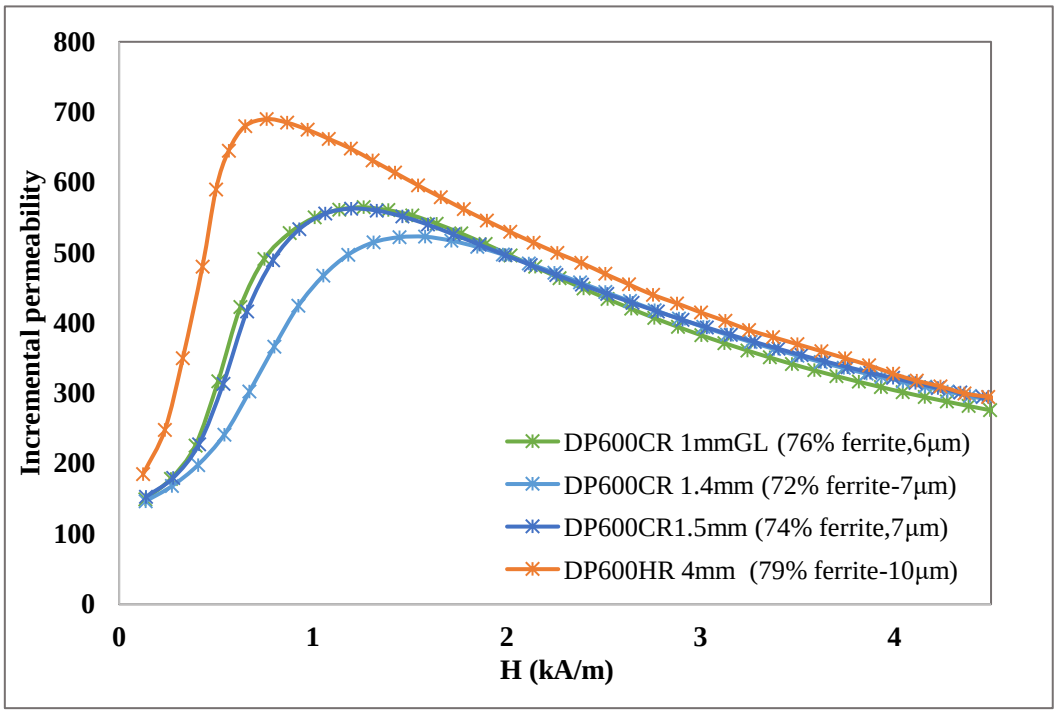

Figure 6.59: Incremental permeability as a function of applied field for the commercial DP 600 steel samples, the average grain size for theDP600 4mm is relatively larger (10 µm) in comparison with the rest of DP600 samples in this study (6-7 µm)

Figure 6.60 illustrates the incremental permeability of the commercial DP800 samples as a function of applied field. A similar scenario happens for these samples where the permeability values of samples at very low amplitude field (100A/m) are very close. The samples with relatively larger ferrite grain size (5-6 μm), reach the maximum incremental permeability at a lower applied field with higher gradient and the samples with smaller ferrite grain size (3 μm) reach a lower peak (compared with larger grain size samples) at higher field and show broader peak (lower gradient). Therefore, based on applied field, grain size and ferrite fraction show different behaviour patterns.

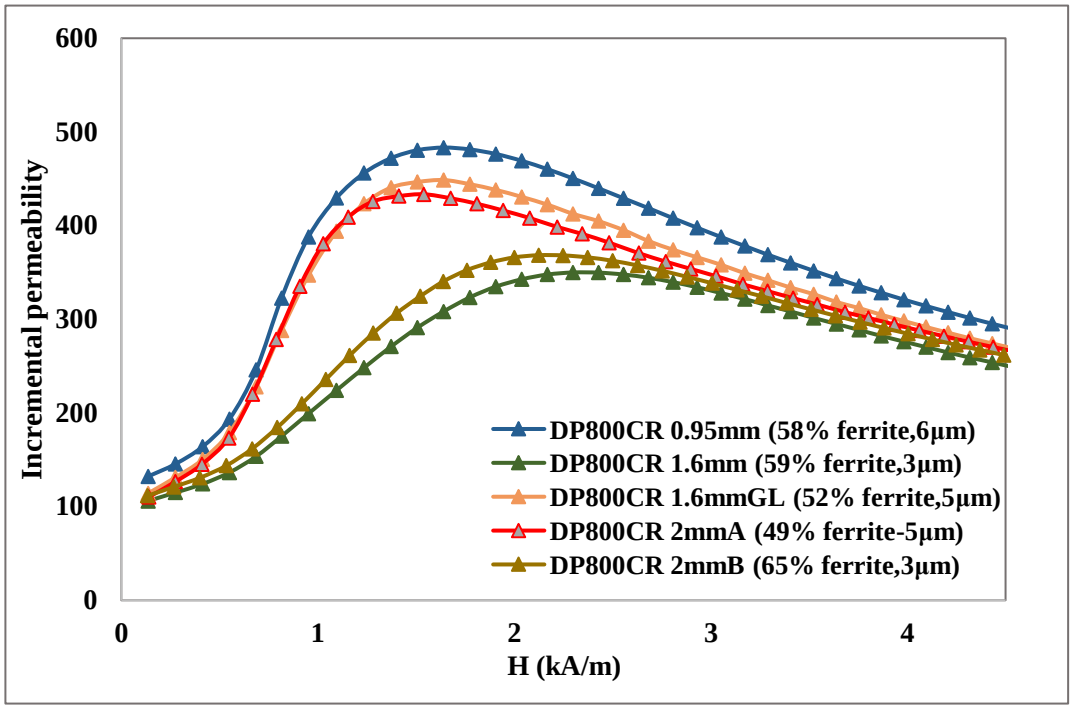

Figure 6.60: Incremental permeability as a function of applied field for the commercial DP 800 steel samples, the average ferrite grain size for the DP800 1.6mm and DP800CR2mmB is relatively smaller (3 µm) in comparison with the other DP800 samples in this study (5-6 µm)

7 EM sensor for Characterisation of DP Steel

It is desirable to be able to use magnetic properties to monitor the mechanical properties non-destructively. In steel, microstructural parameters affect the mechanical properties [1]. For DP steel, the mechanical properties are strongly influenced by ferrite fraction and grain size [1, 5, 152, 171-174]. Previous research has also shown the relationship between microstructural features and magnetic properties [19, 49, 50, 57, 62, 66, 170, 175, 176].

Coercivity measurement, discussed in Section 6.2.2.1 Chapter 6, can be used as a magnetic method to evaluate mechanical properties but coercivity values are not routinely obtained using an open loop (and hence deployable) system that can be used in the laboratory with varying thickness sheet or plate samples, and could be used with other complex shapes with appropriate modeling.

This chapter proposes using an electromagnetic (EM) sensor, suitable for use on strip samples, as a tool for non-destructive steel characterisation.

Firstly, the effect of ferrite fraction for the laboratory heat-treated DP600 samples, with the same thickness (1.4mm), on EM sensor signal (i.e. mutual real inductance) will be studied.

The second part of Chapter focuses on using the EM sensor for samples with a different range of thicknesses in commercial DP steel. Initially the effect of ferrite fraction on the EM sensor signal (real inductance) will be covered, followed by the effect of the thickness of the sample on the real inductance measurement. Modeling results and measurement results will be compared in the development of a calibration curve. At the end of this section, it will be shown that the low field permeability can be determined from the low frequency mutual inductance measured using a U-shaped sensor for any sheet thickness using a calibration curve. The relationship between low field permeability and tensile strength results allowing the tensile strength to be predicted from the EM sensor.

7.1 EM sensor response to uniform thickness

7.1.1 U-shaped EM sensor optimisation

The heat-treated DP600 samples were used to investigate the correlation between ferrite/martensite fraction and EM sensor signal for the samples with constant thickness.

It has been reported that the EM sensor signal of low frequency (10Hz) inductance increases almost linearly with ferrite fraction in the range of 35-73% for constant thickness (1.4mm) samples, which all have a similar grain size [22, 177].

A process of optimisation to select a suitable EM sensor to distinguish DP samples was carried out experimentally using three different U-shaped sensors including; a U-shaped sensor (Length=10mm and N=30 turns), U-shaped sensor (Length=30mm and N=50 turns) and U-shaped sensor (Length=100mm and N=100 turns), to measure the

real inductance in the heat-treated DP samples. More details about three U-shaped sensors are given in Table 7.1.

Table 7-1: Comparison of three different size of U-shaped sensor used to measure inductance for the heat-treated DP samples

U-shaped	Length (mm)	Height (mm)	Excitation coil (turns)	Sensing coil (turns)	Best fit equation (R^2)
U-10	10	10	30	15	0.5728
U-30	30	15	50	20	0.9166
U-100	100	56	100	86	0.9699

This was carried out at an early stage of the overall project before the U-shaped sensor FE model and knowledge of the variation of permeability with applied field was available. Further sensor optimisation was carried out with this knowledge at the latter stages of the project and this is described in section 7.2.1.

Figure 7.1 to 7.3 illustrate the measured real inductance of samples at a frequency of 10Hz against the ferrite fraction used three different U-shaped sensors. The results, an approximately linear increase in real inductance with ferrite fraction, is in agreement with that reported previously [22].

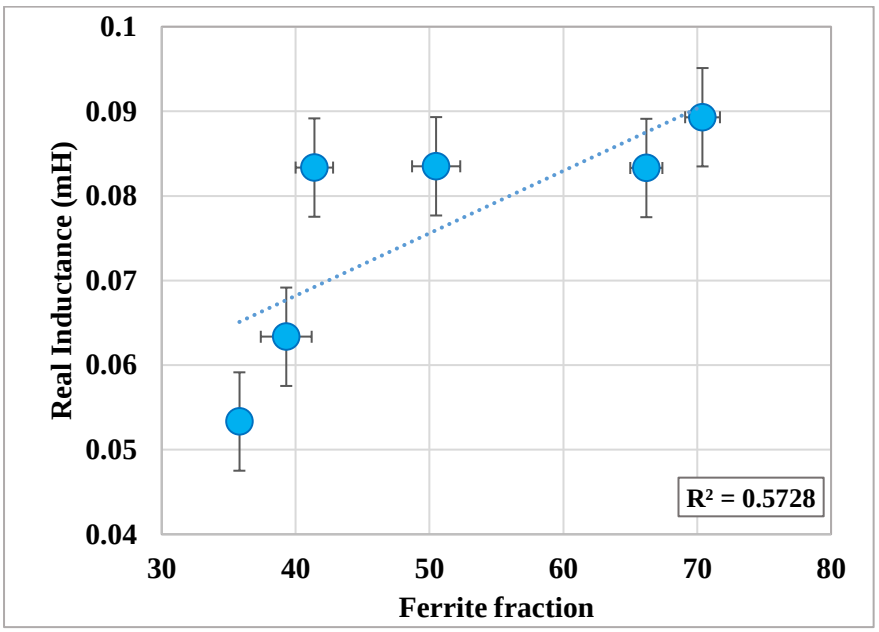

Figure 7.1:Real inductance changes with frequency measured by a U-shaped sensor (Length=10mm and N=30 turns) for the heat treated DP samples

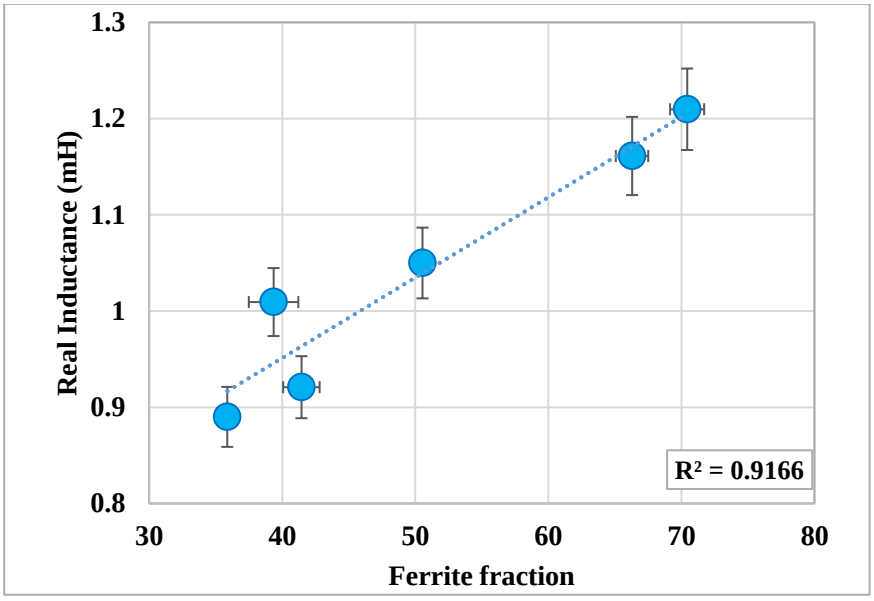

Figure 7.2:Real inductance changes with frequency measured by a U-shaped sensor (Length=30mm and N=50 turns) for the heat treated DP samples

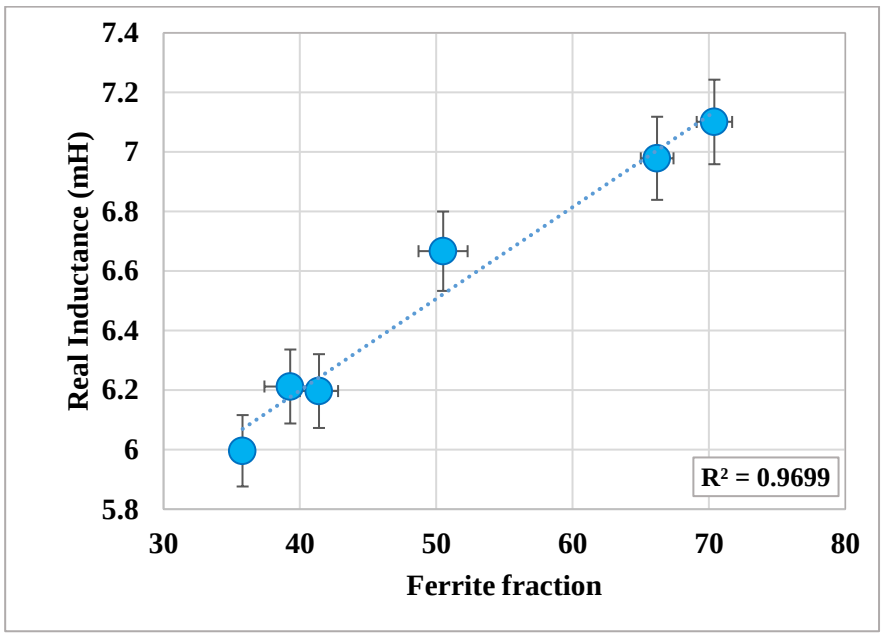

Figure 7.3: The real inductance measurements at a frequency of 10Hz versus ferrite fraction for heat treated DP samples. Using the U shaped sensor with the bridge of 100mm, leg lengths and thickness of 56mm and 25mm respectively

Repeatability of testing showed that these samples could be distinguished from each other. In addition, Figures 7.1 - 7.3 indicate that the sensor/sample configuration of the three sensors has an effect on the absolute values of inductance and ease of distinguishing between the samples, but that the relationship between real inductance (permeability) and ferrite fraction is similar using the three EM sensors.

The correlation coefficient for the best equation for that measurement showed a value of $R^2 = 0.5728$ and $R^2 = 0.9166$ for U-shaped (U-10) and U-shaped (U-30) respectively, shown in Figure 7.1 and Figure 7.2, compared to the U-shaped sensor (U-100), shown in Figure 7.3, with a correlation coefficient of $R^2 = 0.9699$, suggesting, in order to differentiate between the samples, the larger applied field associated with the larger sensor generated in sample/sensor (discussed in Section 6.2.3), gives better

differentiation therefore, the U-shaped (100mm) was selected in this study and used for the rest of the work.

It can be clearly seen from Figure 7.3 and Figure 7.4 that the sensor output can distinguish the different samples at a low frequency of around 10 Hz (i.e. plateau region). The real inductance values at low frequency are dominated by the relative permeability of the samples, which increases with increased ferrite percentage in the sample.

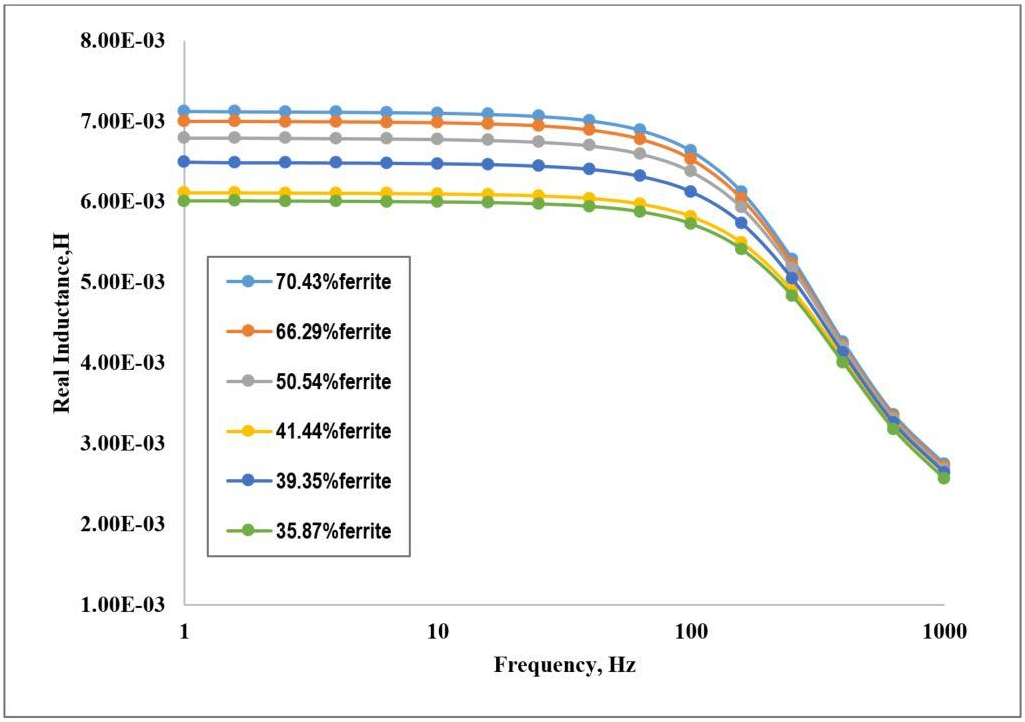

Figure 7.4: Real inductance changes with frequency for the heat treated DP samples measured by U-shaped sensor (Length=100mm, exciting=100 turns, sensing coil=86turns for each coil)

Figure 7.5 reveals that the EM sensor has the potential to assess the mechanical property (hardness) in DP steel sheet of constant thickness with little variance in grain

size. The EM sensor measurement also can be used to provide information on microstructural features in DP steel, in this case ferrite fraction as shown in Figures 7.2 and 7.3.

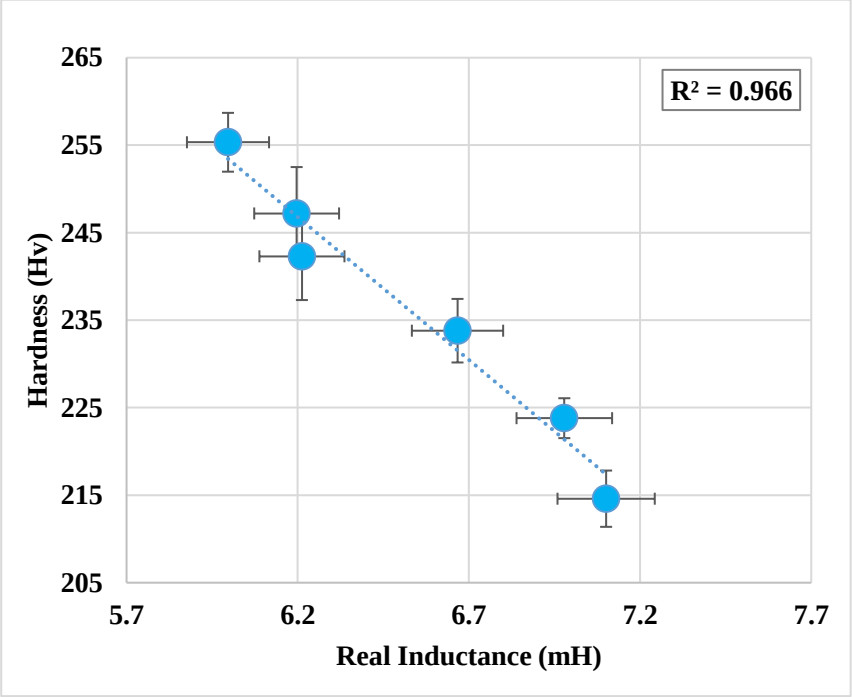

Figure 7.5: Hardness value as a function of sensor signal (real inductance) for the heat treated DP samples

7.2 EM sensor response to different thickness (Commercial DP steel)

The EM sensor measurements were carried out using the U-shaped EM sensor (U-100) described in Section 5.8 in Chapter 5. The EM sensor output, in terms of inductance versus frequency is shown in Figure 7.6 for the commercial DP steel samples.

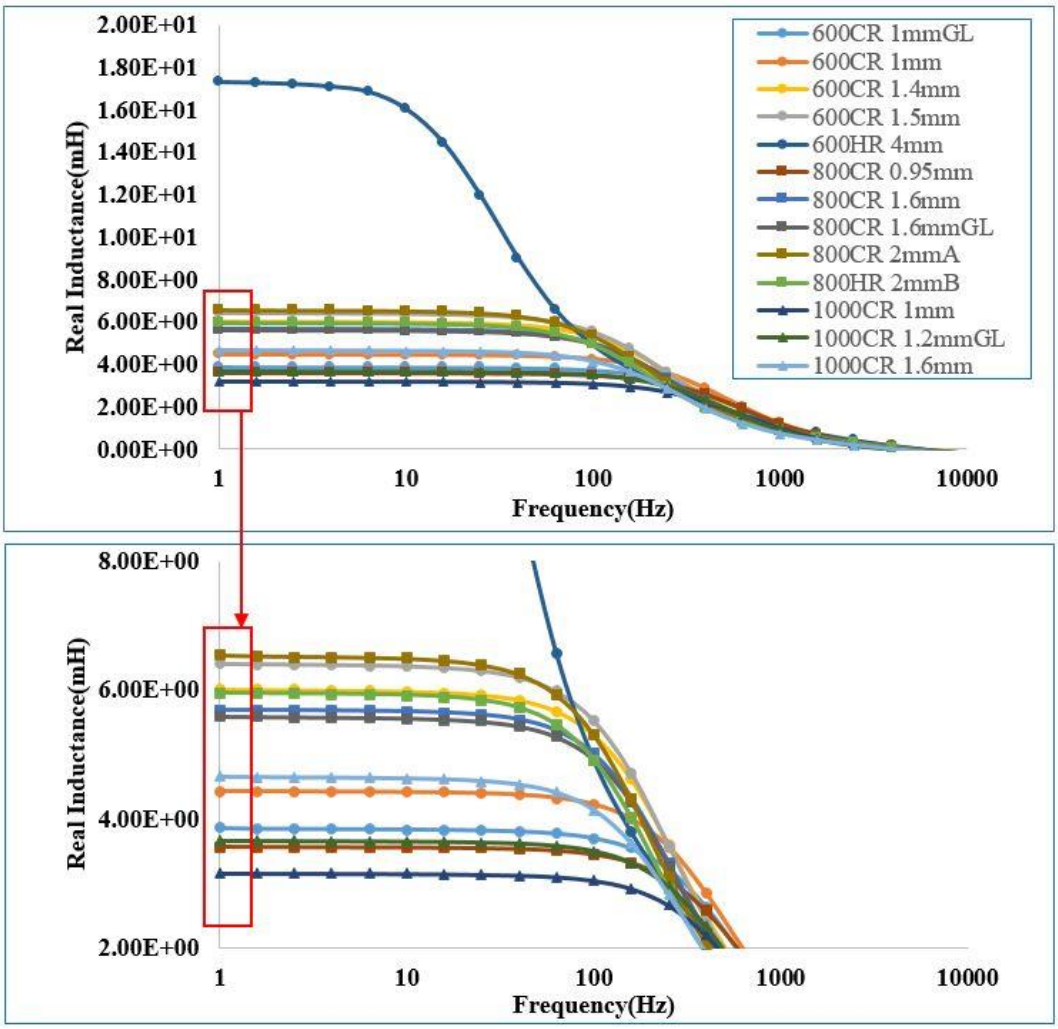

Figure 7.6: Real inductance versus frequency plot for the U-shaped EM sensor for the commercial DP steels with different thicknesses showing the plateau in inductance value at low frequency (1-10Hz).

It has been shown in Section 7.1 that the EM sensor signal of low frequency (10Hz) inductance increases almost linearly with ferrite fraction in the range of 35-70% for constant thickness (1.4mm) samples, which all have a similar grain size (Figure 7.2 and Figure 7.3). On the other hand, from Figure 7.7, it can be observed that for the commercial DP steel with different thicknesses, the inductance is strongly affected by the thickness of the sample.

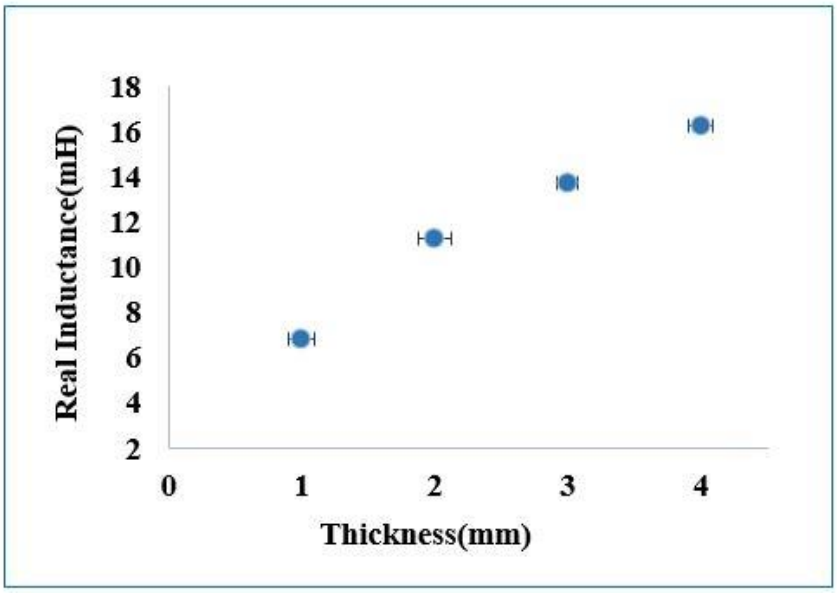

Figure 7.7:The real inductance measurements (using the U-shaped EM sensor at a frequency of 10Hz) for a commercial DP600 material (with 79% ferrite, average grain size 10 ±4μm) machined to thicknesses of 1mm to 4mm

The thickness of material affecting the sensor signal can be estimated by the skin depth (*Δs)* equation;

$$\Delta s = \sqrt{\frac{\rho}{\pi f \mu_0 \mu_r}} \qquad \textit{Equation 7-1}$$

where ρ is the resistivity of the conductor, f is the frequency, μ is absolute magnetic permeability ($\mu = \mu_0.\mu_r$). By using resistivity, $\rho = 2.1x10^{-7}\ \Omega.m$ (measured value for the DP600 steel) and permeability for DP steel of between 100 to 177, the value of skin depth for the operation frequency of 10 Hz was estimated to be approximately 6 mm, which is larger than the sample thicknesses. Therefore, a thicker sample shows a higher mutual inductance sensor response as effectively more material is being measured.

A calibration curve to consider thickness, for different DP samples, was constructed using the 3D finite element model developed in COMSOL Multiphysics (Section 6.2.2.4 Chapter 6) as shown in Figure 7.8. Whilst the model does require a limited number of samples for validation once established it can also be used to consider sample geometry (to account for edge effects if limited size samples are available or cross width near edge properties need to be examined) as well as thickness changes for different grades if required.

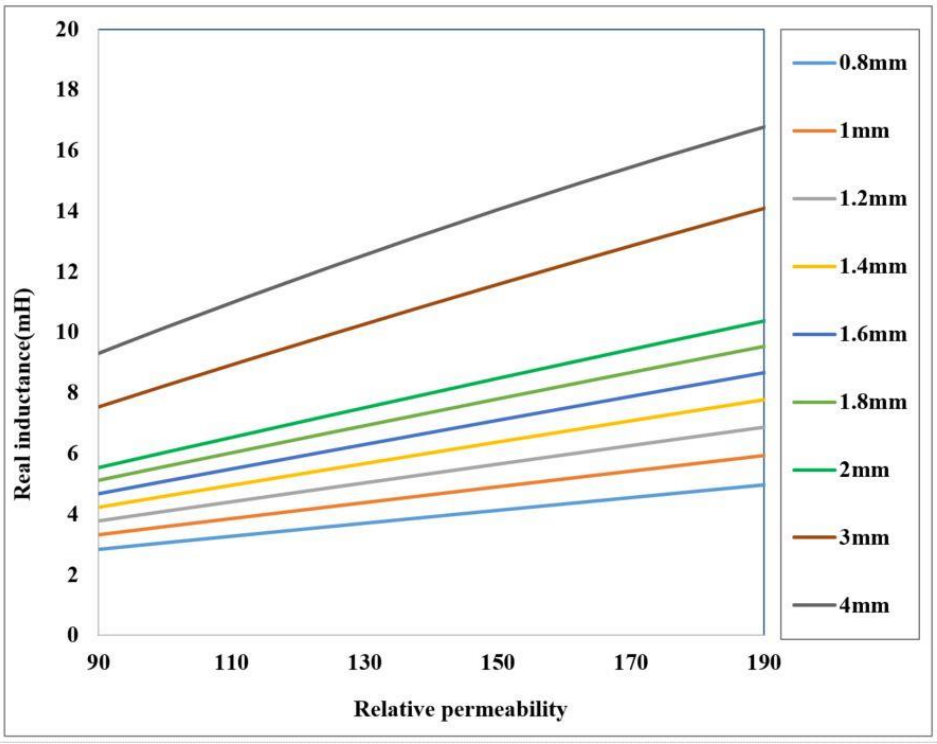

Figure 7.8: Calibration curves relating low frequency (10Hz) real inductance with permeability for different thickness samples, achieved from the U-shaped sensor-sample FE model

Figure 7.9 illustrates the calibration curves to obtain the low field permeability from the EM sensor mutual inductance value (discussed in Section 6.2.2.4.2) and measured sample thickness. The results from the model show good agreement with the experimental results.

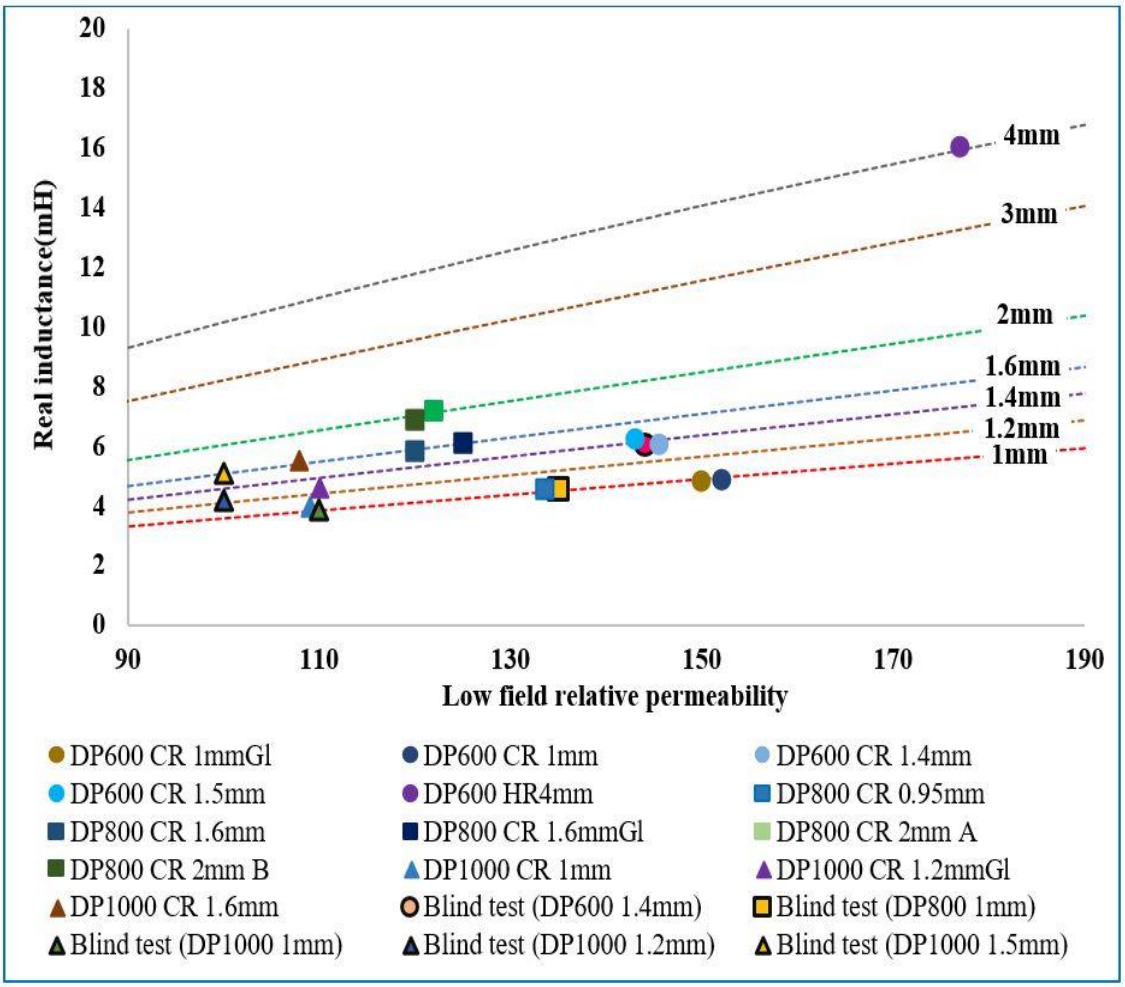

Figure 7.9: Calibration curves relating low frequency (10Hz) real inductance with permeability for different thickness samples. The dashed lines represent modelling results (for 1mm to 4mm strip thickness) and experimental data for commercial DP samples of different thicknesses are indicated by different points.

The permeability (determined from the U-shaped sensor-sample FE model) is plotted against tensile strength in Figure 7.10. The relationship between the relative permeability values and the hardness values of the commercial DP steel samples is given in Figure 7.11.

The results indicate that there is a general correlation between permeability and tensile strength/hardness for the commercial DP steels, i.e. a DP steel with higher volume

fraction of ferrite (and/or larger grain size) showing a higher permeability and lower tensile strength/hardness. The permeability value increases with an increase in ferrite fraction due to the lower fraction of magnetically harder martensite, effect of decreased dislocation density and lath / carbide interfaces (from martensite formation), easier reverse domain formation and domain wall motion taking place at a lower applied field in ferrite [49, 62]. The correlation in Figure 7.10 and Figure 7.11 are not linear but there is less scatter around a line of best fit, particularly for the DP800 grades, than in Figure 7.12 where permeability is only correlated with ferrite fraction.

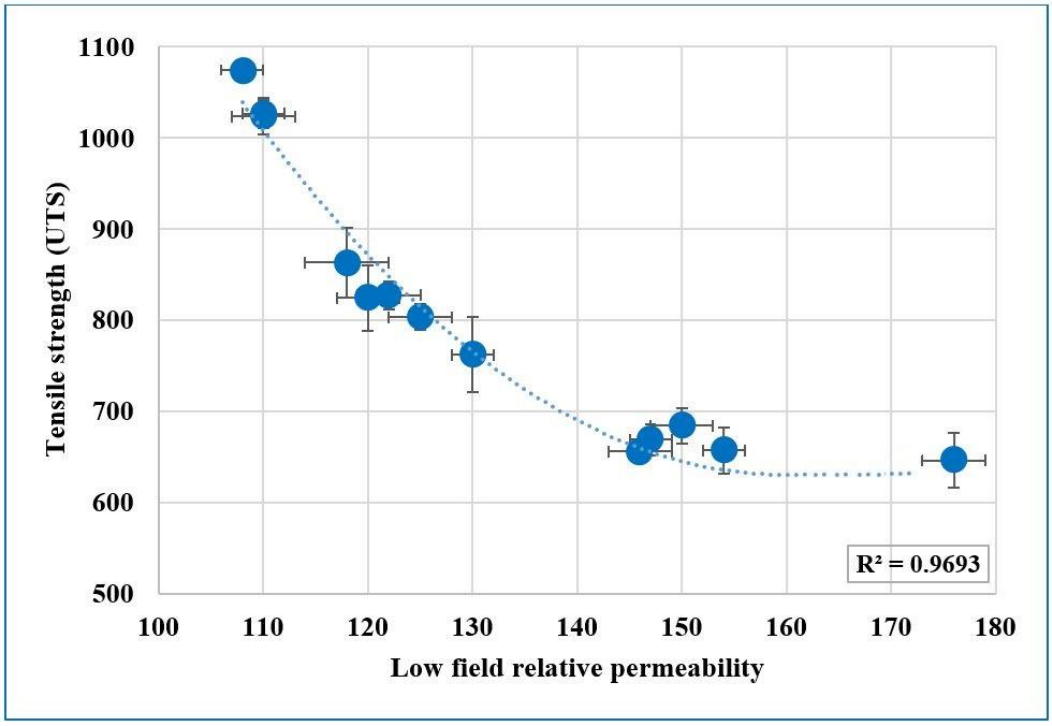

Figure 7.10: Determined low field permeability values from the U- shaped sensor-sample FE model for the commercial DP600, 800 and 1000 steels plotted against tensile strength.

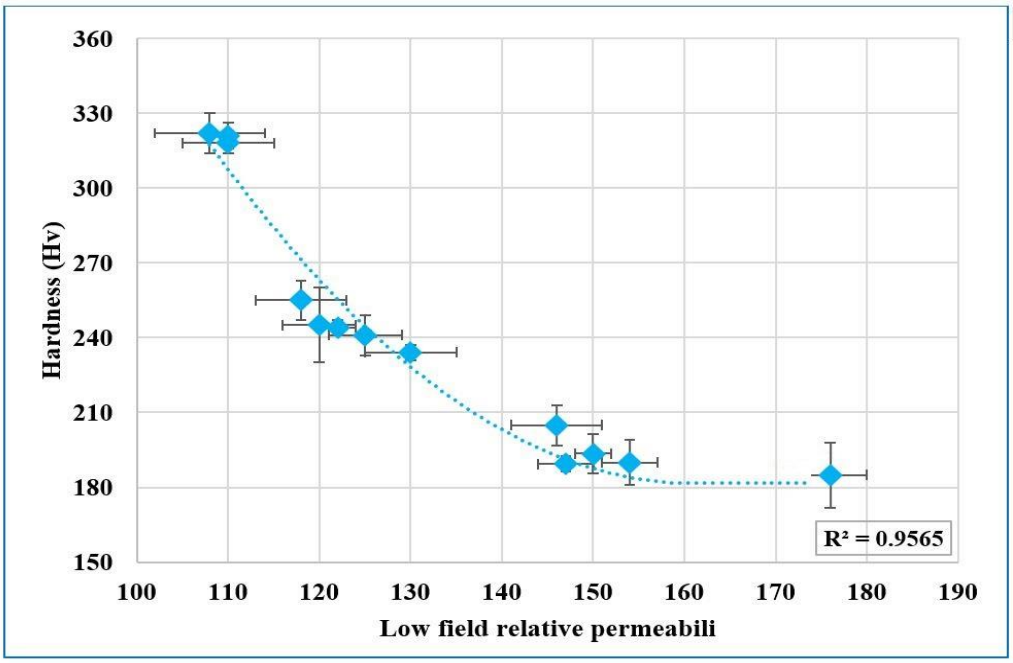

7.11: Determined low field permeability values from the U- shaped sensor-sample FE model for the commercial DP600, 800 and 1000 steels plotted against hardness

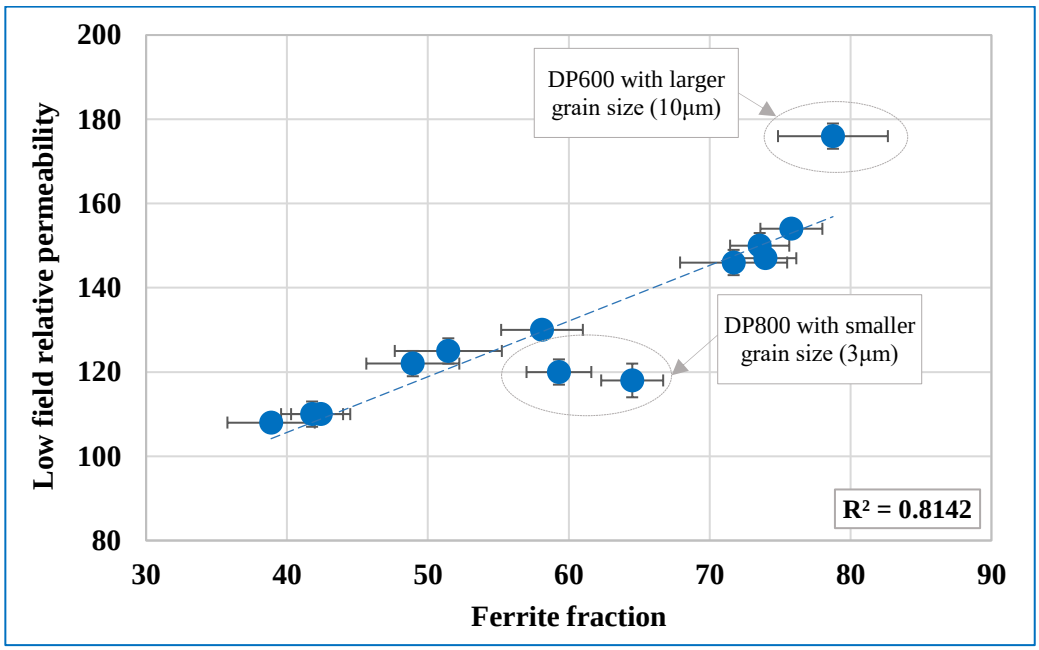

Figure 7.12: Variation of permeability (determined from the U-shaped sensor-sample FE model) with ferrite fraction for the DP steel, the marked samples showing lower than expected permeability due to the smaller gain size

In addition, information about the ferrite fraction in the steel can be obtained from the permeability if the grain size remains similar (for example for steels produced with a similar hot rolling process).

Figure 7.10 and Figure 7.11 reveal that the correlation coefficients for the best fit equation are very high, (R^2= 0.9693) and (R^2= 0.9565) for the tensile strength and hardness respectively, which show that the relative permeability is a good measure to predict tensile strength and hardness for DP steel samples. In particular, these two plots show that there is clear differentiation between the DP600 and DP800 samples. However, it is noted that differentiation for the samples with lower values of permeability (i.e. DP800 and DP1000) is less clear.

In order to evaluate the accuracy of the system (i.e. the EM sensor and the calibration curve), the tensile strength of five unknown DP steels with different thicknesses (i.e.

blind test) were quantitatively predicted. Figure 7.13 presents the measured value of tensile strength against the value predicted from the EM sensor system measurement. The accuracy in prediction of tensile strength was 90%, where the tensile strength for DP600 has been predicted almost 100% by the EM sensor system whilst the prediction is less accurate for DP800 and DP1000, although all blind test samples were correctly identified to grade type based on strength. This inaccuracy is believed to be due to the fact that there is limited difference in permeability values between DP800 and DP1000 grade for the magnetic field generated using this sensor making the measurement more susceptible to error, therefore a higher field would be beneficial since DP800 and DP1000 samples, consisting of higher fraction of martensite, require a higher field to be magnetised. It can also be related to the low field permeability state discussed in Section 6.2.3.

A case study to further increase the accuracy of the system, particularly for the commercial DP steels, in term of sensor design and FE model will be covered in the next section.

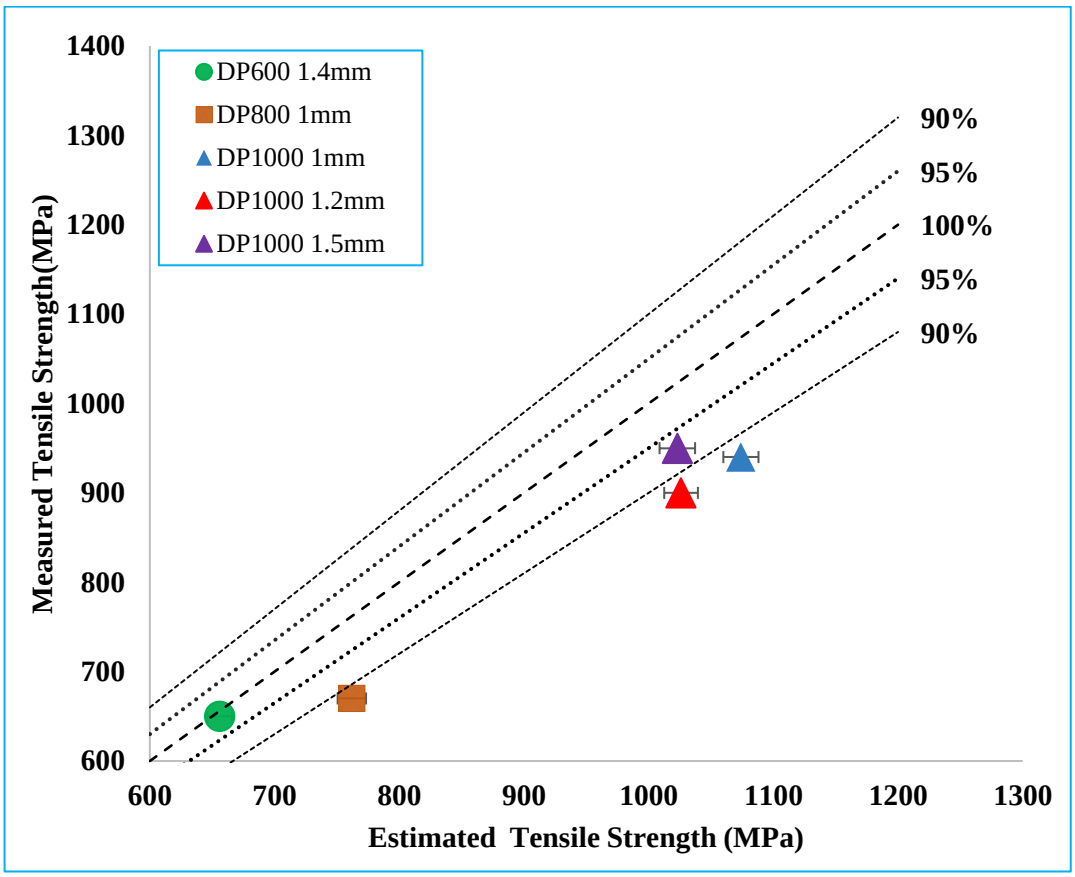

Figure 7.13: Measured value of tensile strength against the value determined from the EM sensor system measurement

It is also worth stating that permeability values are strongly affected by microstructural features and in this case phase fraction and ferrite grain size are the more significant parameters. It is possible that other microstructure combinations (for example grain size and precipitates, or cold work) could give a similar permeability value. Assuming that similar electrical conductivity values are also seen then the EM sensor would not be able to distinguish between the two steel microstructures. If different electrical conductivity values occur then analysis of the full EM sensor signal (i.e. inductance versus frequency) would indicate differences. However, in general during industrial applications the general type of steel is known allowing qualitative rules (such as knowing the main strengthening microstructural features) to be used to distinguish between samples. The ultimate aim for EM sensing technologies would be to

interrogate the full magnetic behaviour (varying magnetic field strength as well as EM sensor frequency) of a sample and to have the known pinning strengths of the domain pinning microstructural features to allow these different features to be identified. This is not yet possible.

7.2.1 Case study to increase accuracy of EM sensor

In Section 7.2 the potential of EM sensor to determine tensile strength in varying thickness commercial dual phase steels was studied. It has been shown that the low field permeability can be determined from the low frequency mutual inductance measured using a U-shaped EM sensor and a calibration curve to account for the effect of thickness and the strength can be predicted from the low field permeability.

In addition, in Section 6.2.3 Chapter 6, the influence of magnetic field on permeability was discussed and it was observed that the incremental permeability values increased with the applied field but with different gradients. In other words, the incremental permeability values increase with a higher gradient for the samples with higher permeability, and with lower gradient for the samples with lower permeability. Therefore, the incremental permeability curves against magnetic field show divergence at a certain field (i.e. very close to the coercivity values) and then drop at higher field and converge.

The initial optimisation process for the U-shaped EM sensor used in the work was carried out based on an experimental approach and the available ferrite cores available, as discussed in Section 7.1.1 resulting in the selection of a sensor consisting of one generating coil with 100 turns of 0.20mm insulated copper wire and two sensing coils with 86 turns of 0.16mm insulated copper). This sensor generates a maximum field of 250±12 A/m (measured by Gauss meter and FE model-point evaluation). This field corresponds to the range where the ‘low field permeability’ is being determined, which has been used to relate to the tensile strength. From Figure 7.11 and Figure 7.12 there is a clear differentiation between the DP600 and DP800 steels but differentiation for

the samples with lower values of permeability (i.e. DP800 and DP1000) is less clear which may cause error in characterisation. Therefore, in order to increase the sensitivity, consideration is needed to ensure that the generated applied magnetic field by the sensor is selected to give increased differentiation between the steels of interest. It is apparent from Figure 7.15 that operating the U-shaped sensor at a higher field (i.e. moving to the right side from the current operating condition) where the curves start to diverge, but before the peak in permeability, will give better differentiation between the samples.

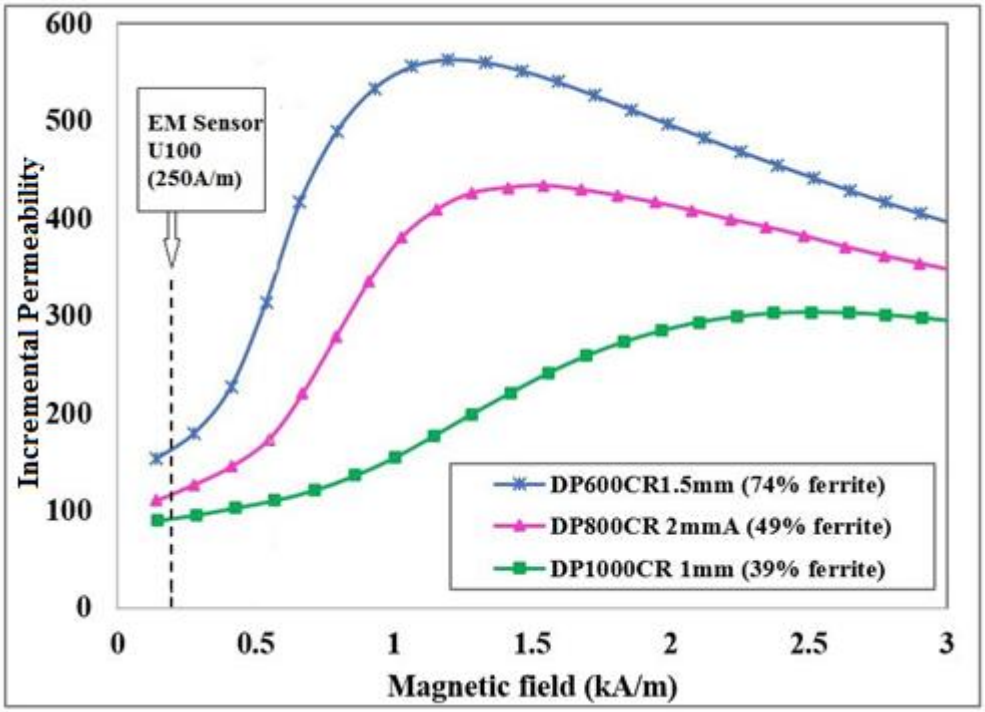

Figure 7.14: Incremental permeability as function of applied field for three commercial DP steel samples and the region where the U-shaped EM sensor (U-100) works to measure low frequency inductance.

Therefore, some modifications are required in order to improve the EM sensor to generate a higher field (higher than 250A/m). From Equation 3.11 and Equation 3.12 (Section 3.2 Chapter 3);

$$H = \frac{n I}{l}$$

$$L = \frac{\mu n^2 A}{l}$$

It is clear that the sensor parameters, including the number of turns in the inductor coils, length of the conductor that makes up the coils, cross sectional area and the electric current, can be changed to obtained higher inductance value.

FE U-shaped sensor modelling suggested for the current U-shaped sensor a field of 450-480 A/m can be obtained by increasing the number of turns in the excitation coil from 100 to 300 turns and increasing the diameter of the wire to 0.24mm. This was achieved for the same ferrite core size as used in the previous work with better control of the sensor build process.

Experimental measurement was carried with the modified U-shaped sensor (300 turns shown in Figure 7.15), along with modelling work to determine the low field permeability.

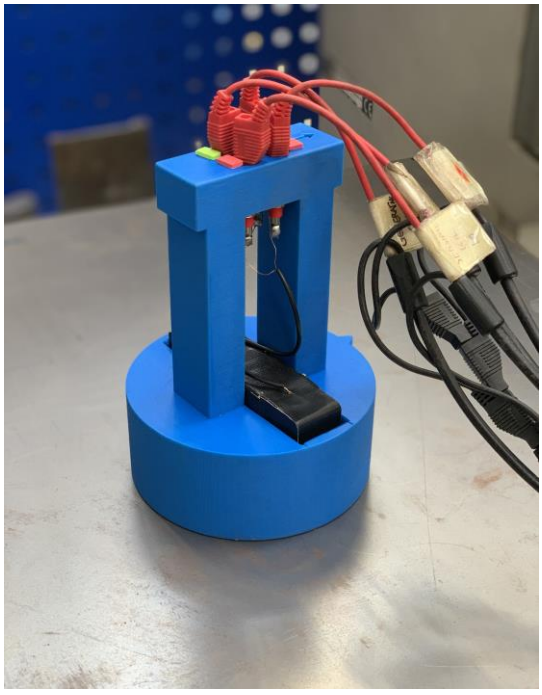

Figure 7.15: Modified EM sensor 300 turns in the sensor holder

Figure 7.16 presents the tensile strength against the inferred low field permeability values using the U-shaped sensor with 100 turns and the U-shaped sensor with 300 turns. It can be seen that the low field permeability increased, as expected. Therefore, the plot of permeability against tensile strength shifts to the right side (higher permeability values) and there is a decrease in the plot's gradient (as there is more differentiation between the steel grades in terms of permeability), which in turn makes the tensile strength determination more accurate. A new calibration curve was determined for this sensor using the sensor model and the sensor was used to measure the 'blind' DP samples. Figure 7.17 illustrates the improved accuracy of the modified sensor (average accuracy of 94%) for the tensile strength determination of blind test samples compared to the previous sensor (accuracy of 90%).

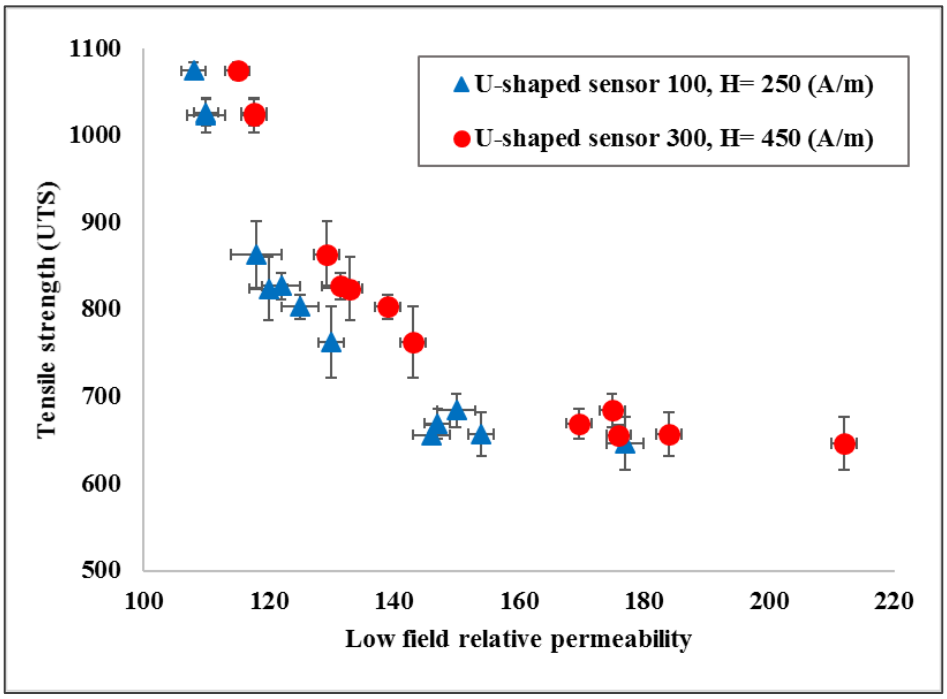

Figure 7.16: Plot of tensile strength against the inferred permeability values using the U-shaped sensor 100 (blue) and the U-shaped sensor 300 (red).

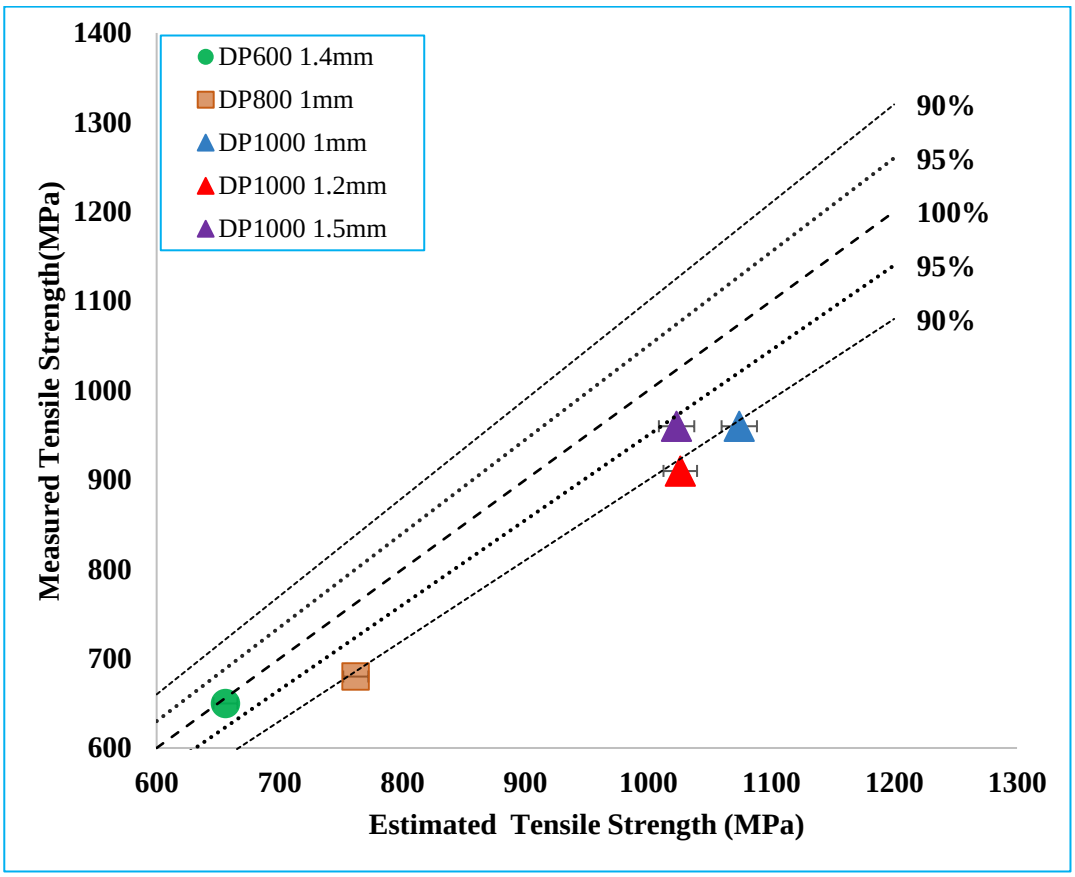

Figure 7.17: Measured values of tensile strength against the values determined from the modified U shaped EM sensor.

7.3 Summary

Results of previous studies and contributions from this research work have shown the potential of using EM sensors for characterisation of DP steels of any sheet thickness. The EM signal can be directly correlated to the mechanical properties for samples of constant thickness. However, the sensor signal cannot be correlated to strength directly if different thickness samples are assessed unless a calibration curve to account for thickness is generated. The calibration curve can be determined using an FE model for the EM sensor and sample and validated using a limited number of reference samples. Using the calibration curve the EM sensor signal, of low frequency (10 Hz) inductance, for any sheet thickness can be used to determine the material low magnetic field permeability value, which can then be used to determine the tensile strength of the material via the determined correlation between permeability and strength curve.

The EM sensor technique can scan and examine a relatively large area of the tested sample (i.e. both area and depth – when using low frequency measurements) compared with other methods such as hardness measurement. The EM equipment is also more readily available for in-situ measurements, particularly for thin sheet material where support is required for hardness measurements.

8 Conclusions

The main aim of this research work was to propose and develop an electromagnetic (EM) sensor system that can be used to assess the microstructure (and hence mechanical properties) of commercially produced DP steels (in particular phase balance and grain size) with a range of thicknesses in a steel works test house environment, specifically, it focuses on employing an EM sensor system in the prediction of ultimate tensile strength for DP commercial steels in any sheet thickness. The sensitivity of the magnetic properties, EM signals and tensile properties to changes in phase balance and ferrite grain size in DP steels has been assessed. The role of magnetic field strength on the magnetic properties for the DP steels and hence optimisation of the EM sensor has been considered. The other factors which can affect the signal measured by the EM sensor were also taken in account including sample thickness and lift off.

The main conclusions from the research are as follows:

In the area of the relationship between EM signal, permeability, microstructure and phase balance:

- Multi-frequency electromagnetic (EM) sensors are sensitive to both changes in relative magnetic permeability and resistivity of steel. Low frequency inductance,

can be related directly to the relative permeability, which can be related to microstructure. Moreover, the low frequency inductance is also influenced by the thickness of the material being tested.

- The low frequency (10Hz) inductance value measured using an EM sensor increases almost linearly with ferrite fraction in the range of 35-72% for constant thickness DP steel samples with a constant ferrite grain size.

- There is a decrease in the low frequency (10 Hz) inductance measured using an EM sensor with the hardness value for the heat treated DP steels with a range of ferrite fraction (35-72%), constant ferrite grain size and constant thickness.

- The effect of the martensite-ferrite phase balance on the EM sensor signal output (i.e. inductance), and hence low field relative permeability was studied for the DP steels. The results showed that the inductance value, and hence the low field relative permeability, increased with an increase in ferrite content (35-70%), due to the high permeability of ferrite compared with martensite (or bainite).

- In order to determine the magnetic field value generated by the EM sensor and experienced by the steel sample, both experimental and FE modelling studies have been carried out. The measured magnetic field in the cylindrical sensor (50±4A/m)

and the U-shaped sensor (250 - 450 A/m) corresponds to the low field permeability. This value is very similar to the initial permeability value obtained from B-H hysteresis loop measurements.

- A FE cylindrical sensor and FE U-shaped sensor model developed using COMSOL software model used to determine the low field permeability in the rod/strip samples (size of 50x4.95mm) and strip samples (size of 300x80 mm) respectively. The determined value of permeability by the U-shaped sensor showed a higher value than that determined by the cylindrical sensor, which is due to the fact that the U-shaped sensor generated a higher field, hence shows higher permeability.

In the area of the determination of permeability value and effective parameters on magnetic properties;

- Three types of minor loop configurations were used to derive incremental permeability values in the commercial DP steel samples including; minor loop deviations from the initial magnetisation curve, major hysteresis loop and minor loop amplitude sweep. It was found that although the permeability values are not precisely the same for the three sets of measurements similar trends for the samples can be observed which can indicate the underlying domain process are similar.

- Ferrite grain size and phase balance (ferrite-martensite fraction) affect the magnetic permeability in DP steel, this was seen for the different permeability measurements made (incremental permeability, major and minor loop permeabilities determined from the BH curve and low field permeability determined from EM sensor measurements). Since both tensile strength and magnetic permeability are influenced by ferrite fraction and grain size, a strong correlation between tensile strength and permeability was established.

- It was observed that the effect of ferrite grain size on permeability and strength for samples with 40% ferrite is less significant and for samples with more than 70% ferrite, is more dominant. This is related to the effective change in number of domain pinning sites with the change in ferrite grain size in the different phase balance samples.

- The study on incremental permeability showed that the effect of ferrite grain boundaries on permeability is more significant than the effect of ferrite fraction in commercial DP steels (for a range of ferrite fraction (72 to 79%) and ferrite grain size (from 6 to 10μm). this is believed to be due to the martensite lath boundaries are typically low angle and would have less strong pinning sites than ferrite with high angle boundaries. Therefore, increasing ferrite grain size means less effective boundaries which is corresponding to less strong pinning sites.

- It was observed that the incremental permeability against the applied magnetic field curves follow a similar profile pattern, where the incremental permeability values for all the samples increase with the applied field amplitude until reaching a maximum value at a certain applied field amplitude (i.e. very close to the coercivity values) and then drop at higher applied field amplitude and converge to a similar permeability value. The initial gradient and the peak position for the samples are different and would allow them to be distinguished from each other.

In the area of the relationship between permeability, tensile strength (hardness) and EM sensor application for DP steel;

- Coercivity measurements showed a strong correlation with the tensile strength and hardness for the DP grades (an approximately linear decrease in coercivity with higher tensile strength and hardness). The correlation coefficient for the best fit equations are R^2_{Hv} =0.9258 and R^2_{UTS} = 0.9333 for the hardness and the tensile strength respectively, which show that the coercivity is a good measure to predict tensile strength for DP steel samples. Since coercivity measurement in the lab generally requires measurement coils wound around the sample this magnetic measurement property was not considered to be appropriate for the deployable system for large strip samples.

- The correlation coefficient of permeability against tensile strength for the best fit equation in the commercial DP steels was very high (R^2 = 0.9696), which showed

that the relative permeability is a good measure to predict tensile strength for DP steel samples.

- It has been shown that the low field permeability can be determined from the low frequency mutual inductance measured using the U-shaped sensor for any sheet thickness using a calibration curve to account for the effect of thickness. As there is a relationship between permeability and tensile strength this allows the tensile strength to be predicted from the EM sensor low frequency mutual inductance.

- A calibration curve to consider thickness and sample geometry for different DP samples, was constructed using the 3D finite element model developed in COMSOL Multiphysics. Whilst the model does require a limited number of samples for validation once established it can be used to determine the low field permeability of any strip sheet thicknesses using the EM sensor.

- The accuracy of the EM sensor system (i.e. the EM sensor and the calibration curve), was evaluated for predicting the tensile strength of five unknown DP steels with different thicknesses (blind test samples). The samples were quantitatively predicted with an accuracy of 90%.

- A case study to increase the accuracy of the EM sensor system was carried out. The U-shaped sensor was modified to increase the magnetic field as it had been shown that within the low magnetic field range a small increase in applied field not only increased the permeability values for the DP steel, but also increases the difference in values between the samples. The modified EM sensor system quantitatively predicted the tensile strength with an accuracy of 94% in commercial DP steels

In conclusion, it can be said that the aims and objectives of this research project have been successfully met; and development of the EM sensor technique can be employed as a reliable method for non-destructive characterisation of DP steels. An on-going activity, detailed in the future work, is to provide a calibrate robust sensor to Tata Steel Jamshedpur for use in the test house laboratory to characterise DP steels.

9 Future work

Results of previous studies and contributions from this research project can be used to extend the work presented in this thesis further. Therefore, in term of EM sensor more work could be done in the following areas;

- A robust EM sensor based on the design presented in the final section of this thesis has been commissioned by Tata Steel Jamshedpur for use in their test house lab facility. The sensor and associated calibration curve, along with validation testing including with DP steels produced in Jamshedpur will be carried out. This provides a route to uptake of the system developed in this project for wider use.

- Extension of the technique for HSLA steels, IF steels, complex phase (CP) and TRIP grades can be considered. Complex steels and TRIP steels have more complex microstructures containing ferrite, bainite, martensite and/or retained austenite where the relationships to permeability and to tensile strength (and also any permeability – tensile strength relationship) are not as well documented. FE modelling of the U-shaped sensor to predict the relative permeability and to extend the calibration curve (thickness - inductance - permeability) to potentially the

lower expected values for these steels would be needed. Predictions of the tensile strength for CP and TRIP grades could then be carried out. As the permeability values of (tempered) martensite and bainite are very close interpreting and predicting the signals will be challenging. A range of samples needs to be studied to enable the development of a calibrated sensor that can provide quantitative measurements for the full range of CP and TRIP grades.

- Future work can be carried out to study the effect of second phase distribution and morphology on the EM sensor signal in DP steel and hence permeability in dual phase steel. The link between this and tensile strength also needs to be explored to see if non-uniform properties (e.g. variation in strength in the transverse and longitudinal orientations of the strip) can be determined.

- The effect of chemical composition and precipitates on permeability of DP steel can be investigated.

In term of modelling and permeability measurement;

- The FE modelling of magnetic microstructure in this work showed an approximately linear relationship between the ferrite fraction and permeability for DP steels with similar ferrite grain size indicating a significant effect of ferrite fraction on the relative permeability. The FE model has been updated to take into

account the role of ferrite grain size to predict relative permeability in low carbon (0.17 wt%C) ferrite and pearlite microstructures [55] and this could be extended to determine its accuracy for predictions in DP steels across a wider range of phase fractions. The experimental work indicates that ferrite grain size variations are less significant on permeability values when the second phase percentage is greater than about 70% and modelling work would be able to determine the extent of sensitivity.

In term of magnetic hysteresis loop;

- Low field permeability is governed by the mean free path to domain wall motion because at low field the predominant domain process is domain walls moving between pinning sites. At higher field, domain processes can be more complicated, particularly in DP steels. It would be interesting to study domain process in different phases (ferrite / martensite / bainite etc.) and then determine the combined effects according to the phase fraction.

10 References

[1] H. Bhadeshia, R. Honeycombe, Steels: microstructure and properties, Butterworth-Heinemann2017.

[2] A.P. Pierman, O. Bouaziz, T. Pardoen, P.J. Jacques, L. Brassart, The influence of microstructure and composition on the plastic behaviour of dual-phase steels, Acta Materialia 73 (2014) 298-311.

[3] S.-J. Kim, Y.-G. Cho, C.-S. Oh, D.E. Kim, M.B. Moon, H.N. Han, Development of a dual phase steel using orthogonal design method, Materials & Design 30(4) (2009) 1251-1257.

[4] T.S. Byun, I.S. Kim, Tensile properties and inhomogeneous deformation of ferrite-martensite dual-phase steels, Journal of Materials Science 28(11) (1993) 2923-2932.

[5] A. Bayram, A. Uğuz, M. Ula, Effects of microstructure and notches on the mechanical properties of dual-phase steels, Materials characterization 43(4) (1999) 259-269.

[6] T. Furukawa, M. Tanino, Structure formation and mechanical properties of intercritically annealed or as-hot-rolled dual-phase steels, Fundamentals of Dual-Phase Steels (1981) 221-248.

[7] Q. Meng, J. Li, J. Wang, Z. Zhang, L. Zhang, Effect of water quenching process on microstructure and tensile properties of low alloy cold rolled dual-phase steel, Materials & Design 30(7) (2009) 2379-2385.

[8] L.R. Bhagavathi, G. Chaudhari, S. Nath, Mechanical and corrosion behavior of plain low carbon dual-phase steels, Materials & Design 32(1) (2011) 433-440.

[9] N.H. Abid, R.K.A. Al-Rub, A.N. Palazotto, Micromechanical finite element analysis of the effects of martensite morphology on the overall mechanical behavior of dual phase steel, International Journal of Solids and Structures 104 (2017) 8-24.

[10] Q. Lai, L. Brassart, O. Bouaziz, M. Gouné, M. Verdier, G. Parry, A. Perlade, Y. Bréchet, T. Pardoen, Influence of martensite volume fraction and hardness on the plastic behavior of dual-phase steels: Experiments and micromechanical modeling, International Journal of Plasticity 80 (2016) 187-203.

[11] A. Marder, Deformation characteristics of dual-phase steels, Metallurgical transactions A 13(1) (1982) 85-92.

[12] M.P. Papaelias, M. Strangwood, A. Peyton, C. Davis, Measurement and modeling of the electromagnetic response to phase transformation in steels, Metallurgical and Materials Transactions A 35(13) (2004) 965-972.

[13] C. Davis, M.P. Papaelias, M. Strangwood, A. Peyton, Measurement of phase transformation in steels using electromagnetic sensors, Ironmaking & steelmaking 29(6) (2002) 469-476.

[14] R.J. Haldane, W. Yin, M. Strangwood, A.J. Peyton, C.L. Davis, Multi-frequency electromagnetic sensor measurement of ferrite/austenite phase fraction—Experiment and theory, Scripta Materialia 54(10) (2006) 1761-1765.

[15] X.J. Hao, W. Yin, M. Strangwood, A.J. Peyton, P.F. Morris, C.L. Davis, Off-line measurement of decarburization of steels using a multifrequency electromagnetic sensor, Scripta Materialia 58(11) (2008) 1033-1036.

[16] S. Johnstone, R. Binns, A. Peyton, W. Pritchard, Using electromagnetic methods to monitor the transformation of steel samples, Transactions of the Institute of Measurement and Control 23(1) (2001) 21-29.

[17] K.H. Lee, H. Kim, Y. Song, Electromagnetic method for analyzing the property of steel casing, Lawrence Berkeley National Lab., CA (United States), 1998.

[18] M.P. Papaelias, M. Strangwood, A.J. Peyton, C.L. Davis, Effect of microstructural variations on smart inductive sensor measurements of phase transformation in steel, Scripta Materialia 51(5) (2004) 379-383.

[19] C. He, Y. Huang, X. Liu, B. Wu, Evaluation of mechanical properties in medium carbon steel with a point mode electromagnetic sensor, Sensors and Actuators A: Physical 269 (2018) 126-136.

[20] C. Davis, M. Strangwood, A. Peyton, Overview of non-destructive evaluation of steel microstructures using multifrequency electromagnetic sensors, Ironmaking & Steelmaking 38(7) (2011) 510-517.

[21] S.J. Dickinson, R. Binns, W. Yin, C. Davis, A.J. Peyton, The Development of a Multifrequency Electromagnetic Instrument for Monitoring the Phase Transformation of Hot Strip Steel, IEEE Transactions on Instrumentation and Measurement 56(3) (2007) 879-886.

[22] L. Zhou, Non-Destructive Characterisation of Steel Microstructures Using Electromagnetic Sensors, University of Birmingham
2015.

[23] R.M. Bozorth, Ferromagnetism, IEEE Magnetics, The Institute of Electrical and Electronics Engineers, Inc., New York, 1959.

[24] J.R. Reitz, F.J. Milford, R.W. Christy, Foundations of electromagnetic theory, Addison-Wesley Publishing Company2008.

[25] P. Monk, Finite element methods for Maxwell's equations, Oxford University Press2003.

[26] D.J. Craik, Magnetism: principles and applications, Magnetism: Principles and Applications, by Derek J. Craik, pp. 468. ISBN 0-471-95417-9. Wiley-VCH, September 2003. (2003) 468.

[27] Adapted from A. G. Guy, Essentials of Materials Science, McGraw-Hill Book Company, New York, 1976.

[28] P. Hammond, Applied electromagnetism, Elsevier2013.

[29] C.W. D Jr, Materials science and engineering: an introduction, John Wiley & Sons. Inc.–New York, USA (2007).

[30] B.D. Cullity, C.D. Graham, Introduction to magnetic materials, John Wiley & Sons2011.

[31] R.F. Butler, R.F. Butler, Paleomagnetism: magnetic domains to geologic terranes, Blackwell Scientific Publications Boston1992.

[32] D. Jiles, Introduction to magnetism and magnetic materials, CRC press2015.

[33] S. Chikazumi, C.D. Graham, Physics of Ferromagnetism Oxford University Press on Demand2009.

[34] C. Kittel, P. McEuen, P. McEuen, Introduction to solid state physics, Wiley New York1996.

[35] A. Aharoni, Introduction to the Theory of Ferromagnetism, Clarendon Press2000.

[36] M. Hetherington, J. Jakubovics, J. Szpunar, B. Tanner, High-voltage Lorentz electron microscopy studies of domain structures and magnetization processes in pearlitic steels, Philosophical Magazine B 56(5) (1987) 561-577.

[37] N.W. Ashcroft, N.D. Mermin, Solid State Physics (Brooks Cole, 1976), Google Scholar (1993).

[38] R. Hall, Measurement of recovery and recrystallisation in interstitial free steels using electromagnetic sensors, University of Birmingham, 2018.

[39] J.M. Coey, Magnetism and magnetic materials, Cambridge University Press2010.

[40] S. Tumanski, Induction coil sensors—A review, Measurement Science and Technology 18(3) (2007) R31.

[41] J. Liu, J. Wilson, M. Strangwood, C.L. Davis, A. Peyton, Magnetic characterisation of microstructural feature distribution in P9 and T22 steels by major and minor BH loop measurements, Journal of Magnetism and Magnetic Materials 401 (2016) 579-592.

[42] R. Baldev, T. Jayakumar, V. Moorthy, S. Vaidyanathan, Characterisation of microstructures, deformation, and fatigue damage in different steels using magnetic Barkhausen emission technique, Russian journal of nondestructive testing 37(11) (2001) 789-798.

[43] J. Anglada-Rivera, L. Padovese, J. Capo-Sanchez, Magnetic Barkhausen noise and hysteresis loop in commercial carbon steel: influence of applied tensile stress and grain size, Journal of magnetism and magnetic materials 231(2-3) (2001) 299-306.

[44] J. Degauque, B. Astie, J. Porteseil, R. Vergne, Influence of the grain size on the magnetic and magnetomechanical properties of high-purity iron, Journal of Magnetism and Magnetic Materials 26(1-3) (1982) 261-263.

[45] H. Kwun, G. Burkhardt, Effects of grain size, hardness, and stress on the magnetic hysteresis loops of ferromagnetic steels, Journal of applied physics 61(4) (1987) 1576-1579.

[46] O. Perevertov, Influence of the residual stress on the magnetization process in mild steel, Journal of Physics D: Applied Physics 40(4) (2007) 949.

[47] O. Perevertov, Describing the effect of tempering on hysteresis curves of 54SiCr6 spring steel by the effective field model, Journal of Magnetism and Magnetic Materials 324(8) (2012) 1645-1648.

[48] C.S. Schneider, Effect of stress on the shape of ferromagnetic hysteresis loops, Journal of applied physics 97(10) (2005) 10E503.

[49] S. Thompson, B. Tanner, The magnetic properties of pearlitic steels as a function of carbon content, Journal of Magnetism and Magnetic Materials 123(3) (1993) 283-298.

[50] S. Thompson, B. Tanner, The magnetic properties of specially prepared pearlitic steels of varying carbon content as a function of plastic deformation, Journal of Magnetism and Magnetic Materials 132(1-3) (1994) 71-88.

[51] W. Yin, A. Peyton, M. Strangwood, C. Davis, Exploring the relationship between ferrite fraction and morphology and the electromagnetic properties of steel, Journal of materials science 42(16) (2007) 6854-6861.

[52] I. Petryshynets, F. Kovac, M. Sopko, J. Marcin, B. Petrov, Study of Microstructure and Texture Evolution in Grain-Oriented Steels Via Coercivity Measurements, IEEE Transactions on Magnetics 50(4) (2014) 1-4.

[53] J. Šternberk, E. Kratochvilova, J. Hřebík, A. Gemperle, Coercivity and Microstructure of Low-Alloy Cr□ Mo Steel, physica status solidi (a) 79(2) (1983) 523-529.

[54] B.K. Tanner, J.A. Szpunar, S.N.M. Willcock, L.L. Morgan, P.A. Mundell, Magnetic and metallurgical properties of high-tensile steels, Journal of Materials Science 23(12) (1988) 4534-4540.

[55] L. Zhou, C. Davis, P. Kok, EM sensors for microstructural measurement – modeling the effect of grain size in single and multi-phase steel microstructures., In-line measurement and control for metals processing IoMMM, Warwick Conference Centre, UK, 2017.

[56] F.J.G. Landgraf, J.R.F. Da Silveira, D. Rodrigues-Jr, Determining the effect of grain size and maximum induction upon coercive field of electrical steels, Journal of Magnetism and Magnetic Materials 323(18-19) (2011) 2335-2339.

[57] J. Pal'a, J. Bydžovský, Barkhausen noise as a function of grain size in non-oriented FeSi steel, Measurement 46(2) (2013) 866-870.

[58] M. Schulte, S. Steentjes, N. Leuning, W. Bleck, K. Hameyer, Effect of Manganese in high silicon alloyed non-oriented electrical steel sheets, Journal of Magnetism and Magnetic Materials (2018).

[59] P. Rastogi, Effect of manganese and sulfur on the texture and magnetic properties of non-oriented steel, IEEE Transactions on Magnetics 13(5) (1977) 1448-1450.

[60] K. Narita, M. Enokizono, Effect of ordering on magnetic properties of 6.5-percent silicon-iron alloy, IEEE Transactions on Magnetics 15(1) (1979) 911-915.

[61] L. Zhou, J. Liu, X.J. Hao, M. Strangwood, A.J. Peyton, C.L. Davis, Quantification of the phase fraction in steel using an electromagnetic sensor, NDT & E International 67 (2014) 31-35.

[62] O. Saquet, J. Chicois, A. Vincent, Barkhausen noise from plain carbon steels: analysis of the influence of microstructure, Materials Science and Engineering: A 269(1) (1999) 73-82.

[63] X.J. Hao, W. Yin, M. Strangwood, A.J. Peyton, P.F. Morris, C.L. Davis, Modelling the electromagnetic response of two-phase steel microstructures, NDT & E International 43(4) (2010) 305-315.

[64] L. Zhou, C. Davis, P. Kok, F. Van Den Berg, Magnetic NDT for Steel Microstructure Characterisation–Modelling the Effect of Second Phase Distribution on Magnetic Relative Permeabilty, Proceedings of the 19th World Conference on Non-Destructive Testing, Munich, Germany, 2016, pp. 13-17.

[65] M. Papaelias, M. Strangwood, A. Peyton, C. Davis, Detection and measurement of phase transformation in steels using electromagnetic sensors–experimental results and modelling simulations, Metallurgical and Materials Transactions A 35(13) (2004) 965-972.

[66] S. Thompson, The magnetic properties of plastically deformed steels, Durham University, Durham University., 1991.

[67] A. Sipeky, A. Iványi, Magnetic hysteresis under applied stress, Physica B: Condensed Matter 372(1-2) (2006) 177-180.

[68] C. Casavola, C. Pappalettere, F. Tursi, Calibration of barkhausen noise for residual stress measurement, Experimental and Applied Mechanics, Volume 4, Springer2013, pp. 255-266.

[69] B. Cullity, Introduction to Magnetic Materials, Addison, Wiley, Reading, 1972.

[70] H.I. Yelbay, I. Cam, C.H. Gür, Non-destructive determination of residual stress state in steel weldments by Magnetic Barkhausen Noise technique, NDT & E International 43(1) (2010) 29-33.

[71] T.W. Krause, L. Clapham, D.L. Atherton, Characterization of the magnetic easy axis in pipeline steel using magnetic Barkhausen noise, Journal of applied physics 75(12) (1994) 7983-7988.

[72] J.W. Wilson, N. Karimian, J. Liu, W. Yin, C.L. Davis, A.J. Peyton, Measurement of the magnetic properties of P9 and T22 steel taken from service in power station, Journal of Magnetism and Magnetic Materials 360 (2014) 52-58.

[73] J. Liu, J. Wilson, C.L. Davis, A. Peyton, Magnetic characterisation of grain size and precipitate distribution by major and minor BH loop measurements, Journal of Magnetism and Magnetic Materials 481 (2019) 55-67.

[74] L. Dijkstra, C. Wert, Effect of inclusions on coercive force of iron, Physical Review 79(6) (1950) 979.

[75] C. Kittel, Physical theory of ferromagnetic domains, Reviews of modern Physics 21(4) (1949) 541.

[76] H.G. Booker, Energy in electromagnetism, Peregrinus1982.

[77] R. Levine, McGraw-Hill Encyclopedia of Science and Technology, AAPT, 1984.

[78] R. Plonsey, R.E. Collin, Principles and applications of electromagnetic fields, McGraw-Hill1961.

[79] W.Y. Du, Resistive, capacitive, inductive, and magnetic sensor technologies, CRC Press2014.

[80] A. Van Heuvelen, Millikan lecture 1999: The workplace, student minds, and physics learning systems, American Journal of Physics 69(11) (2001) 1139-1146.

[81] A. Van Heuvelen, Physics, a general introduction, Little, Brown1986.

[82] N. Bowler, Frequency-Dependence of Relative Permeability in Steel, AIP Conference Proceedings, AIP, 2006, pp. 1269-1276.

[83] D. Brandon, W.D. Kaplan, Microstructural characterization of materials, John Wiley & Sons2013.

[84] N.E. Prasad, R. Wanhill, Aerospace Materials and Material Technologies, Springer2017.

[85] B. Inkson, Scanning electron microscopy (SEM) and transmission electron microscopy (TEM) for materials characterization, Materials characterization using nondestructive evaluation (NDE) methods, Elsevier2016, pp. 17-43.

[86] J.I. Goldstein, D.E. Newbury, P. Echlin, D.C. Joy, C.E. Lyman, E. Lifshin, L. Sawyer, J.R. Michael, Quantitative X-ray analysis: the basics, Scanning Electron Microscopy and X-ray Microanalysis, Springer2003, pp. 391-451.

[87] D. Phelan, M.H. Reid, R. Dippenaar, High Temperature Laser Scanning Confocal Microscopy for real-time studies of phase transformations, Microscopy and Microanalysis 11(S02) (2005) 670-671.

[88] C. Suryanarayana, Microstructure: An Introduction, Aerospace Materials and Material Technologies, Springer2017, pp. 105-123.

[89] Y. Chen, A. Herz, Y. Li, C. Borchers, P. Choi, D. Raabe, R. Kirchheim, Nanocrystalline Fe–C alloys produced by ball milling of iron and graphite, Acta Materialia 61(9) (2013) 3172-3185.

[90] ASTM, A1033 - 10, Standard Practice for Quantitative Measurement and Reporting of Hypoeutectoid Carbon and Low-Alloy Steel, 2010.

[91] D.-W. Suh, C.-S. Oh, H.N. Han, S.-J. Kim, Dilatometric analysis of austenite decomposition considering the effect of non-isotropic volume change, Acta materialia 55(8) (2007) 2659-2669.

[92] T. Kop, J. Sietsma, S. Van Der Zwaag, Dilatometric analysis of phase transformations in hypo-eutectoid steels, Journal of Materials Science 36(2) (2001) 519-526.

[93] M. Gómez, M. SF, G. Caruana, Modelling of phase transformation kinetics by correction of dilatometry results for a ferritic Nb-microalloyed steel, ISIJ international 43(8) (2003) 1228-1237.

[94] D. San Martín, P. Rivera-Díaz-del-Castillo, C. García-de-Andrés, In situ study of austenite formation by dilatometry in a low carbon microalloyed steel, Scripta Materialia 58(10) (2008) 926-929.

[95] J.-Y. Kang, S.-J. Park, D.-W. Suh, H.N. Han, Estimation of phase fraction in dual phase steel using microscopic characterizations and dilatometric analysis, Materials Characterization 84 (2013) 205-215.

[96] J. Epp, X-ray diffraction (XRD) techniques for materials characterization, Materials Characterization Using Nondestructive Evaluation (NDE) Methods, Elsevier2016, pp. 81-124.

[97] A. Bénéteau, E. Aeby-Gautier, G. Geandier, P. Weisbecker, A. Redjaïmia, B. Appolaire, Tempering of a martensitic stainless steel: Investigation by in situ synchrotron X-ray diffraction, Acta Materialia 81 (2014) 30-40.

[98] P. Haušild, V. Davydov, J. Drahokoupil, M. Landa, P. Pilvin, Characterization of strain-induced martensitic transformation in a metastable austenitic stainless steel, Materials & Design 31(4) (2010) 1821-1827.

[99] J.R. Tolchard, A. Sømme, J.K. Solberg, K.G. Solheim, On the measurement of austenite in supermartensitic stainless steel by X-ray diffraction, Materials Characterization 99 (2015) 238-242.

[100] W. Solano-Alvarez, H. Abreu, M. Da Silva, M. Peet, Phase quantification in nanobainite via magnetic measurements and X-ray diffraction, Journal of Magnetism and Magnetic Materials 378 (2015) 200-205.

[101] M. Wieβner, M. Leisch, H. Emminger, A. Kulmburg, Phase transformation study of a high speed steel powder by high temperature X-ray diffraction, Materials Characterization 59(7) (2008) 937-943.

[102] E. Cakmak, H. Choo, K. An, Y. Ren, A synchrotron X-ray diffraction study on the phase transformation kinetics and texture evolution of a TRIP steel subjected to torsional loading, Acta Materialia 60(19) (2012) 6703-6713.

[103] M.R. Miranda, J. Sasaki, S. Tavares, H. De Abreu, J. Neto, The use of X-ray diffraction, microscopy, and magnetic measurements for analysing microstructural features of a duplex stainless steel, Materials characterization 54(4-5) (2005) 387-393.

[104] G.P. Glasgow, Radiation Protection Instrumentation, Encyclopedia of Medical Devices and Instrumentation (2006).

[105] H. Parker, Health-physics, instrumentation, and radiation protection, Advances in biological and medical physics, Elsevier1948, pp. 223-285.

[106] P.J. Shull, Nondestructive evaluation: theory, techniques, and applications, CRC press2016.

[107] G. Hübschen, Ultrasonic techniques for materials characterization, Materials Characterization Using Nondestructive Evaluation (NDE) Methods, Elsevier2016, pp. 177-224.

[108] L. Cartz, Nondestructive testing. ASM International, The Materials Information Society, Materials Park, OH (1995).

[109] J. Wilson, Investigation of electromagnetic NDT&E techniques for comprehensive material assessment, University of Newcastle Upon Tyne, 2009.

[110] B. Wang, X. Wang, L. Hua, J. Li, Q. Xiang, Mean grain size detection of DP590 steel plate using a corrected method with electromagnetic acoustic resonance, Ultrasonics 76 (2017) 208-216.

[111] B. Hutchinson, E. Lindh-ulmgren, L. Carlson, Application of Laser Ultrasonics to Studies of Recrystallisation and Grain Growth in Metals, 1st International symposium on laser ultrasonics: science, technology and applicaions. Montreal, Canada2008, Citeseer.

[112] C.H. Gür, B.O. Tuncer, Characterization of microstructural phases of steels by sound velocity measurement, Materials Characterization 55(2) (2005) 160-166.

[113] A. Vary, Correlations between ultrasonic and fracture toughness factors in metallic materials, Fracture Mechanics: Proceedings of the Eleventh National Symposium on Fracture Mechanics: Part I, ASTM International, 1979.

[114] A. Moro, C. Farina, F. Rossi, Measurement of ultrasonic wave velocity in steel for various structures and degrees of cold-working, NDT International 13(4) (1980) 169-175.

[115] V.L. de Araújo Freitas, V.H.C. de Albuquerque, E. de Macedo Silva, A.A. Silva, J.M.R. Tavares, Nondestructive characterization of microstructures and determination of elastic properties in plain carbon steel using ultrasonic measurements, Materials Science and Engineering: A 527(16-17) (2010) 4431-4437.

[116] H. Willems, Nondestructive determination of hardening depth in induction hardened components by ultrasonic backscattering, Review of Progress in Quantitative Nondestructive Evaluation, Springer1991, pp. 1707-1713.

[117] H. Ogi, M. Hirao, T. Honda, Ultrasonic attenuation and grain-size evaluation using electromagnetic acoustic resonance, The Journal of the Acoustical Society of America 98(1) (1995) 458-464.

[118] S. Takahashi, S. Kobayashi, H. Kikuchi, Y. Kamada, K. Ara, Analysis of minor hysteresis loops of cold rolled low carbon steel, IEEE transactions on magnetics 42(11) (2006) 3782-3784.

[119] S. Takahashi, S. Kobayashi, H. Kikuchi, Y. Kamada, Relationship between mechanical and magnetic properties in cold rolled low carbon steel, Journal of applied physics 100(11) (2006) 113908.

[120] S. Kobayashi, M. Tanaka, T. Kimura, Y. Kamada, H. Kikuchi, S. Takahashi, T. Ohtani, Changes of magnetic minor hysteresis loops during creep in Cr-Mo-V ferritic steel, J. Electr. Eng 59(7) (2008) 29-32.

[121] O. Perevertov, O. Stupakov, I. Tomáš, B. Skrbek, Detection of spring steel surface decarburization by magnetic hysteresis measurements, Ndt & E International 44(6) (2011) 490-494.

[122] K. Gurruchaga, A. Martínez-De-Guerenu, F. Arizti, Monitoring recovery and recrystallization in interstitial free (IF) steel by magnetic hysteresis loop measurements, Proc. European Conf. on NDT (ECNDT), 2006.

[123] Y.S. Lukin, S. Bakhtin, A. Lukin, A. Zaveryukha, Structure of IF steel in continuous annealing, Steel in Translation 42(4) (2012) 365-367.

[124] N. Karimian, J.W. Wilson, A.J. Peyton, W. Yin, J. Liu, C.L. Davis, Differential permeability behaviour of P9 and T22 power station Steels, Journal of Magnetism and Magnetic Materials 352 (2014) 81-90.

[125] G. Fillion, M. Lord, J.F. Bussière, Inference of hardness from magnetic measurements in pearlitic steels, Review of progress in quantitative nondestructive evaluation, Springer1990, pp. 1887-1893.

[126] A. Martínez-de-Guerenu, A.L. D. Jorge-Badiola, I. Gutierrez, Comparative sensitivity study of magnetic hysteresis loops and Barkhausen noise for the non-destructive characterisation of dual-phase and mixed
microstructures, In-Line Measurement and Control for Metals Processing 2017, Warwick Conference Centre, 2017.

[127] F. Rumiche, J.E. Indacochea, M.L. Wang, Assessment of the Effect of Microstructure on the Magnetic Behavior of Structural Carbon Steels Using an Electromagnetic Sensor, Journal of Materials Engineering and Performance 17(4) (2007) 586-593.

[128] S. Zhang, X. Shi, L. Udpa, Y. Deng, Micromagnetic measurement for characterization of ferromagnetic materials' microstructural properties, AIP Advances 8(5) (2018) 056614.

[129] A. Sorsa, K. Leiviskä, S. Santa-aho, T. Lepistö, Quantitative prediction of residual stress and hardness in case-hardened steel based on the Barkhausen noise measurement, NDT & E International 46 (2012) 100-106.

[130] N. Karimian, Monitoring of Power Station Steels Using Electromagnetic Sensors, The University of Manchester (United Kingdom), 2014.

[131] C.-G. Stefanita, Barkhausen noise as a magnetic nondestructive testing technique, Springer2008.

[132] S. Ghanei, M. Kashefi, M. Mazinani, Comparative study of eddy current and Barkhausen noise nondestructive testing methods in microstructural examination of ferrite–martensite dual-phase steel, Journal of Magnetism and Magnetic Materials 356 (2014) 103-110.

[133] W. Zhu, S. Cruchley, W. Yin, X. Hao, C. Davis, A. Peyton, Evaluation of rail decarburisation depth using a H-shaped electromagnetic sensor, NDT & E International 46 (2012) 63-69.

[134] W. Zhu, W. Yin, A. Peyton, H. Ploegaert, Modelling and experimental study of an electromagnetic sensor with an H-shaped ferrite core used for monitoring the hot transformation of steel in an industrial environment, NDT & E International 44(7) (2011) 547-552.

[135] S. Ghanei, M. Kashefi, M. Mazinani, Eddy current nondestructive evaluation of dual phase steel, Materials & Design 50 (2013) 491-496.

[136] H. YANG, F. BERG, A. LUINENBURG, C. BOS, G. KUIPER, J. MOSK, P. HUNT, M. DOLBY, M. FLICOS, A. PEYTON, In-Line Quantitative Measurement of Transformed Phase Fraction by EM Sensors during Controlled Cooling on the Run-Out Table of a Hot Strip Mill, 19th World Conference on Non-Destructive Testing, 2016.

[137] A. Peyton, N. KARIMIAN, J. WILSON, M. STOLZENBERG, R. SCHMIDT, C. DAVIS, L. ZHOU, P. LOMBARD, P. MEILLAND, A. MARTINEZ-DE-GUERENU,

The Application of Electromagnetic Measurements for the Assessment of Skin Passed Steel Samples, WCNDT-2016, Th_2_1_4 (2016).

[138] M. STOLZENBERG, Online material characterisation at strip production (OMC), EUR 25879, 2013.

[139] B. Wolter, G. Dobmann, I. Fraunhofer, Micromagnetic testing for rolled steel, European Conference on Non-destructive Testing (9), 2006.

[140] A. Skarlatos, C. Reboud, T. Svaton, A. de Guerenu, T. Kebe, F. Van-Den-Berg, Modelling the IMPOC response for different steel strips, Proceedings of the 19th World Conference on Non-destructive Testing WCNDT, 2016, p. 22.

[141] J. Shen, L. Zhou, W. Jacobs, P. Hunt, C. Davis, Real-time microstructure control using EMspecTM sensor, IOM3, Warwick University, 2017.

[142] A. International, Standard test methods for determining average grain size, na2010.

[143] A. Standard, E92,“, Standard Test Method for Vickers Hardness of Metallic Materials, ASTM International, West Conshohocken, PA (2003).

[144] A.A.S.f. Testing, Materials, Standard test methods for tension testing of metallic materials, ASTM international2009.

[145] Y. Cao, K. Xu, W. Jiang, T. Droubay, P. Ramuhalli, D. Edwards, B.R. Johnson, J. McCloy, Hysteresis in single and polycrystalline iron thin films: Major and minor loops,

first order reversal curves, and Preisach modeling, Journal of Magnetism and Magnetic Materials 395 (2015) 361-375.

[146] D.C. Jiles, D.L. Atherton, Theory of ferromagnetic hysteresis, Journal of magnetism and magnetic materials 61(1-2) (1986) 48-60.

[147] D.C. Jiles, J. Thoelke, M. Devine, Numerical determination of hysteresis parameters for the modeling of magnetic properties using the theory of ferromagnetic hysteresis, IEEE Transactions on magnetics 28(1) (1992) 27-35.

[148] D. Jiles, A self consistent generalized model for the calculation of minor loop excursions in the theory of hysteresis, IEEE Transactions on Magnetics 28(5) (1992) 2602-2604.

[149] COMSOL, COMSOL Multiphysics:, AC/DC Module User'sGuide, 2012.

[150] J. Shen, W. Jacobs, L. Zhou, P. Hun, C. Davis, Use of COMSOL® AC/DC Module to Model a EM Sensor Deployed to Monitor Steel Transformation, COMSOL CONFERENCE 2018 LAUSANNE, Switzerland, 2018.

[151] W. Yin, X. Hao, A. Peyton, M. Strangwood, C. Davis, Measurement of permeability and ferrite/austenite phase fraction using a multi-frequency electromagnetic sensor, NDT & e International 42(1) (2009) 64-68.

[152] M. Mazinani, W.J. Poole, Effect of Martensite Plasticity on the Deformation Behavior of a Low-Carbon Dual-Phase Steel, Metallurgical and Materials Transactions A 38(2) (2007) 328-339.

[153] A. Ebrahimian, S.S. Ghasemi Banadkouki, Mutual mechanical effects of ferrite and martensite in a low alloy ferrite-martensite dual phase steel, Journal of Alloys and Compounds 708 (2017) 43-54.

[154] A.E. Berkowitz, E. Kneller, Magnetism and metallurgy, Academic Press Inc1969.

[155] G. Krauss, Martensite in steel: strength and structure, Materials science and engineering: A 273 (1999) 40-57.

[156] S. Takebayashi, T. Kunieda, N. Yoshinaga, K. Ushioda, S. Ogata, Comparison of the dislocation density in martensitic steels evaluated by some X-ray diffraction methods, ISIJ international 50(6) (2010) 875-882.

[157] S. Katani, S. Ziaei-Rad, N. Nouri, N. Saeidi, J. Kadkhodapour, N. Torabian, S. Schmauder, Microstructure modelling of dual-phase steel using SEM micrographs and Voronoi polycrystal models, Metallography, Microstructure, and Analysis 2(3) (2013) 156-169.

[158] R. Davies, Influence of martensite composition and content on the properties of dual phase steels, Metallurgical Transactions A 9(5) (1978) 671-679.

[159] M. Pouranvari, Tensile strength and ductility of ferrite-martensite dual phase steels, Metalurgija 16(3) (2010) 187-194.

[160] J.W. Byeon, S.I. Kwun, Magnetic evaluation of microstructures and strength of eutectoid steel, Materials Transactions 44(10) (2003) 2184-2190.

[161] G. Bertotti, Hysteresis in magnetism: for physicists, materials scientists, and engineers, Academic press1998.

[162] X. Hao, W. Yin, M. Strangwood, A. Peyton, P. Morris, C. Davis, Characterization of decarburization of steels using a multifrequency electromagnetic sensor: experiment and modeling, Metallurgical and Materials Transactions A 40(4) (2009) 745-756.

[163] R. Cacak, J. Craig, Magnetic field uniformity around near-Helmholtz coil configurations, Review of Scientific Instruments 40(11) (1969) 1468-1470.

[164] L. Zhou, Non-destructive characterisation of steel microstructures using electromagnetic sensors, University of Birmingham, 2015.

[165] S. Habermehl, D. Jiles, C. Teller, Influence of heat treatment and chemical composition on the magnetic properties of ferromagnetic steels, IEEE transactions on magnetics 21(5) (1985) 1909-1911.

[166] M. Kersten, Grundlagen einer Theorie der ferromagnetischen Hysterese und der Koerzitivkraft, JW Edwards1943.

[167] R. Becker, W. Döring, Ferromagnetismus, Springer-Verlag2013.

[168] E. Kondorsky, On the nature of coercive force and irreversible changes in magnetization, Phys. Z. Sowjetunion 11(597) (1937) 68.

[169] M. Jolfaei, J. Shen, A. Smith, L. Zhou, C. Davis, EM Sensor System for Characterisation of Advanced High Strength Strip Steels, in: Dominique Lesselier, C. Reboud (Eds.) Electromagnetic Non-Destructive Evaluation, IOS Press, Paris, 2017, pp. 49-56.

[170] S. Yamaura, Y. Furuya, T. Watanabe, The effect of grain boundary microstructure on Barkhausen noise in ferromagnetic materials, Acta Materialia 49(15) (2001) 3019-3027.

[171] X. Xu, S. van der Zwaag, W. Xu, The effect of martensite volume fraction on the scratch and abrasion resistance of a ferrite–martensite dual phase steel, Wear 348-349 (2016) 80-88.

[172] H.-C. Chen, G.-H. Cheng, Effect of martensite strength on the tensile strength of dual phase steels, Journal of materials science 24(6) (1989) 1991-1994.

[173] K. Hasegawa, Y. Toji, H. Minami, H. Ikeda, T. Morikawa, K. Higashida, Effect of martensite fraction on tensile properties of dual-phase steels, Tetsu-To-Hagane/Journal of the Iron and Steel Institute of Japan 98(6) (2012) 320-327.

[174] M. Calcagnotto, D. Ponge, D. Raabe, Effect of grain refinement to 1μm on strength and toughness of dual-phase steels, Materials Science and Engineering: A 527(29-30) (2010) 7832-7840.

[175] S. Ghanei, A. Saheb Alam, M. Kashefi, M. Mazinani, Nondestructive characterization of microstructure and mechanical properties of intercritically annealed dual-phase steel by magnetic Barkhausen noise technique, Materials Science and Engineering: A 607 (2014) 253-260.

[176] S. Titto, M. Otala, S. Säynäjäkangas, Non-destructive magnetic measurement of steel grain size, Non-Destructive Testing 9(3) (1976) 117-120.

[177] M. Aghadavoudi-Jolfaei, J. Shen, A. Smith, L. Zhou, C. Davis, Non-destructive measurement of microstructure and tensile strength in varying thickness commercial DP steel strip using an EM sensor, Journal of Magnetism and Magnetic Materials 473 (2019) 477-483.